Electron Microscopy and III-Nitride Nanostructured

Eirini Sarigiannidou

Université Joseph Fourier – Grenoble I
Sciences & Géographie

THÈSE

Pour obtenir le grade de

DOCTEUR DE L'UNIVERSITÉ JOSEPH FOURIER

Discipline : **Physique**

Présentée et soutenue publiquement par

Eirini SARIGIANNIDOU

le 10 décembre 2004

Electron Microscopy and III-Nitride Nanostructures

Composition du jury :

Benoît BOULANGER	Président
Martin HYTCH	Examinateur
Philomela KOMNINOU	Rapporteur
Gérard NOUET	Rapporteur
Jean-Luc ROUVIERE	Directeur de thèse

Cette thèse a été préparée au sein du CEA Grenoble
Département de Recherche Fondamentale sur la Matière Condensée
Service de Physique des Matériaux et des Microstructures

Χαλεπόν οὔτω τι ποιῆσαι ὥστε μηδέν ἁμαρτεῖν,
Χαλεπόν δέ καί ἀναμαρτήτως τι ποιήσαντα
μή ἀγνώμονι κριτῇ περιτυχεῖν.

Ξενοφῶντος, *Απομνημονεύματα*

Ό,τι κατορθώνει ο ποιητής με τις λέξεις, το ξεπερνά η φύση με την εικόνα.
Ό,τι κατορθώνει ο μουσουργός με τους ήχους, το ξεπερνά η φύση με τη σιωπή.
Ό,τι κατορθώνει ο φιλόσοφος με το λόγο, το ξεπερνά η φύση με το παράλογο.

What the poet achieves with the words, the nature overcomes it with the images.
What the composer achieves with the sounds, the nature overcomes it with the silence.
What the philosopher achieve with the speech, the nature overcomes it with the absurd.

Ιάσων Ευαγγέλου, *Ψηφίδες*

To my parents,

Πελαγία and Γιώργο

and by brothers

Βασίλη and Κώστα

Acknowledgements

The present thesis has been developed in CEA-Grenoble in the Service of Physics of Materials and Microstructures (SP2M) of the Department of Fundamental Research in Condensed Materials (DRFMC). I would like to thank **Jean-Louis Pautrat** and **Noël Magnéa** for their warm welcome in the center of CEA.

I would like to thank **Benoit Boulanger**, professor of the University Joseph Fourier, for honoring me by presiding the Jury of my thesis. I am very grateful to **Philomela Komninou** (Aristotle University of Thessaloniki, Greece) and **Gérard Nouet** (ENSI-CAEN/SIFCOM, Caen) for reporting on this work. My acknowledge also to **Martin Hÿtch** for accepting to be a member of the jury. I thank them all for the time that they have consecrated to read this manuscript and for the interest that they have shown in this work.

I would like to express my gratitude to my thesis advisor **Jean-Luc Rouvière** who has successfully supervised this work and guided me during these three years in the world of electron microscopy. He has taught me how to be independent and how to establish new collaborations.

A PhD is never a result coming for one person alone. I would like to thank all the people who have contributed to the realization of this work.

First of all, I want to thank the members (ancients and news) of the my laboratory (Laboratoire d'Etudes des Matériaux par Microscopie Avancée, LEMMA) for making feel part of the family. In particular, I am thankful to **Pascale Bayle-Guillemaud** for instructing me in the techniques of EFTEM and EELS, for her patience and her useful advices. Many appreciations to **Jany Thibault** and to **Jean-Michel Pénisson** for the fruitful discussions and for motivating me to discover the beauty of the French Alps. **Rémi Frossard** and **Florence Madeira** were the ones who have initiated me into TEM sample preparation. It was/is always a great pleasure to have a coffee break with **Karine Rousseau**, **Guillaume Radtke**, **Laurent Clement** and **Violaine Salvador**. These pauses were the occasion to exchange ideas, experiences and thoughts, to find solutions to various scientific and computer problems and personally to enrich my vocabulary and to learn the French culture. A great thank to Violaine not only for her precious technical support but also for helping me with my adventures in writing texts in French.

This work certainly would not be possible without the very close and beneficial collaboration with the elaborators: **Bruno Daudin**, **Eva Monroy**, **Noëlle Gogneau**, **Christoph Adelmann** and **Julien Brault**. Thank you Bruno for your close interest concerning the TEM results and for your gentle way to put pressure on me and make things progress. Many appreciations to Noëlle for the moments that we shared in trying to understand the behavior of nitrides (and not only...). Special thanks to Eva, for her support, for being always available, for her competence and for her precious help in reading and correcting this manuscript.

I acknowledge **Edith Bellet-Amalric** for the X-ray diffraction measurements and her patience to explain me how she obtained the different results. Many thanks also to **Denis Jalabert** for the RBS measurements. I am grateful to **Aleksey D. Andreev** for performing some of the theoretical calculations presented in this thesis. For the anomalous grazing incidence x-ray diffraction experiments, I would like to thank **Virginie Chamard**. I express my gratitude to the people at the ESRF beamline ID 12 **Andrei Rogalev**, **Fabrice Wilhelm** and **Nicola Jaouen** for their help with the X-ray linear dichroism experiments. Thank you Fabrice for your patience and all the days and nights that you spent during these experiments.

Many appreciations to the members of the SP2M secretary and especially to **Carmelo Castagna**, who were always willing to help me with the administration papers.

To all my new friends here in France (Marina, Andrei, Artem, Léonid, Violaine, Eva...) and my everlasting friends back in Greece (Sifis, Antigoni, Haris, Aris, Roula, Mary...) a big thank-you for your constant support, for your advices, for listening, for everything.

Thanks to my Fabrice for making my life happy and complete.

Finally, I would like to express my sincerest gratitude and thank to my family. My parents: $\Pi\varepsilon\lambda\alpha\gamma\iota\alpha$ and $\Gamma\iota\varpi\rho\gamma o$ and to my brothers: $K\varpi\sigma\tau\alpha$ and $B\alpha\sigma\iota\lambda\eta$ for believing in my choice, for their love, for all the freedom and the support. Thank you.

Résumé

Ce travail a porté sur l'étude et la caractérisation des puits et des boîtes quantiques de GaN dans AlN par différentes techniques de Microscopie Electronique en Transmission (MET). Ces types de nanostructures constituent les parties actives des divers dispositifs électroniques et optoélectroniques à base de nitrures d'éléments III. Une caractérisation structurale approfondie de ces hétérostructures est donc nécessaire afin de comprendre et d'optimiser leurs conditions de croissance. Laquelle est directement liée à la réalisation de dispositifs efficaces et reproductifs.

La MET haute résolution utilisée comme technique principale nous a permis d'extraire de manière quantitative des informations concernant la qualité des interfaces, la taille, la composition chimique et la distribution des contraintes dans les différentes nanostructures de nitrures. Cependant, la contribution des autres techniques de microscopie électronique comme la MET en mode conventionnel, en faisceau convergent et l'imagerie filtrée était nécessaire afin de réaliser une étude structurale complète et précise.

Chapitre 1: Semi-conducteurs des nitrures d'élément III

Ce chapitre permet d'introduire le lecteur dans le monde des nitrures. Nous commençons par donner l'historique de ces matériaux dans le but de rappeler quels sont les intérêts physiques et industriels de ces systèmes. Ensuite, nous introduisons leurs propriétés structurales puis nous détaillons la structure cristallographique de la phase hexagonale wurtzite et nous mettons l'accent sur le caractère anisotrope et polaire de cette structure dans la direction [0001]. Par ailleurs, leurs propriétés élastiques sont aussi rappelées.

La dernière partie de ce chapitre est dévouée à l'élaboration des nitrures. En particulier, nous discutons de la difficulté du choix du substrat associé à l'élaboration des nitrures. Nous abordons aussi les différentes techniques de croissance de ces matériaux en privilégiant l'épitaxie par jets moléculaires assistée par plasma d'azote. Cette technique est celle utilisée pour l'élaboration de tous les échantillons étudiés dans cette thèse. La

totalité des ces échantillons a été effectué au laboratoire "Nanophysique et Semiconducteurs" du CEA-Grenoble.

Chapitre 2: Techniques de microscopie électronique

L'objectif de ce chapitre est de présenter les diverses techniques de microscopie électronique que j'ai utilisé enfin d'examiner la qualité structurale des différentes nanostructures de nitrures. Le chapitre est divisé en deux parties.

Dans la première partie, nous avons souhaité rappeler brièvement le principe des techniques utilisées:

- La technique de microscopie conventionnelle en mode "deux-ondes" ou en "faisceau faible"
- La microscopie électronique haute résolution (MEHR ou HRTEM)
- La diffraction électronique en faisceau convergent (CBED)
- L'imagerie filtrée en énergie.

Dans la seconde partie, nous exposons comment nous avons appliqué ces techniques à l'étude des nitrures, en particulier de GaN et d'AlN, les matériaux sur lesquels cette étude a porté. Nous précisons les types d'information que nous avons extrait par chacune de cette technique. Spécifiquement:

- *L'identification des dislocations présentes dans les nanostructures par microscopie conventionnelle.*

  Par cette technique, l'image formée à partir des variations d'amplitude d'un seul faisceau (soit transmis, soit diffracté) permet de caractériser les défauts cristallins. Le critère de visibilité d'un défaut est le produit . Nous avons expliqué comment appliquer ce critère à l'indentification des dislocations parfaites (coin, vis et mixte) de la structure wurtzite.

- *La détermination de la polarité absolue d'un cristal de GaN par CBED.*

  Avec cette technique, les contrastes contenus dans les disques correspondent aux variations d'intensité des faisceaux diffractés en fonction de leur écart à Bragg. Ces contrastes conservent la symétrie du cristal et en particulier l'information de polarité. En général, la détermination de la polarité avec cette technique, fait appel aux simulations et nécessite une calibration des orientations relatives entre les cristaux et les diagrammes de diffraction associés.

- *Le positionnement des colonnes atomiques sur une image haute résolution de cristal parfait de GaN ou d'AlN pour les deux axes d'observation que nous avons utilisés: l'axe de zone <2,-1,-1,0> et l'axe <0,1,-1,0>.*

  En MEHR, le contraste de l'image est dû aux interférences de phase entre le faisceau transmis et plusieurs faisceaux diffractés. L'information portée par la fonction d'onde à la sortie du cristal analysé est déformée par le microscope. Ainsi, des simulations numériques sont nécessaires pour mieux interpréter les images expérimentales parce qu'elles permettent de relier la position des motifs de l'image à celle des colonnes atomiques. Nous verrons dans les chapitres suivants que les images de cristaux de GaN et d'AlN que nous avons simulées seront utiles à l'analyse quantitative des images d'hétérostructures GaN/AlN et à la détermination de la structure atomique des différents défauts cristallins.

Pour toutes les simulations numériques, nous avons utilisé le logiciel EMS (ou JEMS).

Chapitre 3: Analyse quantitative des images haute résolution

Le but principal de cette thèse est l'analyse numérique des images haute résolution de façon à obtenir des informations quantitatives. Dans ce chapitre, nous présenterons les méthodes d'analyses numériques que nous avons utilisé et les différentes conditions expérimentales que nous avons appliquées afin d'acquérir des résultas précis.

En particulier, les deux méthodes utilisées sont : (a) la méthode des projections et (b) l'analyse de la phase géométrique (GPA). Pour chacune de ces méthodes nous précisons leurs principes de base et les informations quantitatives que nous pouvons obtenir, dont la mesure locale des paramètres de maille. Cette mesure permet de déduire l'état de contrainte des matériaux impliqués, la qualité des interfaces, les variations de composition chimique et la quantité d'un matériau B déposé entre deux couches de matériau A dans une hétérostructure de type A/B/A. En outre, nous décrivons les paramètres numériques et expérimentaux qui peuvent limiter la précision de ces méthodes, les façons avec lesquelles nous pouvons les optimiser et quelle précision peut être finalement atteinte. Nous prêtons attention sur GPA, qui est une nouvelle méthode d'analyse quantitative pour les images haute résolution. Nous avons essayé d'approcher cette méthode de manière plus théorique en discutant en détail de sa base mathématique. Le but était de comprendre pourquoi elle est si efficace malgré sa simplicité. Concernant ces deux méthodes, nous pouvons conclure que la méthode des projections est plus puissante pour l'analyse des profils des interfaces alors que GPA a l'avantage de permettre de mesurer et de relever directement

le champ des déplacements et des déformations. Par ailleurs, les deux méthodes ont la même précision concernant la mesure locale des paramètres de maille.

Dans cette thèse, pour l'obtention d'un meilleur contraste dans nos images expérimentales et pour améliorer le rapport signal-sur-bruit, nous avons acquis des images haute résolution hors axes de zone (off-axis). Particulièrement, pour que nous puissions simuler facilement les différentes hétérostructures, nous avons utilisé des axes de zone secondaire comme l'axe <-1,5,-4,0>. Dans ces types d'images, les plans (0002) sont représentés par des lignes continues.

Finalement, ce chapitre nous permet de démontrer que la camera CCD utilisée pour l'acquisition des nos images expérimentales introduit des distorsions. Une fois identifiée, nous avons proposé une manière de les corriger.

Chapitre 4: Analyse des structures de puits quantiques GaN/AlN

Le chapitre 4 présente nos résultats concernant la caractérisation structurale des puits quantiques de GaN sur AlN. Il est constitué de deux parties.

La première partie concerne l'étude comparative de deux super-réseaux (SLs) de GaN / AlN : un à polarité Ga et un à polarité N. La supériorité de la qualité structurale du super- réseau à polarité Ga est démontrée. En particulier, nous avons trouvé que bien que les interfaces du SL face-N sont irrégulières avec une épaisseur qui varie entre 2-3 monocouches (ML), les interfaces du SL face-Ga sont uniformes, abruptes et leurs épaisseurs ne dépassent pas une monocouche. Des défauts prismatiques {0,1,-1,0} sont uniquement observés dans le Sl à polarité N. Par l'analyse des images haute résolution simulées et expérimentales, nous avons identifié ces défauts comme des domaines d'inversion de polarité du model de Holt (types 1 et 2), qui sont énergétiquement non favorable. Concernant l'état des contraintes des puits quantiques, nous avons pu déduire que dans le SL face-N elles sont presque complètement contraintes sur l'AlN, qui est lui-même contraint par le substrat SiC. Pour le SL face-Ga, en éliminant les possibilités que: (i) il existe un interdiffusion entre le GaN et l'AlN, (ii) la matrice AlN est partiellement contrainte et (iii) l'effet de relaxation de la lame mince est important, nous avons conclu que les puits quantiques sont seulement partiellement contraints.

La deuxième partie met l'accent sur les effets d'encapsulation des puits quantiques de GaN par une couche d'AlN. Nous avons démontré par microscopie électronique en transmission et par spectroscopie de rétrodiffusion d'ions (RBS) que la croissance de l'AlN à haute température (750^{o}C) induit un amincissement des puits quantiques. En plus, par MET nous avons prouvé que la minimisation de l'épaisseur des puits quantiques

n'affecte que l'interface supérieure GaN/AlN. Nous avons montré que cette différence d'épaisseur observée entre le puit quantique encapsulé et celui non encapsulé n'est due ni à une décomposition thermique du GaN ni à la diffusion des atomes d'aluminium dans le puits recouvert. Par conséquent, nous avons conclu que le mécanisme conduisant à l'amincissement des puits quantiques encapsulés dans une matrice d'AlN est un mécanisme d'échange entre les atomes d'Al de la "capping layer" et les atomes de Ga du puits quantique. Ce phénomène qui est thermiquement activé, est favorisé par le fait que l'énergie de liaison existant entre Al et N est plus forte que celle existant entre Ga et N.

Chapitre 5: Analyse des structures de boîtes quantiques GaN/AlN

Dans ce chapitre nous présentons l'analyse effectuée sur des boîtes quantiques de GaN sur AlN.

Dans la première partie, nous examinons la distribution des contraintes dans un super-réseau de boîtes quantiques de GaN sur une matrice d'AlN. Pour cette étude nous avons effectué des mesures de MET haute résolution. Les résultats obtenus ont été par la suite comparés et/ou complétés par des calculs théoriques et par des mesures de diffraction des rayons X. Les boîtes quantiques de GaN sur AlN élaborées par le mode de croissance Stranski-Krastanow, ont la forme de pyramides hexagonales tronquées à facettes {1,-1,03}. A partir de nos images haute résolution, nous avons mesuré leur diamètre (∼30 nm), leur hauteur (∼4 nm) aussi bien que l'épaisseur exacte de la couche de mouillage (∼2 ML). Grâce à l'analyse de la phase géométrique nous avons identifié une variation de paramètre de maille c de la matrice d'AlN située entre les boîtes quantiques de GaN alignées verticalement ou celle située entre les couches de mouillages consécutives. Nous avons prouvé que cette variation est due à une différence de l'état de contrainte de l'AlN et non à cause d'une interdiffusion entre les boîtes GaN et la matrice AlN autour. Spécifiquement, par rapport à la contrainte dans la direction de croissance (e_{zz}) nous avons montré que bien que l'AlN entre les boîtes est contraint, l'AlN entre les couches de mouillage est presque totalement relaxé. Par conséquent, nous avons conclu que cette contrainte produit l'alignement vertical des boîtes dans le super-réseau. En outre, nous avons observé que les boîtes quantiques en surface sont relaxées. Tous ces résultats sont en accord avec : (i) des calculs théoriques de contraintes qui combine la transformée de Fourier et la fonction de Green et (ii) des mesures de diffraction des rayons X qui ont été réalisées à la ligne de lumière ID1 à l'ESRF à Grenoble.

Dans la deuxième partie, nous analysons l'évolution des boîtes quantiques de GaN durant le processus d'encapsulation en fonction de la quantité nominale de GaN déposée

et de la température de croissance de l'AlN. Cette étude a porté sur la compréhension des effets de croissance de l'AlN sur les propriétés structurales des boîtes quantiques de GaN. Nous montrerons par des mesures de MET et de RBS que la croissance de l'AlN induit une réduction isotrope de la taille des boîtes quantiques. Cette réduction, comme dans le cas des puits quantiques, est attribuée à une décomposition du GaN résultant d'un mécanisme d'échange entre les atomes d'aluminium de la couche supérieure d'AlN et les atomes de gallium constitutifs des boîtes quantiques. Finalement, nous montrons que l'échange entre les atomes d'Al et de Ga dépend de l'état de contrainte de la couche de GaN.

Chapitre 6: Dopage des couches de GaN avec du Mg

Dans ce chapitre, nous avons étudié les propriétés structurales et optiques des couches de GaN à polarité N dopées avec du magnésium (Mg). Nous démontrons que le dopage avec du Mg favorise la conversion de la structure de wurtzite à zinc-blende. En particulier, pour des concentrations plus importantes de Mg $[Mg_{SIMS}] = 3 \times 10^{18} cm^{-3}$ la phase cubique devient nominale alors que pour des concentrations plus faibles les films GaN:Mg présentent la structure wurtzite. Nous avons prouvé que l'alignement de la structure cubique est fait avec l'axe [111] perpendiculaire au substrat. La présence de la phase cubique influence notablement les propriétés optiques des couches. Pour des concentrations importantes, les spectres de photoluminescence sont dominés par une ligne à 3.25 eV et une large bande bleue à $\sim$2.9 eV.

Contents

Introduction **1**
Bibliography 4

1 III-V Nitride Semiconductors **5**
1.1 A short history 5
1.2 Structural Properties 7
1.2.1 Crystal Structure 7
1.2.2 Polarity 9
1.3 Elastic Properties 10
1.4 Growth of III-Nitride Semiconductors 11
1.4.1 Bulk growth 11
1.4.2 Substrates for the growth of III nitrides 11
1.4.3 Growth techniques 12
Bibliography 15

2 Electron microscopy techniques **17**
2.1 Electron Microscopy Techniques: Basic Principles 17
2.1.1 Electron-Matter Interaction 17
2.1.2 Diffraction Theory Approaches 18
2.1.3 CTEM: Two-beam and Weak-beam Conditions 19
2.1.4 High Resolution Transmission Electron Microscopy 21
2.1.5 Convergent Beam Electron Diffraction 23
2.1.6 Electron Energy-Loss Spectrometry and Energy-Filtered TEM . . . 24
2.2 Electron Microscopy Techniques: Application to nitrides 27
2.2.1 Sample Preparation 27
2.2.2 Contrast from dislocations for the wurtzite structure 28
2.2.3 Polarity determination by CBED 30
2.2.4 HRTEM Images 30
Bibliography 41

3 Quantitative analysis of HRTEM images **43**
3.1 Projection method . . . 43
3.1.1 Principle . . . 44
3.1.2 Experimental conditions and artifacts . . . 46
3.1.3 Precision in peak location . . . 47
3.1.4 Quantitative analysis of the interplanar distances profiles . . . 48
3.1.5 Use of the projection method in this thesis . . . 59
3.2 Geometric Phase Analysis . . . 61
3.2.1 Principle . . . 61
3.2.2 Theoretical discussions on the GPA . . . 65
3.2.3 One-dimensional formulas . . . 71
3.2.4 Mask functions . . . 73
3.2.5 Use of the GPA in this thesis . . . 76
3.3 Polarity determination. . . . 77
3.4 Distortions in the HRTEM images . . . 80
3.5 Off-axis HRTEM images . . . 86
Bibliography . . . 91

4 GaN/AlN Quantum Well Structures **93**
4.1 Comparison of Ga-face and N-face polarity GaN/AlN superlattices . . . 93
4.1.1 Introduction . . . 93
4.1.2 Ga-face polarity GaN/AlN superlattice . . . 94
4.1.3 N-face polarity GaN/AlN superlattice . . . 104
4.1.4 Conclusions . . . 116
4.2 Effect of AlN overgrowth on the structural quality of GaN QWs . . . 117
4.2.1 Introduction . . . 117
4.2.2 Experimental growth conditions . . . 117
4.2.3 RBS Measurements . . . 118
4.2.4 TEM Measurements . . . 120
4.2.5 Origin of thickness reduction . . . 124
4.2.6 Conclusions . . . 128
Bibliography . . . 129

5 GaN/AlN Quantum Dot Structures **131**
5.1 Quantitative strain analysis in GaN/AlN quantum dots superlattice . . . 131
5.1.1 Introduction . . . 131
5.1.2 Experimental details . . . 132
5.1.3 Morphology of quantum dots . . . 133
5.1.4 Lattice parameter measurement . . . 135

5.1.5 Chemical composition-EFTEM measurements . . . 137
5.1.6 Strain distribution in the superlattice . . . 140
5.1.7 Conclusions . . . 153
5.2 AlN overgrowth and structural quality of GaN quantum dots . . . 155
5.2.1 Introduction . . . 155
5.2.2 Experimental growth conditions . . . 155
5.2.3 RBS measurements . . . 156
5.2.4 Origin of thickness reduction . . . 156
5.2.5 Effect of relaxation . . . 160
5.2.6 Conclusion . . . 161
Bibliography . . . 162

6 Mg Doping of GaN layers 165
6.1 Introduction . . . 165
6.2 Experimental conditions . . . 165
6.3 Optical properties . . . 166
6.4 TEM measurements . . . 167
6.4.1 Heavily Mg-doped GaN samples . . . 168
6.4.2 Slightly Mg-doped GaN sample . . . 172
6.4.3 Interpretation of the PL spectra . . . 172
6.5 Conclusions . . . 174
Bibliography . . . 175

General Conclusions 177

Appendices 183

A Crystallographic relationships for the hexagonal lattice 185

B Linear Elasticity 187
B.1 Elastic constants definition . . . 187
B.2 Coherent deposition of a film on a substrate . . . 188

C Basic Parameters of GaN and AlN 191
C.1 Gallium Nitride (GaN) . . . 191
C.2 Aluminium Nitride (AlN) . . . 193
Bibliography . . . 195

D Local lattices and Distances in the Direct and Reciprocal spaces **199**
D.1 Local Lattices 199
D.2 Distances in the Direct and Reciprocal spaces 200

E List of examined samples **201**
Bibliography 205

F X-ray absorption spectroscopy experiments **207**
Bibliography 210

G Acronym **211**

Introduction

The main aim of the work presented in this thesis is to **investigate and characterize by transmission electron microscopy (TEM) GaN/AlN quantum wells and quantum dots heterostructures**.

Semiconductor III-nitrides such as aluminum nitride (AlN), gallium nitride (GaN) and indium nitride (InN) have raised a lot of interest due to their potential use in optoelectronic devices – both emitters and detectors – and high power/temperature electronic devices. Several reviews concerning the challenges and achievements in the fields of III-nitride based materials and their associated devices have been published [1–5]. In principle, these materials and their ternary and quaternary alloys cover an energy bandgap range between the bandgap of InN (0.8 eV) and that of AlN (6.2 eV). In particular, nitrides are suitable for applications such as amber, green, blue and ultraviolet Light Emitting Diodes (LEDs) [6–8], UV detectors [9–11], and Laser Diodes (LDs) [1, 6, 12, 13].

Generally, device applications require the growth of increasingly complex heterostructures such as quantum wells (QWs) and quantum dots (QDs) which constitute the active part of the device. In particular, in a *semiconductor QW*, where a thin layer of for instance GaN is sandwiched between two layers of larger bandgap for instance AlN, electrons and holes are 2-dimensionally "confined" and their motion in the direction perpendicular to the crystal growth direction is quantized. In a *semiconductor QW superlattice*, when the thickness of the wide-band-gap barrier layers (i.e AlN) is small enough, electrons may tunnel through it and individual levels in the quantum wells are split into minibands. However, this will happen only if the different QWs are identical. For this reason a perfect control of the QW thickness is necessary.

A *semiconductor QD* is a "zero-dimensional" object, where the electronic states are spatially localized and the energy is fully quantified. As a result, the atomic-like density of states near the band gap is higher than 3D and 2D systems, which leads to a higher efficiency for optical transitions. Additionally, QDs strongly localize the carriers and inhibit their migration toward non-radiative centers like dislocations. Hence devices incorporating QDs can be more stable against thermal perturbation.

The efficiency of a device depends on the structural quality of the heterostructures and tools have to be developed in order to determine their quality. The use of QWs and

QDs nitride heterostructures in electronic and optoelectronic devices requires a precise control and knowledge of their: size, interface quality and chemical composition. Moreover, in the GaN/AlN system, the lattice mismatch is 2.5 % and large strain builds up. Therefore, the knowledge of strain distribution especially in quantum dots structures is essential to understand the luminescence and to tune the emission wavelength to the desired application.

TEM is the ultimate technique to study the structural quality of crystal structures. In this thesis **high-resolution** TEM (HRTEM) was the basic technique used for the **quantitative analysis** of the different nitride nanostructures having as purpose the optimization and better understanding of their growth conditions. TEM techniques like Energy-Filtered and Conventional TEM together with X-ray experiments and theoretical calculations permit us to accomplish a complete study of the examined nitride samples. It was necessary to invest time in understanding how quantitative information can be extracted, which methods can provide this kind of information, what are their advantages and limits and finally which modifications could be made in order to extract the most accurate results and better adapt them in our research work.

The present work is organized in six parts.

The basic structural and elastic properties and the different growth techniques of III-nitride semiconductors are reviewed in the first chapter.

In the second chapter, we introduce the various electron microscopy techniques employed in this work: conventional, high-resolution, energy-filtered and convergent beam electron diffraction. After reminding shortly the basic principles of each technique, we will explain how we have applied them in the structural characterization of our samples: identification of dislocations, polarity determination and analysis of image contrast and imaging conditions in high resolution images.

The third chapter is devoted to the methods that have been used to extract quantitative information from HRTEM images: (a) a projection method and (b) the geometric phase analysis. The basic principles of each method are presented and we explain how it is possible to obtain accurate information about local lattice parameters and consequently about local strain and/or chemical composition. The parameters that influence the precision of either method and how they have been optimized are also reported. The mathematical basis of the geometric phase analysis is described in detail. Finally, the distortions introduced in HRTEM images acquired with a CCD camera and the use of off-axis HRTEM images in order to improve the signal-to-noise ratio are discussed at the

end of the chapter.

The characterization of GaN/AlN quantum well structures is presented in chapter 4. It is separated in two parts: the first one presents a comparative study between a Ga-face and a N-face polarity GaN/AlN QW superlattice and the second part discuses the effects of AlN overgrowth on the structural quality of GaN QWs.

Chapter 5 contains the analysis realized on GaN/AlN quantum dot structures. A quantitative strain analysis of a GaN/AlN QD superlattice is presented in the first part of the chapter. The way the overgrowth process influences the structural quality of GaN QDs is discussed in the second part.

Finally, chapter 6 contain the results obtained from the investigation of the effects of Mg doping on the structural and optical properties of GaN layers with nominal N-face polarity.

Bibliography

[1] S. Nakamura, S. Pearton, and G. Fosol. *The blue laser diode : The complete story.* Springer - Verlag, Berlin, 2000.

[2] H. Morkoç. *Nitride semiconductors and devices.* Springer - Verlag, Berlin, 1999.

[3] S.J. Pearton, J.C. Zolper, R.J. Shul, and F. Ren. *J. Appl. Phys.*, 86:1, 1999.

[4] F.A. Ponce and D.P. Bour. *Nature*, 386:351, 1997.

[5] S.N. Mohammad and H. Morkoç. *Prog. Quantum Electron.*, 20(5-6):361, 1996.

[6] S. Nakamura, T. Mukai, and M. Senoh. *Appl. Phys. Lett.*, 64:1687, 1994.

[7] S. Nakamura. *Science*, 281:956, 1998.

[8] H. Morkoç and S.N. Mohammad. *Science*, 267:51, 1995.

[9] J.C. Carrano, T. Li, D.L. Brown, P.A. Grudowski, C.J. Eiting, R.D. Dupuis, and J.C. Campbell. *Electronics Lett.*, 34(18):1779, 1998.

[10] M. Razeghi and A. Rogalski. *J. Appl. Phys.*, 79:7433, 1996.

[11] G.Y. Xu, A. Salvador, W. Kim, z. Fan, C. Lu, H. Tang, H. Morcoç, G. Smith, M. Estes, B. Goldenberg, W. Yang, and S. Krishnankutty. *Appl. Phys. Lett.*, 71(15):2154, 1997.

[12] S. Nakamura, M. Senoh, S. Nagahama, N. Iwasa, T. Matsushita, Y. Sugimoto, and H. Kiyoku. *Appl. Phys. Lett.*, 70(7):868, 1996.

[13] S. Nakamura, M. Senoh, S. Nagahama, N. Iwasa, T. Matsushita, H. Kiyoku, Y. Sugimoto, T. Kozaki, H. Umemoto, M. Sano, and K. Chocho. *Jpn. J. Appl. Phys.*, 38:L1578, 1997.

Chapter 1

III-V Nitride Semiconductors

The purpose of this chapter is to introduce briefly the basic properties of III-nitride semiconductors. We will address the structural and elastic properties, which are necessary for the interpretation of the experimental results described in the following chapters. Even today, many difficulties in the growth of high-quality III-nitride epilayers persist, the major obstacle being the lack of a suitable substrate. We will refer to the most commonly used substrates. At the end of this chapter, we will mention the different growth techniques, focalizing mostly in molecular beam epitaxy, which is the technique used for the elaboration of all the samples studied in this thesis.

1.1 A short history

The properties of group III nitride semiconductors were first investigated in the 1970s. Among the most important of these early investigations was the one of Jacques Pankove in the RCA Laboratories. He has recognized that the large, direct bandgap of nitride semiconductors makes them ideal candidates for visible and ultraviolet light emitters [1] (see Figure 1.1). The first demonstration of stimulated emission from GaN at 2K was reported by Dingle *et al.* [2] in 1971. However, the lack of successful p-type doping impeded the research on III-nitrides for more than a decade. Further progress towards GaN semiconductor devices ensued in the 1980s with the discovery that the incorporation of an AlN buffer layer between the sapphire/GaN epitaxial interface improves the quality of the layers [3,4]. Amano and Akasaki were the first to demonstrate p-type doping of GaN films, using Mg as an acceptor, setting the base for the production of the first p-n junction LEDs [5]. The growth of InGaN alloy was an additional key element for the development of a nitride laser diode. Shuji Nakamura and coworkers at Nichia Laboratories introduced blue LEDs using InGaN heterostructures [6]. Finally, the same researchers achieved firstly

pulsed operation and secondly continuous-wave operation (c.w) of nitride laser diodes [7–11].

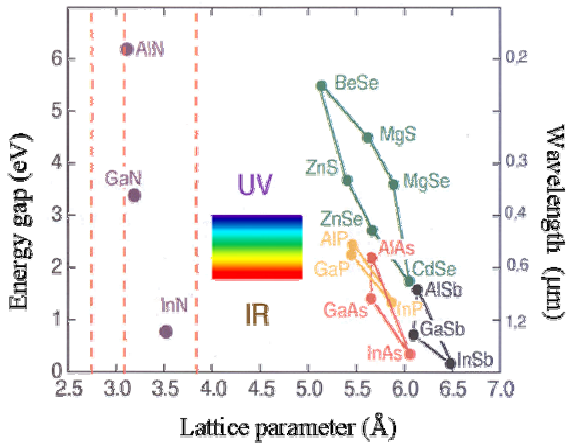

Figure 1.1 : *Bandgap enery and lattice parameter of the most common semiconductor materials.*

Figure 1.2 : *Illustrations of GaN-based LEDs and LDs.*

Present commercial nitride LEDs are very reliable with efficiencies, brightness and longevity sufficient for applications in e.g. outdoor displays, indicators, and traffic lights (see Figure 1.2). Lasers, as coherent sources, are crucial for high-density optical read and write technologies. Actually, *Sony* released in April 2003 the first DVD recorder based on a GaN/InGaN 405nm violet laser that has a memory capacity of 23GBytes [12]. Moreover, nitrides are outstanding materials for ultra-violet photodetectors and solar-blind detectors. Needless to say that the nitride semiconductors have gained considerable interest due to their unprecedented performance as emitters, detectors and power amplifiers. According to the predictions of the *Strategies Unlimited* company, the commercialization of GaN power semiconductors could produce an annual revenue of 436 million dollars until 2009 [13]! Despite a remarkable technological evolution, nitride semiconductors are one of the few cases where wide-spread device applications appeared before a total understanding of material basic properties. Indeed, many problems remain to be solved for the improvement and commercialization of next generation optoelectronics and microelectronics devices based on III-nitride semiconductors. These include for instance the development of III-nitride substrates, the reduction in the density of dislocations (actually at $10^7 - 10^{10}/cm^2$), the accomplishment of low resistance contacts on p-type materials and the reduction in the residual stresses. Fundamental material properties, such as the value of the InN bandgap or the spontaneous polarization, remain controversial.

1.2 Structural Properties

1.2.1 Crystal Structure

III-V nitride semiconductors – AlN, GaN, InN and their alloys – appear in two crystallographic phases: wurtzite (phase α) and zinc-blende (phase β or sphalerite) structures. The above crystallographic phases differ only in the stacking sequence of the polyhedra : sequence ...ABAB ...along the [0001] axis for the wurtzite phase and ...ABCABC ...for the zinc-blende phase along the [111] axis (Figure 1.3). In both structures each atom is tetrahedrically coordinated.

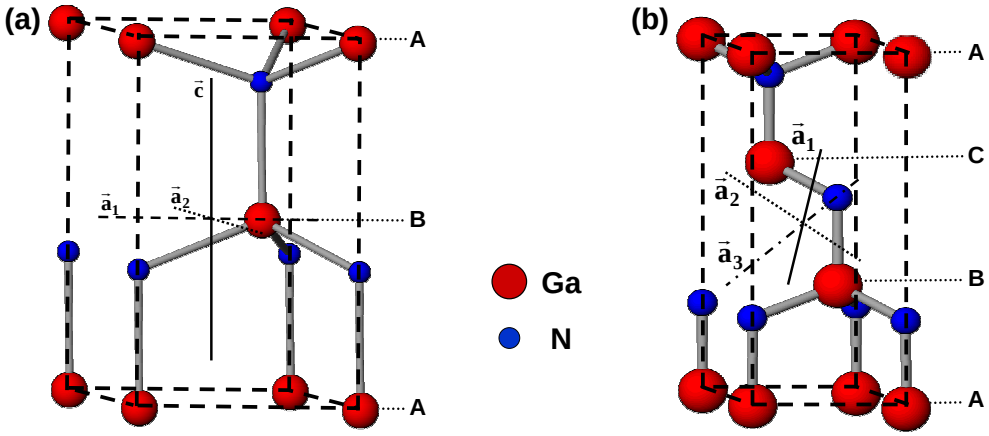

Figure 1.3 : *Schematic representation of (a) the wurtzite (b) the zinc-blende phase. The stacking sequence is ...ABAB ...for the wurtzite structure and ...ABCABC ...for the zinc-blende phase.*

For III-V nitride semiconductors, the wurtzite structure is thermodynamically more stable (see Table 1.1). However, the zinc-blende structure can be achieved by Molecular Beam Epitaxy (MBE) by using of a cubic substrate oriented along the (001) axis [14, 15].

Material	$\triangle E_{a-b}$ (meV/atome)	Reference
AlN	-18.41	[16]
GaN	-9.88	[16]
	-9.52	[17]
	-10.6	[18]
	-15	[19]
InN	-11.44	[16]

Table 1.1 : *Difference in energy $\triangle E_{a-b}$ between the wurtzite and the zinc-blende structure for AlN, GaN and InN.*

The Bravais lattice of the wurtzite structure is composed of two hexagonal closed packed sublattices, which are shifted with respect to each other by 3/8[0001]. The associated space group is $P6_3mc$ (C_{6V}^4). In the unit cell the atomic position of the III metal is (2/3,1/3,0) while for nitrogen is (2/3,1/3,u). The parameter u is the ratio between the III metal-N bond length which is align along the [0001] axis (c_1) and the **c** lattice parameter (see Fig. 1.4). For an ideal wurtzite lattice all tetrahedral bonds have the same length and the parameter $u = u_0$ is equal to 3/8. But for a tetrahedron which is slightly distorted along the [0001] axis,which is the case for AlN,GaN and InN, the length of the c_1 bond differs from the other three (c_3). In Table 1.2 are given the lattice parameters and the $c_1/\mathbf{c}$ ratio for the wurtzite group III nitrides. In this thesis, for the parameter u, we have used the values of Schultz [20].

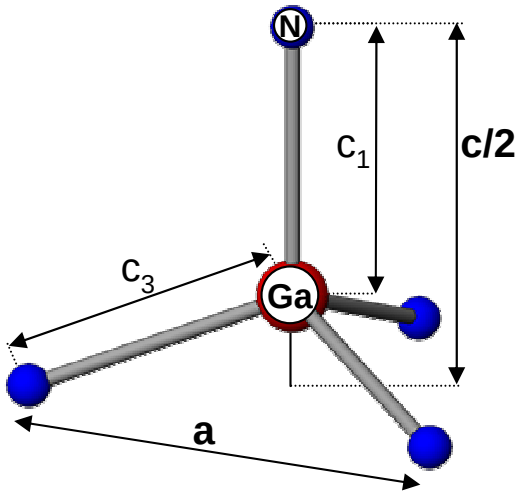

Figure 1.4 : *Bond lengths, c_1 and c_3, of the wurtzite structure. For an ideal tetrahedron: $c_1 = c_3 = u_0 \cdot \mathbf{c}$. For a distorted tetrahedron: $c_3 \neq c_1 = u \cdot \mathbf{c}$. In this thesis we have taken $u_{AlN} = 0.3821$ and $u_{GaN} = 0.377$ [20].*

Material	**a** (nm)	**c** (nm)	u
AlN	0.3112 [21]	0.4982 [21]	**0.3821** [20]
			0.3810 [16]
GaN	0.3189 [22]	0.5185 [22]	0.3780 [16]
			0.3767 [18]
			0.3748 [17]
			0.3770 [20]
InN	0.3544 [23]	0.5718 [23]	0.3770 [24]

Table 1.2 : *Lattice parameters and $c_1/\mathbf{c}$ ratio for wurtzite AlN, GaN and InN.*

By contrast, the Bravais lattice for the zinc-blende structure is composed by two face-centered cubic sublattices, the second shifted by 1/4[111] with respect to the first. The

associated space group is $F\bar{4}3m$ (T_d^2). The lattice constants a (nm) of AlN, GaN and InN are respectively 0.438, 0.452 and 0.498 nm [25].

Miller-Bravais indices and four-dimensional vectors. All samples studied in this thesis were nitride semiconductors having the *wurtzite* structure. In the hexagonal system the Miller-Bravais notation is described by four axes, three of which are coplanar. In Appendix A are given some basic crystallographic relationships for the hexagonal lattice in case that the reader of this manuscript is not very familiar with the four indices notation.

1.2.2 Polarity

Wurtzite structures have no center of inversion and are so called polar materials. Due to this absence of an inversion point, the directions [0001] and [000$\bar{1}$] are not equivalent and need to be defined. We have chosen to define as [0001] direction the vector that begins from a III-metal atom (Al,Ga or In) and points to a N atom and is aligned along the **c** polar axis [26]. According to this definition, we say that we have a Ga-polarity (or Ga-face) layer when the growth direction follows the [0001] direction, while we have a N-polarity (or N-face) layer if the [0001] direction is opposite the growth direction (Figure 1.5).

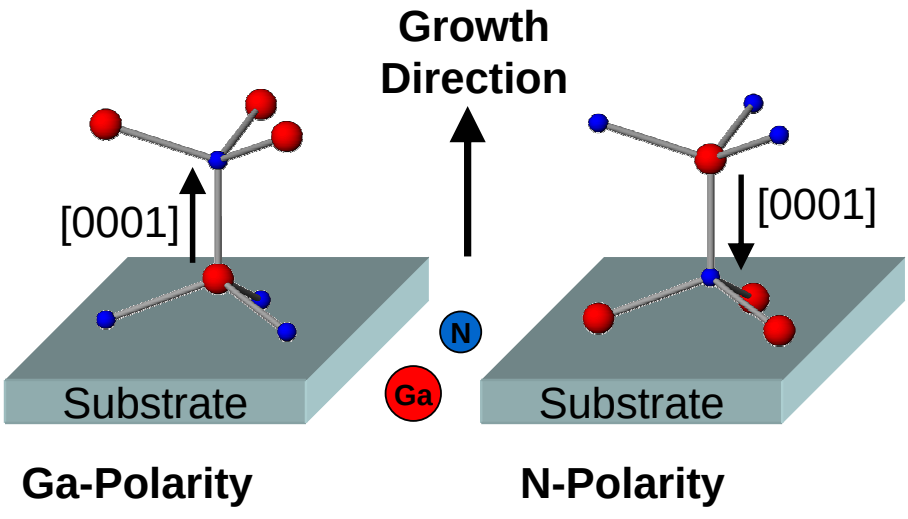

Figure 1.5 : *Definition of the [0001] direction and of the polarity for the case of a GaN crystal. The [0001] direction connects a Ga atom with a N atom. The crystal has Ga-polarity if the [0001] direction follows the growth direction and N-polarity if it is opposite the growth direction.*

The polarity is one of the key parameters in the growth of III-nitride semiconductors because it influences both the surface and bulk properties of the layers. An important

part of this thesis is devoted to the comparison between Ga-face and N-face quantum well nanostructures (section 4.1).

Several techniques have been used to determine and study the polarity of wurtzite nitride structures. For a critical review see E.S. Hellman [27] article. In this work, we have mostly employed the Convergent Beam Electron Diffraction (CBED) technique to determine the polarity of our samples.

1.3 Elastic Properties

Since the determination of strain in nitride structures and the study of strain relaxation processes represent an important part of this thesis, we found useful to include in this chapter the elastic properties of III-V nitrides. A brief introduction to the formalism of linear elasticity for hexagonal crystals is given in Appendix B.

The values of the elastic constants C_{ij} are summarized in Table 1.3. It is obvious that the reported values vary largely. In this thesis we have adopted for the elastic constants C_{ij} the values calculated by A.F. Wright [28] (Bold values in Table 1.3). This should be kept in mind when determining the strain in nitride multilayers (Chapters 4 and 5).

Material	C_{11}	C_{12}	C_{13}	C_{33}	C_{44}	Reference
AlN	410	140	100	390	120	[29]
	396	**137**	**108**	**373**	**116**	[28] *
	398	140	127	382	96	[30] *
	411	149	99	389	125	[31]
GaN	370	145	110	390	90	[29]
	390	145	106	398	105	[32]
	365	135	114	381	109	[33]
	367	**135**	**103**	**405**	**95**	[28] *
	377	160	114	209	81.4	[34]
	396	144	100	392	91	[30] *
	296	130	158	267	24	[35]
InN	**223**	**115**	**92**	**224**	**48**	[28] *
	271	124	94	200	46	[30] *

Table 1.3 : *Elastic coefficients of wurtzite III nitrides. The references marked with an asterisk are theoretical calculations. All values of the C_{ij} are in GPa.*

Appendix C gives the basic parameters of GaN and AlN.

1.4 Growth of III-Nitride Semiconductors

1.4.1 Bulk growth

The production of bulk GaN crystals is difficult because of the high melting point of GaN (2600K) and the extremely high nitrogen pressures involved in their growth. Hence, currently, there is not a commonly-available single-crystal substrate wafers for nitride epitaxy. Nevertheless, GaN single crystals are grown at UNIPRESS (Poland) at temperatures of $1400 - 1700^oC$ and at nitrogen pressure of 12-20kbar [36]. They have the form of hexagonal platelets and their size reachs about 1cm in the largest dimension. Although they present excellent structural properties, such a growth method is not scalable for industrial production. In fact, these substrates are of great interest for evaluation of homoepitaxial GaN or structures with high crystalline quality.

1.4.2 Substrates for the growth of III nitrides

Essentially all III-nitride films are grown heteroepitaxially. For the growth of wurtzite nitrides, the most commonly used substrates are sapphire (Al_2O_3), silicon carbide (SiC) and silicon (Si) on which a buffer layer of GaN, AlN or AlGaN has been previously deposited.

Although sapphire has become the most common substrate for nitride LDs and LEDs fabrication [10] it is far from being an optimum substrate for AlN and GaN growth. The biggest advantage of sapphire is the fact that large-area high crystals are commercially available at low cost. During growth, the **c**-axis of the AlN (or GaN) and the sapphire are parallel to each other while the other two main axes are rotated by 30^o around the **c**-axis. For this case, the lattice mismatch between GaN, AlN and Al_2O_3 is given by the relationship : $(\sqrt{3}\mathbf{a}_{GaN,AlN} - \mathbf{a}_{sapphire})/\mathbf{a}_{sapphire}$ and it is equal to 16.1% and 13.3% respectively (see Table 1.4). In reference [37] is given a detailed study of the orientation relationships in the III-V nitride/sapphire system.

A comparison of sapphire and SiC as possible substrates shows that SiC has advantages in terms of lattice parameters and coefficients of thermal expansion (see Table 1.4). Furthermore, SiC has good thermal and electrical conductivity, and both n- and p-type bulk crystals are commercially available. However, SiC is much more expensive compared to sapphire, and the crystalline quality of SiC wafers must still be improved.

On the other hand, silicon is a low cost substrate and can be found in the form of large wafers. The problem is that the lattice mismatch is larger than that of sapphire, and the difference in the thermal expansion result in a high density of cracks in the epilayers (see Table 1.4). However, to accomplish integration of III-nitride LEDs or LDs with Si electronics, these devices will have to be grown locally on an already processed

Si chip. Therefore considerable research work has been done on the nitride growth using Si as substrate, with the final interest of reducing costs and integrating the III-nitride optoelectronics with Si technology. Several other materials have been used as substrates

	Al_2O_3 (0001)	6H-SiC (0001)	4H-SiC (0001)	Si (111)
Structure	hexagonal	hexagonal 6H	hexagonal 4H	diamond
Epitaxial relationships	$(11\bar{2}0)\|\|(10\bar{1}0)$	$(11\bar{2}0)\|\|(11\bar{2}0)$	$(11\bar{2}0)\|\|(11\bar{2}0)$	$(11\bar{2}0)\|\|(1\bar{1}0)$
Lattice Constants (nm)	**a**=0.4758 **c**=1.2991	**a**=0.308 **c**=1.512	**a**=0.308 **c**=1.0085	$\mathbf{a}/\sqrt{2}$=0.38397
$f_0 GaN(\%)$	16.1	3.5	3.5	-17
$f_0 AlN(\%)$	13.3	1.1	1.1	-19.4
$\Delta a/a(10^{-6}/K)$	7.5	4.3	4.2	2.59
$\Delta c/c(10^{-6}/K)$	8.5	4.7	4.8	

Table 1.4 : *Properties of the most common substrates used for the growth of wurtzite III-nitrides : structure, epitaxial relationships with (0001) group III nitride epilayers, lattice constants* ***a*** *and* ***c****, lattice mismatch* f_0 *with GaN and AlN and thermal expansion coefficients* $\Delta a/a$ *and* $\Delta c/c$.

for nitride growth. Some of them are : $(111)MgAl_2O_4$ [38], (100) GaAs [39] and (0001) ZnO [40]. For the moment none of the above materials seems to be the substitute of the classic substrates used for nitride growth.

All samples studied in this thesis were growth either on (0001) Al_2O_3 or on (0001) 6H (or 4H)-SiC substrates.

1.4.3 Growth techniques

In an effort to grow high-quality III-V nitride thin films, many crystal growth techniques, substrate type and orientations have been tried. Growth techniques include metal-organic vapor phase epitaxy (MOVPE), molecular beam epitaxy (MBE), hydride vapor phase epitaxy (HVPE), pulsed laser deposition (PLD) and high-pressure synthesis (HPS). MOVPE and MBE are by far the most extensively used techniques to grow III-nitride epilayers.

Although, most GaN-based films and device structures are grown via MOVPE, this technique has the disadvantage of the high substrate temperature necessary to thermally dissociate NH_3. Due to thermal mismatch with all of the available substrates, postgrowth cooling introduces significant amounts of strain and defects into the nitride film. In addition, the high growth temperatures may encourage other undesirable effects such as dopant and group III-metal desorption, diffusion and segregation.

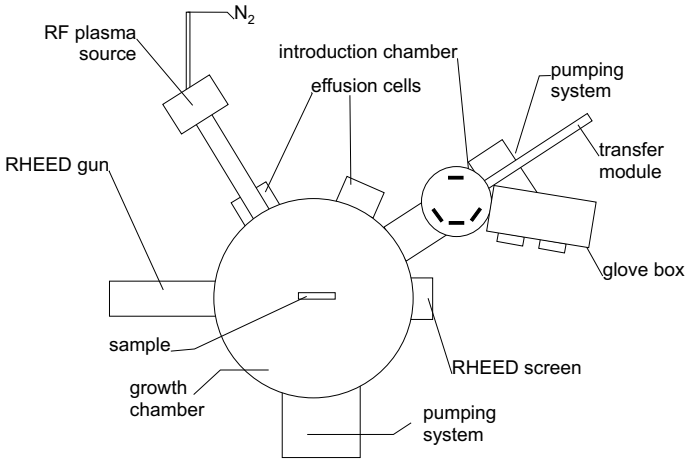

Figure 1.6 : *Scheme of the MBE system used for the growth of the examined samples.*

In an effort to reduce substrate temperatures, many groups have begun exploring a MBE approach in which the reactive nitrogen is supplied by microwave plasma excitation. It exists two kinds of nitrogen plasma sources: the electron cyclotron resonance (ECR) and the radio frequency (RF) plasma source. The ECR plasma sources have two major disadvantages, namely, the low efficiency and the presence of charged N^+ ions in the nitrogen beam, which are accelerated by the potential difference between the sample and the cell and can create defects in the growing sample. For these reasons, presently, RF plasma cells are almost exclusively used. These cells allow growth rates up to $1\mu m/h$ and the nitrogen beam is practically free of ions and contains only neutral species [41].

All samples studied in this thesis were grown by Plasma Assisted MBE (PAMBE) using a RF nitrogen plasma source. The growth of all samples have been made in CEA-Grenoble in the laboratory "Nanophysique et Semiconducteurs".

Molecular Beam Epitaxy in CEA Grenoble

Molecular-beam epitaxy (MBE)[1] is a technique for epitaxial growth carried out in ultra-high vacuum [42], which allows the deposition of monocrystalline thin layers with a well-defined orientation on a monocrystalline substrate. The use of molecular (or atomic) beams for the constituents comprise the basic feature of MBE. The mass transport between the sources and the substrate is ballistic.

A schema of the MBE system used for the growth of the samples studied in this work is shown in Figure 1.6. The base pressure of the chamber is about 5×10^{-11} mbar. Metal fluxes are provided by conventional Knudsen cells. The chamber disposes seven Knudsen cells: four cells for metals, which provide Ga (2 cells), Al, and In, and three cells for dopants (Si,Mg,and Mn or Eu). As we have already mentioned, active nitrogen is

[1]The term epitaxy is derived from the Greek words "epi" (meaning "on") and "taxis" (meaning "arrangement").

provided by a radio-frequency plasma source. The sample is mounted on a manipulator, which allows the movement in the x, y, and z directions, as well as a rotation around the z- and x-axis. A high-energy electron gun and a fluorescent screen are also available, to perform in-situ reflection high-energy electron diffraction (RHEED) measurements. In particular, from a RHEED diffraction pattern we can be informed about the growth mode of the elaborated thin film (amorphus, polycristalline, 2D or 3D-mode, ...), the surface reconstructions and the evolution of the in-plane lattice parameter of the film. Moreover, the period of the RHEED intensity oscillations has been shown to be equal to the deposition time of a monolayer in a layer-by-layer growth mode [43, 44], so thanks to them, growth rates can be measured in-situ. A comprehensive review for the RHEED technique is given in references [45, 46].

Bibliography

[1] J.I. Pankove, E.A. Miller, and J.E. Berkeyhauser. *RCA Rev.*, 32:383, 1971.

[2] R. Dingle, K.L. Shaklee, R.F. Leheny, and R.B. Zetterst. *Appl. Phys. Lett.*, 19(1):5, 1971.

[3] S. Yoshida, S. Misawa, and S. Gonida. *Appl. Phys. Lett.*, 42(5):427, 1983.

[4] H. Amano, N. Sawaki, I. Akasaki, and Y. Toyoda. *Appl. Phys. Lett.*, 48(5):353, 1986.

[5] H. Amano, M. Kito, K. Hiramatsu, and I. Akasaki. *Jpn. J. Appl. Phys.*, 28:2112, 1989.

[6] S. Nakamura and T. Mukai. *Jpn. J. Appl. Phys.*, 31:1457, 1992.

[7] S. Nakamura, M. Senoh, S. Nagahama, N. Iwasa, T. Matsushita, and T. Mukai. *Appl. Phys. Lett.*, 76:22, 2000.

[8] S. Nakamura, M. Senoh, S. Nagahama, N. Iwasa, T. Yamada, T. Matsushita, H. Kiyoku, and Y. Sugimoto. *Jpn. J. Appl. Phys.*, 35:74, 1996.

[9] S. Nakamura, M. Senoh, S. Nagahama, N. Iwasa, T. Yamada, T. Matsushita, H. Kiyoku, and Y. Sugimoto. *Appl. Phys. Lett.*, 69:4056, 1996.

[10] S. Nakamura and G. Fosol. *The blue laser diode.* Springer - Verlag, Berlin, 1997.

[11] S. Nakamura, M. Senoh, N. Iwasa, and S. Nagahama. *Jpn. J. Appl. Phys.*, 34:797, 1332, 1995.

[12] Sony unveils first violet-laser DVD recorder. *Compound Semiconductor*, 9(3):6, 2003.

[13] The Silicon Killer. *Red Hirring*, page 102, 2001.

[14] B. Daudin, G. Feuillet, J. Hübner, Y. Samson, F. Widmann, A. Philippe, C. Bru-Chevallier, G. Guillot, E. Bustarret, G. Bentoumi, and A. Deneuville. *J. Appl. Phys.*, 84(4):2295, 1998.

[15] D. Schikora, M. Hankeln, D. J. As, K. Lischka, T. Litz, A. Waag, T. Buhrow, and F. Henneberger. *Phys. Rev. B*, 54(12):R8381, 1996.

[16] C.-Y. Yeh, Z.W. Lu, S. Froyen, and A. Zunger. *Michigan Math. J.*, 45(5):10038, 1992.

[17] B.J. Min, C.T. Chan, and K.M. Ho. *Phys. Rev. B*, 45:1159, 1992.

[18] P.E. Van Camp, V.E. Van Doren, and J.T. Devreese. *Solid State Commun.*, 81:23, 1992.

[19] A. Munoz and K. Kunc. *Phys. Rev. B*, 44:10372, 1991.

[20] H.Schultz and K.H. Thiemann. *Solid State Com.*, 23:815, 1977.

[21] W.M. Yim, E.J. Stofko, P.J. Zanzucchi, J.I. Pankove, M. Ettenberg, and S.L. Gilbert. *J. Appl. Phys.*, 44:292, 1973.

[22] H.P. Maruska and J.J. Tietjen. *Appl. Phys. Lett.*, 15:327, 1969.

[23] S.Strite and H. Morkoç. *J. Vac. Sci. Technol. B*, 10(4):1237, 1992.

[24] F. Bernardini, V. Fiorentini, and D. Vanderbilt. *Phys. Rev. B*, 56(16):10024, 1997.

[25] H. Morkoç, S. Strite, G.B. Gao, M.E. Lin, B. Sverdlov, and M.Burns. *J. Appl. Phys.*, 76:1363, 1994.

[26] J.L. Rouviere, J.L. Weyher, M. Seelmann-Eggebert, and S. Porowski. *Appl. Phys. Lett.*, 73(5):668, 1998.

[27] E.S. Hellman. *MRS Internet J. Nitride Semicond. Res.*, 3:11, 1998.

[28] A.F. Wright. *J. Appl. Phys.*, 82(6):2833, 1997.

[29] C. Deger, E. Born, H. Angerer, O. Ambacher, M. Stutzmann, J. Hornsteiner, E. Riha, and G. Fischerauer. *Appl. Phys. Lett*, 72(19):2400, 1998.

[30] K. Kim, W.R.L. Lambrecht, and B. Segall. *Phys. Rev. B*, 53(24):16310, 1996.

[31] L.E. McNeil, M. Grimsditch, and R.H. French. *J. Am. Ceram. Soc*, 76(5):1132, 1993.

[32] A. Polian, M. Grimsditch, and I. Grzegory. *J. Appl. Phys.*, 79(6):3343, 1997.

[33] M. Yamaguchi, T. Yagi, T. Azuhata, T. Sota, K. Suzuki, S. Chichibu, and S. Nakamura. *J. Phys. Condens. Mat.*, 9(1):241, 1997.

[34] R.B. Schwarz, K. Khachaturyan, and E.R. Weber. *Appl. Phys. Lett.*, 70(9):1122, 1997.

[35] V.A. Savastenko and A.U. Sheleg. *Phys. Stat. Solidi (a)*, 48(2):135, 1978.

[36] S. Porowski. *J. Cryst. Growth*, 189-190:153, 1998.

[37] A.N. Efimov, A.O. Lebedev, and A.M. Tsaregorodtsev. *J. Appl. Cryst.*, 31:461, 1998.

[38] C.J. Sun, J.W. Wang, Q. Chen, M. Asif Khan, T. George, P. Chang-Chien, and S. Mahajan. *Appl. Phys. Lett.*, 68(8):1129, 1996.

[39] A. Nakadaira and H. Tanaka. *Appl. Phys. Lett.*, 70:2720, 1997.

[40] F. Hamdani, M. Yeadon, D.J. Smith, W. Kim, H. Tang, A. Salvador, A.E. Botchkarev, J.M. Gibson, A.Y. Polyakov, M. Skowronski, and H. Morkoç. *J. Appl. Phys.*, 83(2):983, 1998.

[41] W. C. Hughes, W. H. Rowland, M. A. L. Johnson, S. Fujita, J. W. Cook, J. F. Schetzina, J. Ren, and J. A. Edmond. *J. Vac. Sci. Technol. B*, 13(4):1571, 1995.

[42] M. A. Herman and H. Sitter. *Molecular Beam Epitaxy.* Springer, Berlin, 2nd edition, 1996.

[43] J. M. van Hove, C. S. Lent, P. R. Pukite, and P. I. Cohen. *J. Vac. Sci. Technol. B*, 1(3):741, 1983.

[44] J. H. Neave, B. A. Joyce, P. J. Dobson, and N. Norton. *Appl. Phys. A*, 31:1, 1983.

[45] Z. L. Wang. *Reflection Electron Microscopy and Spectroscopy for Surface Analysis.* Cambridge Univ. Press, Cambridge, 1996.

[46] W. Braun. *Applied RHEED — Reflection High-Energy Electron Diffraction During Crystal Growth.* Springer, Berlin, Heidelberg, 1999.

Chapter 2

Electron microscopy techniques

The aim of this chapter is to introduce the various electron microscopy techniques that I have used to investigate the structural quality of different nitride nanostructures. It is divided in two parts. The first part reminds the basic principles of the different techniques. The second part points out how these techniques are applied to nitride materials and what information was extracted from each one of them.

2.1 Electron Microscopy Techniques: Basic Principles

In this section we will give the very basics of the TEM techniques that were used in this thesis. There are many books that describe the principles of electron microscopy [1–7]. Personally, I enjoyed reading the book of David B. Williams and C. Barry Carter [8], which is very pedagogic for someone who begins in the field of TEM.

2.1.1 Electron-Matter Interaction

Electrons[1] show both particle and wave characteristics. Based on the de Broglie's ideas of the wave-particle duality, the particle momentum p is related to the wavelength λ of the electrons by the relationship:

$$\lambda = \frac{h}{p} \tag{2.1}$$

where h is the Planck's constant. Since the velocity of the electrons (as particles), after leaving the electron gun, approaches the speed of light, relativistic effects have to be

[1]Etymology: Electron is the Greek word for amber, the rubbing of which causes electrostatic phenomena.

included in p and equation 2.1 becomes:

$$\lambda = \frac{h}{[2m_0eV(1+\frac{eV}{2m_0c^2})]^{1/2}} \tag{2.2}$$

where m_0 is the rest mass of the electron, e the charge and V is the accelerating voltage. For example, for a microscope[2] with V=400 kV the wavelength of relativistic electrons is $\lambda = 0.00164\ nm$. This value is much smaller than the resolution of any electron microscope, which is limited by aberrations of the objective lens and not by the wavelength of the electrons.

In Transmission electron Microscopy (TEM), we are particularly interested on the elastic scattering processes, which can be quantitatively described by the time-independent Schrödinger equation for a fast electron accelerated by a potential E and travelling through a crystal potential V($\mathbf{r}$):

$$\bigtriangledown^2\Psi(\mathbf{r}) + \frac{8\pi^2me}{h^2}[E+V(\mathbf{r})]\Psi(\mathbf{r}) = 0 \tag{2.3}$$

Ψ is the wave function of the electrons and m the relativistically corrected electron mass.

2.1.2 Diffraction Theory Approaches

The kinematical treatment is the simplest approach to calculate the amplitudes of scattered beams. It assumes that, each electron may only experience a single scattering event on its passage through the specimen. Any dynamical exchanges within the beams are neglected and, moreover, inelastic interaction between the incoming electrons and the crystal atoms are ignored.

To describe quantitatively the continuous changes of phase and amplitude as the electron beam passes through the crystal, dynamical theories must be used. The different theoretical formulations muster into two groups: the Bloch-wave approach and the wave-optical approach.

The bloch-wave approach Bethe in 1928 [9] was the first to fully describe the dynamical coupling in electron diffraction. He set up the wave equation for electrons in the periodic potential field of a crystal and then applied the boundary conditions appropriate for a crystal surface with incident and diffracted waves in vacuum. Later, this general theory was developed for the transmission case [10], with the simplification of limiting the dynamical exchange to two beams. Afterwards, the treatment was expanded to include many beams [11], [12] and nowadays many-beam dynamical calculations can be

[2]Etymology: From the Greek words "micro-" which means small and "skopein" which means to look.

performed.

The wave-optical (or multislice) approach This approach is based on the idea of representing mathematically the phenomenological progressing of radiation through the crystal. An incident plane wave is successively scattered and the multiply scattered components are added up according to their relative amplitudes and phases to form the out-going waves. A way to simplify the problem is to take advantage of the forward scattering geometry of the diffraction of fast electrons and consider the scattering by successive planes of infinitesimal thickness. Cowley and Moodie [13],devised the multislice approximation. Here, the crystal is divided into multiple thin slices perpendicular to the electron beam. It is then assumed that scattering from any individual slice occurs on a single plane and it is described by a transmission function. To define the transfer of the wave function to the next plane a propagation function is used. Finally, the process of transmission followed by propagation is repeated sequentially for each slice, until the bottom surface is reached and the exit wavefunction of the electron is obtained.

The two dynamical theory formulations are basically equivalent. Nevertheless, in the case of High Resolution Transmission Electron Microscopy (HRTEM) the multislice approach is more convenient. For conventional TEM images the use of the Bloch-wave methods is preferred. However, for particular orientations the calculations can be based on the two-beam approximation as described by Hirsch *et al* [1] and Thomas and Goringe [4].

2.1.3 CTEM: Two-beam and Weak-beam Conditions

In a Transmission Electron Microscope (TEM), the uniform electron intensity in the incident beam is transformed into a nonuniform intensity after scattering by the specimen. This variable electron intensity is translated into contrast on the screen and depends on the local thickness of the sample, the crystallographic orientation, the chemical composition and the presence of defects.

The diffraction contrast is a special form of amplitude contrast because the scattering occurs at special Bragg angles. To obtain strong diffraction contrast the specimen must be tilted in such a way that only one diffracted beam is strong (**two-beam conditions**). This is achieved by placing an aperture in the back focal plane of the objective lens. Depending now on whether the transmitted or the diffracted beam is selected to the image formation, the image is called Bright field (BF) or Dark Field (DF), respectively (see Figure 2.1). Under two-beam conditions BF and DF images show complementary contrast.

The term "**weak beam**" refers also to the formation of a diffraction contrast image in either BF or DF, although the DF approach has been more widely used because it gives

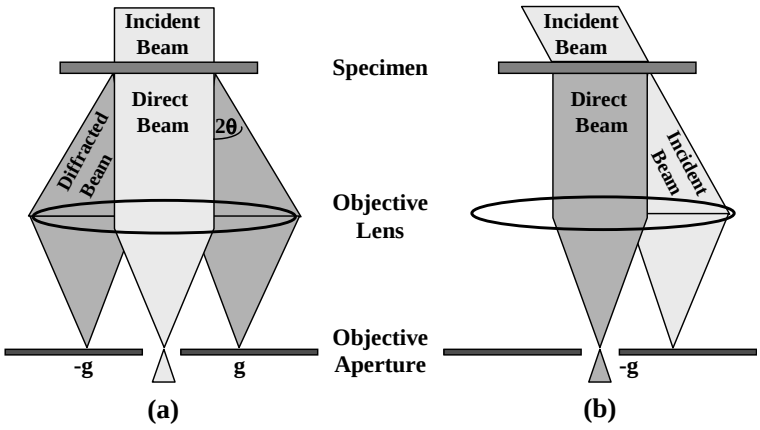

Figure 2.1 : *Ray diagrams for (a) bright field and (b) dark field imaging under two-beam conditions. A bright field image is formed when the direct beam is selected by the objective aperture. For dark field images, the incident beam is tilted so that the scattered beam remains on the optic axis.*

stronger contrast. The Weak Beam (WB) method was developed by Cokayne *et al.* [14] and became important because dislocations can be imaged as narrow lines. Moreover, the position of these lines are well defined with respect to the dislocation cores. For these reasons, the WB method became a powerful tool for the study of dissociated dislocations. In practice, to obtain WB images we first choose a particular $\mathbf{g}$ and bring this onto the optic axis as if it were to take a two-beam DF image. Afterwards, the specimen is tilted in order to have large excitation error $\mathbf{s_g}$ and excite preferentially a (n$\mathbf{g}$) reflection. The DF image is obtained by using the reflection $\mathbf{g}$. The above procedure is illustrated in Figure 2.2. Under WB conditions we have the highest resolution of all conventional imaging modes but we have to note that due to the very low intensity of the WB images long exposure times are needed.

For the two-beam image mode, the intensity in the diffracted beam, $|\phi_{\mathbf{g}}|^2 = \phi_{\mathbf{g}}\phi^*_{\mathbf{g}}$, is given by the equation:

$$|\phi_{\mathbf{g}}|^2 = (\frac{\pi t^2}{\xi_{\mathbf{g}}})\frac{\sin^2(\pi t s_{eff})}{\pi t s_{eff}} \tag{2.4}$$

where t is the thickness of the sample, $\xi_{\mathbf{g}}$ the extinction distance and s_{eff} is the effective excitation error which is given by equation:

$$s_{eff} = \sqrt{s^2 + \frac{1}{\xi_{\mathbf{g}}}} \tag{2.5}$$

Some important properties of the effective excitation error are:

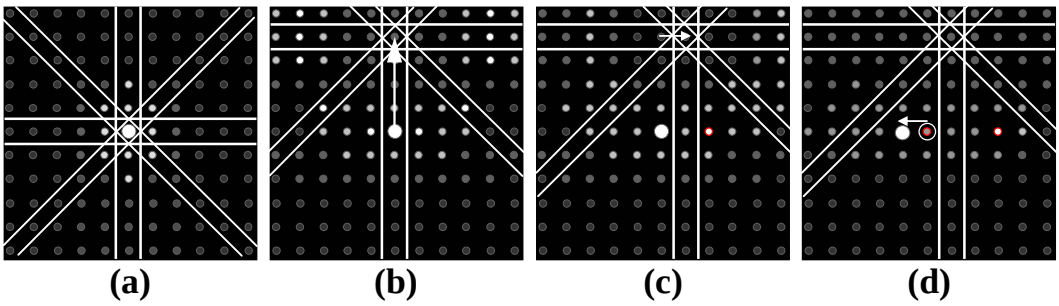

Figure 2.2 : *Schematic representation of the procedure to obtain weak beam images. (a) In Selected-Area Diffraction mode (SAD), the crystal is oriented along a zone axis. (b) We tilt the specimen perpendicular to the direction of the hlk spot range that we have chosen to use, in such a way that only this range is excited. In the schema, tilting the specimen is visualized by a displacement of the Kikuchi lines. (c) We tilt the specimen to the direction of the chosen* $\mathbf{g}$*, until only one* n$\mathbf{g}$ *reflection (*n*=integer) is excited (here the 2*$\mathbf{g}$ *reflection is excited). (d) We use the DF beam-deflecting coils to bring the reflection* $\mathbf{g}$ *on to the optic axis and we place the objective aperture around it. By passing to the imaging mode, we have a weak beam image with the required* $\mathbf{g}$-n$\mathbf{g}$ *conditions (here* $\mathbf{g}$*-3*$\mathbf{g}$*).*

- The quantity s_{eff} is never equal to zero.
- When s=0, which is the case in two-beam conditions, then s_{eff} is $\xi_{\mathbf{g}}^{-1}$.
- When s is very large, as it is the case under WB conditions, then s_{eff} becomes essentially the same as s.

2.1.4 High Resolution Transmission Electron Microscopy

If we consider the microscope as a device which transfers information from the specimen to the image, we would like to transfer *all* the information to the image. But in reality, we can never accomplish a complete transferring of *all* the information since the lens system of a microscope is far from being perfect. Additionally, in HRTEM imaging we need to use an atomistic model of the examined material in order to interpret the images. Ideally, this model will include a full description of the atomic potential and the bonding of the atoms, but we don't know all these information.

Since HRTEM is the basic technique that I have used to analyze the nitride nanostructures, I will briefly describe the image formation process in HRTEM. Once the exit wave has left the specimen, the electron wavefront has to be converted into an image. Since the exit wave contains mainly phase information, these phase differences have to be converted to intensities (contrast). Defocus, and spherical aberrations of the objective lens, induce extra phase shifts in the wavefunction. The influence of these extra phase shifts can be taken into account by multiplying the wavefunction at the back focal plane

with functions describing each specific effect. The phase factor $\chi(\mathbf{u})$, also called phase-distortion function, used to describe the phase differences introduced by the defocus and spherical aberration is equal to:

$$\chi(\mathbf{u}) = \pi \Delta f \lambda u^2 + \frac{1}{2}\pi C_s \lambda^3 u^4 \tag{2.6}$$

with Δf the defocus value of the objective lens, C_s the spherical aberration coefficient and $\mathbf{u}$ the distance of the reciprocal lattice point from the optic axis. The function that multiples the exit wave is then:

$$B(\mathbf{u}) = \exp(i\chi(\mathbf{u})) \tag{2.7}$$

If the specimen behaves as a weak-phase object, then only the imaginary part of the above function contributes to the image contrast, and one can set:

$$B(\mathbf{u}) = 2\sin(\chi(\mathbf{u})) \tag{2.8}$$

We can now define a new quantity, T($\mathbf{u}$), which is the transfer function and is given by:

$$T(\mathbf{u}) = 2A(\mathbf{u})\sin\chi(\mathbf{u}) \tag{2.9}$$

where A($\mathbf{u}$) is an aperture function which is unity for $\mathbf{u} < \mathbf{u}_0$ and zero outside this radius. When T($\mathbf{u}$) is negative, positive phase contrast results and the atoms in the specimen would appear dark spots against a bright background and vice-versa. An ideal behavior of T($\mathbf{u}$) would be zero at $\mathbf{u} = 0$ (very long distances in the specimen) and $\mathbf{u} > \mathbf{u}_0$ (frequencies beyond the aperture size) and large and negative for $0 < \mathbf{u} < \mathbf{u}_0$. Figure 2.3 illustrates the process of image formation in a high-resolution TEM.

It is now clear that the contrast in high-resolution images depends strongly on the microscope settings and parameters. In practice, additional terms have to be included in T($\mathbf{u}$). This is because of electrical instabilities in the microscope causing a spread of focus because of the chromatic aberration of the objective lens. Mechanical instabilities and energy loss due to inelastic scattering of the electrons by the specimen also contribute to the spread in defocus. The beam convergence is also a factor that affects the resolution. All these effects reduce the amount of information present in the image. They can be represented by multiplying the $\sin\chi(\mathbf{u})$ with the damping envelopes functions E_α and E_Δ which represent the damping by the convergence and spread in defocus respectively:

$$E_\alpha(\mathbf{u}) = \exp[-\pi^2\alpha^2(C_s\lambda\Delta + \lambda^2 C_s\mathbf{u}^2)^2\mathbf{u}^2] \tag{2.10}$$

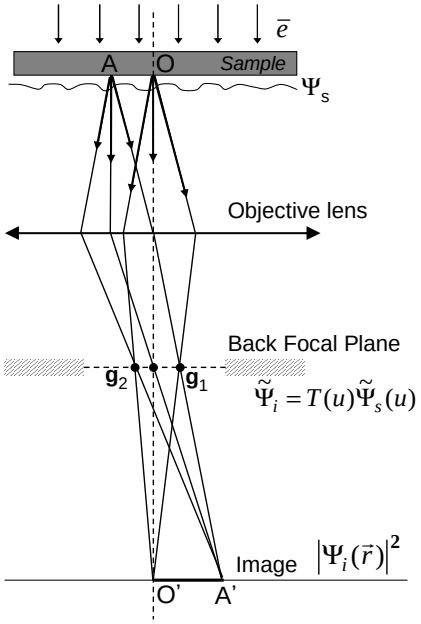

Figure 2.3 : *Image formation process in HRTEM.*

$$E_{\Delta}(\mathbf{u}) = \exp[-\frac{1}{2}\pi^2\lambda^2\Delta^2\mathbf{u}^4] \tag{2.11}$$

The electron-optical properties of the two transmission electron microscopes (JEOL 4000EX [15] and JEOL 3010) used in this study can be found in Table 2.1.

	JEOL 4000EX Top Entry	JEOL 3010 Side Entry
V(kV)	400	300
λ(pm)	1.64	1.97
C_s(mm)	1.06	0.6
C_c(mm)	1.7	1.3
Point Resolution (nm)	0.17	0.12
Scherzer defocus (nm)	50	42
Tilt	$\pm 20^{\circ}$	$\pm 20^{\circ}$

Table 2.1 : *Properties of the transmission electron microscopes used in our work.*

2.1.5 Convergent Beam Electron Diffraction

The CBED technique was originally developed by Kossel and Möllenstedt [16] in 1939 and it is the oldest TEM diffraction technique. The big advantage of CBED is that most of the information is generated from minuscule regions (some nm) beyond the reach of other diffraction methods. In our work, we have used this technique to determine the

polarity of our specimens. Here, we will only report the formation of a CBED diffraction pattern, whereas a more detailed description of the method can be found in the book of Spence and Zuo [17].

The convergent incident beam can be considered as a set of incoherent incident beams having all possible orientations within the incident cone. Each one of these incident beams produces a transmitted point and a diffracted point in the back focal plane, and if we take into account all the incident beams contained in the incident cone, the pairs of transmitted and diffracted points form a transmitted and a diffracted disk. The diameter Φ of these two disks is given by the relationship:

$$\Phi = 2f \tan\alpha \approx 2f\alpha \tag{2.12}$$

where α is the convergence angle and f the focal length. Their centers are separated by a distance equal to:

$$D = f \tan 2\theta_B \approx 2f\theta_B \tag{2.13}$$

Independently of the conditions under which a CBED pattern is obtained (two-beam or many beam conditions), it can be considered as a map of the transmitted and diffracted intensities versus the deviation parameter **s**. These intensities reflect the symmetry of the examined crystal, so if the structure of the crystal contains a polar axis [hkl], then the intensity inside the disks +(hkl) and -(hkl) would be different. Based on this property, we identified the polarity of our specimens, as it will be described later on in this chapter (2.2.3). The formation of diffraction patterns and the Ewald sphere construction in CBED, for the case of three incident beams, are illustrated in Figure 2.4.

2.1.6 Electron Energy-Loss Spectrometry and Energy-Filtered TEM

As a rule, the technique of Electron Energy-Loss Spectrometry (EELS) analyzes the energy distribution of electrons that have inelastically interacted with the specimen [18,19]. We are interested in these inelastic collisions because they carry information about the electronic structure of the specimen atoms, which determine the nature of these atoms, their bonding and nearest-neighbor distributions and their dielectric response. There are two types of electron spectrometers for TEM: the magnetic prism spectrometer (by Gatan) and the omega filter (by LEO). In our case, our microscope (JEOL 3010) is equipped with a Gatan Image Filter (GIF), which can combine both spectral and imaging capabilities by means of the Electron Spectroscopic Imaging (ESI). A schematic diagram of the principal function of a GIF filter is shown in Figure 2.5.

In a TEM, the GIF is installed beneath the camera system. Once the electrons have

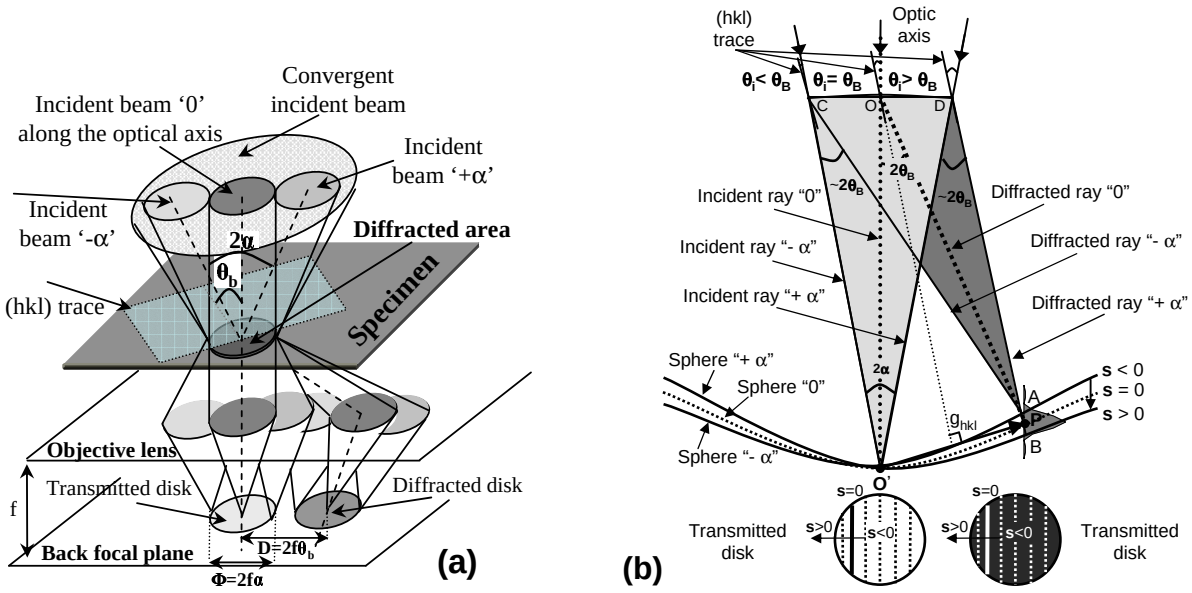

Figure 2.4 : *CBED diffraction patterns under "two-beam conditions". (a) Formation of the diffraction pattern: the convergent incident beam is composed of a set of incident beams having all possible orientations within the incident cone. Three incident beams have been shown: "0", "−α" and "+α". The "0" incident beam directed along the optic axis is at exact Bragg conditions for the (hkl) plane. The diffraction pattern, located at the back focal plane of the objective lens, consist of a transmitted disk and an hkl diffracted disk. (b) Each incident beam is associated with an Ewald sphere. These spheres produce the diffracted beams OP,CA and DB. The variation of the deviation parameter* $\boldsymbol{s}$ *is observed inside each kl diffracted disk. This variation occurs along line parallel to the excess line obtained for* $\boldsymbol{s}$*=0. The same variations occurs inside the transmitted disk.*

passed through all the lenses belonging to the TEM, they are selected by a variable entrance aperture (diameters: 1,2 and 3mm) and travel down a "drift tube" through the spectrometer and are deflected through $\geq 90^o$ by the surrounding magnetic field. Electrons having different energies are focused on different positions in the plane of the energy-selecting slit. The energy-selecting slit selects electrons with a particular range of energy losses. Afterwards, a set of lenses (quadrupole and sextupole lenses) re-disperse the selected electrons to form the image (or spectra). Finally, the image is recorded digitally in a CCD camera (1024x1024 pixels in our case).

One way to illustrate the energy-selected electron images, ESI technique, is to use a 3D-data space, in which the z-axis is replaced by the energy loss of electrons (ΔE), and the x and y axis are the real space coordinates of the 2D-image of the specimen (Figure 2.6). In an EELS spectrum we can observe all the inelastic scattering processes. This is shown schematically on the right side of Figure 2.6. The zero-loss peak is composed of elastically and thermal diffusely scattered electrons. Images produced by the elastically electrons are incoherent. Energy-selected images of plasmon-loss electrons, as their scattering is closely

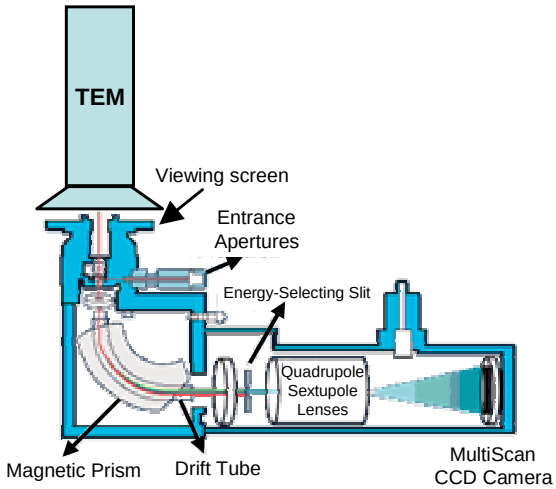

Figure 2.5 : *Schematic diagram of a Gatan image filter, GIF, attached to a TEM.*

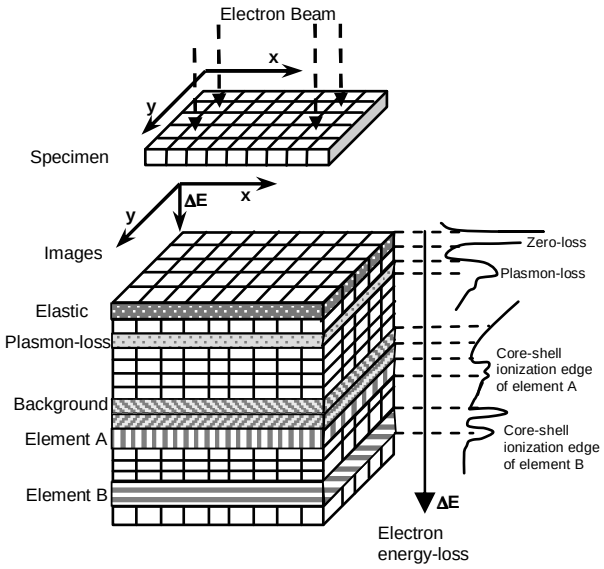

Figure 2.6 : *Schematic diagram of the electron spectroscopic imaging, ESI, technique in a TEM. It illustrates the energy-selected electron images corresponding to the different characteristic energy loss features.*

related to the valence-band structure of the examined material, they are not very sensitive in the composition information. Composition sensitive images can by obtained from the atomic inner-shell ionization edges. However, the contribution of processes like scattering of multiple valence losses, electromagnetic radiation and electron Compton scattering, observed in the background area of an EELS spectrum, must be subtracted from the recorded data. The concentration of the corresponding element in the specimen, is given by the inner-shell ionization signal.

A more conventional Energy Filtered TEM (EFTEM) method is the so-called "three-window method", which use three spectrally separated images, two pre-edge images and one post-edge, to calculate chemical distribution maps (elemental maps). The two pre-edge images are used to extrapolate the background intensity curve to the energy-loss interval of interest. A background image for the ionization edge of the element of interest is then calculated. Finally, the background image will be subtracted from the image recorded when the energy-selecting window is positioned at the ionization edge (post-edge image). This final substraction results in an image (elemental map) produced by electrons that have been inelastically scattered by the element of interest, showing its distribution [20]. It is clear that the three-window method is only suitable for cases where in the energy-loss spectrum the element peak is much higher than the background intensity.

2.2 Electron Microscopy Techniques: Application to nitrides

2.2.1 Sample Preparation

For TEM experiments, the quality of the obtained data are at least directly proportional to the quality of the examined specimen! Sample preparation is hence a crucial issue. In general, a TEM sample needs to be electron transparent, therefore, it has to be thin due to the important absorption of electrons in the material. The requirement for electron transparency is a function of the accelerating voltage of the electrons and the average atomic number of the investigated material. Typically, the thickness range of a TEM specimen is in the order of $< 50 - 500nm$.

In our work, for the preparation of our cross-section samples, we have used the standard techniques of mechanical polishing and ion milling. A description of the method is shown in Figure 2.7. At the beginning, the sample was cut in squares of $\sim 2.5\ mm$ with a diamond-wire saw. In order to obtain both the $[2\bar{1}\ \bar{1}0]$ and the $[01\bar{1}0]$ zone axis in the same sample, two squares notated by A and B in Figure 2.7 tilted by 90° with respect to each other were glued together to create a sandwich. Afterwards, the sandwich structure was cut in thin slices ($\sim 0.5mm$). A slice was mechanically polished down to $\sim 40\mu m$ using a sequence of progressively finer grit diamond lapping films. The last step is the ion milling. In this study, a Gatan's ion polishing system (PIPS), which is equipped with two high-powered Ar ion guns was used. The ion milling conditions for all samples were prepared: beam energy of 3 KeV, angles at $+7^o/-7^o$ and a rotation of 3prm.

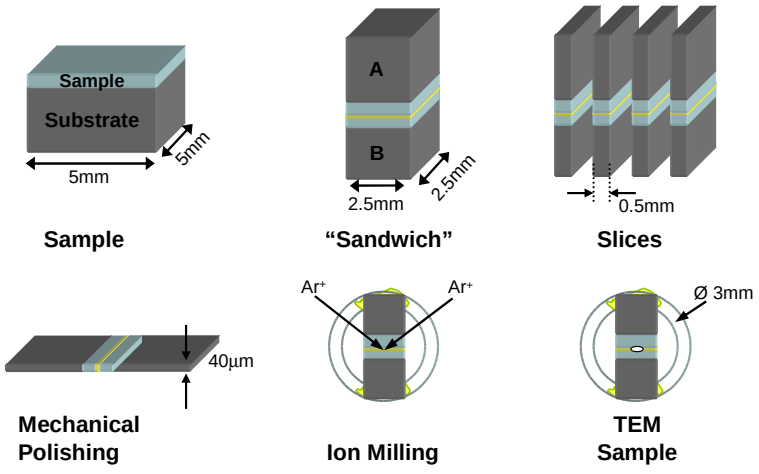

Figure 2.7 : *Schematic sequence for cross-section sample preparation using the standard techniques of mechanical polishing and ion milling*

2.2.2 Contrast from dislocations for the wurtzite structure

In order to identify which type of dislocations were present in our samples, we have applied the invisibility criterion and realized CTEM experiments.

The dislocations in the wurtzite structure are the same as in the hcp one. Table 2.2 summaries the basic properties of dislocations in hcp crystals [21]. Further on, we will refer to the perfect dislocations with Burgers vector $\mathbf{b}= 1/3 < 11\bar{2}0 >$ as **a**-type dislocations, those with $\mathbf{b}=[0001]$ as **c**-type and finally those with $\mathbf{b}= 1/3 < 11\bar{2}3 >$ as **a**+**c** dislocations. The above perfect dislocations, **a**, **b** and **a**+**c**, show edge, screw and mixed character respectively.

The invisibility criterion says that if the product $\mathbf{g}\cdot\mathbf{R}$ is equal to zero, then we won't see any contrast because the diffraction planes giving rise to the image contrast are parallel to **R**, where **R** is the displacement field. Since $\mathbf{g}\cdot\mathbf{R}$ is proportional to $\mathbf{g}\cdot\mathbf{b}$, we can apply this criterion to identify the Burgers vector of a dislocation using TEM diffraction contrast.

Screw Dislocations: In the case of a screw dislocation its line direction ξ is parallel to **b** and its displacement **R** is equal to [21]:

$$\mathbf{R}_{screw} = \frac{\mathbf{b}}{2\pi}\tan^{-1}(\frac{y}{x}) = \mathbf{b}\cdot R_z \tag{2.14}$$

where x and y are coordinates in the plane perpendicular to ξ. Therefore, since $\mathbf{R}\|\mathbf{b}$, a screw dislocation is invisible when $\mathbf{g}\cdot\mathbf{b}=0$.

Edge Dislocations: For an edge dislocation the displacements are given by the following relationship:

$$\begin{aligned}\mathbf{R}_{edge} = \frac{1}{2\pi}\Bigg\{\mathbf{b}\cdot\tan^{-1}(\frac{y}{x}) + \mathbf{b}\frac{xy}{2(1-\nu)(x^2+y^2)} \\ +(\mathbf{b}+\xi)\left[\frac{x^2-y^2}{4(1-\nu)(x^2+y^2)} + \frac{1-2\nu}{4(1-\nu)}ln(x^2+y^2)\right]\Bigg\} \\ = \mathbf{b}\cdot R_x + (\mathbf{b}\times\xi)\cdot R_y\end{aligned} \tag{2.15}$$

where ν is the Poisson's ratio. Therefore, an edge dislocation provokes a deformation in all the planes that are perpendicular to its line. The invisibility criterion $\mathbf{g}\cdot\mathbf{R}$ contains now two terms $\mathbf{g}\cdot\mathbf{b}$ and $\mathbf{g}\cdot(\mathbf{g}\times\xi)$. As a result, a edge dislocation is invisible if $\mathbf{g}\cdot\mathbf{b}$ and $\mathbf{b}\cdot(\mathbf{b}\times\xi)$ are both zero.

Mixed Dislocations: For a mixed dislocation, displacement **R** is the sum of the displacements introduced by its edge and screw components. Since, the vectors $\mathbf{b}_{screw}$, $\mathbf{b}_{edge}$

Type	Burgers vector (**b**)	Magnitude (b)	Energy (b^2)	Character
AB	$1/3 < 11\bar{2}0 >$	α	α^2	Perfect
TS	[0001]	c	$8/3\alpha^2$	Perfect
SA/TB	$1/3 < 11\bar{2}3 >$	$\sqrt{(c^2+\alpha^2)}$	$11/3\alpha^2$	Perfect
Aσ	$1/3 < \bar{1}100 >$	$\alpha/\sqrt{3}$	$1/3\alpha^2$	Shockley Partial
σ**S**	1/2[0001]	c/2	$12/3\alpha^2$	Frank Partial
AS	$1/6 < \bar{2}203 >$	$\sqrt{(\frac{\alpha^2}{3}+\frac{c^2}{4})}$	α^2	Frank Partial

Table 2.2 : *Dislocations in the Hexagonal Close-packed Structures*

and ($\mathbf{b}_{edge} \times \xi$) are orthogonal between them, the mixed dislocations are visible for all diffraction conditions.

We report in Table 2.3 the value of the $\mathbf{g} \cdot \mathbf{R}$ product for the three types of perfect dislocations in an hexagonal crystal. It can been seen that to determine the dislocation type, and as a consequence the dislocations density in a sample, we need only two images taken under the two-beam or weak-beam conditions. For example, we see that if we want to measure the density of dislocations having an edge character it is better to choose the [0,1,-1,0] zone axis rather than the [2,-1,-1,0]. Thus, along the [0,1,-1,0] zone axis, contrast of edge dislocations is visible only on images obtained with a **g**=n(2-1-10) (n=integer). Screw dislocations are visible only for **g**=n(0001) and finally mixed dislocations are visible in both conditions.

Zone Axis	[2,-1,-1,0]		[0,1,-1,0]		[0001]	
b/**g**	(01-10)	(0001)	(2-1-10)	(0001)	(01-10)	(2-1-10)
1/3[2-1-10]	$R_y/3$	0	$2R_x$	0	$2R_y/3$	$2R_x$
1/3[-1-120]	$R_x + R_y/3$	0	$R_x + R_y$	0	$R_x + R_y/3$	$R_x + R_y$
1/2[-12 -10]	$R_x + R_y/3$	0	$R_x + R_y$	0	$R_x + R_y/3$	$R_x + R_y$
[0001]	0	R_z	0	R_z	0	0
[000-1]	0	R_z	0	R_z	0	0
1/3[2-1-13]	$R_y/3$	R_z	$2R_x$	R_z	$2R_y/3$	$2R_x$
1/3[-1-123]	$R_x + R_y/3$	R_z	$R_x + R_y$	R_z	$R_x + R_y/3$	$R_x + R_y$
1/3[-12-13]	$R_x + R_y/3$	R_z	$R_x + R_y$	R_z	$R_x + R_y/3$	$R_x + R_y$

Table 2.3 : *Values of the* $\boldsymbol{g} \cdot \boldsymbol{R}$ *product for the perfect dislocations in a hexagonal crystal and for the different* $\boldsymbol{g}$ *vectors used in CTEM experiments of wurtzite materials. The dislocations propagate along the* $\boldsymbol{c}$*-direction.*

2.2.3 Polarity determination by CBED

As we have already mentioned, the polarity of a nitride layer is an important parameter that influences the surface and bulk properties of the examined layers. In this work, we have applied the CBED technique to determine the polarity of our samples.

The relative polarity of different samples can be measured by comparing the relative orientations of experimental CBED patterns with the associated TEM images of the examined samples. However, the absolute polarity of a sample can be determined by comparisons of experimental patterns with simulated ones, if the rotation of the diffraction pattern is known. For the case of wurtzite GaN layers, it was found that for CBED patterns taken along the $< 01\bar{1}0 >$ zone axis, the (0002) and (000-2) diffraction disks are greatly asymmetric. To produce the simulated CBED patterns, we have used the JEMS software [22], checking always that the simulated diffraction spots are correctly labelled with respect to the simulated starting crystal structure. Moreover, for the polarity determination of our samples we have taken into account the measured 180^o rotation between the TEM images and the CBED patterns produced in the JEOL3010 electron microscope. In Figure 2.8 we present simulated CBED diffraction patterns, calculated by the JEMS software, of a GaN crystal for different thicknesses. The asymmetry of the (0002) and (000-2) diffraction disks is clearly seen even for small thickness values.

2.2.4 HRTEM Images

The main part of this work consist of extracting quantitatively from HRTEM images information about the interface quality, the chemical composition and the strain distribution of different nitride nanostructures. In general, HRTEM images can not be directly interpreted and image simulations have to be done in order to get the exact atomic structure information of the experimental image. In this thesis, both the EMS [23] and JEMS [22] software by P. Stadelmann were used to realize the HRTEM image simulations. All HRTEM experiments were realized in the JEOL4000EX electron microscope.

Before starting analyzing simulated images of nitride heterostructures, we found useful to examine the contrast of perfect GaN and AlN crystals. By doing so, we wanted to determine the HRTEM imaging conditions (thickness and defocus) of our experimental images and also to learn the exact position of the atomic columns for these conditions. For these reasons we have calculated HRTEM maps as a function of the specimen thickness and the defocus for both GaN and AlN perfect crystals and along the [2,-1,-1,0] and [0,1,-1,0] zone axis, which are the traditional zone axis. In chapter 3.5 we will introduce the zone axis [-1,5,-4,0] that we have used in order to improve the signal-to-noise ratio in our HRTEM images. Images acquired with this direction will be named off-axis images.

Figure 2.9 demonstrates the geometry of the wurtzite structure and the associated

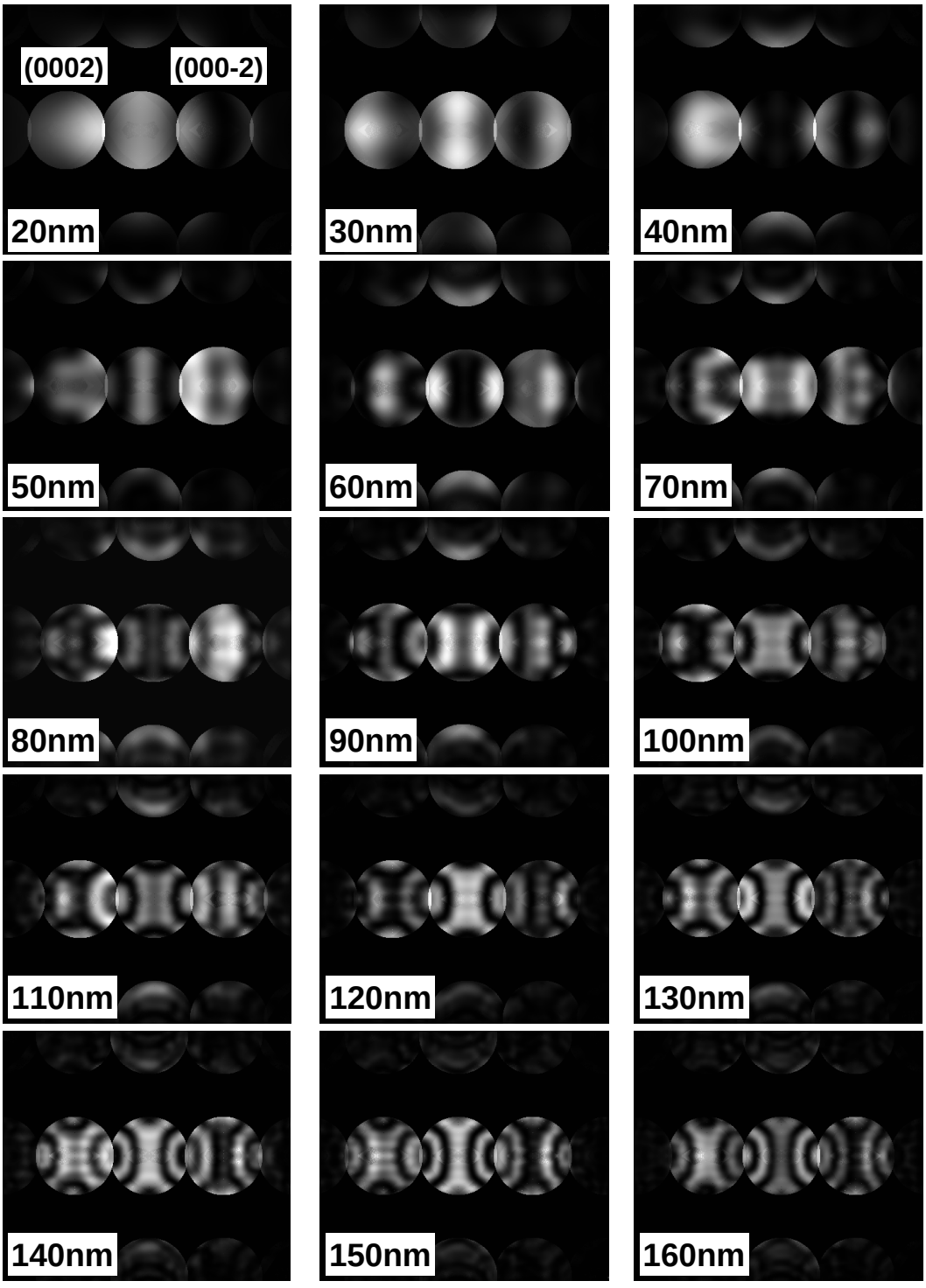

Figure 2.8 : *Simulated CBED diffraction patterns of a GaN crystal along the* $< 01\bar{1}0 >$ *zone axis for different thickness values. Maximum deviation=0.2* nm^{-1}*, Laue zone number=9 and half-convergence=4mrad.*

diffraction patterns for the two traditional zone axis. An equivalent schema for the off-axis structure is given in chapter 3.5, Figure 3.26. In particular, in Figure 2.9, we see that the wurtzite structure constitutes of "(0002)" planes containing only one type of atoms (Ga-planes alternate with N-planes). The distance between a Ga- and N-plane is alternately equal to c_1 or c_3 (see also Fig. 1.4 in chapter 1.2.1).

We note that in the JEMS software, the multislice method was used to produce all the simulations reported in this thesis.

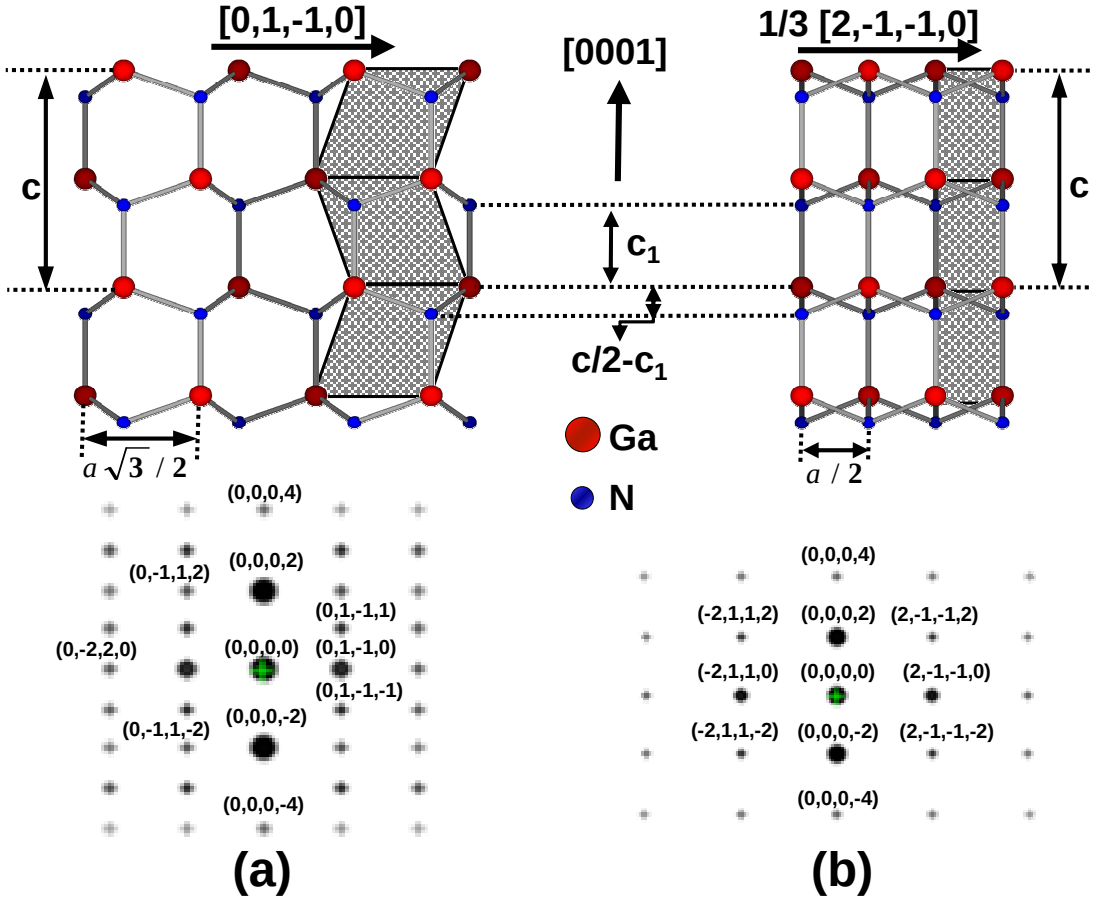

Figure 2.9 : *Schematic illustration of the wurtzite structure and the corresponding diffraction pattern along the a)[2,-1,-1,0] and b)[0,1,-1,0] zone axis.*

[2,-1,-1,0] Zone axis. A schematic illustration of the wurtzite structure viewed along the [2,-1,-1,0] zone axis is shown in Figure 2.9 (a) together with the associated diffraction pattern. Each atomic column contains one type of element. The distance between two atoms of the same type is equal to $\mathbf{a}\sqrt{3}/2$ along the [0,1,-1,0] direction, and $\mathbf{c}/2$ along the [0001]. The stacking along the [0001] axis of the projected structure can be described by consecutive parallelepiped, defined by four atoms of the same type, and which are inclined

one toward the right and one toward the left.

Contrast maps as a function of the thickness t and the defocus δz for a GaN and an AlN perfect crystal along the [2,-1,-1,0] direction are seen in Figure 2.10 and Figure 2.11 respectively. They were calculated by the JEMS software for a JEOL4000EX microscope using the multislice method and an objective aperture diameter of 15 nm-1. The Debye-Waller factors were included in the calculation, in order to take into account the thermal vibration of atoms. We have taken the Debey-Waller factors equal to 0.005 nm^{-2} for all atoms. The absorption coefficient for Ga, Al and N were set equal to 0.052, 0.034 and 0.028 respectively. They were introduced to account for inelastic interactions. In these contrast maps only the domains where the contrast is intense can be used for the determination of the atomic positions. In the other domains the contrast is not interpretable due to the presence of double frequencies. The imaging conditions in which we obtain a maximum contrast for a GaN and an AlN perfect crystal viewed along the [2,-1,-1,0] direction are grouped in Table 2.4. We notice that for thicknesses from 1.6 nm until 7 nm, the optimal defocus range is more or less equivalent for both crystal.

Material	**GaN**						
Thickness t (nm)	$1.6 < t < 7$			$8 < t < 13$			$9 < t < 23$
Interval of defocus	[-20,0]	[25,40]	[65,75]	[-15,0]	[35,45]	[70,80]	[-15,-5]
Material	**AlN**						
Thickness t(nm)	$1.6 < t < 9$			$9 < t < 11$			$20 < t < 23$
Interval of defocus	[-10,0]	[30,40]	[70,80]	[-10,0]			[-10,0] [55,65]

Table 2.4 : *Imaging conditions of thickness and defocus, along the [2,-1,-1,0] zone axis, in which we obtain the maximum contrast for perfect crystals of GaN and AlN.*

In HRTEM simulated images, the position of the atomic columns depends on the examined crystal and the imaging conditions. Figure 2.12 reveals the connection between atomic columns and pattern in simulated images of a GaN and an AlN crystal. The simulated images are calculated for imaging conditions inside the optimal ranges defined before (see Table 2.4). We observe that the patterns are directly related to the Ga-N or Al-N doublets. Specifically, dots in the patterns are associated to two atomic columns. Therefore, the projected atomic structure is not entirely determined. The atomic columns are projected onto white spots for interval of defocus equal to: (i) [-20,0] and [65,75] for the GaN crystal and (ii)[-10,0] and [70,80] for the AlN. For defocus values between 25 to 40 nm atomic columns are found onto black tunnels for both crystals.

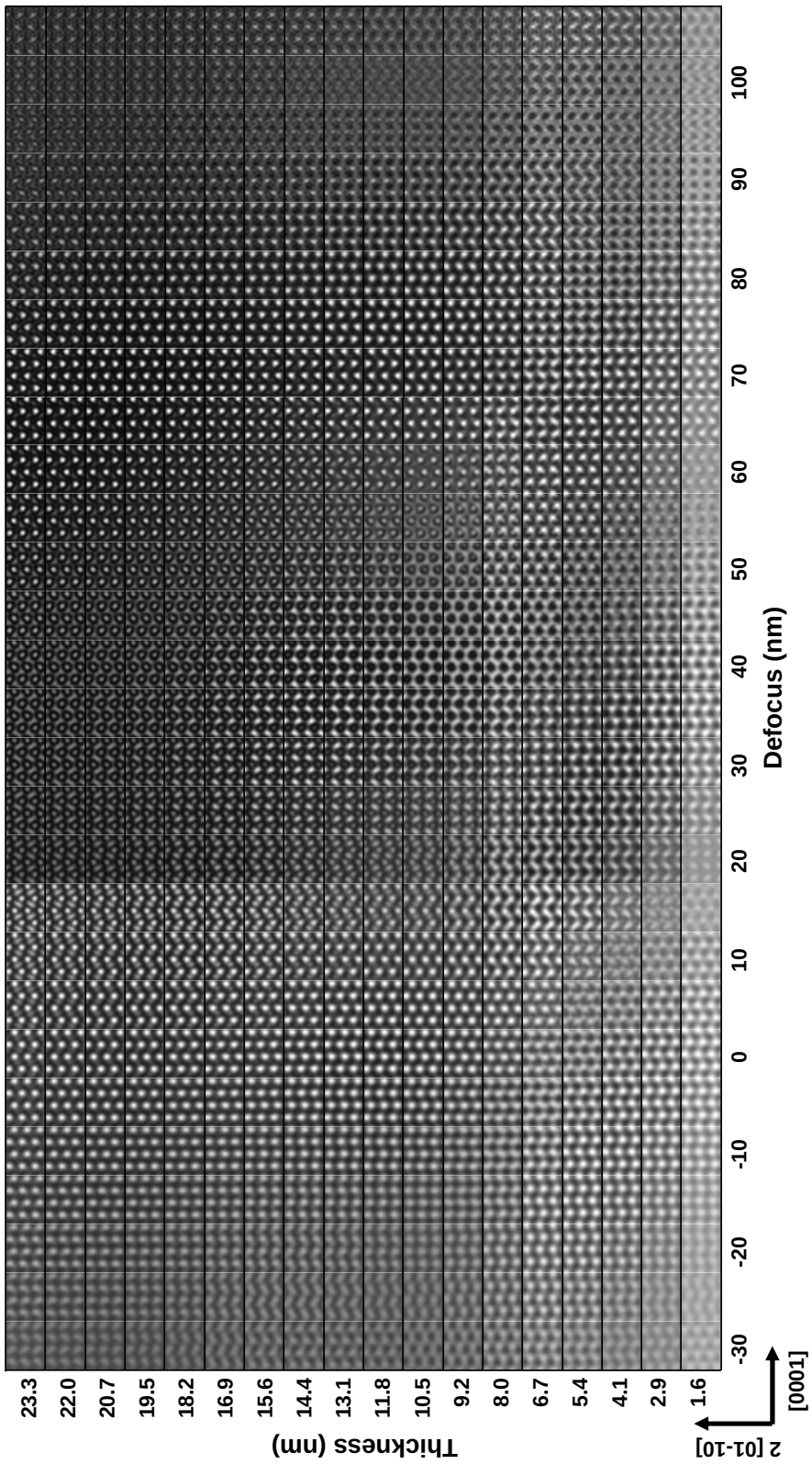

Figure 2.10 : *Thickness/Defocus contrast map of HRTEM simulated images of a GaN perfect crystal along the [2,-1,-1,0] zone axis. (Accelerating voltage: 400KV and Objective aperture diameter:15nm-1)*

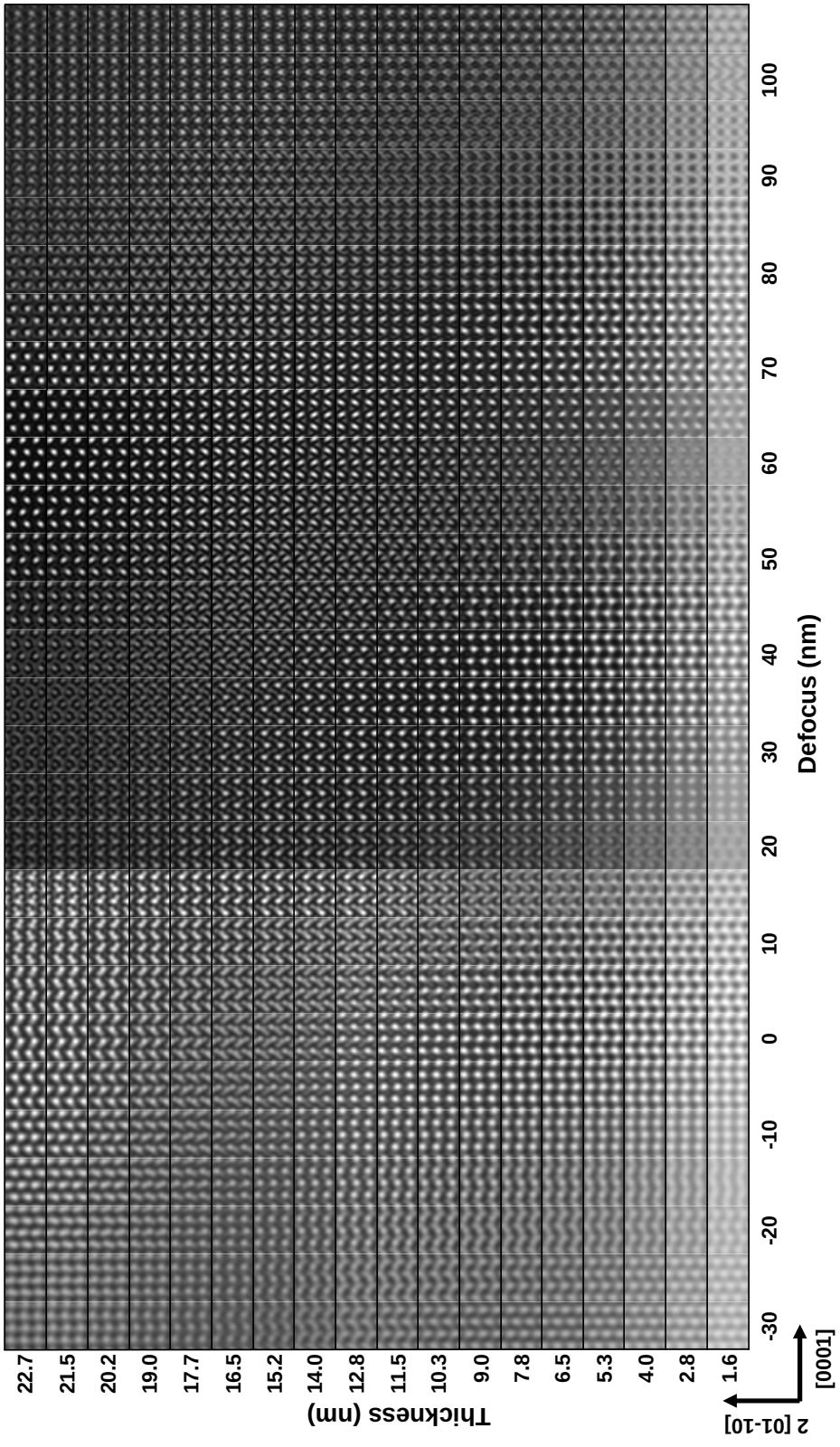

Figure 2.11 : *Thickness/Defocus contrast map of HRTEM simulated images of an AlN perfect crystal along the [2,-1,-1,0] zone axis. (Accelerating voltage: 400KV and Objective aperture diameter:15nm-1)*

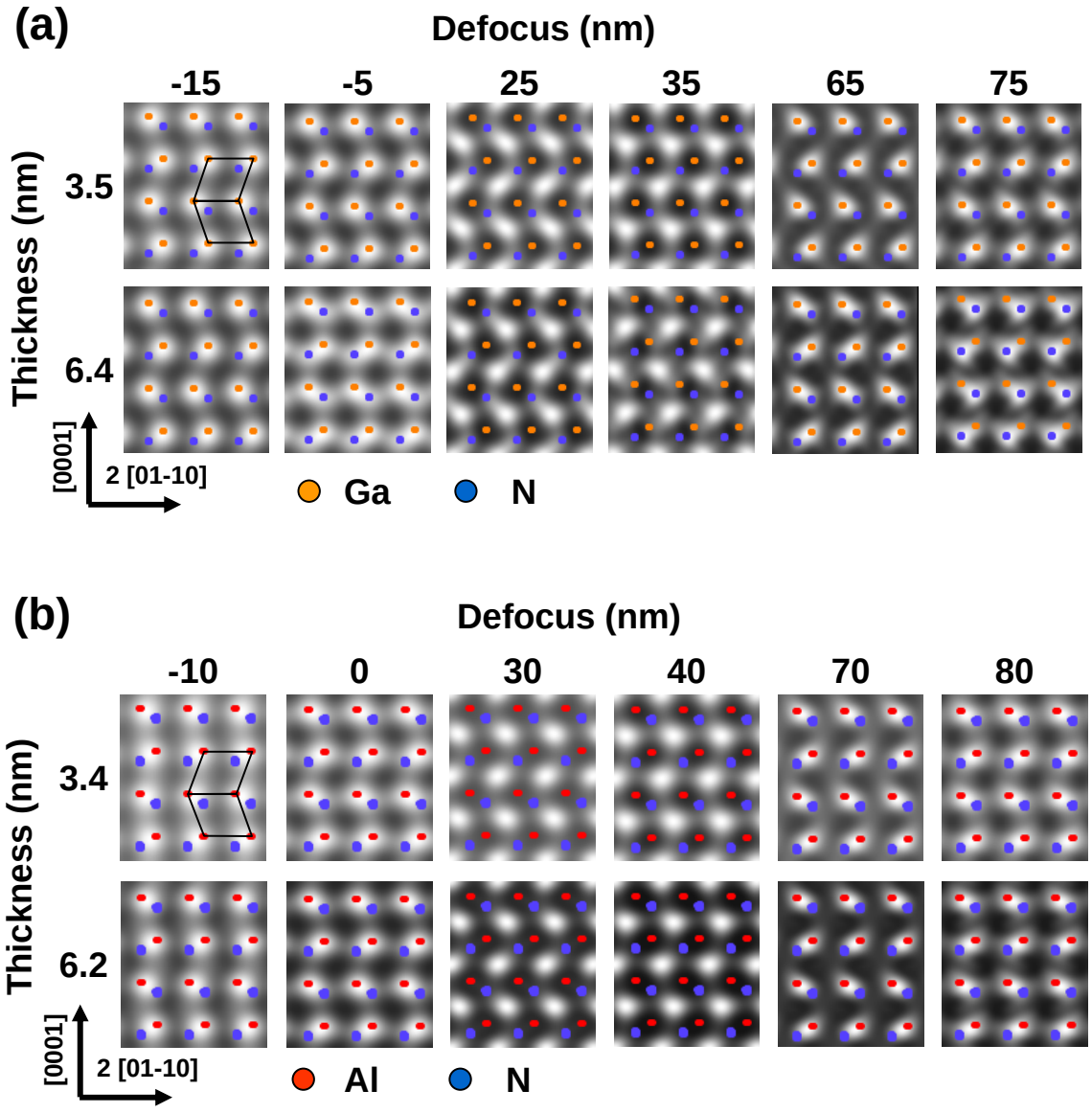

Figure 2.12 : *HRTEM simulated images of (a) a GaN and (b) an AlN crystal viewed along the [2,-1,-1,0] direction in a JEOL4000EX electron microscope with accelerating voltage of 400KV. The atomic positions have been superimposed to the images. (a) Simulations were performed for defocus values of -15, -5, 25, 35, 65 and 75 nm and for two levels of specimen thickness: 3.5 and 6.4nm. The patterns in the images are related to the Ga-N doublets.(b) Simulations were performed for defocus values of -10, 0, 30, 40, 70 and 80 nm and for two levels of specimen thickness: 3.4 and 6.2nm. The patterns are related to the Al-N doublets.*

[0,1,-1,0] Zone axis. Figure 2.9 (b) illustrates the projection of the wurtzite structure along the [0,1,-1,0] direction with the corresponding diffraction pattern. Each atomic column is occupied by one type of element. The unit cell of the projection is a rectangle whose edge sizes are $\mathbf{a}/2$ and $\mathbf{c}/2$. The stacking along the [0001] axis can be described by consecutive rectangles, which are defined by four atoms of the same type. The distance between two atoms of the same type along the [0001] direction is equal to $\mathbf{c}/2$, while along the [2,-1,-1,0] direction this distance becomes $\mathbf{a}/2$. Thus, it is equal to 0.15945 nm for the case of a GaN crystal and 0.1556 nm for an AlN one. The point resolution of the JEOL4000EX electron microscope is 0.17 nm. Therefore, in HRTEM images taken with the [0,1,-1,0] zone axis, a GaN (or AlN) crystal were generally viewed as discontinuous lines rather than distinguished spots, as it was the case along the [2,-1,-1,0] direction. Only at high defocus values, spots can been seen. However, the spots are not associated to single atomic columns.

Contrast maps for GaN and AlN perfect crystals were also calculated for this zone axis, using the same parameters as previously (Figure 2.13 and Figure 2.14 respectively). Table 2.5 summarizes the optimal ranges of defocus and thickness in which GaN and AlN crystals have maximum contrast. We see that it exists common ranges of defocus and thickness for which both crystals have the maximum contrast. The correspondence between patterns and atomic columns are shown in Figure 2.15. The Ga-N and Al-N doublets are projected onto black tunnels for defocus values between 25-50 nm and onto white lines for the other ranges of defocus.

Material	**GaN**					
Thickness t (nm)	$1.7 < t < 9$			$17 < t < 32$		$21 < t < 32$
Interval of defocus	[-15,-5]	[25,40]	[65,80]	[-20,5]	[30,45]	[70,80]
Material	**AlN**					
Thickness t(nm)	$1.6 < t < 10$			$24 < t < 37$		$28 < t < 37$
Interval of defocus	[-10,15]	[35,50]	[70,85]	[-15,5]	[30,45]	[70,80]

Table 2.5 : *Imaging conditions of thickness and defocus, along the [0,1,-1,0] zone axis, in which we obtain the maximum contrast for perfect crystals of GaN and AlN.*

We have seen in Section 2.2.3 that the [0,1,-1,0] zone axis is the best choice for determining the polarity of a GaN layer from CBED patterns. In addition, we will see in chapter 3.1.4 that the fact that only the (0002) planes are visible as lines, is a great advantage in quantitative interplanar distance profiles along the **c** direction. Consequently, [0,1,-1,0] and off-axis (see section 3.5) images were chosen for quantitative c-profiles. By contrast, HRTEM images taken with the [2,-1,-1,0] zone axis were necessary for characterizing the nature and structure of different defects that were present in our samples.

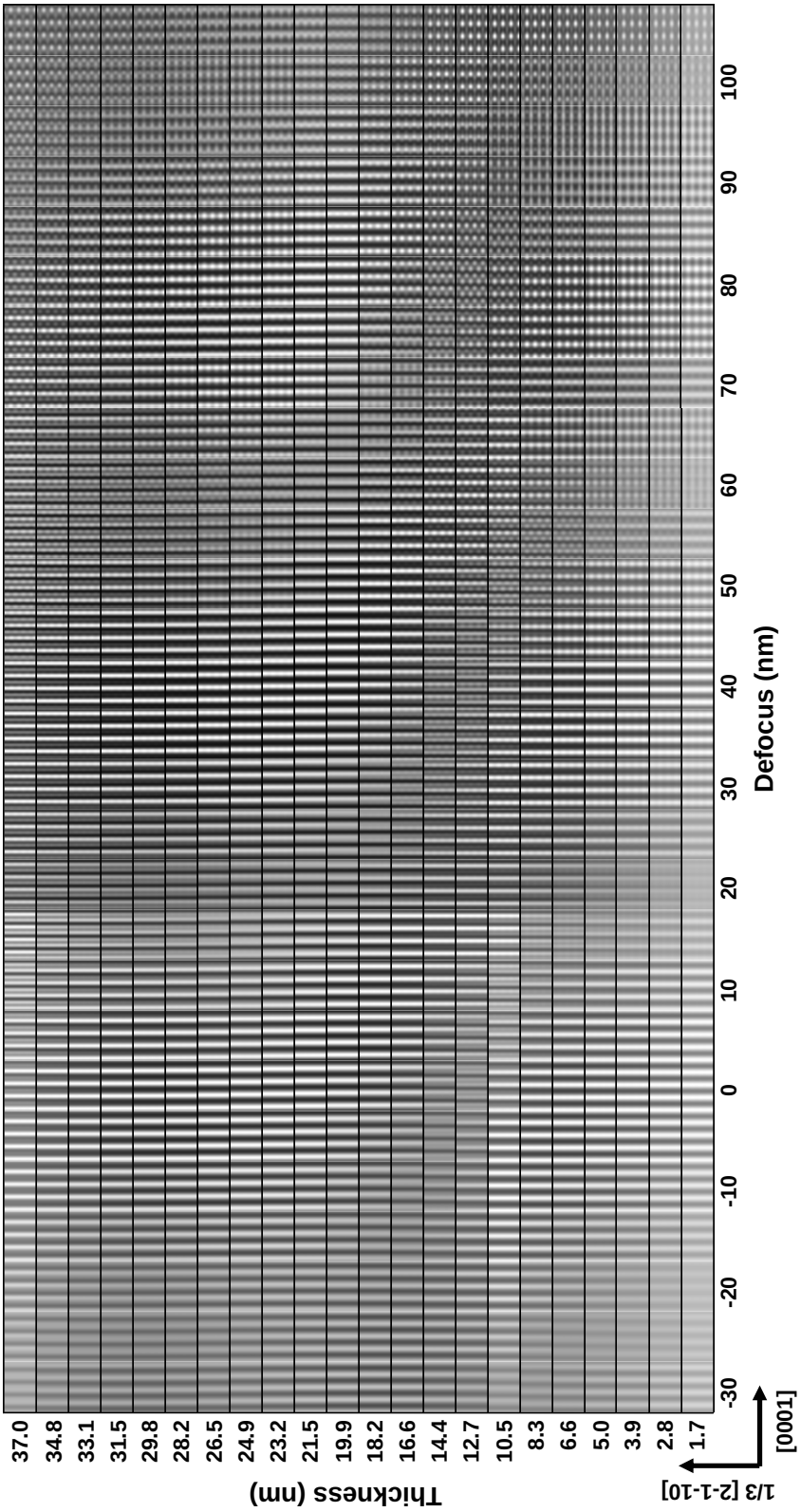

Figure 2.13 : *Thickness/Defocus contrast map of HRTEM simulated images of a GaN perfect crystal along the [0,1,-1,0] zone axis. (Accelerating voltage: 400KV and Objective aperture diameter:15nm-1)*

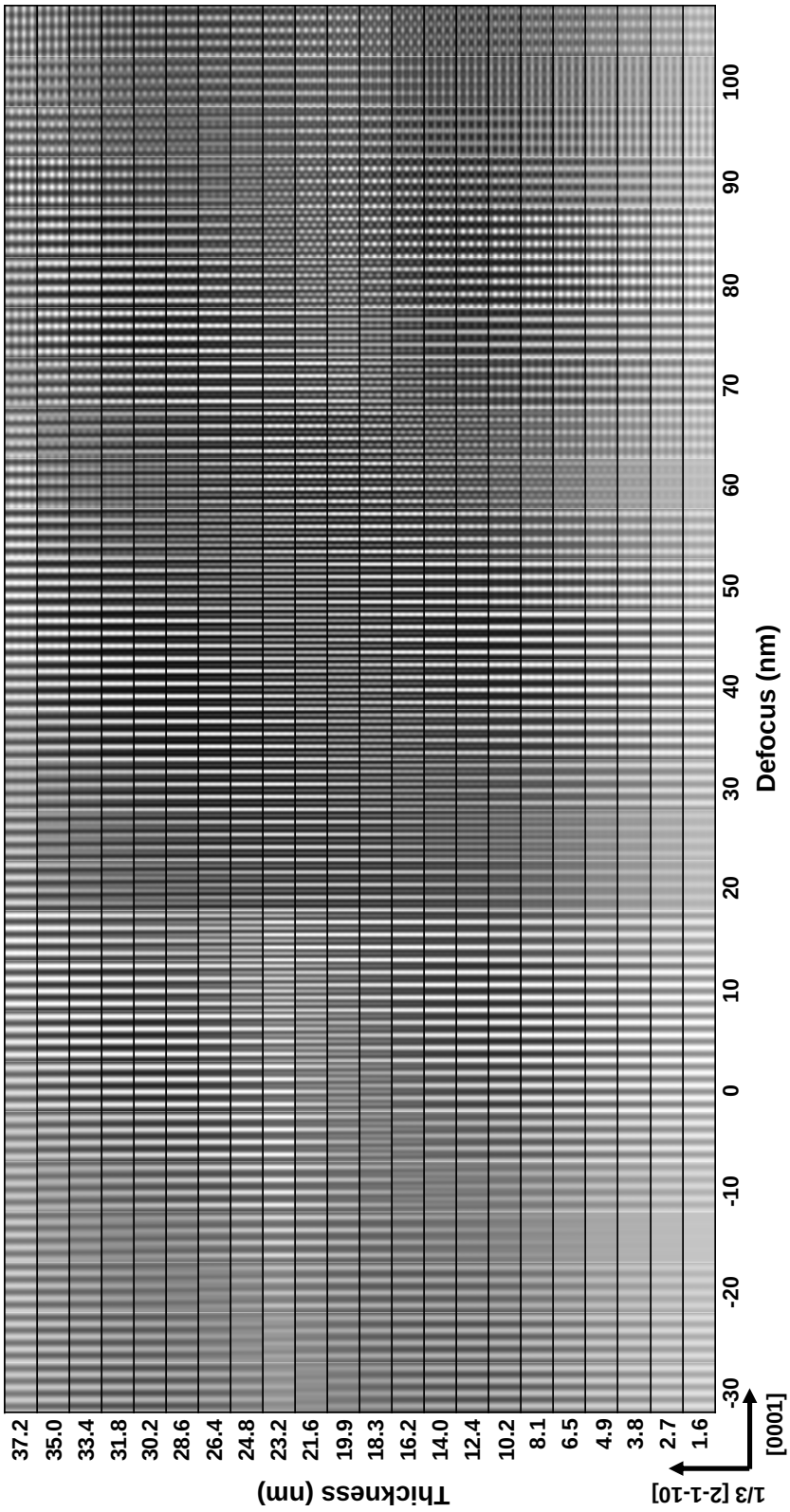

Figure 2.14 : *Thickness/Defocus contrast map of HRTEM simulated images of a AlN perfect crystal along the [0,1,-1,0] zone axis. (Accelerating voltage: 400KV and Objective aperture diameter:15nm-1)*

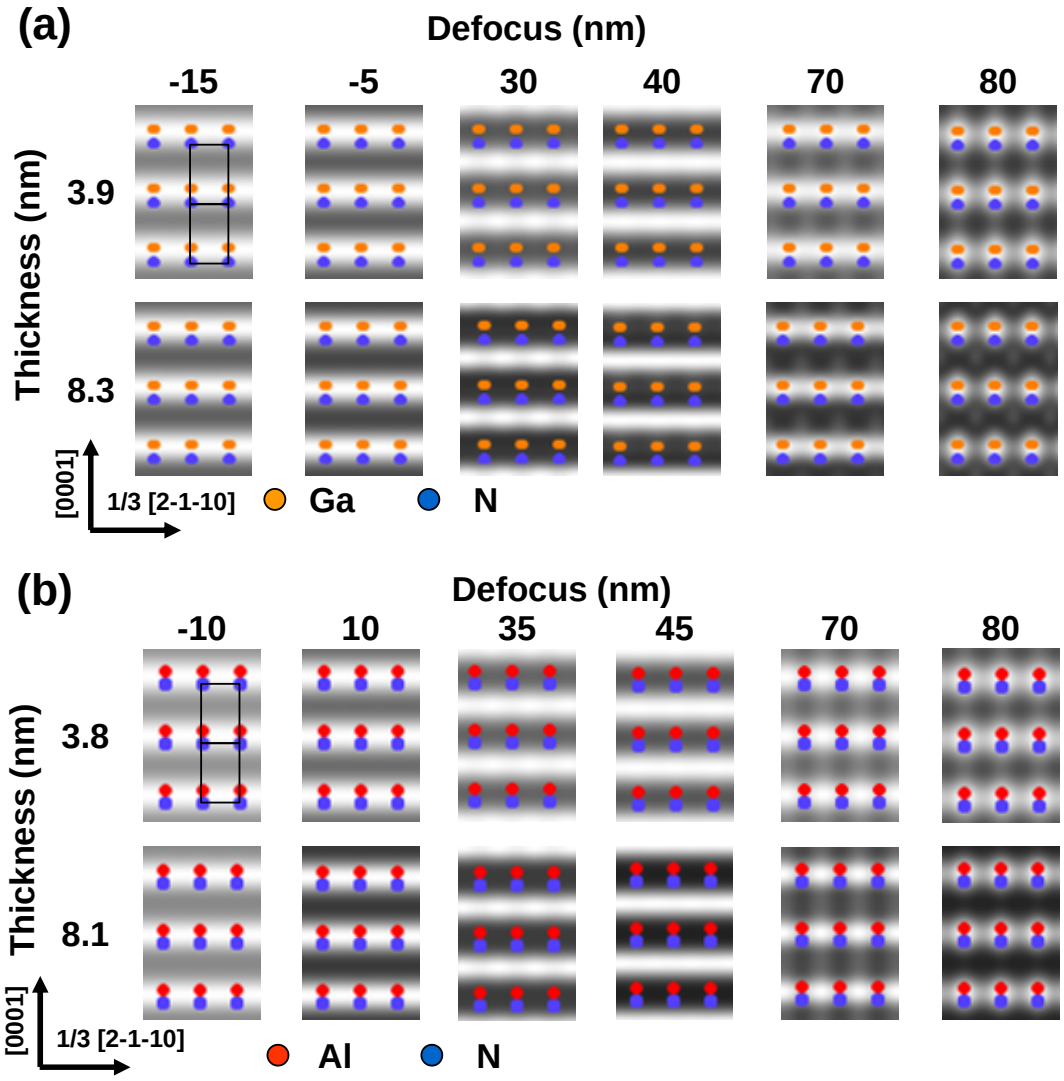

Figure 2.15 : *HRTEM simulated images of (a) a GaN and (b) an AlN crystal viewed along the [0,1,-1,0] direction in a JEOL4000EX electron microscope with accelerating voltage of 400KV. The atomic positions have been superimposed to the images. (a) Simulations were performed for defocus values of -15, -5, 30, 40, 70 and 80 nm and for two levels of specimen thickness: 3.9 and 8.3nm. The patterns are related to the Ga-N doublets.(b) Simulations were performed for defocus values of -10, 10, 35, 45, 70 and 80 nm and for two levels of specimen thickness: 3.8 and 8.1nm. The patterns are related to the Al-N doublets.*

Bibliography

[1] P.B. Hirsch, A. Howie, R.B. Nicholson, and D.W. Pashley M.J. Whelan. *Electron Microscopy of Thin Crystals*. Krieger, Huntington, New York, 2nd edition, 1977.

[2] J.W. Edington. *Practical Electron Microscopy in Materials Science*. Van Nostrand Reinhold, New York, 1976.

[3] P.J. Goodhew and F.J. Humphreys. *Electron Microscopy and Analysis*. 2nd edition Taylor and Francis, New York, 1988.

[4] G. Thomas and M.J. Goringe. *Transmission Electron Microscopy of materials*. Wiley, New York, 1979.

[5] S. Amelinckx, R. Gevers, and J. Van Landuyt. *Diffraction and Imaging Techniques in Material Science*. 2nd edition North-Holland, New York, 1978.

[6] C.E. Hall. *Introduction to Electron Microscopy*. McGraw-Hill, New York, 1953.

[7] J.M. Cowley. *Electron Diffraction Techniques*. Oxford University Press, New York, 1992.

[8] D.B. Williams and C.B. Carter. *Transmission Electron Microscopy: A Textbook for Materials Science*. Plenum Press, New York and London, 1996.

[9] H.A. Bethe. *Ann. Phys. Lpz*, 87:55, 1928.

[10] C.H. MacGillavry. *Physica*, 7:329, 1940.

[11] R.D. Heidenreich. *J. Appl. Phys.*, 20:993, 1949.

[12] N. Kato. *J. Phys. Soc. Japan*, 14:1513, 1959.

[13] J.M. Cowley and A.F. Moodie. *Acta Crystallogr.*, 10:609, 1957.

[14] D.J.H. Cockayne, I.L.F. Ray, and M.J. Whelan. *Phil. Mag.*, 20:1265, 1969.

[15] A. Bourret and J.M. Penisson. *JEOL news*, 25E:2, 1987.

[16] W. Kossel and G. Mollenstedt. *Ann. der Phys.*, 36:113, 1939.

[17] J.C.H. Spence and J.M. Zuo. *Electron Microdiffraction*. Plenum Press, 1992.

[18] R.F. Egerton. *Electron Energy-Loss Spectroscopy in the Electron Microscope*. Plenum Press, 2nd edition, New York, 1996.

[19] M.M. Disko, C.C. Ahn, and B. Fultz. *Transmission Electron Energy Loss Spectrometry in Materials Science*. TMS, Warrendale, Pennsylvania, 1992.

[20] F. Hofer and P. Warbichler. *Ultramicroscopy*, 63:21, 1996.

[21] J.P. Hirth and J. Lothe. *Theory of Dislocations*. MacGraw-Hill, New York, 1968.

[22] P. Stadelmann. *EMS Java version*. http://cimewww.epfl.ch/people/stadelmann/jemsWebSite/jems.html.

[23] P.A. Stadelmann. *Ultramicroscopy*, 21:131, 1987.

Chapter 3

Quantitative analysis of HRTEM images

The extraction of quantitative information from HRTEM images of different nitride nanostructures is the main aim of this thesis. For this purpose, two different techniques were used: (a) a projection method and (b) the geometric phase analysis. In this chapter we describe the basic principles of these two methods and explain how accurate information about the local lattice parameters and consequently about local strain and/or chemical composition can be obtained. The parameters that influence the precision of either methods and how they have been optimized are also reported. Moreover, the mathematical basis of the geometric phase analysis is discussed in detail with a view to better understand how this novel and efficient method works. A possible way to determine the polarity of a nitride heterostructure from interplanar distance profiles will be also discussed. Special attention will be given concerning the distortions that are introduced in HRTEM images acquired with a CCD camera. Finally, the use of off-axis HRTEM images in order to improve the signal-to-noise ratio is described in the last section of the chapter.

3.1 Projection method

Quantitative analysis of HRTEM images requires a highly accurate localization of the atomic columns on experimental images [1]. The projection method lies on measuring the interplanar distances by precisely localizing the intensity maxima in an experimental HRTEM image. The precision of the method depends on the quality of the experimental image and on the adjustable parameters that are involved in the program.

Firstly, the basic principles of the projection method used in this study are given

(section 3.1.1), following by the experimental conditions to be fulfilled in order that the method to be accurate (section 3.1.2). Afterwards, the precision of the method is calculated and the numerical parameters included in the program are optimized (section 3.1.3). The information that can be extracted from the resulting interplanar distances profiles is discussed in section 3.1.4. Finally, the conditions used in this thesis are discussed at the end of this section.

3.1.1 Principle

The projection or peak finding method was first published by Bierwolf *et al.* in 1993 [1]. It has been widely used at the Electron Microscopy group of CEA-Grenoble/DRFMC, which has developed its own codes [2–4]. The method comprise four stages (Figure 3.1):

1. **Selection and Digitization of the HRTEM image**. (Figure 3.1 (a))
   The first step is to select in the experimental HRTEM image an area of homogenous contrast and digitize it if necessary.

   In this thesis, the HRTEM images acquired in the JEOL4000EX microscope, were recorded either on photographic films or directly on a CCD camera[1]. No extra filtering was performed in the experimental images.

2. **Projection of the experimental image**. (Figure 3.1 (b))
   The digitized image is afterwards projected parallel to the planes that we want to measure the interplanar distances, i.e. the program integrates the intensity along the direction of the projection. The result is an average intensity profile I(x).

3. **Precise localization of the intensity maximum**. (Figure 3.1 (c))
   The exact position of every intensity peak is localized by fitting the intensity profile I(x) with a second degree polynomial. The fitting is performed on $2 * n_p + 1$ pixels centered on every maxima.

4. **Interplanar distances profile**. (Figure 3.1 (d))
   Finally, the distance d_i between two successive intensity peaks, corresponding to the interplanar distance of the projected planes, is displayed as a function of the plane numbers.

Attention, the projection method gives the very accurate localization of the intensity maxima not the localization of the atomic columns. In this thesis, all the image processing

[1]In January 2003 the JEOL4000EX microscope was equipped with an $Ultrascan^{TM}1000$ charge-coupled device (CCD) camera of size (2048 x 2048) pixels. My participation in the installation and the calibration of the CCD camera has proven to be a very exciting and useful experience, which helped me in the better usage of the CCD camera during my experiments.

with the projection method, are carried out using macros written in SEMPER [5].

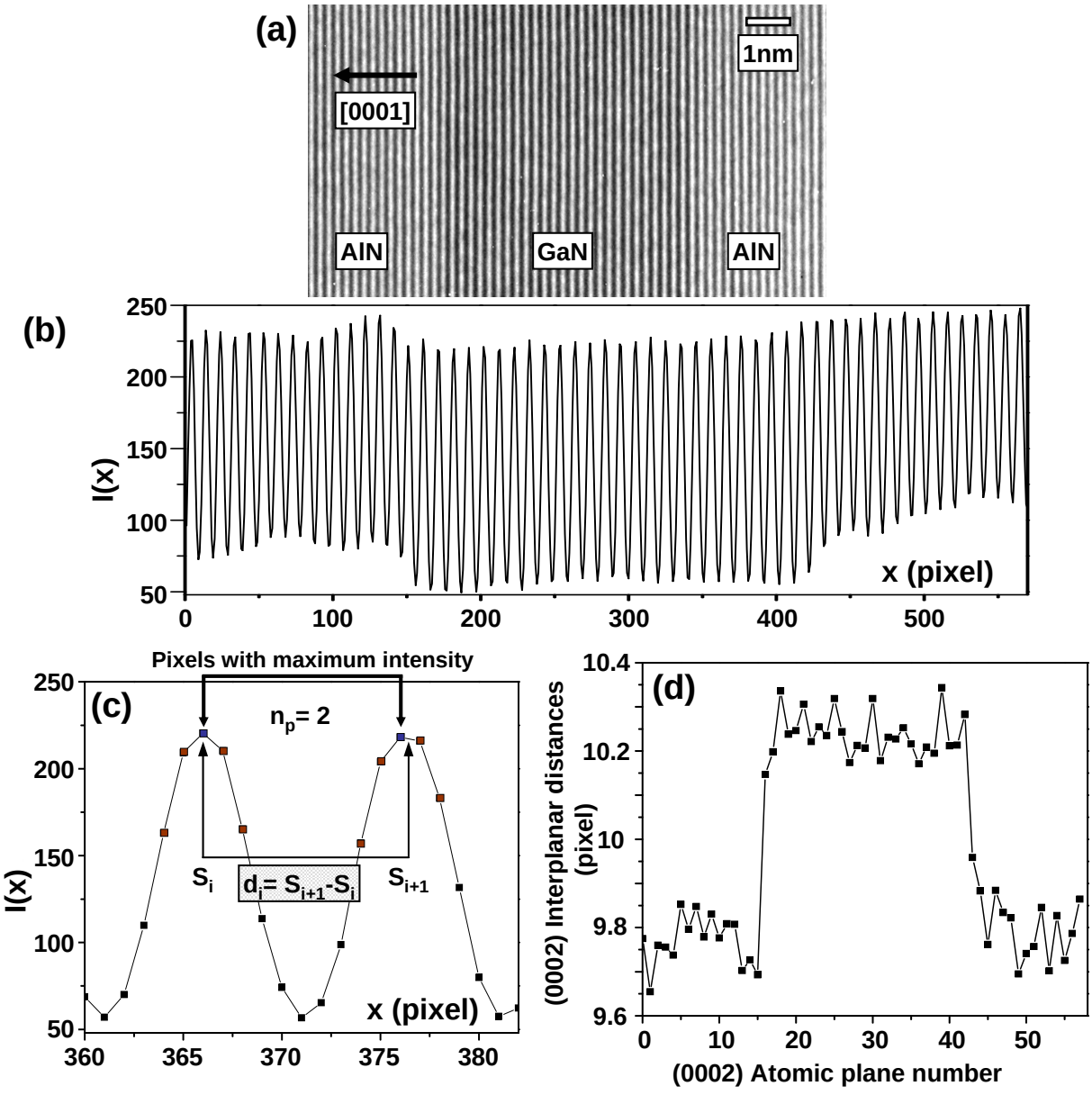

Figure 3.1 : *Basic principles of the projection method. (a) Experimental HRTEM image along the [0,1,-1,0] direction, of a GaN quantum well inside an AlN matrix. (b) Intensity profile of (a). The image is projected along the (0002) planes. (c) Determination of the real position, S_i, of every intensity peak by fitting the intensity profile, $I(x)$, with a second degree polynomial. The fitting is realized for n_p pixels around each maxima. Here $n_p = 2$. Measure of the distances d_i between successive (0002) planes. (d) Interplanar distances profile of (a).*

3.1.2 Experimental conditions and artifacts

It exists a certain number of conditions to be fulfilled in order that the interplanar distance profile represents the real state of the examined material. The analyzed area must:

1. **contain no noticeable extended defects**.
2. **be rather "thick"** [2] In the GaN/AlN system, the strain relaxation which may occur near the free surfaces of the specimen [6,7] and the contribution of the amorphous or mixed layers produced by the ion beam thinning [3] generally prevent the observation of very thin areas.
3. **have a sufficiently high signal-to-noise ratio.** Noise can originate from instabilities of the microscope or from the perturbed ion-milled surfaces of the sample.

In addition, the experimental HRTEM images must satisfy certain conditions in order to give intensity profiles easy to fit. The most crucial ones are:

- the choice of the **zone axis**.
  In this work, we applied the projection method mostly on HRTEM images taken along the [0,1,-1,0] zone axis or on off-axis directions rather than the [2,-1,-1,0] one. As explained in chapter 2.2.4, this choice was based on the fact that, in [0,1,-1,0] or off-axis images only the (0002) planes are visible as black (or white) lines (Figure 3.1(a)). As a consequence, the images are less noisy.

- the **imaging conditions** (thickness and defocus).
  In this work, the imaging conditions were chosen in such a way that the examined images have a maximum and uniform contrast. Maximum contrast means that the optimal ranges of defocus given in Table 2.5 and Table 2.4 have been used. To have a thorough understanding of the profiles at the interfaces and to determine the experimental conditions, image simulations were realized using the multislice method in the JEMS software. The appropriate supercell files were created either in the Atoms software [8] or in a fortran program.

Finally, optical distortions due to the projection system of the microscope influence the accuracy of the projection method. According to JEOL, these distortions are less than 1% for the JEOL 4000EX electron microscope. In practice, for images registered on photographic films, we have always analyzed the center area of the films where the distortions are less important. The distortions in images acquired with a CCD camera will be discussed in section 3.4.

[2] A specimen for HRTEM experiments has usually a thickness range between 1 to 30 nm. So rather thick means around to 5 to 15nm.

3.1.3 Precision in peak location

In the previous paragraph we have given the different conditions that can influence the accuracy of our measurements. In general, we can say that the precision of the projection method is directly related to the precision to locate and fit an intensity maximum. How accurately an intensity peak can be fitted depends on: (a) the noise and (b) the sampling of the examined image.

There are two parameters than can be adjusted when applying the projection method:

- $n_p =$ The number of pixels used to fit each intensity maxima. We remind that the total number of pixels used to fit an intensity peak is $2 * n_p + 1$.
- sb = The number of pixels used to smooth an interplanar distance profile (option).

The way we have chosen to adjust those parameters in order to obtain the maximum precision is discussed below.

The precision was evaluated either on noise free sinusoidal images or on sinusoidal images containing a gaussian noise. The period d of the model images was varied between 7.5 and 22.5 pixels. Each image contained 45 periods. The width of the gaussian-distributed noise in the images was equal to 1. No smoothing was applied in the resulting profiles. By applying the projection method, 45 distances d_i were measured, varying between d_{min} and d_{max}.

The precision Δd was simply defined as the half difference between d_{min} and d_{max}:

$$\Delta d = \frac{\mid d_{max} - d_{min} \mid}{2} \tag{3.1}$$

The important parameter to minimize is the **relative precision $\mathbf{\Delta d/d}$**.

Figure 3.2 plots the relative precision $\Delta d/d$ for the case of **noise free images**, as a function of the number of pixels in period d, for different numbers of pixels n_p. It can be seen that the error made by the projection method when measuring the period d is almost equal to zero. We also notice that independently of the period d the best precision is obtained for n_p=1 (fit on 3 pixels). This is because 3 points located near the maxima of a perfect sinusoid are enough to determine accurately the maxima.

In **noisy images** (Figure 3.3 (a)), for any value of d it exists a value of n_p which gives the best precision Δd. This best *precision* is always equal to $\sim \mathbf{0.08}$. However, the best *relative precision* $\Delta d/d$ is obtained for the highest value of d. Increasing the number of pixels d inside a period, increases the accuracy by which the intensity maxima are located. This is certainly due to the fact that in calculations a new sinusoidal function, i.e. a new image, is created when d is changed.

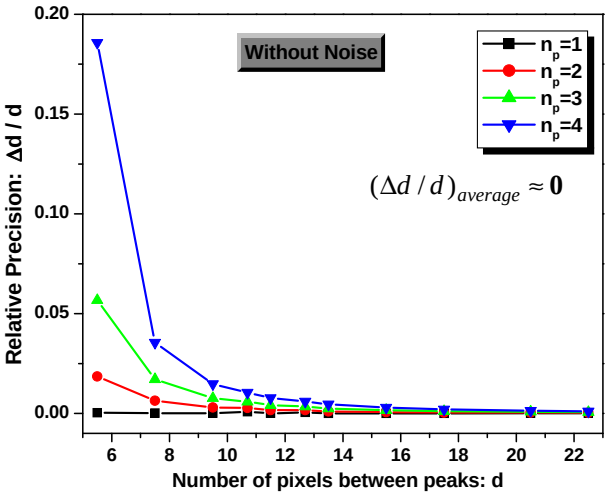

Figure 3.2 : *Relative precision $\Delta d/d$ of the projection method for the case of noise free images.*

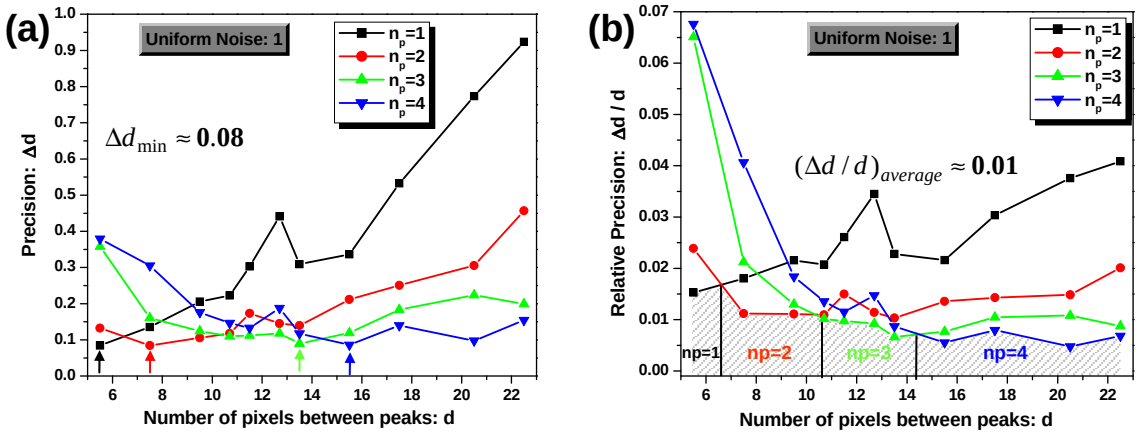

Figure 3.3 : *(a) Precision Δd and (b) Relative precision $\Delta d/d$ of the projection method for the case of images in which uniform noise of width equal to 1 is added. No smoothing was applied in the resulting profiles.*

Similar analysis realized for different **experimental images** showed a different behavior (Figure 3.4). Increasing the number of pixels d between peaks, does not increase the relative precision $\Delta d/d$. The *optimal* relative precision is obtained for d = 8 to 12 pixels and n_p=2. It is equal to **0.021**. If d corresponds to *0.25 nm* ($\simeq$ c/2 of AlN or GaN), we obtain: $\mathbf{\Delta d = 0.00525\ nm = 5.25\ pm}$.

3.1.4 Quantitative analysis of the interplanar distances profiles

So far, we have demonstrated how and with what precision the projection method can measure interplanar distances in a HRTEM image. In this section, we present the different pieces of information that can be extracted from an interplanar distance profile of an A/B/A heterostructure.

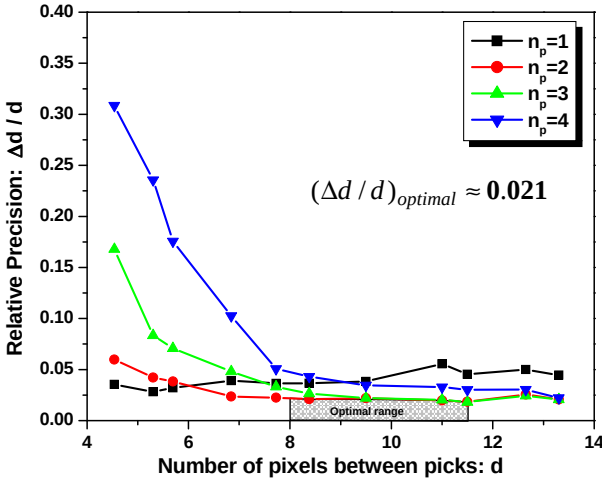

Figure 3.4 : *Relative precision $\Delta d/d$ of the projection method for the case of an experimental image of an AlN crystal. The image contained 50 periods. The period* d *was varied between 4.5 pixels (digitalization at 480 dpi) and 13.3 pixels (digitalization at 5000 dpi). No smoothing was applied in the resulting profiles.*

Average lattice parameter

By averaging interplanar distances inside the different layers, average lattice parameters, d_A and d_B of respectively the materials A and B can be obtained. The accuracy depends on the number N of averaged distances [9]. We note it as $\Delta d_A(N)$. By measuring a distance L containing N periods ($L = N * d_A$), an uncertainty Δd is obtained on the measure of L: $\Delta L = \Delta d = N\Delta d_A$, where Δd is the accuracy defined in the previous part. Therefore we have: $\Delta d_A = \Delta d/N$.

Localization of a material B inside a matrix A

The interplanar distance profile of an heterostructure gives the exact number of monolayers (ML) of the material B. This number, n_B, is given by the equation:

$$n_B = \frac{\sum_{i=0}^{M-1} d_i - M d_A}{d_B - d_A} \tag{3.2}$$

where d_A and d_B are the average lattice parameters of the material A and B respectively and d_0 to d_{M-1} are the interplanar distances of M planes that totally include the material B. This equation can be applied only if the Vegard law is (or is supposed to be) valid and it does not depend on the character of the examined interfaces (abrupt or soft).

The parameters d_A and d_B are calculated from areas in which the lattice parameters of the materials A and B are stable thus away from the interfaces. Since the material A is located on either side of the material B, we measure the lattice parameters of A in those two areas and d_A is the average value of the two measurements. By doing so, we take notice of any eventual difference in the lattice parameter of the material A.

In equation 3.2, the two terms of the numerator can be calculated with a precision

equal to Δd. As a result, the precision in calculating n_B becomes equal to:

$$\Delta_{n_B} = \frac{\Delta(numerator)}{|d_B - d_A|} + numerator \cdot \frac{\Delta(d_A, d_B)}{|d_B - d_A|^2} \tag{3.3}$$

Where $\Delta(numerator)$ is equal to $\Delta d \cdot (1 + M/N_A)$ and $\Delta(d_A, d_B)$ is equal to $\Delta d/N_A + \Delta d/N_B$. N_A and N_B are the number of planes on which we have averaged to get the d_A and d_B respectively. By replacing these values in equation 3.3 we obtain:

$$\Delta_{n_B} = \frac{\Delta d}{|d_B - d_A|}\left(1 + \frac{M}{N_A} + \frac{n_B(N_A + N_B)}{N_A \cdot N_B}\right) \tag{3.4}$$

The number of monolayer, n_B, of a material B inside an heterostructure of type A/B/A, can be measured with a precision equal to $\pm\Delta_{n_B}$.

For instance, by taking $N_A \simeq 2n_B$, $N_B \simeq n_B$ and $M \simeq 3n_B$ the previous equation becomes:

$$\Delta_{n_B} \simeq 4\,\frac{\Delta d}{|d_B - d_A|} \tag{3.5}$$

Replacing Δd by 0.00525 nm, $d_A = \mathbf{c/2}_{AlN}$ and $d_B = \mathbf{c/2}_{GaN}$ (GaN completely strained) we get: $\Delta_{n_B} = 1.567$. This error is rather large. This is because we considered the different terms in equation 3.4 as non correlated values. In fact the error on Md_A is correlated with the error in $|d_B - d_A|$. More precisely, if we consider that material B is strained by material A, the ratio d_B/d_A is completely determined by the theory of elasticity. In the case of B=GaN and A=AlN, $d_B/d_A = 1.054$. Rewriting equation 3.2 as:

$$n_B = \frac{L}{d_A(\frac{d_B}{d_A} - 1)} - \frac{M}{(\frac{d_B}{d_A} - 1)} \tag{3.6}$$

where $L = \sum_{i=0}^{M-1} d_i$ is the distance (length) of the analyzed area. The second fraction is completely determined thus only the two terms L and d_A are introducing errors. Therefore, Δ_{n_B} becomes:

$$\Delta'_{n_B} = \frac{\Delta L}{d_A(\frac{d_B}{d_A} - 1)} + \frac{\Delta d_A\, L}{d_A^2(\frac{d_B}{d_A} - 1)} + 0 = \frac{\Delta d}{|d_B - d_A|}(1 - \frac{L}{N_A\, d_A}) \tag{3.7}$$

By placing $L/d_A \simeq M$ the previous equation becomes:

$$\Delta'_{n_B} \simeq \frac{\Delta d}{|d_B - d_A|}\left(1 + \frac{M}{N_A}\right) \tag{3.8}$$

Taking $N_A \simeq 2n_B$ and $M \simeq 3n_B$ equation 3.8 becomes:

$$\Delta_{n_B} \simeq 2.5 \, \frac{\Delta d}{|d_B - d_A|} \tag{3.9}$$

This value is slightly smaller than the value given in equation 3.5. Taking the same values for Δd, d_A and d_B as before, we have: $\Delta_{n_B} = 0.979$.

Chemical composition and strain

Under different assumptions, the information of an interplanar distance profile can be translated into a chemical composition. This is possible by associating the local strain of a crystal lattice to its chemical composition and by assuming that the under consideration layer is totally strained by the substrate.

More precisely we have to assume a linear variation with the Al chemical composition x of:

1. the lattice parameters $a_0(x)$ and $c_0(x)$ of the involved materials. In our case GaN and AlN.

$$c_0(x) = xc_0^{AlN} + (1-x)c_0^{GaN} \qquad a_0(x) = xa_0^{AlN} + (1-x)a_0^{GaN} \tag{3.10}$$

2. the elastic constants $C_{13}(x)$ and $C_{33}(x)$ of $Al_xGa_{1-x}N$ alloys.

$$C_{ij}(x) = xC_{ij}^{AlN} + (1-x)C_{ij}^{GaN} \tag{3.11}$$

Based on the linear elasticity theory for the case of an hexagonal crystal (see Appendix B), the lattice parameter **c** of an $Al_xGa_{1-x}N$ alloy which is strained along the growth direction is given by the relation:

$$c(x) = c_0(x)\Big[1 + 2\,\frac{C_{13}(x)}{C_{33}(x)}\,\frac{a_0(x) - a_s}{a_s}\Big] \tag{3.12}$$

The strain $\epsilon = \frac{a_0(x)-a_s}{a_s}$ is a function of the lattice parameter a_s imposed by the substrate. In Figure 3.5(a) the function c(x) described by equation 3.12 is traced, assuming an AlN substrate ($a_s = a_0^{AlN} = 0.3112$ nm).

We notice the involvement of the ratio C_{13}/C_{33} when finding the chemical composition of a $Al_xGa_{1-x}N$ layer or a AlN/GaN interface using this procedure. We have reported in chapter 1 (paragraph 1.3) that the published values for the elastic constants $C_{ij}(x)$ of AlN and GaN are rather scattered. In Figure 3.5(a), c(x) functions are plotted (equation 3.12) using for the $C_{13}(x)/C_{33}(x)$ ratio the lower (0.2545 [10] for AlN and 0.2543 [11] for GaN)

or the upper (0.3325 [12] for AlN and 0.5918 [13] for GaN) reported values. We can see that for the same value of c(x), for example c(x)=0.5249 nm, if we use the graph traced using the lower value for the $C_{13}(x)/C_{33}(x)$ ratio the result is a pure GaN layer, while the result is a $Al_{0.2}Ga_{0.8}N$ alloy if we use the graph traced using the upper values for the $C_{13}(x)/C_{33}(x)$ ratio. This difference of 20% corresponds to the maximum error that can be made in measuring the chemical composition by this procedure and it is obvious that it is not negligible.

As a result, the error in calculating the chemical composition of a layer, from interplanar distance profiles strongly depends on the adopted $C_{13}(x)/C_{33}(x)$ ratio. In this thesis for the elastic constants C_{13} and C_{33} of AlN and GaN the values are arbitrary chosen equal to: $C_{13}^{AlN} = 108$, $C_{33}^{AlN} = 373$, $C_{13}^{GaN} = 103$ and $C_{33}^{GaN} = 405$ [11]. Therefore by using the graph of Figure 3.5(b) we could correspond for every parameter **c** measured by the projection method a chemical composition x.

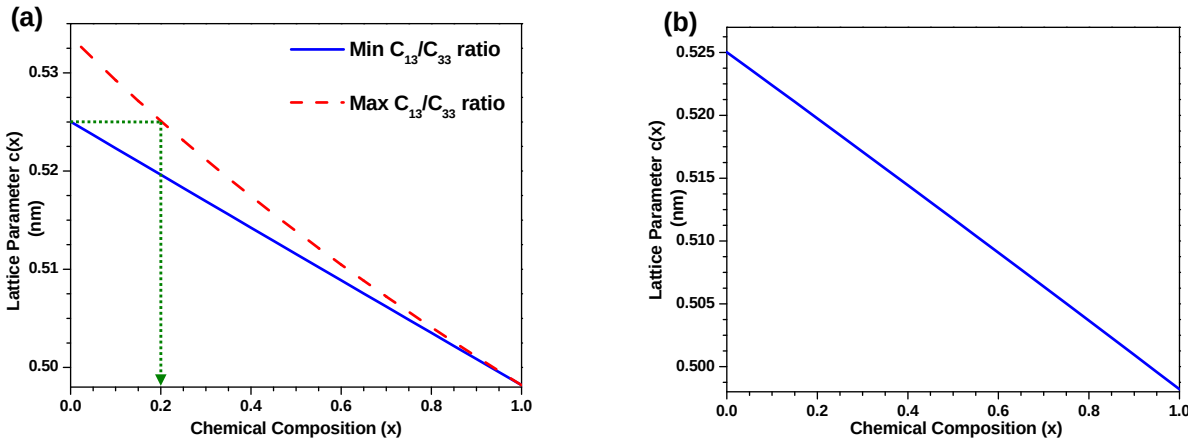

Figure 3.5 : *Lattice parameter c(x) of an $Al_xGa_{1-x}N$ alloy as a function of the chemical composition x. As substrate an AlN layer is considered. (a) Blue line: lower reported values for the $C_{13}(x)/C_{33}(x)$ ratio. Red dashed line upper reported values for the $C_{13}(x)/C_{33}(x)$ ratio. (b) $C_{13}(x)/C_{33}(x)$ equal to 0.2543 for GaN and 0.2895 for AlN. Adopted in this thesis values for the elastic constants.*

Interface width

From the interplanar distance profiles the width of the interfaces in an A/B/A heterostructure can be measured. Different definitions of interface width can be used. We have defined the widths of the interfaces A/B (W_1) and B/A (W_2) by using continuous interplanar distance profile as shown in Figure 3.6. In particular, d_{A1}, d_B and d_{A2} are respectively the averaging lattice parameters of the material A located on the left side of the material B, the material B and the material A located on the right side of the material B. Additional, $\Delta d_{A1} = d_B - d_{A1}$ and $\Delta d_{A2} = d_B - d_{A2}$.

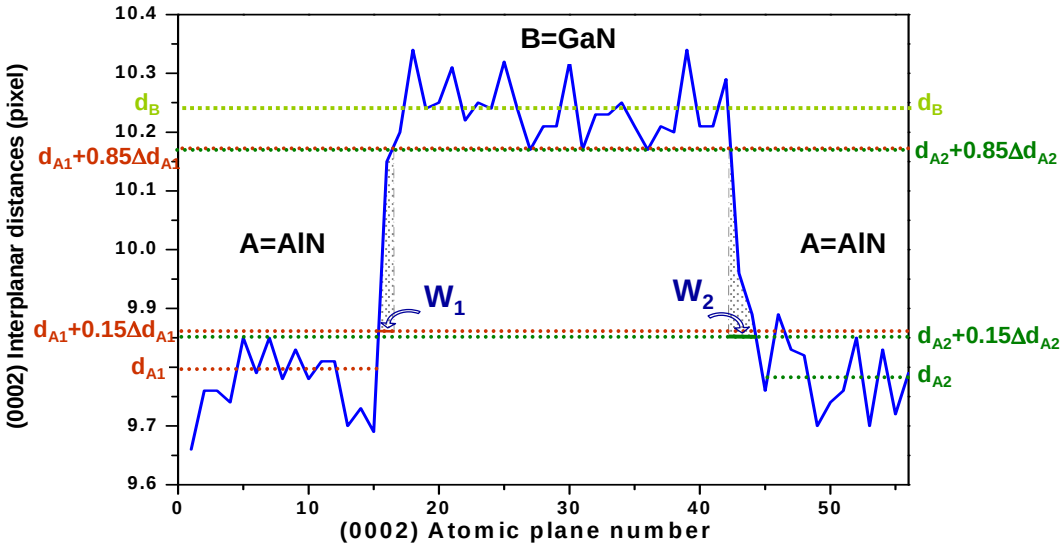

Figure 3.6 : *Definition of interface width W_1 and W_2. Case of the AlN/GaN/AlN heterostructure shown in Figure 3.1(a). No smooth was applied in the experimental profile.*

Although, this measurement of interface width appears easy and accurate enough, in reality it strongly depends on the quality and the imaging conditions under which the examined experimental image has been acquired (see end of this section 3.1.4). A solution to reduce the noise which originates from the experimental images, is to smooth the resulting profile over a selected number of pixels (sb). This point, which is discussed in the following paragraph, will not however improve the accuracy of width measurements.

We have to notice that an interplanar distance profile cannot make a distinction between a diffuse and a rough interface.

Smoothing of the interplanar distances profiles.

The possibility of smoothing an interplanar distance profile was introduced in the SEMPER routines. In the smoothing process, each interplanar distance d_i is replaced by an average over (sb) adjacent points centered on point i. For example for sb=3, $d_i^{'} = (d_{i-1} + d_i + d_{i+1})/3$, for sb=4 $d_i^{'} = (d_{i-2} + d_{i-1} + d_i + d_{i+1})/4$. The edges are processed as if the boundary values were repeated indefinitely outwards.

For illustration, the effect of smoothing is presented in Figure 3.7, using the experimental image of Figure 3.1(a). The nominal thickness of the GaN QW is equal to 7 nm$\simeq$ 27 ML. Different values of sb are used (sb $= 2 \rightarrow 6$). It can be clearly seen that the interfaces become wider as sb increases. Moreover, we have used the obtained profiles to measure the thickness of the GaN layer and the width of the two interfaces (AlN/GaN and GaN/AlN) using the definitions given previously. Table 3.1 assembles the obtained results. The error Δn_B was calculating using equation 3.8. The important result is that

the thickness layer is not notably affected by the smoothing of the profiles. However, the width of the interfaces greatly varies with sb.

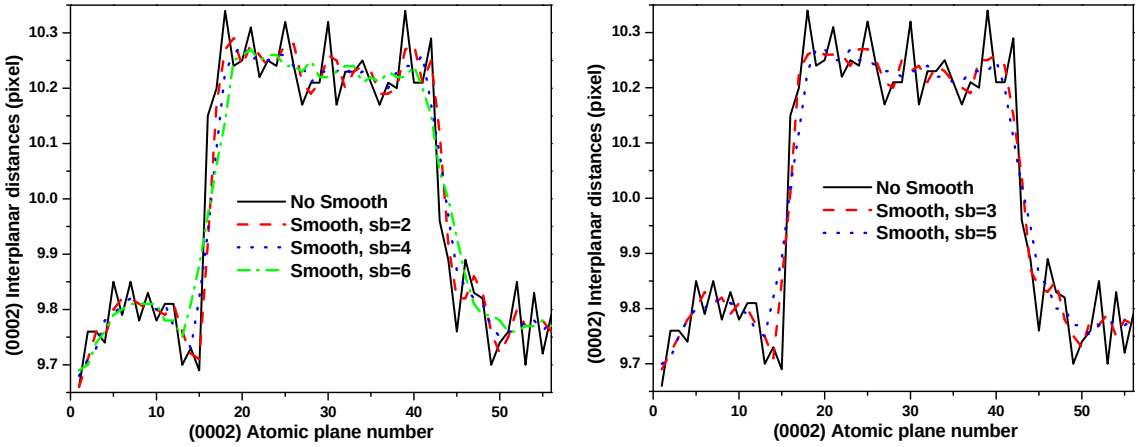

Figure 3.7 : *Effect of smoothing an interplanar distances profile. Case of the AlN/GaN/AlN heterostructure shown in Figure 3.1(a). The size of block (sb) over which the local average is calculated was varying from 2 to 6. The widening of the interfaces, as we increase the parameter sb, is clearly seen.*

	$n_B \pm \Delta_{n_B}$ (ML)	W_1 (ML)	W_2 (ML)
No smooth	26.48 ± 0.16	1.1	1.9
Smooth, sb=2	26.45 ± 0.16	1.3	2.1
Smooth, sb=3	26.91 ± 0.19	1.6	3.5
Smooth, sb=4	26.81 ± 0.20	2.2	4.1
Smooth, sb=5	26.99 ± 0.21	2.9	4.6
Smooth, sb=6	26.59 ± 0.21	3.5	4.7

Table 3.1 : *Effect of smoothing in measuring the thickness of a layer and the width of the interfaces. Case of the AlN/GaN/AlN heterostructure shown in Figure 3.1(a).*

The importance of the imaging conditions

We have indicated in section 3.1.2 that the knowledge of the imaging conditions under which an experimental image is acquired is important. In this section, we examine how these conditions can influence the information extracted from an interplanar distance profile. In that way the optimum experimental conditions are determined.

For this purpose, the structure of a GaN quantum well (QW) embedded inside an AlN matrix has been simulated. It consists of 6 ML of GaN surrounded on each side by 7 ML of AlN. The interfaces are abrupt. The simulations were realized for the [0,1,-1,0] zone

axis. A schematic illustration of the simulated structure together with thickness/defocus contrast maps for two values of the objective aperture diameter, $15nm^{-1}$ and $9nm^{-1}$ can be seen in Figure 3.8. The (0002) planes are viewed as discontinuous lines of spots for an aperture of $15nm^{-1}$ (Figure 3.8 (d)) and as continuous lines for an aperture of $9nm^{-1}$ (Figure 3.8 (c)). The choice of the objective aperture diameter has been based on the values used to acquire the experimental images.

The simulated images were afterwards analyzed by the projection method and the results can be seen in Figures 3.9 and 3.11. In particular, Figure 3.9 illustrates the resulting interplanar distances profiles for the case where the thickness value is kept constant and equal to 4.3 nm and the defocus value is varying. Interpretable profiles are obtained only for defocus ranges between 30 to 50 nm (Figure 3.9 (b_1)) and 70 to 90 nm (Figure 3.9 (c_1)) for an objective aperture of $15nm^{-1}$ and between 30 to 50 nm (Figure 3.9 (b_2))and 65 to 95 nm (Figure 3.9 (c_2)) for an objective aperture of $9nm^{-1}$. For the other defocus values the presence of Fresnel fringes influence importantly the profiles and a direct interpretation is not possible (see Figures 3.9 (a_2), (a_2), (d_1) and (d_2)).

Better profiles arise for small values of the objective aperture. For instance, by comparing Figure 3.9 (b_1) and (b_2) and/or (c_1) and (c_2), we see that for an objective aperture of $9nm^{-1}$, the resulting profiles are less noisy from the corresponding profiles obtained for an objective aperture of $15nm^{-1}$. This certainly comes from the fact that the simpler is the contrast of the HRTEM image, the more accurate is the location of the maxima. Consequently, HRTEM images composed of lines are better adapted for quantitative strain analysis that dot like HRTEM images, when strain measurements along only one direction is looked for.

The position of the AlN/GaN and GaN/AlN interfaces, depending on whether the atomic columns are located on black tunnels (defocus between 30 to 50 nm) or on white lines (or spots) (defocus between 65 to 95 nm) is shown in Figures 3.9 (b_2) and (c_2). We notice that in the 65 to 95 nm defocus range, the widths are slightly broader due to Fresnel fringes. This is better shown in Figure 3.10, where the interplanar distances profiles of two simulated images with the same value of thickness and defocus equal to 40 and 80 nm are superimposed and shifted in order to emphasize the width difference. For a defocus of 40 nm the widths of the AlN/GaN and GaN/AlN interfaces are respectively 0.57 ML and 0.55 ML. The thickness of the GaN well was measured equal to 6.13 ± 0.16 ML. In contrast, for a defocus of 80 nm, the AlN/GaN interface width was measured equal to 1.36 ML, while the width of GaN/AlN interface was 1.37 ML. The GaN well was found equal to 5.92 ± 0.16 ML.

Finally, from Figure 3.11 we can see that the interplanar distances profiles are not to sensible in the variations of sample thickness when the defocus value is kept constant.

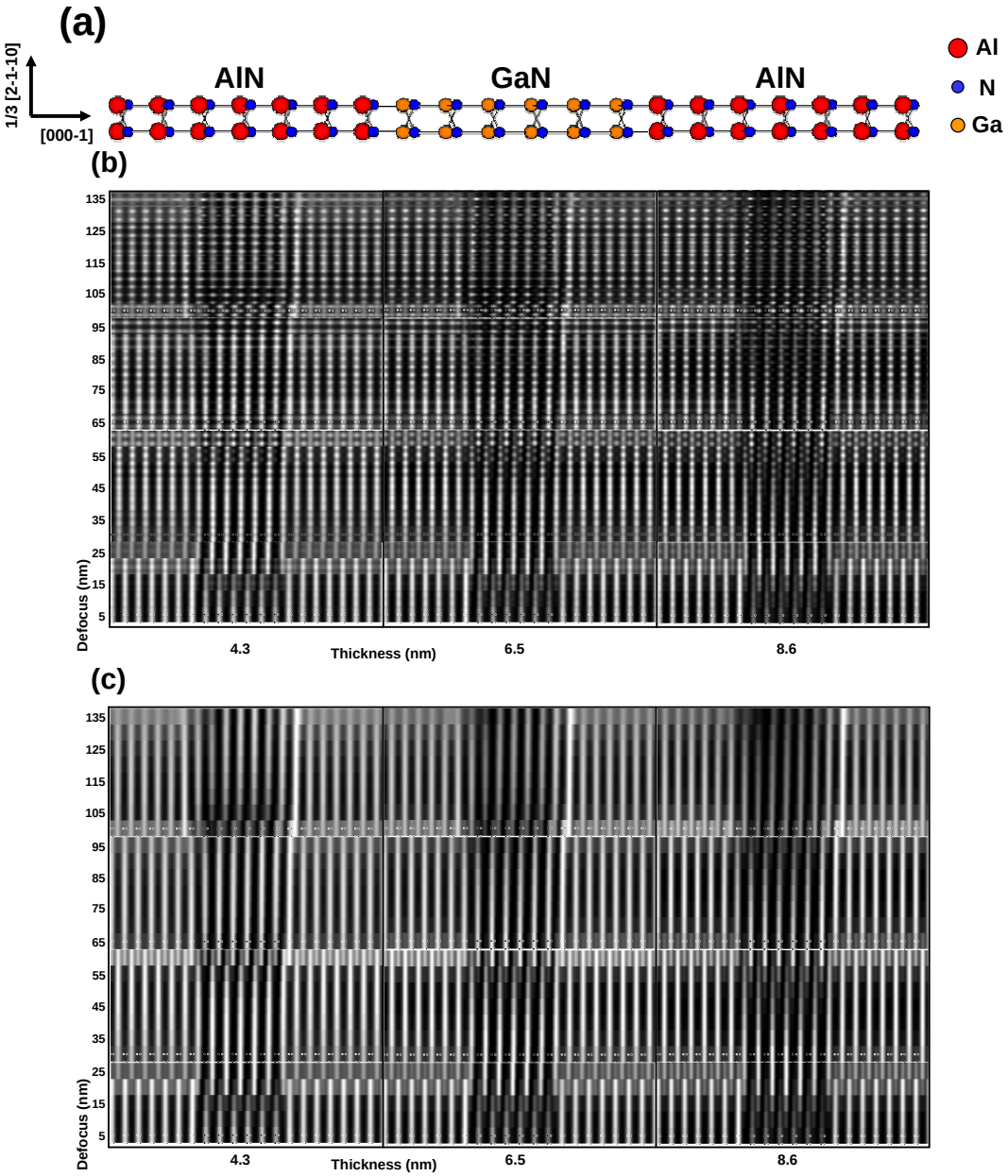

Figure 3.8 : *(a)Schematic illustration of the QW structure used to check the influence of imaging conditions on the projection method analysis. The structure is viewed along [0,1,-1,0] zone axis. It consists of 6 ML of GaN surrounded on both sides by 7 ML of AlN. (b)-(c) Thickness/Defocus contrast map of the QW structure along the [0,1,-1,0] zone axis for three different values of thickness (4.3, 6.5 and 8.6 nm). The defocus range was taken from 5 to 135 nm with a step of 5nm. Accelerating voltage: 400KV. For certain imaging conditions the atomic structure of the simulated QW is superimposed. (b) Objective aperture diameter:* $15nm^{-1}$ *and (c) Objective aperture diameter:* $9nm^{-1}$

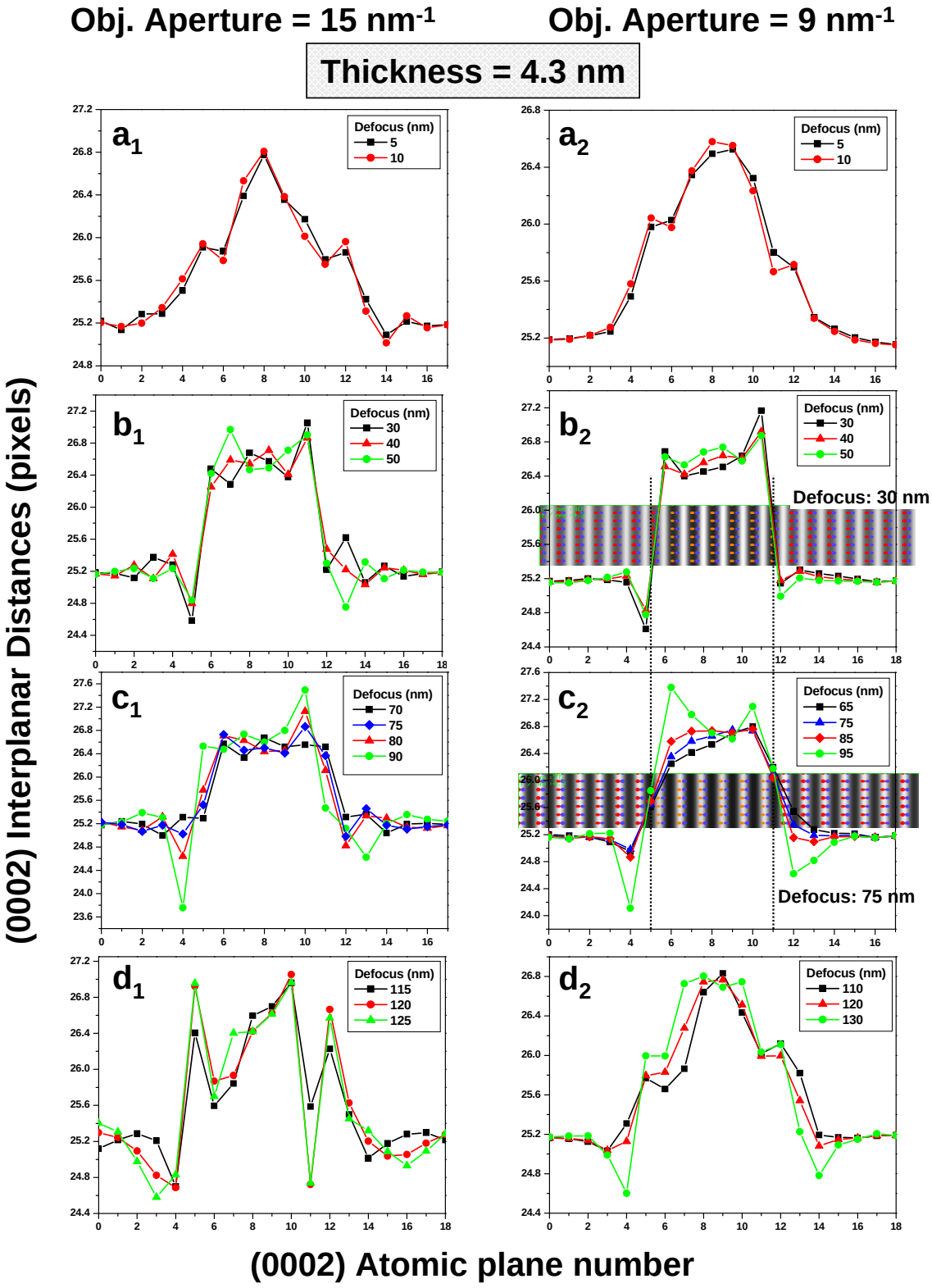

Figure 3.9 : *Interplanar distances profiles of the simulated images with thickness 4.3 nm of Figure 3.8 (b)-(c). Interpretable profiles are obtained for defocus ranges between [30,50] nm (atoms on black tunnels) and [65,95] nm (atoms on white lines). By selecting a small objective aperture diameter we decrease the noise in the resulting profiles.*

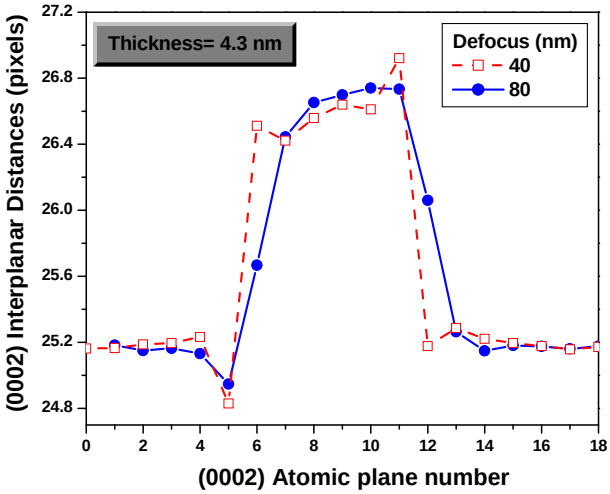

Figure 3.10 : *Superposition of two interplanar distances profiles obtained by in focus (red line) and out of focus (blue line) simulated images. The interfaces become broader as we move away the Scherzer defocus. The thickness of the QW remains approximately constant. Thickness= 4.3 nm and objective aperture diameter=9nm^{-1}.*

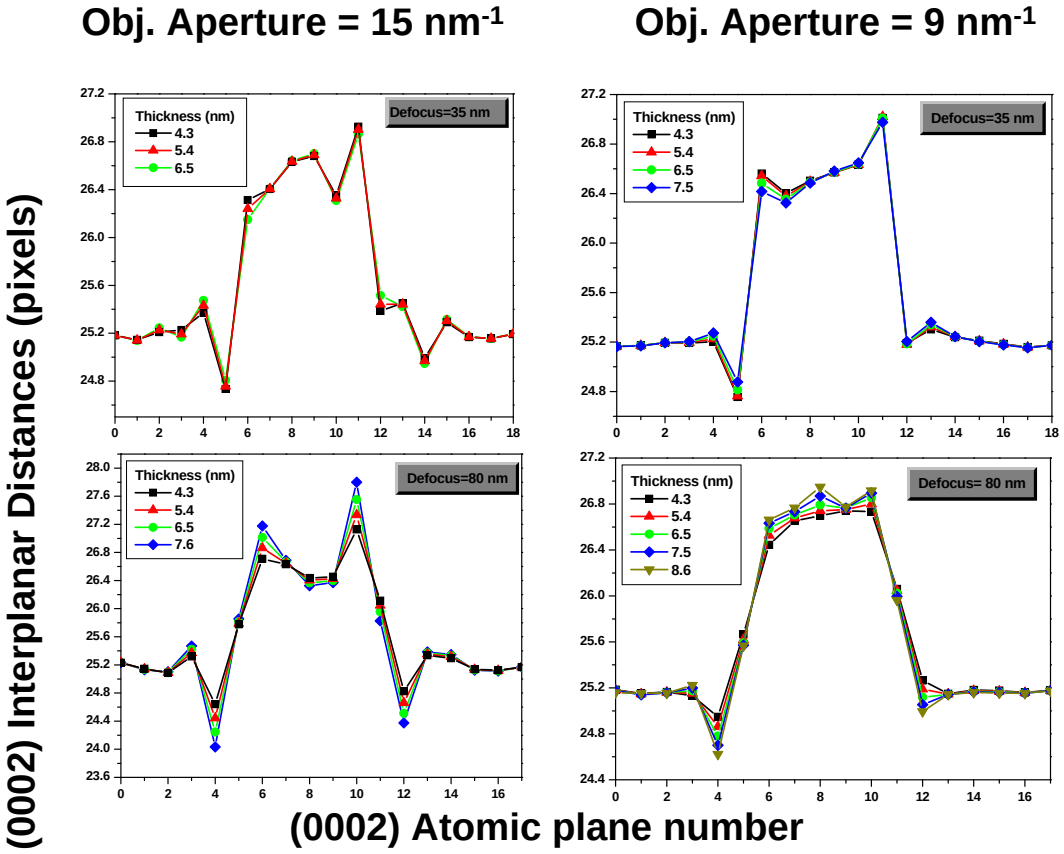

Figure 3.11 : *Interplanar distances profiles resulting from simulated images of the structure shown in Figure 3.8 (a). Keeping the defocus value constant and varying the thickness does not influence significantly the resulting profiles.*

3.1.5 Use of the projection method in this thesis

We have described in this section the basic principals of the projection method and the kind of information that can be extracted from the resulting interplanar distance profiles. We close this section by addressing the conditions that are adopted in this thesis in order to extract in the most precise way the desirable quantitative information.

Apart from the general conditions which were discussed in paragraph 3.1.2, in the experimental results presented in the following chapters the following points were adopted and satisfied:

- **Zone axis and imaging conditions** We have performed the projection method on HRTEM images having lines (i.e images of atomic planes) instead of dots (i.e. images of atomic columns). The [0,1,-1,0] zone axis or off-axis conditions were generally chosen. Finally, images having a defocus value close to the Scherzer defocus were prefered.

- **Value of $\mathbf{n_p}$**. In general, the period d was equal approximately to 0.25 nm ($\simeq$ c/2 of AlN or GaN) and was represented by around 8-10 pixels. Based on the analysis presented in 3.1.3, n_p was always taken equal to 2.

- **Precision of the average lattice parameter measurement.** In order to be as precise as possible when measuring the lattice parameter of a crystal, I have always realized the above measurement in at least 10 different areas of interest. The normality of the resulting distribution of average values was checked using either the Shapiro-Francia [14] or the Shapiro-Wilk test [15]. In cases where this distribution was normal, the lower and upper limit for a confidence interval level of 90% calculated by one sample t-test [3] was considered as the measurement error. When the distribution was not normal the standard deviation was considered as the measurement error.

- **Precision in localizing a material B inside a matrix A.** The number of monolayer, n_B, of a material B can be measured with a precision of $\pm\Delta_{n_B}$ (see equation 3.4).

- **Defining the chemical composition.** Due to the uncertainty in the C_{13}/C_{33} ratios (20% accuracy), the absolute chemical composition determination is not reliable.

[3] According to Mather, 1971, p.75, the t-ditribution was originally derived by W.S. Gossett in 1908. Gossett carried out his work while he was working in the Guiness Brewery in Dublin. It was based upon samples taken from a population made up of the heights of 3000 criminals. The company at the time wouldn't allow employees to publish their own work. So Gassett printed his work under the pseudonym "Student". Hence the t-test is called sometimes "Student's t-test".

For this reason, *EFTEM measurements* were performed in order to extract information about the chemical composition of the examined heterostructures.

- **Interface width measurement.** For the measurement of an interface width by the projection method we have always:

  (a) used images with defocus value close to the Scherzer (50 nm for the JEOL 4000EX)

  (b) compare and verify the obtained result with *image simulations* and/or *EFTEM experiments*. By doing so, we were sure about both the nature (diffuse or rough) and the width of the examined interfaces.

- **Smoothing.** The interplanar distances profiles presented in this thesis are the original ones, meaning that no smoothing is applied.

- **Polarity determination.** We have used CBED experiments to determine the polarity of our samples. However, in some cases we able to confirm the validity of the rule given in 3.3.

3.2 Geometric Phase Analysis

We have already mentioned that we need to be very careful when interpreting HRTEM images since the image contrast depends on several parameters such as specimen thickness, composition, surface contamination, specimen damage due to ion milling and imaging conditions. During the last decades, many efforts have been made in order to achieve the extraction of quantitative information from HRTEM images. For a review see the paper of S. Kret *et al.* [16]. The geometric phase analysis (GPA) has proven to be a powerful tool for measuring and mapping displacements and strain fields from HRTEM images. The method was independently introduced by M. Takeda *et al.* [17] and M. Hÿtch *et al.* [18] and rapidly it has been applied successfully in quite a number of HRTEM image analysis works [19–22].

This section contains the basic principles and a theoretical analysis of the GPA.

3.2.1 Principle

HRTEM lattice images from "perfect" crystalline materials are characterized by strong Bragg-reflections in their Fourier transforms. The location of a Bragg-reflection gives the periodicity and the orientation of the fringes in the image, while its phase gives the location of the fringes. For perfect crystals, the phase of any Bragg reflection $\mathbf{g}$ is constant across the image. However, for a distorted lattice small deformation can be seen as local lateral shifts of the lattice fringes and consequently as small changes in the phase corresponding to $\mathbf{g}$. This is the property that GPA uses.

The phase determined by the GPA is related to the position of the lattice fringes in the HRTEM image and has been called geometric [23] to avoid confusion with the phase of the diffraction beam $\mathbf{g}$ at the exit plane of the specimen [24]. The basic concept of the GPA is not new. Similar process has been used in optical interferometry [25] and off-axis electron holography.

The principal steps of the GPA [18] are illustrated in Figure 3.12, for the case of a simulated HRTEM image of a grain boundary.

Firstly, the Fourier transform of the image intensity $\mathrm{I}(\mathbf{r})$ is calculated. In order to select a reciprocal lattice vector $\mathbf{g_1}$ (Figure 3.12(b)) a mask $\widetilde{M_1}$ characterized by its shape (Gaussian, Lorentzian, circular,...) and its size is chosen and applied to the Fourier transform $\widetilde{I}(\mathbf{g})$ of the image. In particular, the masking function $\widetilde{M_1}(\mathbf{k})$ is such that (Figure 3.12(c)):

- It is centered around $\mathbf{g_1}$

- The origin is excluded
- No more than one main frequency of the different crystals is included in it

Next, the inverse Fourier transform of the previous masked function is calculated. The result is a complex image, $I_{M_1}^{filt}(\mathbf{r})$:

$$I_{M_1}^{filt}(\mathbf{r}) = A_{g_1}(\mathbf{r}) \exp\{iP_{g_1}(\mathbf{r})\} = A_{g_1}(\mathbf{r}) \exp\{2\pi i\, \mathbf{g_1} \cdot \mathbf{r} + iP_{g_1}^r(\mathbf{r}) - 2\pi i c_1\} \tag{3.13}$$

where $A_{g_1}(\mathbf{r})$, $P_{g_1}(\mathbf{r})$ and $P_{g_1}^r(\mathbf{r})$ are respectively the amplitude, phase and reduced phase images.

A more accurate value of the vector $\mathbf{g_1}$ can be (and must be) calculated by selecting a reference region O in the image (Figure 3.12(e)) and by minimizing with respect to $\mathbf{g}$ and the constant c the function:

$$\sum_{\mathbf{r}\epsilon O} \|P_{g_1}(\mathbf{r}) - 2\pi(\mathbf{g} \cdot \mathbf{r} - c)\|^2 \tag{3.14}$$

where the summation runs over all the pixels $\mathbf{r}$ of the reference region O. The minimum is obtained for a vector $\mathbf{g_1}(O)$ and a constant $c(O)$. A new reduced phase image $P_{g_1}^O(\mathbf{r})$ can then be introduced.:

$$P_{g_1}^O(\mathbf{r}) = P_{g_1}(\mathbf{r}) - 2\pi \mathbf{g_1}(O) \cdot \mathbf{r} + 2\pi c(O) \tag{3.15}$$

$P_{g_1}^O(\mathbf{r})$ is in average equal to zero inside the region O.

The refinement of $\mathbf{g_1}$ is an important step when applying the GPA, as it determines the reference region O and thus the reference vector $\mathbf{g_1}(O)$ with high accuracy.

The GPA does not use the amplitude image (Figure 3.12(f)) but analyze the phase image. The information presented in the phase image $P_{g_1}(\mathbf{r})$ can be extracted in two ways.

- Either the variations of the phase are considered as variations of $\mathbf{g}(\mathbf{r})$. These variations are noted as $\Delta\mathbf{g}(\mathbf{r})$. From equation 3.15 we have: (the problem of the constant *c (r)* is discussed in section 3.2.2)

  $$P_{g_1}(\mathbf{r}) \equiv 2\pi \mathbf{g}(\mathbf{r}) \cdot \mathbf{r} - 2\pi c(O) = 2\pi(\mathbf{g_1}(O) + \Delta\mathbf{g}(\mathbf{r})) \cdot \mathbf{r} - 2\pi c(O) \tag{3.16}$$

  $$P_{g_1}^O(\mathbf{r}) = 2\pi \Delta\mathbf{g}(\mathbf{r}) \cdot \mathbf{r} \tag{3.17}$$

  By derivation with respect to $\mathbf{r}$ and assuming that $\mathbf{g}(\mathbf{r})$ varies slowly with $\mathbf{r}$ we obtain:

  $$\bigtriangledown P_{g_1}(\mathbf{r}) = 2\pi \mathbf{g}(\mathbf{r}) \tag{3.18}$$

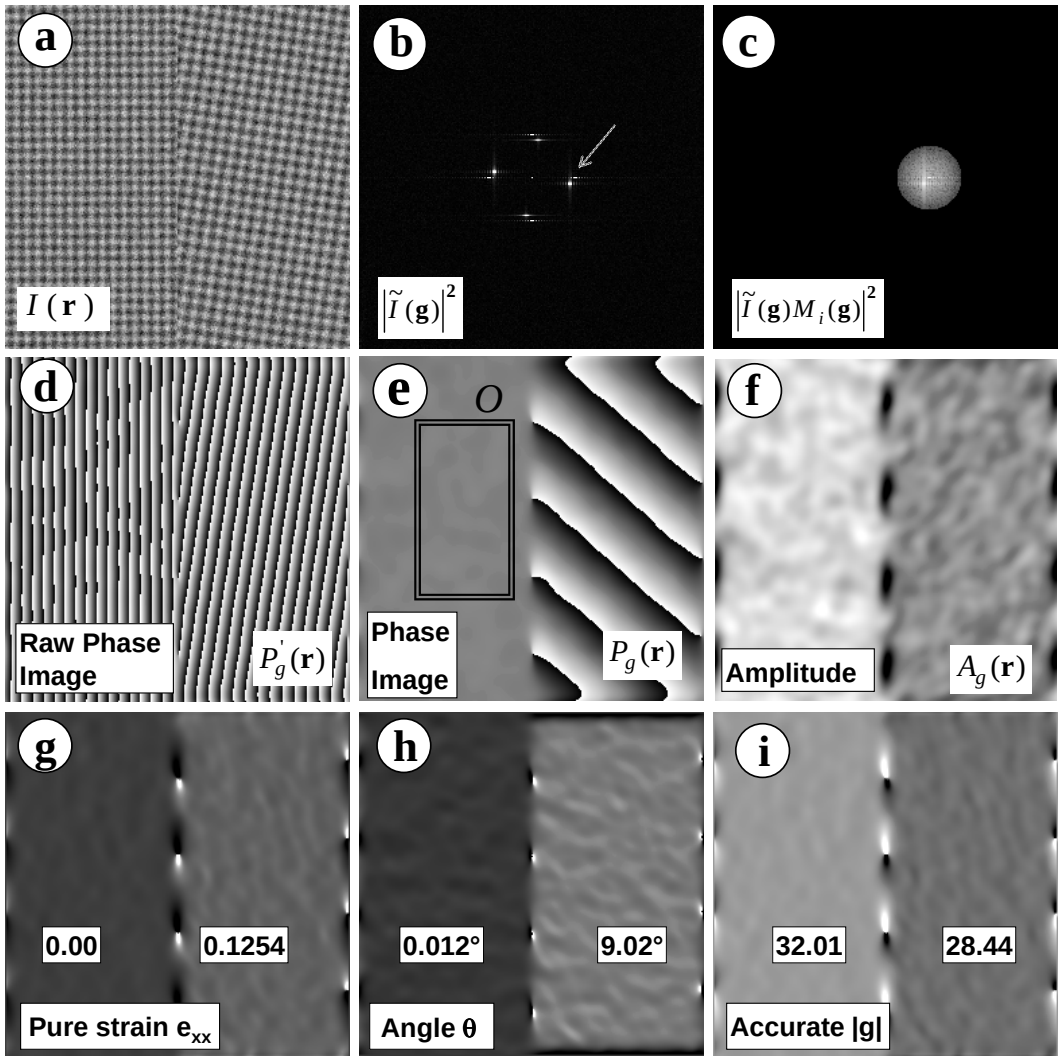

Figure 3.12 : *Principal steps of the GPA. (a) The initial image simulating a HRTEM image of a grain boundary. Size 256x256 pixels. The left square crystal has a lattice parameter of 8 pixels. The right crystal is rotated by -9° and has a lattice parameter of 9 pixels. (b) Power Spectrum of image (a) allowing to select a frequency* $\mathbf{g}_1$ *(pointed by an arrow) and the mask size. (c) The power spectrum of the filtered Fourier transform. (d) The raw phase image of the inverse filtered Fourier transform. Boundary effects due to the non-periodicity of the image can be seen at the edge of this image and of the following ones. (e) The phase image with the chosen reference region* 0*. (f) The amplitude image of the inverse filtered Fourier transform. (g) Pure strain along the x-axis (dilatation) after subtraction of the rotation. On average, the strain is 0 in the left crystal and equal to 0.1254 (9-8)/8 on the right crystal. (h) Image giving the angle of the local rotation. In average values of 0.012 and 9.02° are found in respectively the left and right crystal. (i) Image giving the modulus of the local reciprocal lattice vector g1(R). In average this modulus is equal to 32.007 256/8 and 28.437 28.444=256/9 in respectively the left and right crystal.*

$$\bigtriangledown P_{g_1}^{O}(\mathbf{r}) = 2\pi\Delta\mathbf{g}(\mathbf{r}) \tag{3.19}$$

- Or the variations of the phase are supposed to come from a local displacement field $\mathbf{u}(\mathbf{r})$. Following an argument that was firstly developed for the theory of dynamical scattering from defects [18, 26], when $\mathbf{r}$ is replaced by $\mathbf{r} - \mathbf{u}(\mathbf{r})$:

$$P_{g_1}(\mathbf{r}) = 2\pi\mathbf{g_1}(O)\cdot(\mathbf{r} - \mathbf{u}(\mathbf{r})) - 2\pi c(O) \tag{3.20}$$

$$P_{g_1}^{O}(\mathbf{r}) = -2\pi\mathbf{g_1}(O)\cdot\mathbf{u}(\mathbf{r}) \tag{3.21}$$

In the standard procedure introduced by Hÿtch *et al.* [18], the principal steps described before are repeated with a second $\mathbf{g_2}$ vector, that is non-collinear to the first one ($\mathbf{g_1}$). From the resulting phase images, the local displacement, strain and rotation can be calculated [18, 27].

In particular we obtain the following matrix relations:

$$\begin{pmatrix} P_{g1}^{O}(\mathbf{r}) \\ P_{g2}^{O}(\mathbf{r}) \end{pmatrix} = -2\pi \begin{pmatrix} g_{1x}(O) & g_{1y}(O) \\ g_{2x}(O) & g_{2y}(O) \end{pmatrix} \begin{pmatrix} u_x(\mathbf{r}) \\ u_y(\mathbf{r}) \end{pmatrix} = -2\pi\mathbf{G_O^T} \begin{pmatrix} u_x(\mathbf{r}) \\ u_y(\mathbf{r}) \end{pmatrix} \tag{3.22}$$

where $g_{1x}(O)$, $g_{1y}(O)$ and $g_{2x}(O)$, $g_{2y}(O)$ are respectively the coordinates of the vectors $\mathbf{g_1}(\mathbf{O})$ and $\mathbf{g_2}(\mathbf{O})$ optimized in the reference region O. These vectors define a matrix $\mathbf{G_O}$ of the reciprocal lattice. Appendix D.1 shows that a matrix $\mathbf{A_O}$ of the direct lattice can also be defined and that $\mathbf{A_O^{-1}} = \mathbf{G_O^T}$ where $\mathbf{T}$ denotes the transpose of the matrix. $u_x(\mathbf{r})$ and $u_y(\mathbf{r})$ are the x and y components of the displacement field at position $\mathbf{r}$=(x,y) in the image. The displacement field can thus be calculated as:

$$\begin{pmatrix} u_x(\mathbf{r}) \\ u_y(\mathbf{r}) \end{pmatrix} = -\frac{1}{2\pi}\mathbf{G_O^T}^{-1} \begin{pmatrix} P_{g1}^{O}(\mathbf{r}) \\ P_{g2}^{O}(\mathbf{r}) \end{pmatrix} = -\frac{1}{2\pi}\mathbf{A_O} \begin{pmatrix} P_{g1}^{O}(\mathbf{r}) \\ P_{g2}^{O}(\mathbf{r}) \end{pmatrix} \tag{3.23}$$

It is this equation that GPA uses to calculate the vectorial displacement field from two geometric phase images.

The derivatives of the displacements which are calculated from the phase images give the strain matrix:

$$e = \begin{pmatrix} e_{xx} & e_{xy} \\ e_{yx} & e_{yy} \end{pmatrix} = \begin{pmatrix} \frac{\partial u_x}{\partial x} & \frac{\partial u_x}{\partial y} \\ \frac{\partial u_y}{\partial x} & \frac{\partial u_y}{\partial y} \end{pmatrix} = -\frac{1}{2\pi}\mathbf{A_O} \begin{pmatrix} \frac{\partial P_{g1}^{O}}{\partial x} & \frac{\partial P_{g1}^{O}}{\partial y} \\ \frac{\partial P_{g2}^{O}}{\partial x} & \frac{\partial P_{g2}^{O}}{\partial y} \end{pmatrix} \tag{3.24}$$

Abrupt phase changes for $-\pi$ to $+\pi$ (and vice versa) causes apparent discontinuities in the geometric phase images. These produce discontinuities in the derivatives which have

no physical significance. In the GPA method this problem is solved by calculating the derivative from the complex image $\exp\{iP_g(\mathbf{r})\}$ [18].

The strain tensor (Figure 3.12(g)) is simply obtained by taking the symmetric part of the distortion matrix (equation 3.24), whereas the rotation (Figure 3.12(h)) is equal to the anti-symmetric part:

$$\varepsilon = 1/2\{e + e^T\}, \tag{3.25}$$

$$\omega = 1/2\{e - e^T\} \tag{3.26}$$

3.2.2 Theoretical discussions on the GPA

The motivation for approaching GPA in a more theoretical way came from the desire to understand why the GPA is so efficient although simple [27] and to introduce one dimensional formulas. Among the questions that we wanted to clarify were:

1. whether the equation that relates the phase $P_{\mathbf{g}}(\mathbf{r})$ with the displacement $\mathbf{u}(\mathbf{r})$ (equation 3.20) is a first order approximation or if this equation is general and can be applied to large displacements in any objects.

2. what is the meaning of a continuous displacement $\mathbf{u}(\mathbf{r})$ in a dot-like HRTEM image.

3. how the method can measure strain in a HRTEM image without determining the positions of dots.

4. problems arising from the constant term *c (r)* of the phase.

Notion of local lattice. We have seen at the end of the previous section that GPA can determine the local reciprocal lattice parameters, $g_i(\mathbf{r})$ around each pixel $\mathbf{r}$ of the image, that is to say inside a region R whose center is $\mathbf{r}$. However, what is the notion of a local lattice in a HRTEM image?

If we are in the direct space, defining local lattices is quite simple. For any dot D we determine its center $\mathbf{r}^{'}$, and the local lattices, $\mathbf{a}_1(\mathbf{r}^{'})$ and $\mathbf{a}_2(\mathbf{r}^{'})$, can be defined as the vectors joining D to the adjacent lattice dots D_1 and D_2 (see Figure 3.13 (a)). According to this construction, the corners of the local lattice are then dot centers. The problem in working in the direct space is the presence of noise, which affects the accuracy of locating dots. Of course, the HRTEM image can be filtered and/or local averages can be performed in order to overcome this problem [16, 28].

The GPA provides an alternative solution by mixing the analysis in the direct and the reciprocal space, and by doing in one-step filtering and local averages. In particular, for any pixel $\mathbf{r}^{'}$ of the image, one can always define a region R centered on this pixel in

such a way that this region contains at least three dots D, D_1 and D_2 (see Figure 3.13 (b)). In the region R, local reciprocal vectors $\mathbf{g}_1(R)$ and $\mathbf{g}_2(R)$ can be defined in a similar way as the vector $\mathbf{g_1}(O)$ was obtained by minimizing equation 3.14. (We will see later that in fact $\mathbf{g_i}(R)$ is the slope of the tangent plane to the phase.) From these vectors now, a reciprocal lattice matrix $\mathbf{G}(R)$, a direct local lattice $\mathbf{a}_1(R)$ and $\mathbf{a}_2(R)$ and a local lattice matrix $\mathbf{A}(R)$ can be defined. The local lattice is then the best lattice fitting the surrounding of pixel $\mathbf{r}^{'}$. In this definition $\mathbf{r}^{'}$ does not need to be a dot of the HRTEM image (see Figure 3.13 (b)).

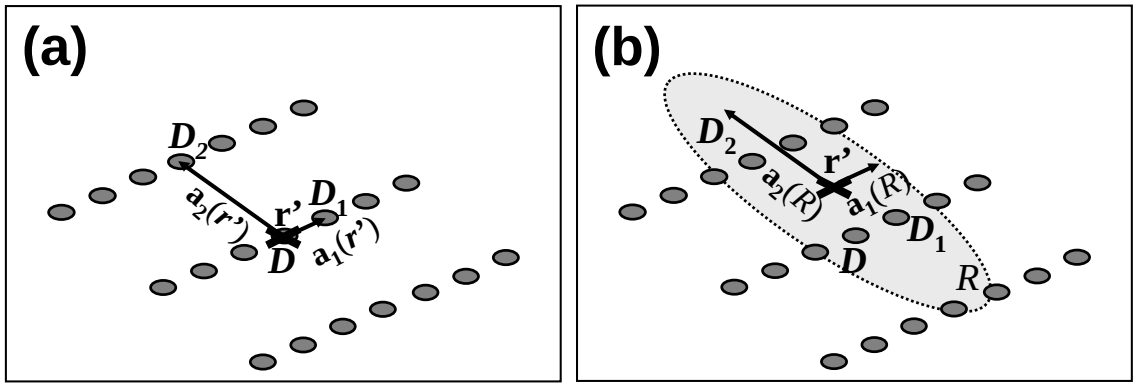

Figure 3.13 : *Schemes showing the definition of local lattice in the case of an elementary cell containing only one atom. (a) A direct space approach and (b) the GPA approach. The region R is centered on pixel* $\mathbf{r}^{'}$ *and contains at least 3 dots.* $\mathbf{a}_1(R)$ *and* $\mathbf{a}_2(R)$ *are the basis lattice vectors of the local lattice in the direct space.*

Adopted Notation. Before moving on in investigating the mathematical basis of the GPA, it is useful to introduce the notation that we have adapted for this purpose. First of all, reciprocal lattice vectors are notated as $\mathbf{g}(R)$ instead of $\mathbf{g}(\mathbf{r}^{'})$ in order to point out that they do not only depend on the value of the image at pixel $\mathbf{r}^{'}$ but they are functions of both the selected pixel $\mathbf{r}^{'}$ and the region R. Similarly, we have seen before that a phase image is a function of: (i) the selected frequency $\mathbf{g_1}$ and (ii) the mask M_1, but if we consider that the mask is centered on $\mathbf{g_1}$, then the phase image becomes a function of the sole mask. So, phase images are noted as $P_{M_1}(\mathbf{r})$ instead of $P_{\mathbf{g_1}}(\mathbf{r})$. Additionally, when an 'O' appears aside a vector or number as an exponent or as an index it indicates that the vector or number is calculated in the reference region O. The central position of a region is indicated by a prime. Matrices are represented by bold capital letters except for the distortion and strain matrices. A bold font is used for vectors. Finally, in Appendix D the relations between distances in the real and reciprocal space are presented.

Basic equations. When introducing the basic principles of the method, section 3.2.1, we have seen that the resulting filtered image $I_{M_1}^{Filt}(\mathbf{r})$ produced by applying a mask M_1 around the selected frequency $\mathbf{g}_1(R)$ can be written as (equation 3.13):

$$I_{M_1}^{Filt}(\mathbf{r}) = A_{M_1}(\mathbf{r}) \exp(iP_{M_1}(\mathbf{r})) \tag{3.27}$$

$P_{M_1}(\mathbf{r})$ is defined modulo 2π, but we choose the value in the $]-\pi, \pi]$ range. By assuming that after the filtering only the selected frequency $\mathbf{g}_1(R)$ is left in any region R of the image, then the filtered image at any point $\mathbf{r}$ of R is very well approximated by a function of types:

$$A_1(R) \exp[2\pi i \mathbf{g}_1(R) \cdot \mathbf{r} - 2\pi i c_1(R)] \tag{3.28}$$

$$\text{or } A_1(R) \exp[2\pi i \mathbf{g}_1(R) \cdot (\mathbf{r} - \mathbf{r}') - 2\pi i \alpha_1(R)] \tag{3.29}$$

where the constants $c_1(R)$ and $\alpha_1(R)$ are defined modulo 1. The previous equations constitute the basic assumption of the GPA.

Comparing equations 3.27, 3.28 and 3.29 we have, to first order, the following equalities for any pixel $\mathbf{r}$ of the region R:

$$A_1(R) = A_{M_1}(\mathbf{r}) \tag{3.30}$$

$$2\pi \mathbf{g}_1(R) \cdot \mathbf{r} - 2\pi c_1(R) = P_{M_1}(\mathbf{r}) \pmod{2\pi} \tag{3.31}$$

$$2\pi \mathbf{g}_1(R) \cdot (\mathbf{r} - \mathbf{r}') - 2\pi \alpha_1(R) = P_{M_1}(\mathbf{r}) \pmod{2\pi} \tag{3.32}$$

In particular, at the point $\mathbf{r} = \mathbf{r}'$, which is the center of region R, we obtain:

$$2\pi \mathbf{g}_1(R) \cdot \mathbf{r}' - 2\pi c_1(R) = P_{M_1}(\mathbf{r}') \tag{3.33}$$

$$-2\pi \alpha_1(R) = P_{M_1}(\mathbf{r}') \tag{3.34}$$

The differentiation of equations 3.31 or 3.32 with respect to $\mathbf{r}$ gives the relation:

$$\mathbf{g}_1(R) = \frac{1}{2\pi} \nabla P_{M_1}(\mathbf{r}) \tag{3.35}$$

where $\mathbf{r}$ is any pixel of region R.

At first, equations 3.33 and 3.34 are defined modulo 2π, but we choose the constants $c_1(R)$ and $\alpha_1(R)$ so that these equations are plain equality and not only first order equations. Specifically, as the phase is taken in the $]-\pi, \pi]$ range, $\alpha_1(R)$ is defined in the $]-1/2, 1/2]$ range and $c_1(R)$ can take high values. The two constants are related to each

other by the relation:

$$\alpha_1(R) = c_1(R) - 2\pi \mathbf{g}_1(R) \cdot \mathbf{r}^{'} = c_1(R) + r_1^{'} \tag{3.36}$$

where $r_1^{'}$ is the coefficient of $\mathbf{r}^{'}$ along the vector $\mathbf{a}_1(R)$ such that $\mathbf{g}_1(R) \cdot \mathbf{a}_1(R) = 1$. The constants $c_1(R)$ and $\alpha_1(R)$ determine the central position of the dots, i.e. the maxima position, along the vector $\mathbf{a}_1(R)$.

With these choices of constants: $\alpha_1(R)\mathbf{a}_1(R)$ gives the position of the maxima whose projection along $\mathbf{a}_1(R)$ is the nearest to the position $\mathbf{r}^{'}$ (center of region R) and $c_1(R)\mathbf{a_1}(R)$ is the position of the dot of the deformed lattice whose projection along $\mathbf{a}_1(R)$ is nearest to the pixel origin of the image (the "deformed" lattice of region R is extended throughout the whole image).

The other dots defined by equations 3.27 and 3.29 are "located" at positions:

$$\mathbf{r}_m = r_{m1}\mathbf{a}_1(R) \quad \text{where} \quad r_{m1} = c_1(R) + p = a_1(R) + p + r_1^{'} \tag{3.37}$$

and p is a signed integer number.

In fact, since equations 3.28 and 3.29 are approximations of equation 3.27, the equalities of equations 3.30, 3.31, 3.32 and 3.35 are only true to first order! By defining at any pixel $\mathbf{r}^{'}$, the tangent plane to the raw phase image $P_{M_1}(\mathbf{r}^{'})$, we can introduce similar equations where the equalities will be this time real and not approximations. The linear equation of this tangent plane is noted by:

$$tanplane_{\mathbf{r}'}(\mathbf{r}) \equiv 2\pi \mathbf{g}_1(R) \cdot (\mathbf{r} - \mathbf{r}^{'}) + P_{M_1}(\mathbf{r}^{'}) = 2\pi \mathbf{g}_1(R) \cdot (\mathbf{r} - \mathbf{r}^{'}) - 2\pi\alpha_1(\mathbf{r}^{'}) \tag{3.38}$$

where $\mathbf{r}$ is again a variable pixel of region R located near pixel $\mathbf{r}^{'}$. By definition, the tangent plane to the raw phase image is equal to the raw phase at point $\mathbf{r}^{'}$, and its slope is equal to the gradient of the raw phase image. These two properties implies that:

$$\frac{1}{2\pi}\nabla P_{M_1}(\mathbf{r}^{'}) \equiv \mathbf{g}_1(R) \tag{3.39}$$

$$-\frac{1}{2\pi}P_{M_1}(\mathbf{r}^{'}) \equiv \alpha_1(R) \tag{3.40}$$

These equations imply that the equalities of equations 3.33, 3.34 and 3.36 are real equalities not first order equations and what we deduce from them is still true [27].

By introducing the reduced phase $P_{M_1}^{O}(\mathbf{r})$ equation 3.31 gives:

$$P_{M_1}^{O}(\mathbf{r}) = 2\pi(\mathbf{g}_1(R) - \mathbf{g}_1(O)) \cdot \mathbf{r} - 2\pi(c_1(R) - c_1(O)) \tag{3.41}$$

for any pixel $\mathbf{r}$ in region R.

*Therefore, the **central assumption** of GPA is to suppose that the tangent plane defined by equation 3.41, describes correctly the phase over a rather large region* R *centered on the pixel* $\mathbf{r}'$*. This implies that the phase is slowly varying. As a result, the GPA is physically relevant only for particular images, like dot-like HRTEM images. For instance, the method cannot be applied to an amorphous region. Local crystals can be defined on every pixel* $\mathbf{r}'$ *of the image. The GPA analyzes the deformation of these local lattices. Consequently, contrary to a direct space analysis that only considers the dot positions and only defines displacement and deformation at the dot positions, the GPA defines displacement and deformation at any pixel of the image.*

Displacement and Strain. When the previous analysis is applied on two non-collinear reciprocal lattice vectors, the position of a dot in a HRTEM image can be defined. In particular, in the reference region O whose center is the pixel $\mathbf{r}'_{\mathbf{O}}$, the position of a dot $\mathbf{r}_{pq}(O)$ based on equation 3.37 is given by:

$$\mathbf{r}_{pq}(O) = (c_1(O) + p)\mathbf{a}_1(O) + (c_2(O) + q)\mathbf{a}_2(O) \tag{3.42}$$

where $\mathbf{a}_1(O)$ and $\mathbf{a}_2(O)$ are the local basis vectors of the reference region O. If now, we represent the coordinates of the point $\mathbf{r}_{pq}(O)$ in an orthogonal basis B by $(x_{pq}(O), y_{pq}(O))$ and write equation 3.42 as a matrix form:

$$\begin{pmatrix} x_{pq}(O) \\ y_{pq}(O) \end{pmatrix} = \begin{pmatrix} a_{x1}(O) & a_{x2}(O) \\ a_{y1}(O) & a_{y2}(O) \end{pmatrix} \begin{pmatrix} c_1(O) + p \\ c_2(O) + q \end{pmatrix} \equiv \mathbf{A}(O) \begin{pmatrix} p \\ q \end{pmatrix} + \mathbf{A}(O) \begin{pmatrix} c_1(O) \\ c_2(O) \end{pmatrix} \tag{3.43}$$

Similarly, the coordinates of a lattice point $\mathbf{r}_{pq}(R)$ in the deformed region R will be given by:

$$\begin{pmatrix} x_{pq}(R) \\ y_{pq}(R) \end{pmatrix} = \begin{pmatrix} a_{x1}(R) & a_{x2}(R) \\ a_{y1}(R) & a_{y2}(R) \end{pmatrix} \begin{pmatrix} c_1(R) + p \\ c_2(R) + q \end{pmatrix} \equiv \mathbf{A}(R) \begin{pmatrix} p \\ q \end{pmatrix} + \mathbf{A}(R) \begin{pmatrix} c_1(R) \\ c_2(R) \end{pmatrix} \tag{3.44}$$

From equations 3.43 and 3.44 we can establish a relation between the coordinates of a point $\mathbf{r}_{pq}(R)$ of the deformed region as a function of the coordinates of a point $\mathbf{r}_{pq}(O)$ of the reference region O:

$$\begin{pmatrix} x_{pq}(R) \\ y_{pq}(R) \end{pmatrix} = \mathbf{A}(R)\mathbf{A}(O)^{-1} \begin{pmatrix} x_{pq}(O) \\ y_{pq}(O) \end{pmatrix} + \mathbf{A}(R) \begin{pmatrix} c_1(R) - c_1(O) \\ c_2(R) - c_2(O) \end{pmatrix} \tag{3.45}$$

or by using another notation style:

$$\mathbf{r}_{pq}(R) = \mathbf{A}(R)\mathbf{A}(O)^{-1}\mathbf{r}_{pq}(O) + \mathbf{A}(R)(\mathbf{c}(R) - \mathbf{c}(O)) \tag{3.46}$$

Equation 3.46 is satisfied for any interior point $\mathbf{r}(O) = \mathbf{r}_{pq}(O) + \lambda_1\mathbf{a}_1(O) + \lambda_2\mathbf{a}_2(O)$ of the reference lattice O and $\mathbf{r}(R) = \mathbf{r}_{pq}(R) + \lambda_1\mathbf{a}_1(R) + \lambda_2\mathbf{a}_2(R)$ of the deformed lattice R. In a similar way two of the previous points are linked to each other by the relation:

$$\mathbf{r}(R) = \mathbf{A}(R)\mathbf{A}(O)^{-1}\mathbf{r}(O) + \mathbf{A}(R)(\mathbf{c}(R) - \mathbf{c}(O)) \tag{3.47}$$

We can lighten the previous notation by noting as $\mathbf{r}_O$ and $\mathbf{r}$ any given point of the crystal O and R respectively, and by replacing $\mathbf{A}(R)$ with $\mathbf{A}$, $\mathbf{A}(O)$ with $\mathbf{A_O}$ and similar notations for the other matrices and vectors. Then, equation 3.47 becomes:

$$\mathbf{r} = \mathbf{A}{\mathbf{A_O}}^{-1}\mathbf{r_O} + \mathbf{A}(\mathbf{c} - \mathbf{c_O}) \tag{3.48}$$

or equivalently:

$$\mathbf{r_O} = \mathbf{A_O}\mathbf{A}^{-1}\mathbf{r} + \mathbf{A_O}(\mathbf{c_O} - \mathbf{c}) \tag{3.49}$$

In the original GPA the displacement $\mathbf{u}_{OGPA}(\mathbf{r})$ is defined as the vector that have to be subtracted from the deformed point $\mathbf{r}$ in order to obtain the un-deformed position $\mathbf{r_O}$:

$$\mathbf{u}_{OGPA}(\mathbf{r}) = \mathbf{r} - \mathbf{r_O} = \mathbf{r} - \mathbf{A_O}\mathbf{A}^{-1}\mathbf{r} - \mathbf{A_O}(\mathbf{c_O} - \mathbf{c}) = (\mathbf{I} - \mathbf{A_O}\mathbf{A}^{-1})\mathbf{r} + \mathbf{A_O}(\mathbf{c} - \mathbf{c_O}) \tag{3.50}$$

By replacing in the previous equation the relations $\mathbf{I} = \mathbf{A_O}{\mathbf{A_O}}^{-1}$ and $\mathbf{A}^{-1} = \mathbf{G}^T$ we obtain:

$$\mathbf{u}_{OGPA}(\mathbf{r}) = -\mathbf{A_O}[(\mathbf{G}^T - {\mathbf{G_O}}^T)\mathbf{r} - (\mathbf{c} - \mathbf{c_O})] \tag{3.51}$$

If moreover we put $\mathbf{\Delta G} = \mathbf{G} - \mathbf{G_O}$ and $\mathbf{\Delta c} = \mathbf{c} - \mathbf{c_O}$, we have:

$$\mathbf{u}_{OGPA}(\mathbf{r}) = -\mathbf{A_O}(\mathbf{\Delta G}^T\mathbf{r} - \mathbf{\Delta c}). \tag{3.52}$$

Equation 3.41 can be written for the two vectors $\mathbf{g_1}$ and $\mathbf{g_2}$ in a matrix form as:

$$P^O_{M_1}(\mathbf{r}) = 2\pi(\mathbf{\Delta G^T r} - \mathbf{\Delta c}) \tag{3.53}$$

Thus from equations 3.52 and 3.53 we obtain:

$$P^O_{M_1}(\mathbf{r}) = -2\pi{\mathbf{A_O}}^{-1} \cdot \mathbf{u} = -2\pi\mathbf{G^T_O} \cdot \mathbf{u} \tag{3.54}$$

which is the same as equation 3.22.

This expression is exact whatever are the magnitudes of $\mathbf{\Delta G}$ *and* $\mathbf{\Delta c}$ *and also what-*

ever are the distortion. As a result, the GPA can be applied for large displacement, even if this displacement contains finite rotations. In the latest case, the difference is that more complex equations need to be used.

Generally in strain theory, one considers the displacement that has to be applied to the initial position $\mathbf{r_O}$ in order to get the deformed point $\mathbf{r}$. This displacement, noted as $\mathbf{u}_{GPA}(\mathbf{r_O})$, will be equal to:

$$\begin{aligned} \mathbf{u}_{GPA}(\mathbf{r_O}) &= \mathbf{r} - \mathbf{r_O} = (\mathbf{A}{\mathbf{A_O}}^{-1} - \mathbf{I})\mathbf{r_O} + \mathbf{A}(\mathbf{c} - \mathbf{c_O}) = & (3.55)\\ &= \mathbf{A}[({\mathbf{G_O}}^T - \mathbf{G}^T)\mathbf{r_O} + \mathbf{c} - \mathbf{c_O}] = & (3.56)\\ &= -\mathbf{A}[\mathbf{\Delta G}^T\mathbf{r_O} - \mathbf{\Delta c}] & (3.57) \end{aligned}$$

In the case of infinitesimal displacement, local distortion matrices $\mathbf{e}_{GPA}(R)$ and $\mathbf{e}(R)$ can be defined by taking the derivatives of the displacements defined in equations 3.52 and 3.57 respectively. The result is:

$$\mathbf{e}_{OGPA}(R) = -\mathbf{A_O}\mathbf{\Delta G}^T \tag{3.58}$$

and

$$\mathbf{e}_{GPA}(R) = -\mathbf{A}\mathbf{\Delta G}^T \tag{3.59}$$

By using the relations between $\mathbf{A}$ and $\mathbf{G}$, and $\mathbf{A_O}$ and $\mathbf{G_O}$ (see Appendix D.1) we find that:

$$\mathbf{e}_{OGPA}(R) = \mathbf{I} - \mathbf{A_O}\mathbf{G}^T \tag{3.60}$$

$$\mathbf{e}_{GPA}(R) = \mathbf{A}{\mathbf{G_O}}^T - \mathbf{I} = \mathbf{A}{\mathbf{A_O}}^{-1} - \mathbf{I} \tag{3.61}$$

which directly gives:

$$\mathbf{I} + \mathbf{e}_{GPA}(R) = (\mathbf{I} - \mathbf{e}_{OGPA}(R))^{-1} \tag{3.62}$$

Consequently, the two distortion matrices are equivalent to first order since, for infinitesimal distortions the second part of equation 3.62 becomes approximately equal to $\mathbf{I} + \mathbf{e}_{OGPA}(R)$.

3.2.3 One-dimensional formulas

In the previous section, we have exposed in details the mathematical basis of the GPA for the case of two dimensional lattices that need the analysis of two non-collinear vectors

$\mathbf{g_1}$ and $\mathbf{g_2}$. However, in some cases, the 2D image is composed of only one set of lines, which correspond to the projections of atomic planes. This is for example the case of HRTEM images, viewed along the [0,1,-1,0] direction and for which a small objective aperture diameter of $9nm^{-1}$ is used. Under these conditions, the resulting HRTEM image is formed by the transmitted the (0002) and (000-2) diffracted beams. In this part the formulas concerning an one-dimensional geometric phase analysis are given.

In the case of a 1D image, similarly to 3.41, the reduced phase at any pixel of region R is given by:

$$P^{O}_{M_1}(x) = 2\pi(g(R) - g(O)) \cdot x^{'} - (c(R) - c(O)) \tag{3.63}$$

where $x^{'}$ is the central position of region R. The dot positions in regions O and R are respectively given by:

$$x(O) = (c_1(O) + p)a_{x1}(O) \qquad x(R) = (c_1(R) + p)a_{x1}(R) \tag{3.64}$$

where p is a signed integer number. If in the previous equations we suppress p, we have:

$$x(R) = x(O)a_{x1}(R)/a_{x1}(O) + (c_1(R) - c_1(O))a_{x1}(R) \tag{3.65}$$

This equation, as in equation 3.46, can be extended to any point of the lattice situated between the dots. $x \equiv x(R)$ is then any dot of region R and $x_O \equiv x(O)$ is its corresponding dot in the reference region O. By introducing lighter notation we obtain:

$$a = a_{x1}(R) = 1/g \quad a_O = a_{x1}(O) = 1/g_O \quad c = c_1(R) \quad c_O = c_1(O) \tag{3.66}$$

The derivation of equation 3.63 gives equation similar to 3.39 and 3.40:

$$g = 1/a = \frac{1}{2\pi}\frac{\partial P^{O}_{M1}(x)}{\partial x} + g_O = \frac{1}{2\pi}\frac{\partial P_{M1}(x)}{\partial x} \tag{3.67}$$

Based on the previous equation, equation 3.65 is transformed into:

$$x = x_O g_O/g + (c - c_O)/g \tag{3.68}$$

Similarly to equations 3.52, 3.57, 3.58 and 3.59, two displacements and two strains can be defined:

$$u_{GPA}(x_O) = x - x_O = x_O\,\frac{g_O - g}{g} + \frac{c - c_O}{g} \tag{3.69}$$

$$u_{OGPA}(x) = x - x_O = x\,\frac{g_O - g}{g_O} + \frac{c - c_O}{g_O} \tag{3.70}$$

$$e_{GPA}(x_O) = \frac{a - a_O}{a_O} = \frac{g_O - g}{g} \tag{3.71}$$

$$e_{OGPA}(x) = \frac{a - a_O}{a} = \frac{g_O - g}{g_O} \tag{3.72}$$

Comparing now equation 3.63 and 3.70, the well-known relation is obtained:

$$P^O_{M1}(x) = -2\pi g_O.u_{OGPA}(x) \tag{3.73}$$

This relations is of course not true if $u_{GPA}(x)$ is substitute to $u_{OGPA}(x)$, because it is $u_{GPA}(x_O)$ and not $u_{GPA}(x)$ that it is equal to $u_{OGPA}(x)$.

3.2.4 Mask functions

When describing the principle of GPA (section3.2.1), we have seen that a mask M_1 must be selected and applied to the Fourier transform of the examined image, around the selected $\mathbf{g_1}$. In order to know **over which region R GPA averages the information**, it is necessary to define a relation between the radius r_{dir} of region R and the radius r_{rec} of the applied mask M_1.

To do so, we have used the simple case of an 1D image where a gaussian mask is centered on g_i ($\widetilde{F}_{M_i}(g) = \exp(-\frac{(g-g_i)^2}{2\sigma^2})$, Figure 3.14(a)). The radius of the gaussian mask $\widetilde{F}_{M_i}(g)$ is about $r_{rec} = 3\sigma$. The multiplying in the reciprocal space by this gaussian mask is equivalent in the direct space to a convolution by the inverse Fourier transform of $\widetilde{F}_{M_i}(g)$. In other words, it is equivalent to a convolution by the function:

$$F_{M_i}(x) = \sqrt{2\pi}\sigma \exp(-2\pi^2\sigma^2x^2)\exp(-2\pi g_i x) \tag{3.74}$$

The modulus of $F_{M_i}(x)$ is a gaussian function whose standard deviation is $\frac{1}{2\pi\sigma}$. Or, equivalently $F_{M_i}(x)$ is not negligible over a region of radius $r_{dir} = \frac{3}{2\pi\sigma} = \frac{9}{2\pi r_{rec}}$ (Figure 3.14(b)).

If we take, $\sigma = g/n = 1/nd$, where d is the period in the direct space, the convolution in the direct space is realized over a region of radius $r_{dir} \sim \frac{3n}{2\pi}d \approx \frac{n}{2}d$. That is to say, the signal at r is "averaged" over a region of radius $r_{dir} \sim \frac{n}{2}d$.

If for instance, we take $r_{rec} \sim g = 1/d$, we obtain the largest mask that does not include the origin and the radius in the direct space is then equal to $r_{dir} \sim 3/2d \sim 1.5d$. This is the smaller region R over which the GPA averages the information.

In general, the mask M_i, is characterized by its shape and its size. To optimize those two parameters, we have examined their effect on a strain profile obtained by the GPA.

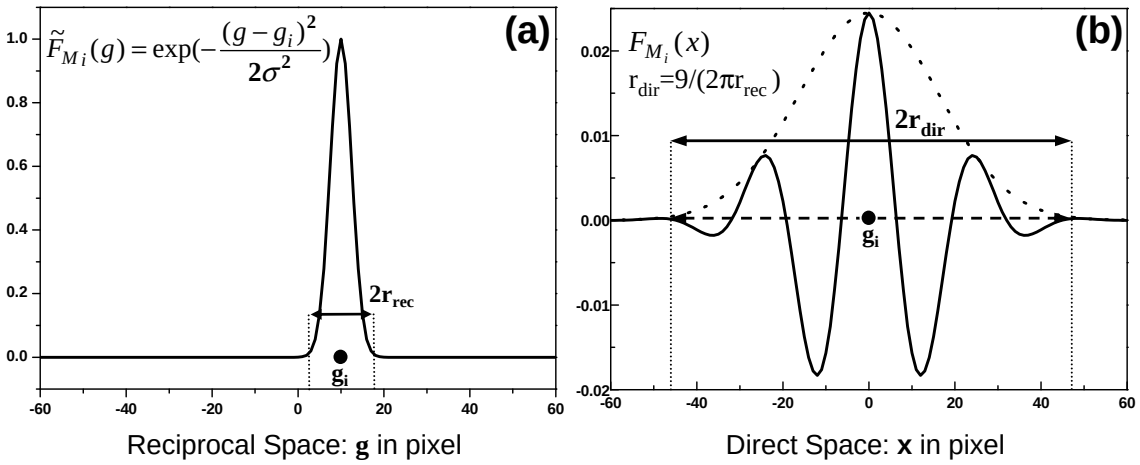

Figure 3.14 : *(a) A gaussian function $\widetilde{F}_{M_i}(g)$ representing a mask M_i in the reciprocal lattice. Here $g_i = 10$ pixels and $\sigma = g_i/4 = 2.5$ pixels. The radius of the mask, which is defined when $\widetilde{F}_{M_i}(g)$ is smaller than 0.01, is about $r_{rec} = 3\sigma = 7.5$ pixels. (b) The Fourier transform $F_{M_i}(x)$ of $\widetilde{F}_{M_i}(g)$. The dotted line is the gaussian envelope of $F_{M_i}(x)$. The latest is not negligible over a region of radius $r_{dir} = 3/(2\pi\sigma)$, which in pixel unit is equal to 49 pixels (the size of the simulated image is 256 pixels.)*

In particular, a simulated abrupt interface between two crystals A and B with period d in the direct space of 8 and 8.1 pixels respectively was used as a model (Figure 3.15(a)). The size of the image was 256x64 pixels. Crystal A was chosen as the reference lattice O. In the Fourier transform of the image, the reflection $\mathbf{g}$ ($g_x = N_x/d = 256/8 = 32$pixels, see Appendix D) was selected and a gaussian mask was centered around it (Figure 3.15(b)).

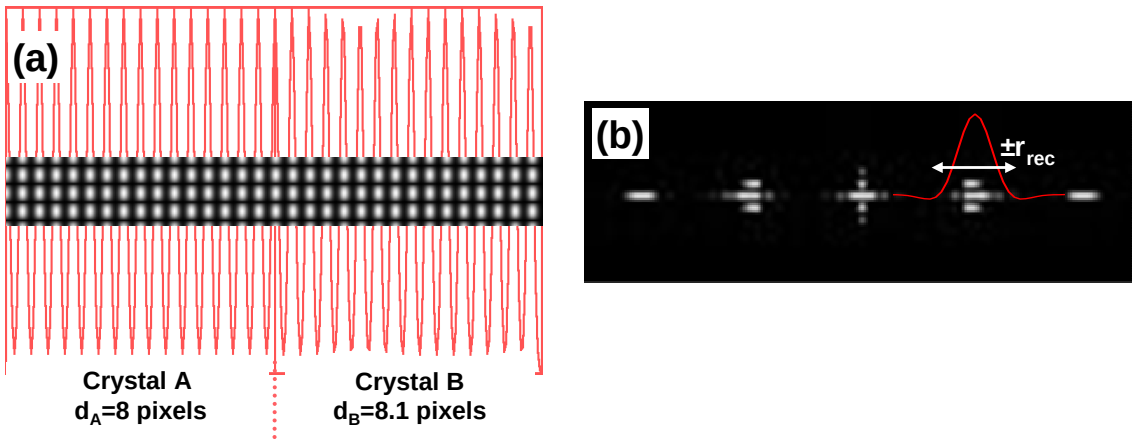

Figure 3.15 : *(a) Simulated image of an abrupt interface of two crystals A and B (in 1D and 2D). In the direct space the period d of the crystal A is 8 pixels and of crystal B is 8.1 pixels. As reference lattice the crystal A has chosen. (b) Fourier transform of the image in (a). Around the selected **g** a gaussian mask was placed.*

The effect of the mask size has been examined by varying the size of the applied

gaussian mask σ from $g/3.4$ to $g/8$ pixels. The resulting strain profiles can been seen in Figure 3.16. We notice the widening of the interface by decreasing the size of the mask. This was expected, since we have seen previously that reducing the size of the mask increases the region R over which the GPA averages the information. Moreover, we know that the GPA is not exactly valid at a crystal discontinuity like a boundary or picture edges, since it average the information on either side of the discontinuity. Consequently, by increasing the region R, or equivalently decreasing the mask size, the areas in which the results of the GPA are less accurate (i.e. picture edges) become larger. This result clearly appears in Figure 3.16 (a). For $\sigma = g/3.4$ (see Figure 3.16(b)), we see the apparition of oscillations because the mask include the intense peak situated at the origin (Gibbs phenomenon [29]).

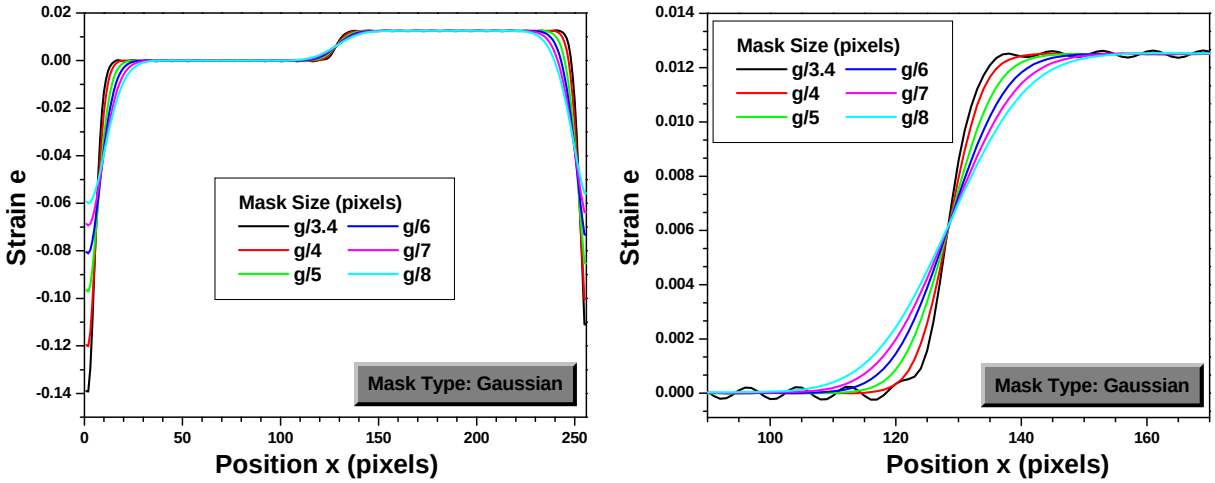

Figure 3.16 : *(a) Strain profiles obtained from the image of Figure 3.15(a) for different sizes of the applied gaussian mask. (b) The interface area of the previous profiles. By increasing the size of the mask, the interface appears more narrow.*

The simulated image of Figure 3.15 (a) was also used to investigate the effect of the mask type on GPA strain profiles. This time the size of the applied mask was kept constant and equal to g/5 (=6.4pixels), while the type of the mask was changing. Four different types of masks were used: a gaussian, a exponential, a triangle and a cosine one [4]. Figure 3.17 illustrates the obtained strain profiles. We notice that it is only the gaussian mask that does not suffer from the presence of the oscillations due to the Gibbs phenomenon. However, the gaussian mask is the one that gives the most wide profile for the interface. The narrowest interface is obtained with the exponential mask.

[4]The names of the masks are given in function of their form in the direct space.

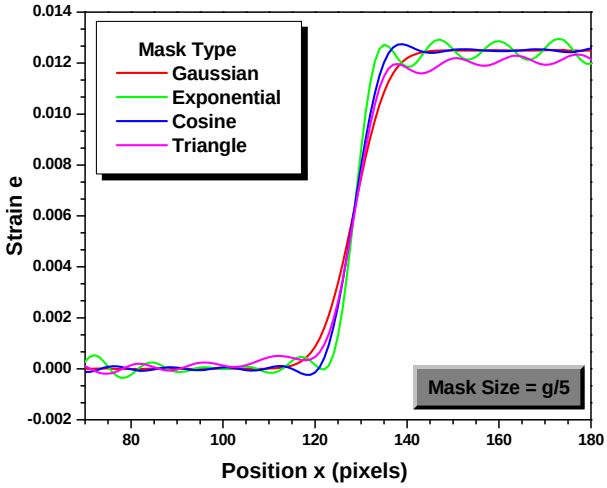

Figure 3.17 : *Strain profiles for different types of mask. The size of the mask is kept constant while the type was changing. Although the gaussian mask does not include errors linked to the Gibbs phenomenon, it gives the larger interface.*

3.2.5 Use of the GPA in this thesis

Previously, we have described the basic principles of the GPA. Moreover, we have discussed the mathematical basis of the method in order to better understand how the method can determine displacement and strain from HRTEM images. We will close this section by giving the parameters that we have adopted in this thesis when applying the GPA.

First of all, all the image processing involved in the GPA, was realized on routines written either with SEMPER [5] or on Digital Micrograph[5]. In this routines we have included the case of one-dimensional analysis in order to be able to analyze HRTEM images viewed along the [0,1,-1,0] direction in which after the use of a small objective aperture diameter only one set of lines is present (like the one in Figure 3.1 (a)). We remind that in the standard procedure of the GPA the analysis of two non-parallel vectors $\mathbf{g_1}$ and $\mathbf{g_2}$ is necessary.

To define the displacement and the strain we have used respectively equations 3.57 and 3.59 for the case of two dimensional lattices and equations 3.69 and 3.71 for the 1D analysis.

Concerning the mask functions, we have always used a gaussian type of mask. As for the size of the mask, depending of the case study and in particular whether we wanted to average the information over a small of a large region, it was varying between $\mathbf{g}/4$ to $\mathbf{g}/6$.

[5]An advantage in working on SEMPER routines is that we can apply a Fourier transform on images with size of $2^n * 3^m$, with n and m being integer numbers. However, In Digital Micrograph the analyzed images must be power of two.

3.3 Polarity determination.

In the section 3.1.4, the interplanar distances profiles of a quantum well structure, AlN (7ML) / GaN (6 ML) / AlN (7ML), have been examined with regard to the imaging conditions of thickness and defocus. From this analysis, we could notice that regardless the imaging conditions, the interplanar distances profiles are asymmetric with characteristics minima and maxima situated at the atomic plane numbers before the AlN/GaN and GaN/AlN interface respectively (see Figures 3.9 and 3.11). This asymmetry is more clearly revealed when a small objective aperture diameter is used. Here, we show that this asymmetry can be used to define the polarity of the layers.

In Figure 3.18 simulated HRTEM interplanar distances profiles are presented for the case of a 27 ML GaN quantum well embedded in an AlN matrix, and for defocus values of 40 and 85 nm. The thickness is kept equal to 5.9 nm and the structure is observed along the [0,1,-1,0] direction. From these profiles we see that the extremum m, which gives the smallest value for the (0002) interplanar distances and the extremum M, which corresponds to the higher value are always present. Previously (section 3.1.4), we have seen that the form of a profile does not change significantly with the variations of thickness (see Figure 3.11). Thus, the presence of the extremum m and M is distinctive even when the defocus value is fixed while the thickness of the specimen is varying.

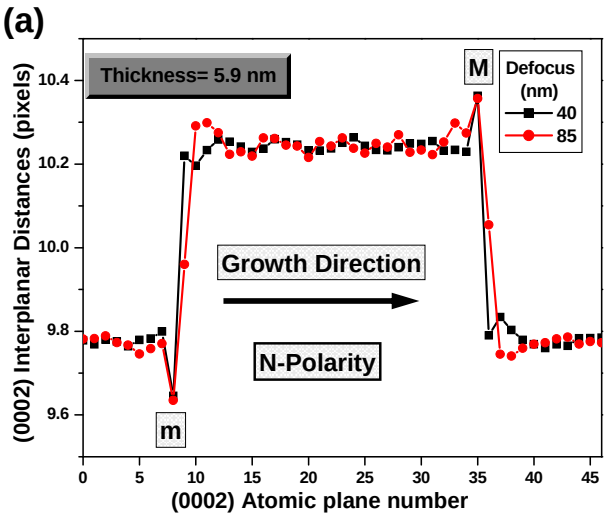

Figure 3.18 : *Simulated interplanar distances profiles of a GaN QW in an AlN matrix, for defocus values of 40 nm (black line) and 85 nm (red line). The presence of the extremum m and M does not depend on the imaging conditions but it is linked to the polarity of the layers. Arbitrarily, the "growth direction" in the simulations was chosen from left to right. Since it is the minima m which is first meet when following the growth direction, the layers have N-polarity.*

We have associated the observed asymmetry of the profiles to the polarity of the layers. In Figure 3.19 using the the case of a quantum well structure viewed along the [0,1,-1,0] direction, we remind the definition of the polarity and note the involved interatomic distances.

As seen by M. Charleux in her PhD work [30], oscillations in lattice fringe profiles can come from the interferences between planes coming from adjacent layers and sometimes

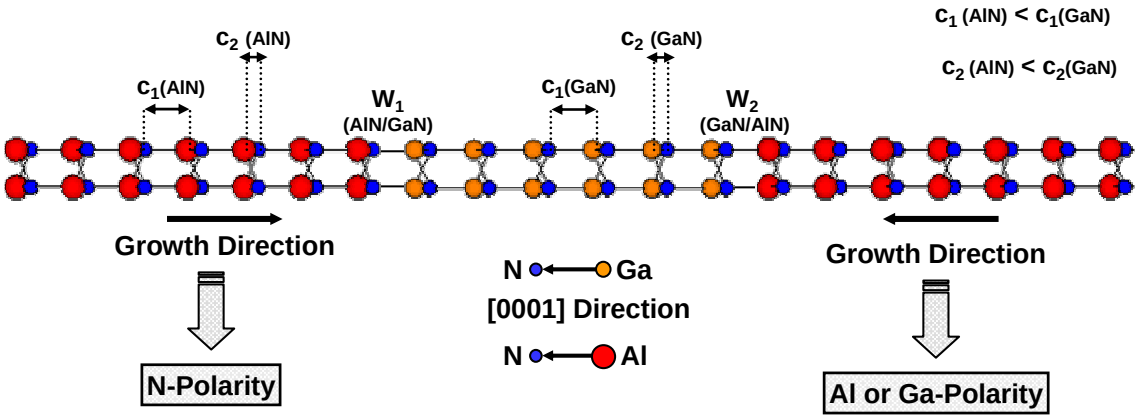

Figure 3.19 : *Interatomic distances and Definition of polarity for the case of a GaN QW inside an AlN matrix. The layers have Al (or Ga) polarity if the [0001] direction follows the growth direction and vice-versa.*

from the shape of the mask in the Fourier space. The first origin -interference origin- produces what is called Fresnel fringes. These interferences are always present when a defocused image of an interface between two materials is realized. These interferences mainly depend on the mean inner potentials of the materials. The second origin -mask shape- can be called Gibbs oscillations [29]. We wanted to check if this second origin was present in our case. Thus, the projected potentials of ideal AlN/GaN and GaN/AlN interfaces (Figure 3.20 (a)) were filtered and analyzed both by the projection method and the GPA. Figure 3.20 (b) superposes the obtained profiles with a geometrical interplanar profile. The geometrical interplanar profile was calculated by assuming that the fringes of the analyzed image are situated just in between the atomic columns of the III and N species (Figure 3.20 (a)). One can see in Figure 3.20 (b) that no oscillations are present in the projection method and that the obtained profile is nearly identical to the geometrical profile. On the contrary, GPA does not reproduce accurately the geometrical profile.

From these simulations we can conclude that: (i) the Fresnel fringes are the origin of the extremum m and M, (ii) these Fresnel fringes/extremum positions do not depend only on the mean inner potential (if this was the case, the interplanar profiles would be symmetric) but are sensitive to the asymmetry of the interplanar distances and (iii) GPA is not very powerful in obtaining the exact interplanar distances at interfaces.

The rule that connects the extremum m and M with the polarity of the layers is: if by following the growth direction the extremum m is met first, the layers have N-polarity. Respectively, the polarity is Al (or Ga) if the extremum M is first met [22]. We need to mention that the use of an interplanar distance profile to determine the polarity of an AlN/GAN heterostructure is only possible if the examined experimental images are of high quality, that is to say with a good signal-to-noise ratio. For this reason, in

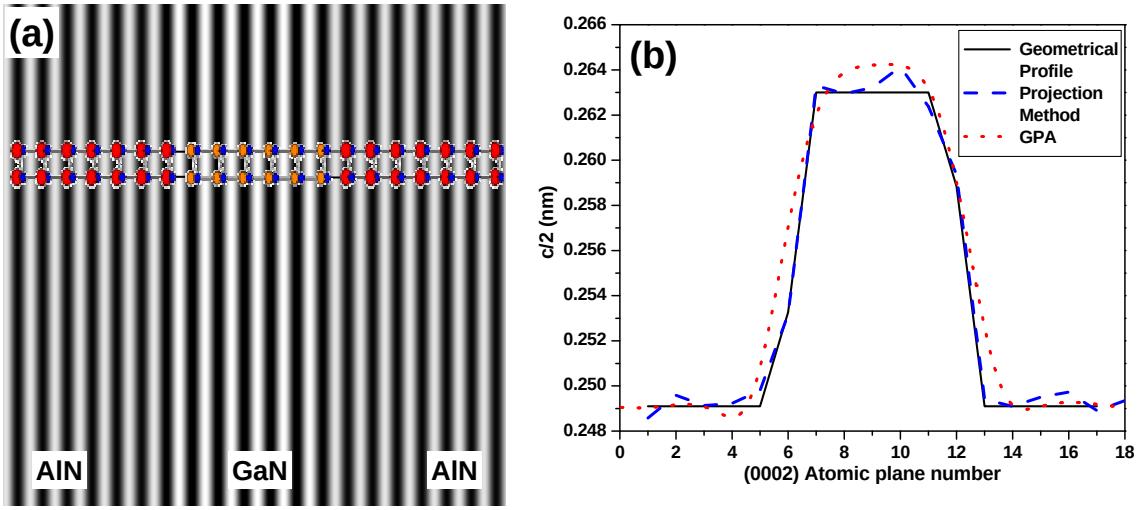

Figure 3.20 : *(a) Projected potential of ideals AlN/GaN and GaN/AlN interfaces. (b) Superposition of the profiles obtained from (a) using a geometrical interplanar profile (black line), the projection method (dash line) and the GPA (dot line).*

experimental images the variations of the extremum m and M can be sometimes hidden by noise. However, in section 5.1.3 Figure 5.6 the polarity of a GaN/AlN QD superlattice was verified by using this rule.

3.4 Distortions in the HRTEM images

In order to test the quality of our image formation system, a set of HRTEM images of perfect Si crystals were acquired with the CCD camera and analyzed using the Geometric Phase Analysis.

Figure 3.21 shows a HRTEM image of the perfect Si crystal viewed along a [110] zone axis together with its corresponding diffraction pattern. The GPA was applied for different pairs of non-collinear reflections $\mathbf{g_i}$, using the original routines written by M Hÿtch [18]. A gaussian type of mask of size equal to $\mathbf{g_i/4}$ was used.

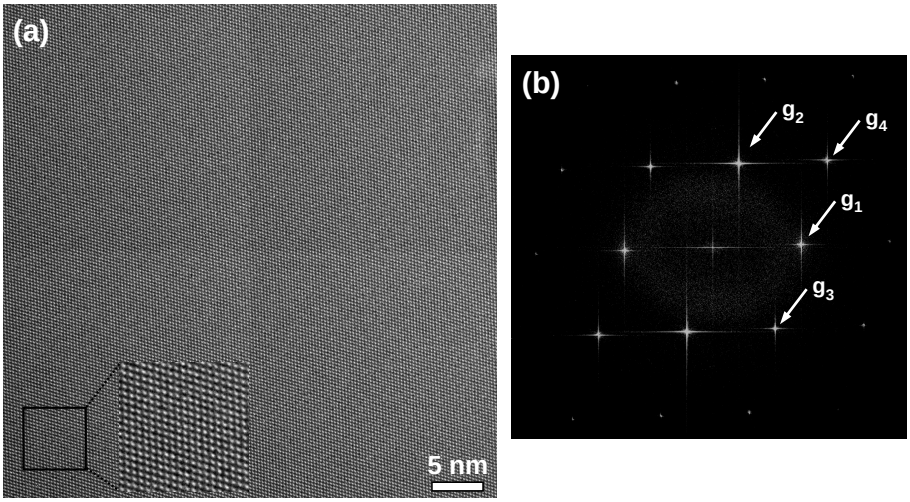

Figure 3.21 : *(a) HRTEM image of a Si crystal viewed alon the [110] direction. (b) Corresponding diffraction pattern.*

The obtained results for the $(\mathbf{g_1}, \mathbf{g_2})$ and $(\mathbf{g_3}, \mathbf{g_4})$ pairs of non-collinear reflections are illustrated in Figure 3.22. We can clearly identify the presence of distortions introduced by our image formation system (microscope and CCD). They affect the form of the measured displacement fields $\mathbf{u_x}$ and $\mathbf{u_y}$ and strain fields $\mathbf{e_{xx}}$ and $\mathbf{e_{yy}}$. In particular we see that independently of the direction along which the projection is realized, the displacement fields are no longer constant straight lines as we are approaching the edges of the image.

From the profiles of the strain fields we see also that we do not obtain constant straight lines of zero value. In particular, when the projection is realized from up to down a variation of e_{xx} of $\sim$0.2% is measured. When the projection is realized from left to right, the variation of e_{xx} does not follow a straight line but it change from $\sim$0.8% in the left part of the image to $\sim$0% in the right part. The e_{yy} varies linearly from $\sim$-0.6% at the top part until $\sim$ +0.6% at the bottom part. However, when the projection is realized from left to right the variation of e_{yy} is not uniform and change from $\sim$-0.2% at the left part to $\sim$0.15% to the right part.

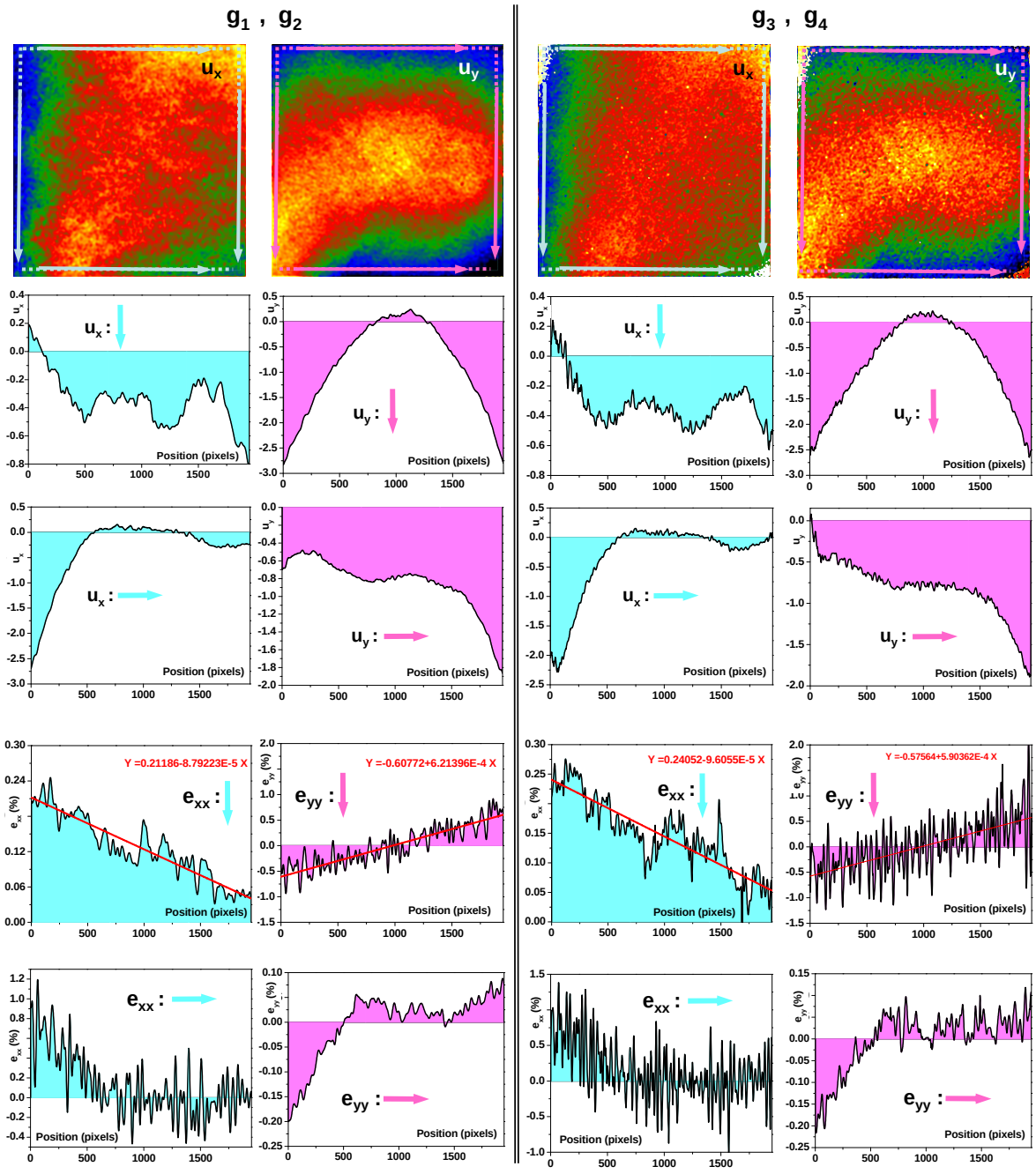

Figure 3.22 : *GPA of the image shown in Figure 3.21 (a) for two pairs of non-collinear reflections:* $(\mathbf{g_1}, \mathbf{g_2})$ *and* $(\mathbf{g_3}, \mathbf{g_4})$*. The displacement* ($\mathbf{u_x}$ *and* $\mathbf{u_y}$) *and strain* ($\mathbf{e_{xx}}$ *and* $\mathbf{e_{yy}}$) *fields were obtained from the corresponding phase images. Arrows give the direction of the profiles. The profiles (displacement and strain) were obtained by projection of the corresponding image perpendicular to the direction indicated by the arrows.*

Moreover, we can notice that both the displacements fields $\mathbf{u_x}$ and $\mathbf{u_y}$ and the strain fields $\mathbf{e_{xx}}$ and $\mathbf{e_{yy}}$ have the same form and magnitudes, independently of the pair of non-

collinear reflections used in GPA. This is the case for any possible combination between non-collinear reflections $\mathbf{g_i}$. This means that GPA is indeed internally coherent. However, the {111} frequencies $(\mathbf{g_1}, \mathbf{g_2})$ give less noisy images.

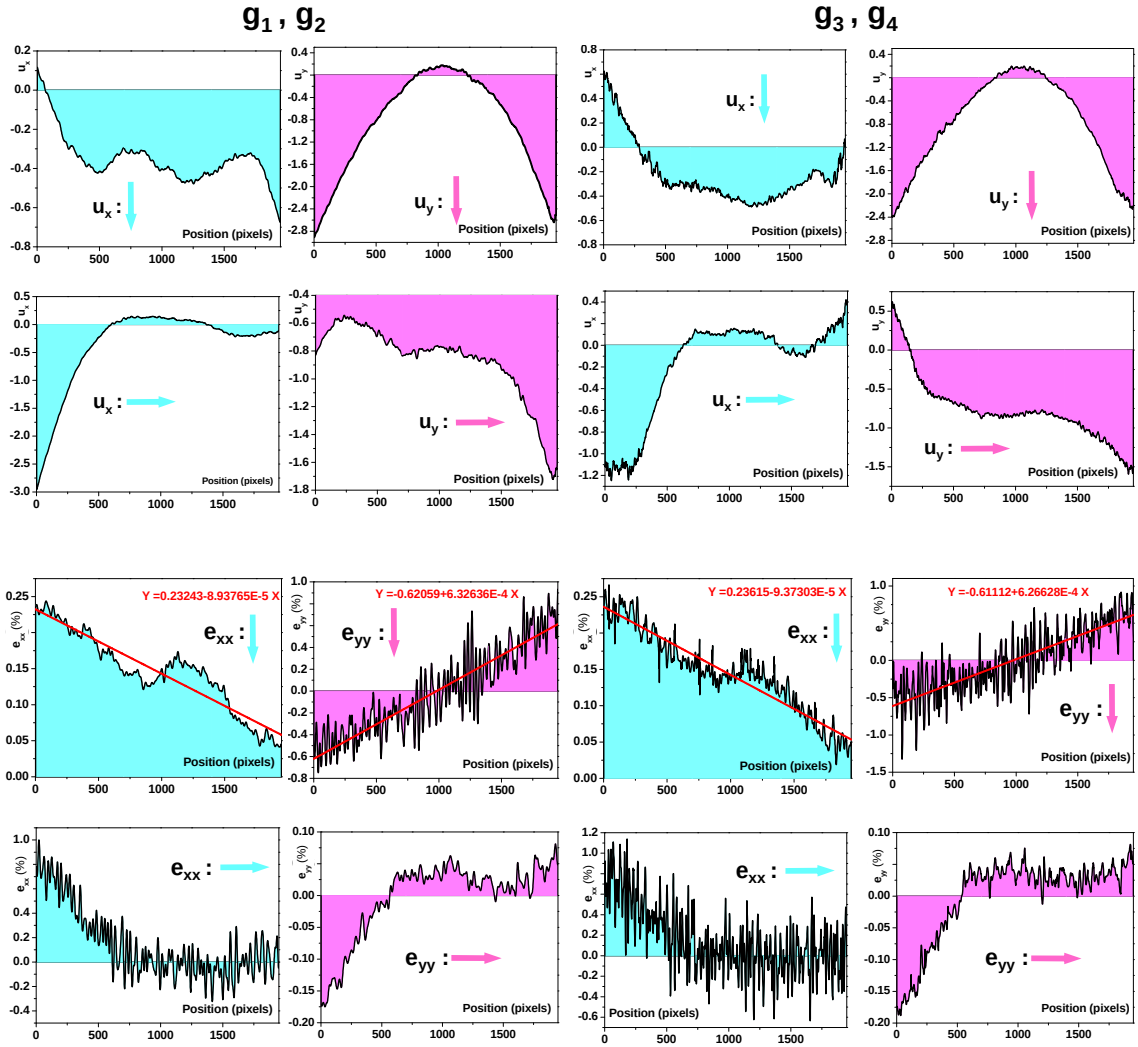

Figure 3.23 : *GPA of an image illustrating the same area of the Si crystal given in Figure 3.21 (a) but using a different magnification.*

In order to check if the observed distortions are mostly caused by the projection system of the microscope or by the CCD camera, the same analysis as previously was realized for different sets of images. In particular, we have acquired images having different magnifications and images after realignment of the electron microscope. The obtained displacement and strain profiles are given in Figures 3.23 3.24. In Figure 3.23 the analysis was carried out on the same Si crystal area as in Figure 3.21 (a) but for a different magnification. Figure 3.24 is a different area of the Si crystal acquired another day after the realignment of the microscope at a different voltage (375kV). We obtain the same

results as the ones given in Figure 3.22, meaning that the observed distortions are related mostly to the CCD camera than to the projection system of the microscope.

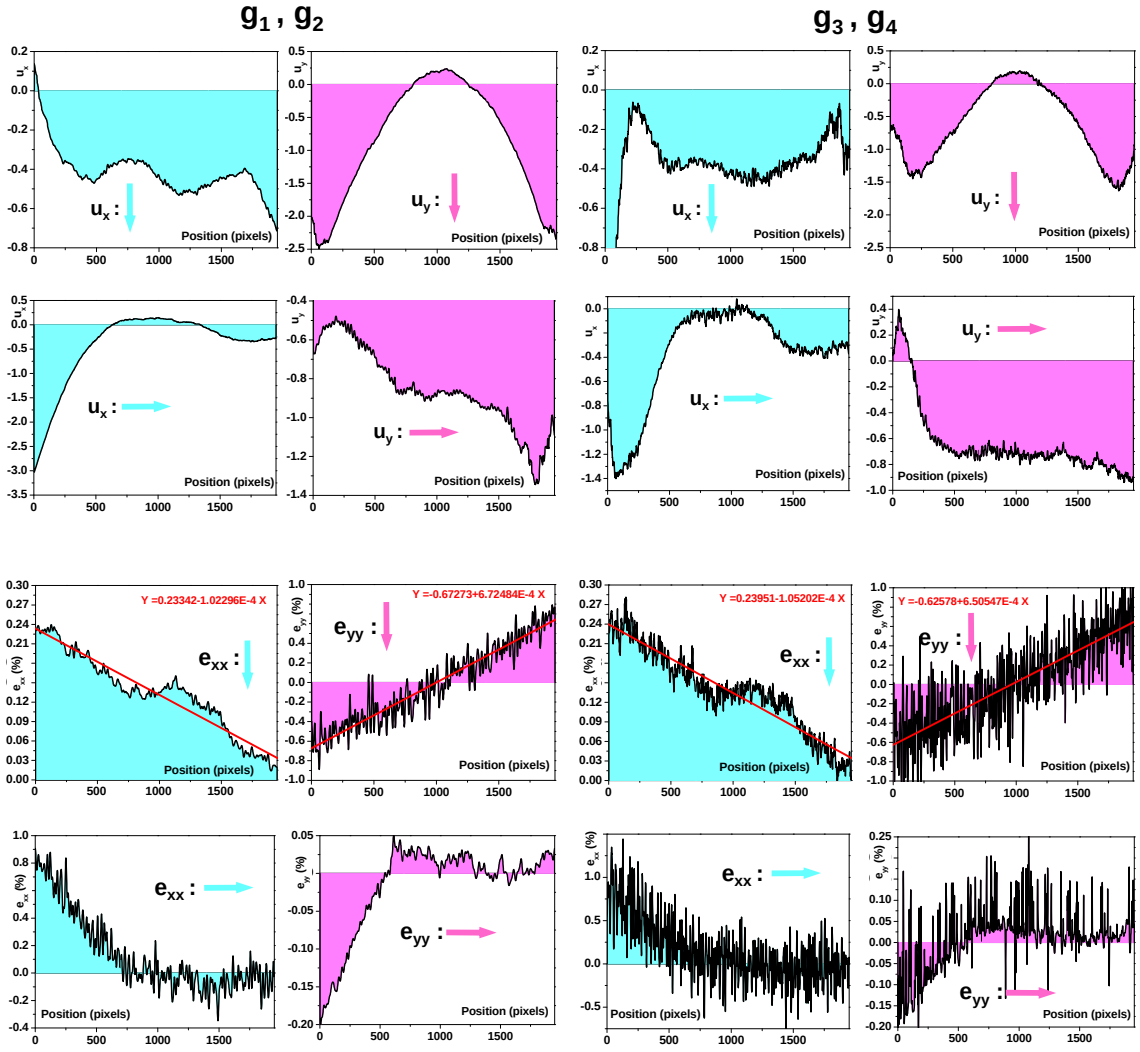

Figure 3.24 : *GPA of an image of the same Si crystal but acquired another day after realignment of the microscope at a different voltage (375kV).*

Knowing now the distortions introduced by the CCD camera for the case of a perfect Si crystal, we can suggest that, in a first approximation, we can correct an experimental HRTEM image by subtracting the previously measured distortions from it. For example, in a HRTEM image where only the (0002) planes are visible, the corrected e_{xx} strain map will be equal to:

$$e_{xx}^{corrected} = e_{xx}^{GPA} - e_{gg}^{Si,GPA} \qquad \text{with} \quad e_{gg}^{Si,GPA} = \frac{e_{xx}^{Si,GPA}\, g_x + e_{yy}^{Si,GPA}\, g_y}{\sqrt{g_x^2 + g_y^2}} \tag{3.75}$$

The image $e_{gg}^{Si,GPA}$ and the corresponding profile is given in Figure 3.25 (a). In Fig-

ure 3.25 (b) is shown an experimental HRTEM image taken along the [0,1,-1,0] direction of a GaN/AlN quantum well superlattice, that will be analyzed in more details in chapter 4.1. Only the (0002) planes are visible. The resulting GPA strain map (e_{xx}^{GPA}) and the corresponding to the outline area profile are given in Figures 3.25 (c) and (d) respectively. We observe that the strain in the left part of the image is higher. By subtracting the image $e_{gg}^{Si,GPA}$ (Figure 3.25 (a)) from image e_{xx}^{GPA} (Figure 3.25 (c)) we obtain the the corrected GPA strain image $e_{xx}^{corrected}$ (Figure 3.25 (e)). From the new strain profile (Figure 3.25 (f)) we can see that all GaN QWs have similar strain values. We also notice that the noise in the $e_{xx}^{corrected}$ is increased. This is because in equation 3.75 we are adding images and as a result we are adding the noise that they contain.

To conclude, we are in a favorable case because: (i) distortions do not depend very much on the tuning of the microscope and (ii) distortions are reduced at the center of the CCD image. Consequently, when observing areas situated at the center of the image, no corrections are necessary for an accuracy of about $\pm$ 0.1% in the strain measurement. Only when edges of the images are analyzed, the CCD distortions have to be corrected according to the previous analysis.

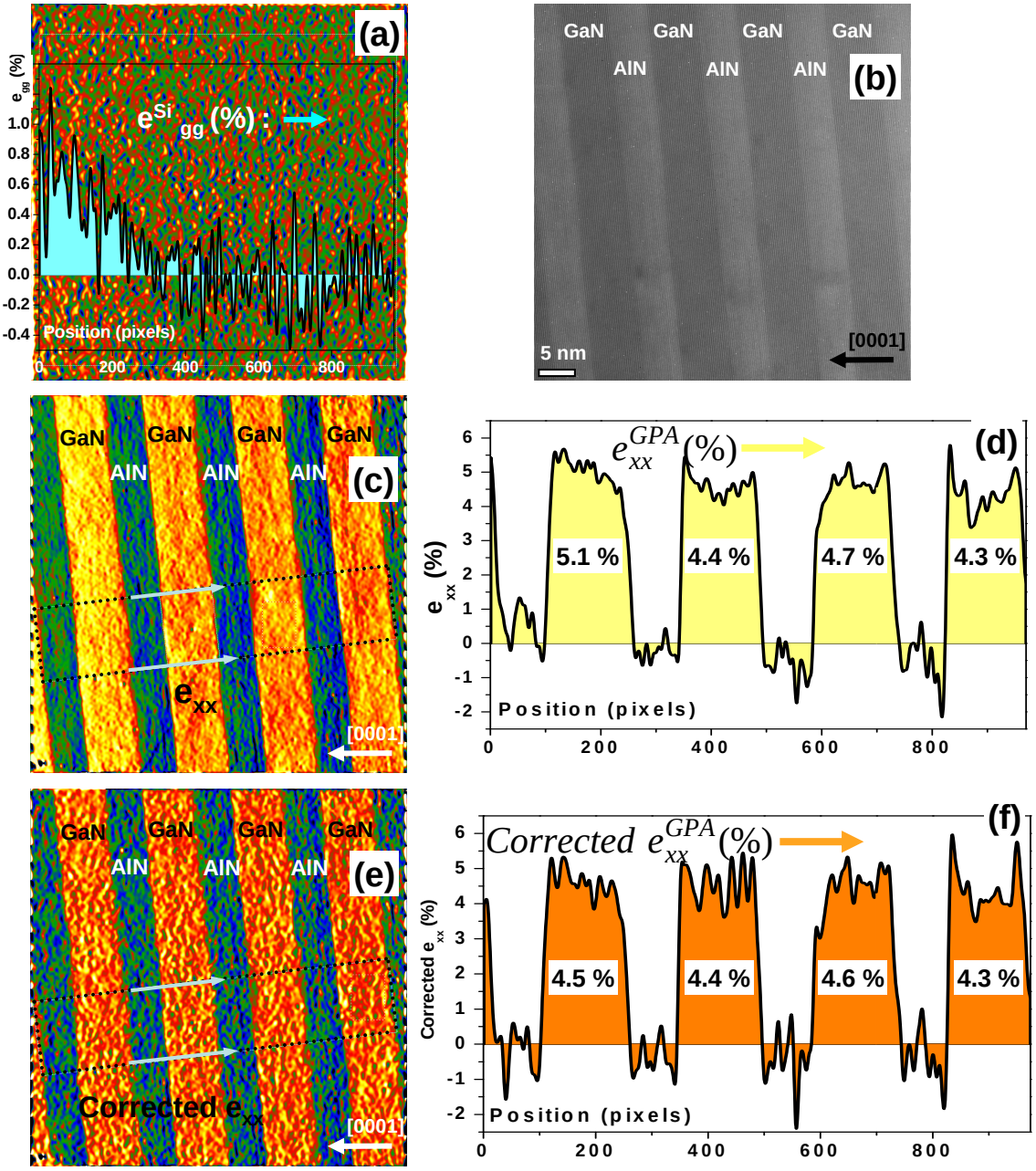

Figure 3.25 : *(a) $e_{gg}^{Si,GPA}$ image resulting from equation 3.75 using the $e_{xx}^{Si,GPA}$ and $e_{yy}^{Si,GPA}$ images of Figure 3.22. (b) HRTEM image of a GaN/AlN quantum well superlattice viewed with the [0,1,-1,0] zone axis. (c) e_{xx}^{GPA} strain map of (a). (d) Corresponding to the outline area of (c) strain profile. (e) Corrected strain map obtained by subtracting image (a) from image (d). (f) Corresponding to the outline area of (e) strain profile. In GPA a gaussian mask of size $\mathbf{g}/4\,nm^{-1}$ was used. The arrows indicate the profile direction.*

3.5 Off-axis HRTEM images

Images taken away (off) a low index zone axis will be named as off-axis HRTEM images. They are obtained by tilting the sample away a low index axis and by keeping the viewing direction in the plane of the interface. In a first approximation, off-axis images correspond to the projection of the (0002) lattice planes.

Generally, in this thesis, in order to simulate easily the structure, secondary zone axis were usually selected. In particular, the off-axis images were obtained either by tilting the sample ~ 11 degrees away the [0,1,-1,0] zone axis, which corresponds to the secondary zone axis [-1,5,-4,0], or equivalently by tilting the sample ~ 19 degrees away the [2,-1,-1,0] zone axis, which corresponds to the [5,-1,-4,0] zone axis[6].

A schematic illustration of the wurtzite structure along the [-1,5,-4,0] direction together with the associated diffraction pattern can be seen in Figure 3.26. Following the [0001] direction the distance between two atoms of the same type is equal to $\mathbf{c}/2$, while along the [-3,1,2,0] direction this distance is equal to $\frac{\sqrt{21}}{14}\,\mathbf{a}$.

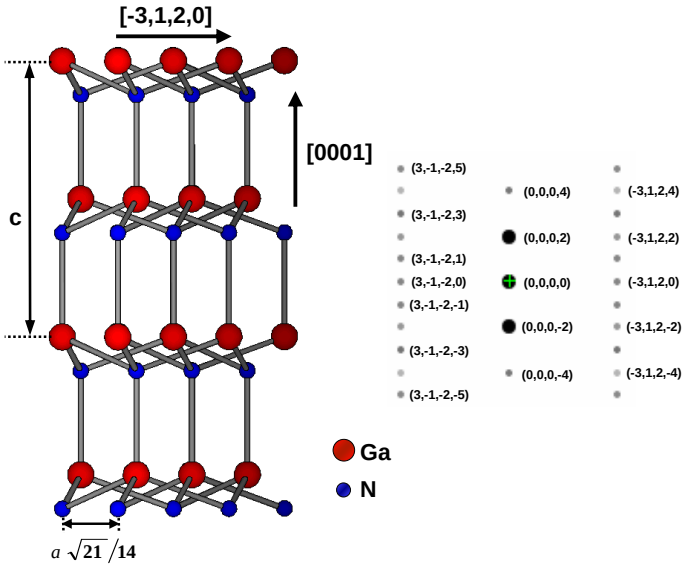

Figure 3.26 : *Schematic illustration of the wurtzite structure along the [-1,5,-4,0] direction and the associated diffraction pattern.*

The advantage of such tilted conditions is the enhancement of the image contrast and the improvement of the signal-to-noise ratio.

Figure 3.27 shows a HRTEM contrast map (thickness t versus defocus δz) of a perfect GaN crystal viewed along the [-1,5,-4,0] direction. The objective aperture diameter was chosen equal to 15 nm-1. The contrast of this map is greater than the contrast calculated for the [0,1,-1,0] direction (Figure 2.13).

[6]The angle between the [0,1,-1,0] and [-1,5,-4,0] directions, based on equation A.7, is 10.9 degrees. Between the directions [2,-1,-1,0] and [5,-1,-4,0] equation A.7 gives 19.1 degrees.

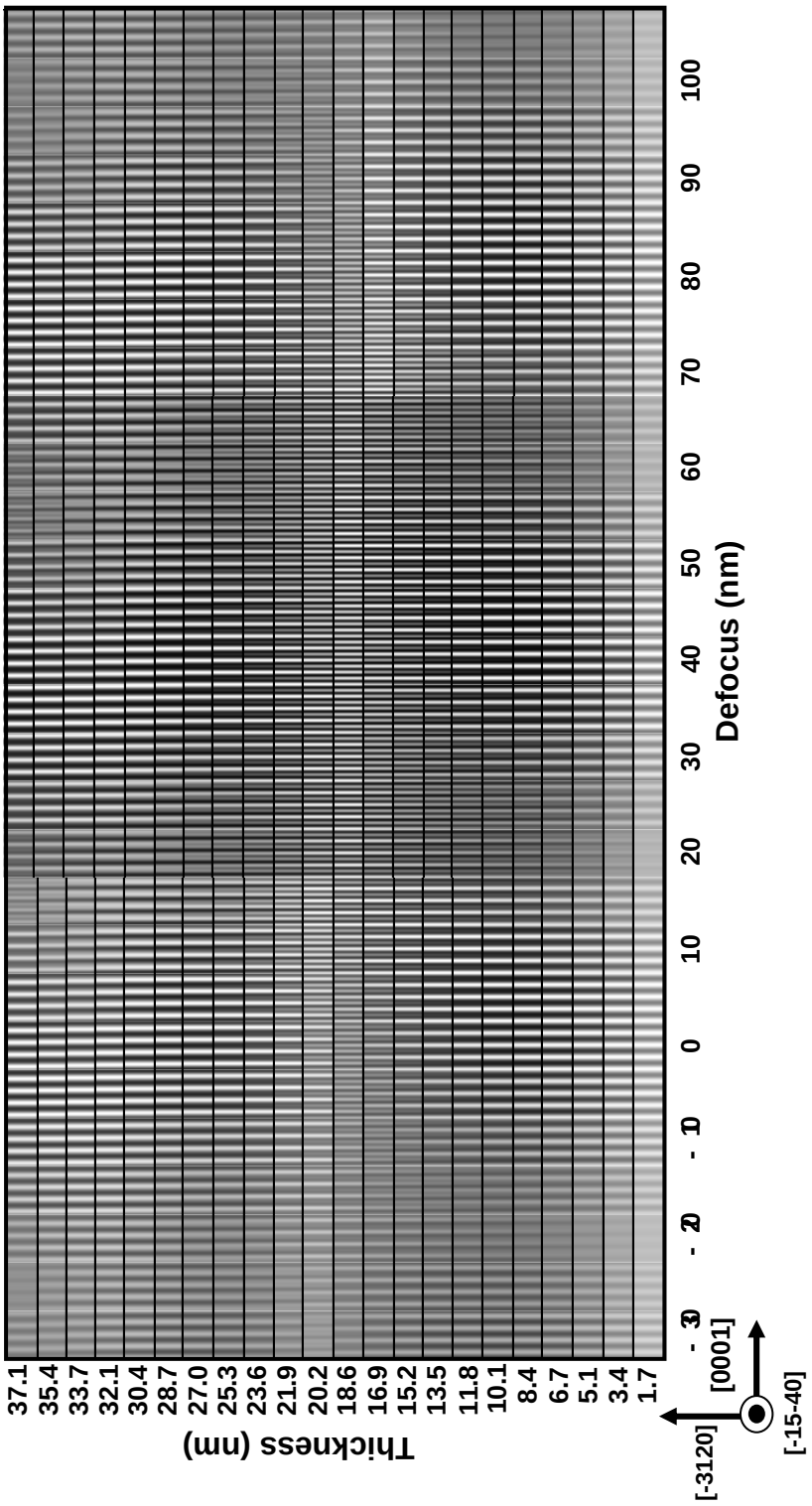

Figure 3.27 : *Thickness/Defocus contrast map of HRTEM simulated images of an GaN perfect crystal along the [-1,5,-4,0] zone axis. (Accelerating voltage: 400KV and Objective aperture diameter:15nm-1)*

This is better seen in Figure 3.28, where we compare the contrast of two simulated images of a GaN crystal having the same value of defocus (50 nm) and thickness (3.3 nm), one taken with the [0,1,-1,0] zone axis (Figure 3.28 (a_1)) and one calculated with the [-1,5,-4,0] direction (Figure 3.28 (b_1)). By considering each simulated image as a sum of lines and columns and by plotting the profiles corresponding to the maximum and minimum values of lines (Figure 3.28 (a_2) and (b_2)) and columns (Figure 3.28 (a_3) and (b_3)), we can clearly see the enhancement of the contrast in the off-axis image. Moreover, due to the fact that in the off-axis images the (0002) planes are presented as continuous lines rather than discontinuous lines of spots (on-axis image), the contrast of the off-axis image for the profiles obtained for different columns remains constant.

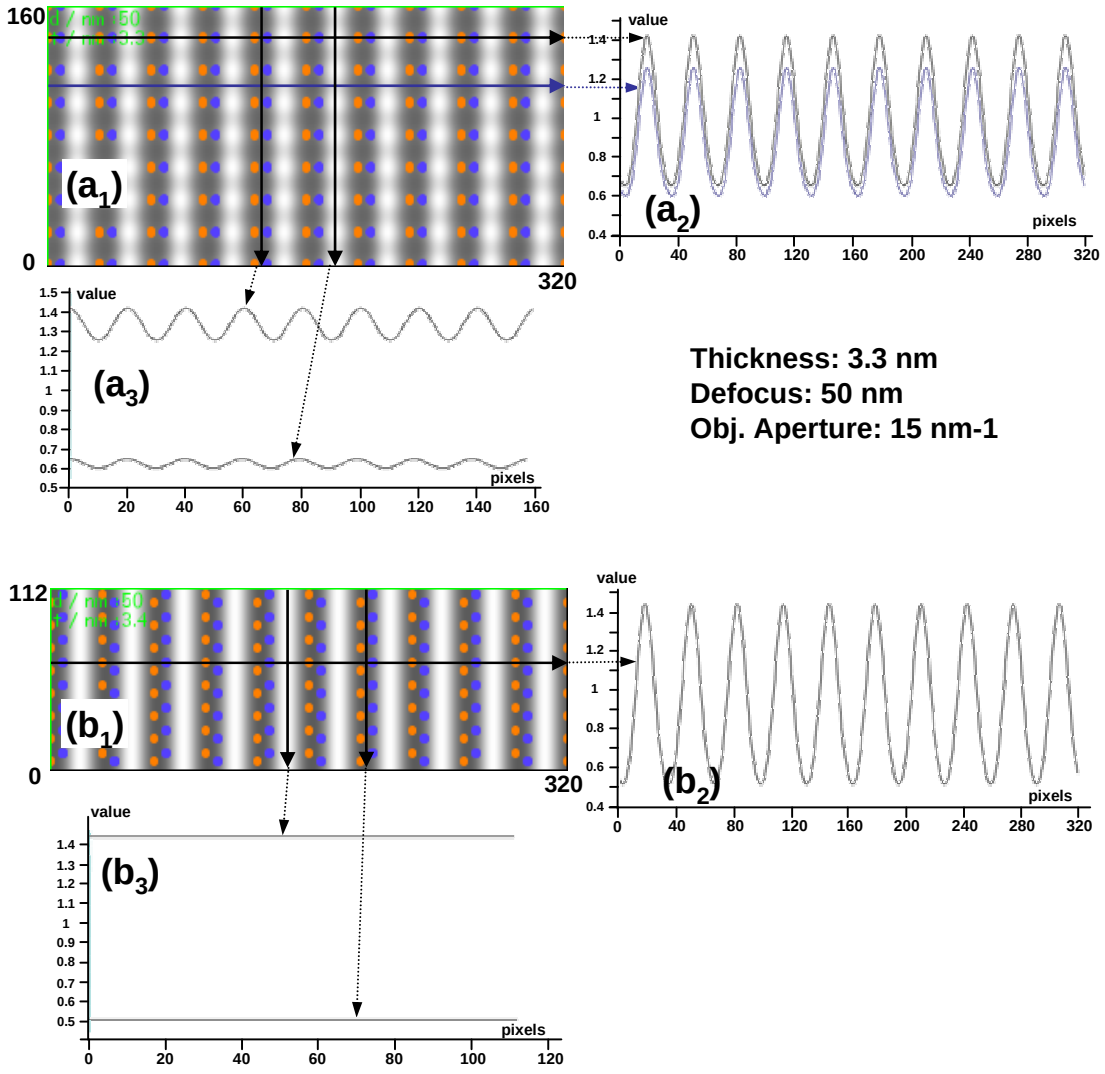

Figure 3.28 : *Comparison of the contrast between on-axis and off-axis HRTEM simulated images. The arrows indicate the directions along which the different projections have been realized.*

In general, when being in off-axis conditions, a smaller number of beams is excited by the incident beam and the amplitude of these excited beams is greater than the ones of the on-axis images. This is illustrated in Figure 3.29 where the amplitudes of the different excited beams are given as a function of the sample thickness for both on-axis and off-axis conditions for the case of a GaN crystal. The objective aperture diameter was chosen equal to 15 nm-1.

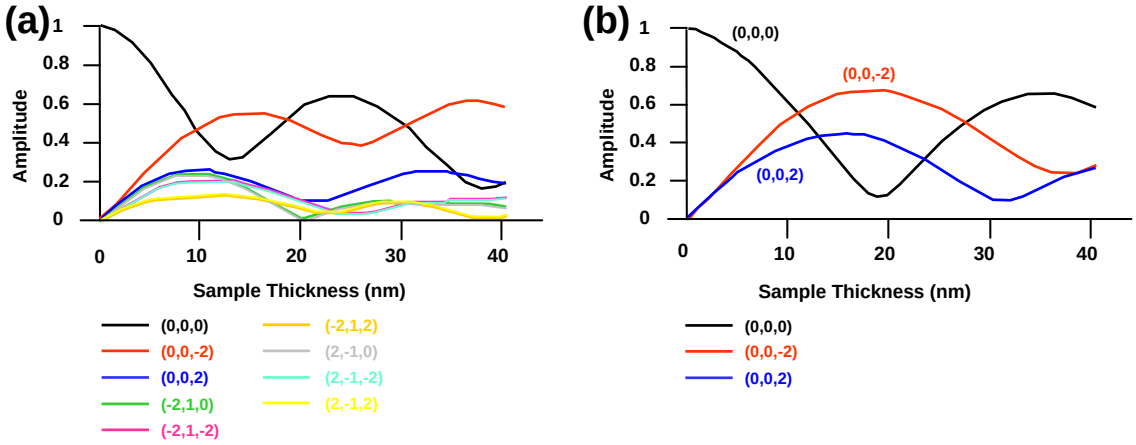

Figure 3.29 : *Amplitude of the beams contributed in the creation of a HRTEM image as a function of the sample thickness for (a) On-axis and (b) Off-axis conditions. Objective aperture diameter= 15 nm-1.*

Additionally, compared to on-axis images, the off-axis images are less noisy because: (i) they are less sensitive to surface defects and (ii) the (0002) planes appears as straight lines rather than discontinuous lines of spots (Figure 3.28).

The advantages of the off-axis images are also demonstrated in the following example [31]. In particular, the case of a GaN quantum well embedded in a $Al_{0.13}Ga_{0.87}N$ matrix has been used to compare on-axis HRTEM images with off-axis ones. The lattice mismatch between these materials is small (0.7%), thus, images with very few noise are necessary. In Figure 3.30 (a) and (b), an on-axis and an off-axis HRTEM image of exactly the same area of the GaN QW are respectively shown. The corresponding interplanar distances profiles obtained with the projection method are superimposed. It can be clearly seen, that the on-axis image is too noisy to detect the presence of the GaN thin QW. The same images were analyzed with the GPA. The resulting strain images and their projections are shown in Figure 3.30 (c) and (d) respectively. Once again, the QW is detected only in the strain image that comes from the analysis of the off-axis image (Figure 3.30 (d)).

Another example which proves the superiority of the off-axis images will be given in chapter 4.1.2 Figure 4.5. We will see that due to the reduce noise contained in off-axis images, the precision in calculating the local lattice parameters of an heterostructure becomes higher.

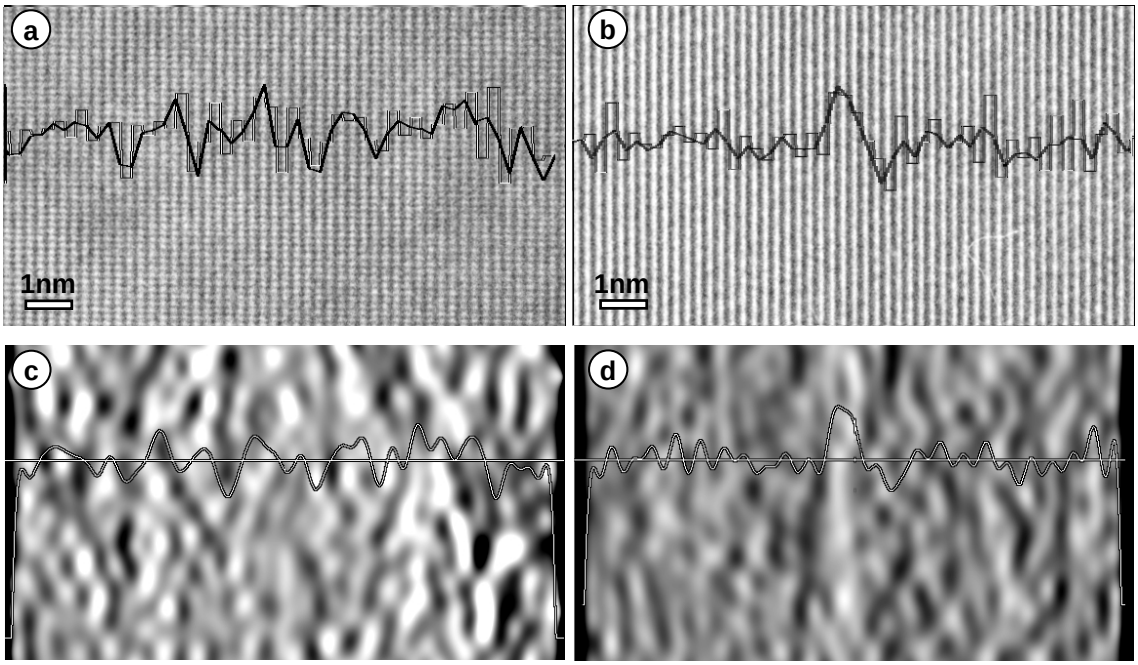

Figure 3.30 : *(a) On-axis HRTEM image of a thin GaN QW embedded in a $Al_{0.13}Ga_{0.87}N$ matrix. The interplanar distances profiles obtained by the projection method (original and after smoothing) are superimposed. (b) Off-axis HRTEM image and corresponding interplanar distances profiles of exactly the same area as in (a). (c)-(d) Strain images e_{zz} and their projections of the HRTEM pictures respectively shown in (a) and (b). Only in off-axis images ((b) and (d)), that are less noisy, the GaN QW can be detected.*

Bibliography

[1] R. Bierwolf, M. Hohenstein, F. Phillipp, O. Brandt, G. E. Crook, and K.Ploog. *Ultramicroscopy*, 49:273, 1993.

[2] M. Arlery, J. L. Rouviere, F. Widmann, B. Daudin, G. Feuillet, and H. Mariette. *Appl. Phys. Lett.*, 74(22):3287, 1999.

[3] P. Bayle-Guillemaud and J. Thibault. *Microscopy Microanalysis Microstructure*, 8:125, 1997.

[4] V. Chamard, T. Schülli, M. Sztucki, T. H. Metzger, E. Sarigiannidou, J. L. Rouvière, M. Tolan, C. Adelmann, and B. Daudin. *Phys. Rev. B*, 69:125327, 2004.

[5] W.O. Saxton, T.J. Pitt, and M. Horner. *Ultramicroscopy*, 4:343, 1979.

[6] M.M.J. Treacy, J.M. Gibson, and A. Howie. *Phil. Mag. A*, 51:389, 1985.

[7] J.M. Gibson and M.M.J. Treacy. *Ultramicroscopy*, 14:345, 1984.

[8] Shapesoftware. *Atoms*. http://www.shapesoftware.com/.

[9] J.L. Rouviere. *ICEM*, 13:123, 1994.

[10] L.E. McNeil, M. Grimsditch, and R.H. French. *J. Am. Ceram. Soc*, 76(5):1132, 1993.

[11] A.F. Wright. *J. Appl. Phys.*, 82(6):2833, 1997.

[12] K. Kim, W.R.L. Lambrecht, and B. Segall. *Phys. Rev. B*, 53(24):16310, 1996.

[13] V.A. Savastenko and A.U. Sheleg. *Phys. Stat. Solidi (a)*, 48(2):135, 1978.

[14] S.S. Shapiro and R.S. Francia. *J. Americal Statistical Association*, 67:215, 1972.

[15] S.S. Shapiro and M.B. Wilk. *Biometrika*, 52(3-4):591, 1965.

[16] S. Kret, P. Ruterana, A. Rosenauer, and D. Gerthsen. *Phys. Stat. Sol. (b)*, 227(1):247, 2001.

[17] M. Takeda and J. Suzuki. *J. Opt. Soc. Amer. A*, 13:1495, 1996.

[18] M.J. Hÿtch, E. Snoeck, and R. Kilaas. *Ultramicroscopy*, 74:131, 1998.

[19] M.J. Hÿtch, J.L. Putaux, and J.M. Penisson. *Nature*, 423:270, 2003.

[20] C. Adelmann, E. Sarigiannidou, D. Jalabert, Y. Hori, J.-L. Rouvière, B. Daudin, S. Fanget, C. Bru-Chevallier, T. Shibata, and M. Tanaka. *Appl. Phys. Lett.*, 82:4154, 2003.

[21] M. Penisson J and T. Vystavel. *Ultramicroscopy*, 90(2-3):163, 2002.

[22] E Sarigiannidou, J L Rouvière, G Radtke, P Bayle-Guillemaud, E Monroy, and B Daudin. *Inst. Phys. Conf. Ser. to appear.*

[23] M.J. Hÿtch and M. Gandais. *Phil. Mag. A*, 72:619, 1995.

[24] K. Scheerschmidt and F. Knoll. *Phys. Stat. Sol. A*, 146:491, 1994.

[25] M. Takeda, H. Ina, and S. Kobayashi. *J. Opt. Soc. Amer. A*, 72:156, 1982.

[26] P.B. Hirsch, A. Howie, and M.J. Whelan. *Philos. Trans. Roy. Soc. London A*, 252:499, 1960.

[27] J.L. Rouviere and E. Sarigiannidou. *Ultramicroscopy to appear.*

[28] H. Seitz, K. Ahlborn, M. Seibt, and W. Schröter. *J. Microscopy*, 190:184, 1998.

[29] A.J. Jerri. *The Gibbs Phenomenon in Fourier Analysis, Splines and Wavelet Approximation.* Kluwer Academic, Dordrecht, 1998.

[30] M. Charleux. *Etude par Microscopie Electronique d'hétérostructures de semiconducteurs II-VI élaborées par Epitaxie par Jets Moléculaires Alternés : vers la réalisation de fils quantiques.* PhD thesis, INPG, Grenoble.

[31] J.L. Rouviere, P. Bayle-Guillemaud, G. Radtke, S. Groh, and O. Briot. *Inst. Phys. Conf. Ser.*, 169:17, 2001.

Chapter 4

GaN/AlN Quantum Well Structures

Device applications generally require the growth of increasingly complex heterostructures like quantum wells and quantum dots. The structural characterization of GaN/AlN quantum well structures is the issue of this chapter. It is organized in two parts. In the first part a comparative study between a Ga-face and a N-face GaN/AlN superlattice is presented. With the help of various TEM techniques the higher structural quality of the Ga-face superlattice will be proven. In the second part the effects of AlN overgrowth on the structural quality of GaN QWs are described. We will demonstrate that the overgrowth process implies a thinning of the GaN QWs and we will attribute this phenomenon to a thermally activated exchange mechanism between Al from the capping layer and Ga atoms from the nanostructure.

4.1 Comparison of Ga-face and N-face polarity GaN/AlN superlattices

4.1.1 Introduction

The Ga-face and the N-face of GaN present different chemical properties and growth kinetics [1].

On the other hand, the issue of crystal polarity is closely related to the investigation of polarization and its influence on the electronic and optical properties of III-nitrides. Polarization in wurtzite structure nitrides have both a spontaneous P_{sp} [2] and a piezoelectric P_{pz} component. The electric fields due to variations of the polarization at interfaces and surfaces modify the shape of the band edges and influence the carrier distribution along nitride heterostructures. This dramatically affects the performance of nitride based devices. In this context, the polarity of a sample is relevant, since it determines the di-

rection of spontaneous polarization. Particularly, the polarization vector in the case of a Ga-face polarity sample points towards the substrate, while in a N-face polarity sample it points towards the surface [3, 4]. The direction of the P_{pz} depends both on the polarity and on whether the material is under tensile or compressive stress [4].

For these reasons, it is of great importance to examine and compare the structural quality of samples with different polarities. To do so, transmission electron microscopy techniques, like high-resolution TEM, are the most appropriate.

This section contains the results that we have obtained from a comparative study of GaN/AlN quantum well superlattices with either metal-face or N-face polarity. Information about the layer thickness, the interface quality, the chemical composition and the strain distribution inside the superlattices was extracted quantitatively from HRTEM images using both a projection method and the geometrical phase analysis technique. The higher structural quality of the Ga-polarity heterostructure will be demonstrated.

4.1.2 Ga-face polarity GaN/AlN superlattice

Growth conditions and sample structure

The growth of Ga-face GaN by plasma-assisted molecular beam epitaxy (PAMBE) has been extensively studied and discussed [5–8]. In this study, the investigated sample was a Ga-face [1] 25-period GaN/AlN (7nm / 5nm) quantum well superlattice (SL) grown by PAMBE (Figure 4.1). As a substrate, an AlN template, consisting of a 1μm thick layer of AlN grown on *c*-sapphire by MOVPE, was used. The substrate temperature was equal to $T_S = 730°C$. Prior to the SL deposition, an AlN buffer layer of 200 nm thickness was initially deposited. For the growth of both GaN and AlN, the best interface results were obtained by using Ga as surfactant, i.e. during the growth of the SL, the Ga shutters were remained permanently opened and AlN nitride was obtained by additionally opening the Al cell [2]. No growth interruptions were performed at the interfaces.

Figure 4.1 is a cross section TEM (CTEM) image of the examined SL. It illustrates the uniformity of the QW thickness. It can be seen that the threading dislocations cross the SL and the GaN cap layer to terminate at the free surface. The image was taken close to two-beam conditions ($\mathbf{g}$=(0002)) in such a way to favor the contrast of the dislocations.

[1] Sample number E201.

[2] At the substrate temperature required to synthesize AlN/GaN with a good structural quality (700-750°C) Al desorption is negligible, i.e. its sticking coefficient is unity [9, 10]. In contrast, Ga shows a high desorption rate for temperatures higher than 700°C, and a tendency to segregate on the growing surface due to the different binding energies of GaN and AlN [Ga-N(∼9 eV) < Al-N(∼12 eV)] [11]. Thus, to incorporate Ga into the growing layer, it is necessary that the Al flux remains lower than the nitrogen flux [9, 10].

Under these conditions, only **c**-type (screw) and **a**+**c**-type (mixed) dislocations are in contrast (see section 2.2.2). Their density is 1.7×10^{10} dislocations/cm^2.

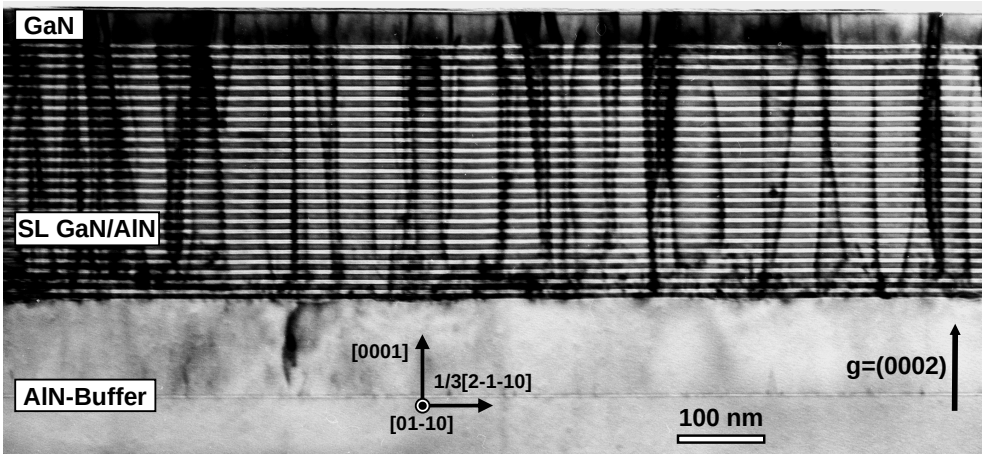

Figure 4.1 : *Cross section TEM image of the Ga-face supperlattice. The QWs appear to be uniform and flat. Threading dislocations are crossing the SL and end at the free surface.*

Lattice parameter c

The structural properties of the SL were first examined by X-ray Diffraction (XRD) reciprocal space mapping[3]. In Figure 4.2 a map of the reciprocal space of the Ga-face SL obtained for the (10.5) reflex is shown. We can see that the lattice parameters of the AlN buffer layer are equal to the bulk AlN. The X-ray experiments revealed also that the AlN matrix in the superlattice was relatively relaxed and as a consequence it has its bulk lattice parameters. This can be seen in the $\theta - 2\theta$ scan of the 002 reflection (Figure 4.3), where the simulated profile is realized for a completely relaxed AlN matrix.

HRTEM images were realized, with a view to measure the lattice parameter of the layers and consequently their exact thickness, the interface width, the chemical composition and the local strain. A high resolution image taken along the [0,1,-1,0] zone axis of three GaN QWs of the SL is shown in Figure 4.4. Before starting the quantitative analysis of the HRTEM images, our first goal was to determine the experimental conditions, defocus of objective lens δz and specimen thickness t, of each image to be analyzed. For this purpose a series of simulated images of a GaN QW inside an AlN matrix were performed and compared with the experimental. In our simulations we have tried to reproduce both the contrast of our layers and the symmetry of the lattice fringes profiles. In the case of the image of Figure 4.4 the best fit was obtained for a defocus value of 40 nm and a sample thickness of 5.9 nm. The corresponding HRTEM simulated image is given as an

[3]The X-ray experiments were realized by Edith Bellet-Amalric in CEA-Grenoble.

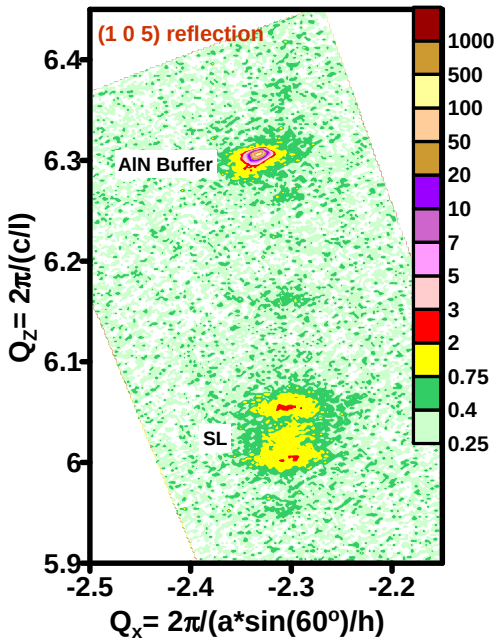

Figure 4.2 : *Reciprocal space map of the Ga-face sample.*

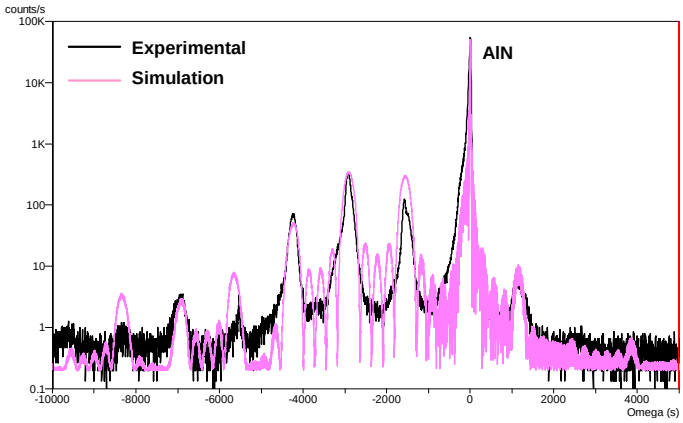

Figure 4.3 : $\theta - 2\theta$ *scan of the 002 reflection for the Ga-face SL.*

inset. For these imaging conditions, atomic columns are projected onto the black lines. Finally, we note that for all simulated images presented here, a small objective aperture diameter of $9nm^{-1}$ was used.

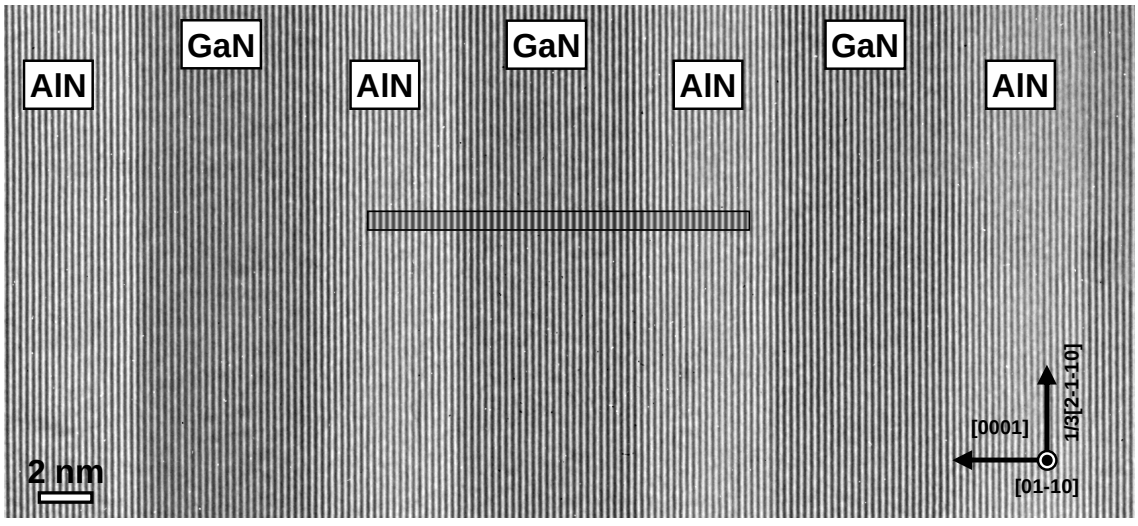

Figure 4.4 : *Experimental HRTEM image observed along the [0,1,-1,0] zone axis of three GaN QWs. Only the 0002 planes are visible. The corresponding simulated image is superimposed. The best fit was obtained for abrupt interfaces, thickness t=5.9 nm and defocus δz=40 nm.*

Once the imaging conditions of the HRTEM images were determined, the lattice pa-

rameter **c** of the GaN layers was measured from both interplanar distances profiles taken by a projection method and from phase images obtained by the GPA. Particularly, for the measurements obtained by the projection method we have chosen n_p to be equal to 2 pixels, while in the GPA the phase images were obtained by selecting the local reciprocal vector $\mathbf{g}_{0002}$ and place a gaussian mask of size $\sim \mathbf{g}/5\,\mathrm{nm}^{-1}$ around it. In both methods, the AlN was taken as reference lattice since based on the results obtained by the XRD measurements it has its bulk lattice parameters. For the reasons which were presented in the previous chapter (section 3.1.4), we have chosen to analyze HRTEM images with defocus value close to the Scherzer one. Both on-axis and off-axis images were used to measure the parameter **c**.

We have examined 32 different areas of 15 GaN QWs in the on-axis images and 23 areas of 10 GaN QWs in the off-axis. The average value of **c** was found equal to:

- $\mathbf{c}_{GaN} = 0.5236 \pm 0.0023\,\mathrm{nm}$ for the on-axis images,
- $\mathbf{c}_{GaN} = 0.5239 \pm 0.0014\,\mathrm{nm}$ for the off-axis images.

We notice that although there is no significant difference between the two average values of **c**, due to the fact that off-axis images contain less noise (see section 3.5), the precision with which the lattice parameter is calculated is higher.

Figure 4.5 illustrates the frequency count of the obtained ranges of lattice parameters values. The set of boxes were created by beginning at the minimum value of each range and adding a step size. We have defined as step size, the standard deviation of the average value of each range. The number of times a value falls within each box was after encountered and recorded. We can see that the distribution of the **c** values is more homogenous in the off-axis images.

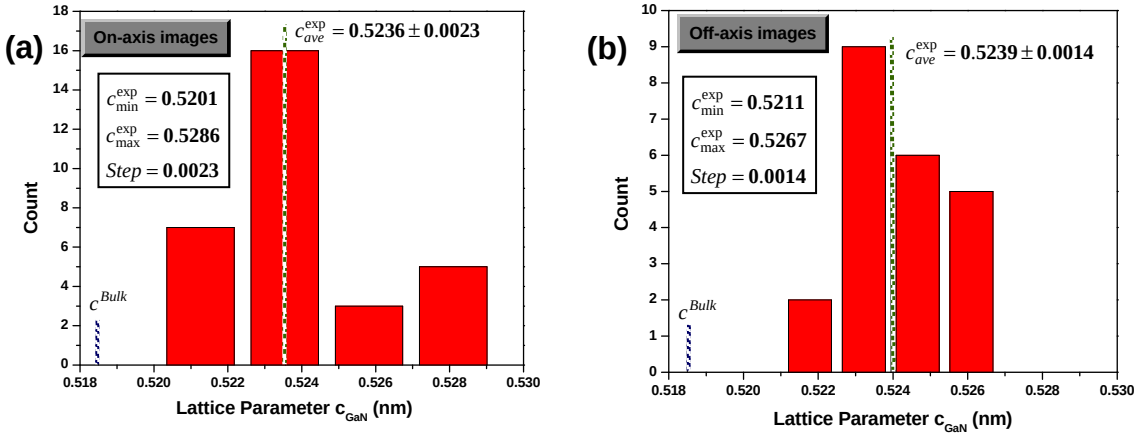

Figure 4.5 : *Frequency count of the values of the lattice parameter* $\mathbf{c}_{GaN}$ *obtained from the analysis of: (a) on-axis and (b) off-axis HRTEM images.*

By averaging the two ranges of values, the lattice parameter **c** of the GaN QWs is equal to:

$$\mathbf{c}_{GaN}^{exp} = \mathbf{0.5237 \pm 0.0020\,nm}$$

Size and interface quality

With the lattice parameter **c** known, the exact size of the QWs can be calculated either with the use of equation 3.2 or by analyzing geometrical phase images. The interplanar distances profiles and geometrical phase images used to evaluate the lattice parameter were also used to measure the thickness of the examined QWs. We have found that in average the thickness of the GaN and AlN QWs is equal to :

$$\mathbf{t}_{GaN} = \mathbf{6.94 \pm 0.4\,nm}$$
$$\mathbf{t}_{AlN} = \mathbf{5.02 \pm 0.4\,nm}$$

These values are in very good agreement with the nominal values of thicknesses (7 and 5 nm respectively). A frequency count of the measured thickness values, resulting from the analysis of 55 different areas (from on-axis and off-axis images) of the GaN QWs is given in Figure 4.6. We can conclude that the thickness of the GaN wells remain relatively constant along the wells and independently of their position in the superlattice.

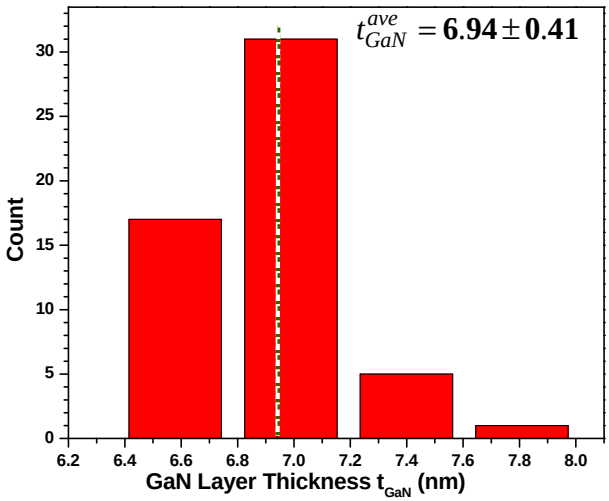

Figure 4.6 : *Frequency count of the thickness of the GaN QWs. The GaN wells exhibit an homogenous thickness of* 6.94 ± 0.41 ***nm***.

The same images were also used to measure the width of the interfaces. Figure 4.7 (a) illustrates the variation of the lattice parameter **c/2** in the HRTEM image shown in Figure 4.4. The image is obtained by the GPA. We can observe that the interfaces are uniform along the different QWs, with a thickness which doesn't exceed 1 ML. Moreover, we see that both the AlN/GaN and the GaN/AlN interfaces have the same quality. In Figure 4.7 (b), the experimental (open circles) and simulated (close circles) HRTEM

interplanar distances profiles obtained from the middle GaN QW of Figure 4.4 are shown. The simulated profile corresponds to a pure GaN QW of 27 ML with abrupt interfaces and completely strained by the AlN matrix. The very good agreement in the interface areas between those two profiles indicates that the QW have abrupt interfaces of less than 1ML. The dotted horizontal lines represent the average (0002) interplanar distances values in the AlN matrix and the GaN QW.

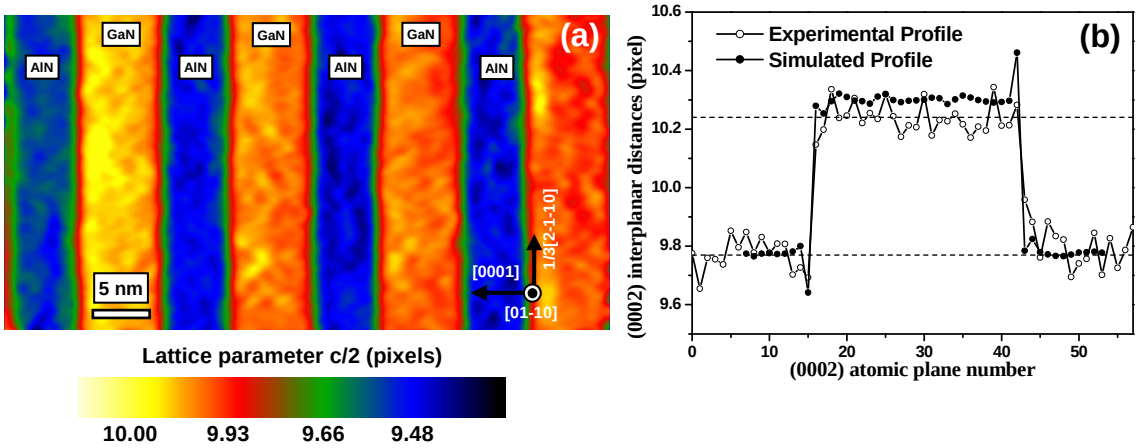

Figure 4.7 : *(a) Image, obtained by the GPA, illustrating the variation of the lattice parameter* $\mathbf{c/2}$ *in the HRTEM image of Figure 4.4. The uniformity and the abruptness of the QWs is clearly shown. (b) Experimental (open circles) and simulated (close circles) HRTEM interplanar distances profile obtained by a projection method for the middle GaN QW shown in Figure 4.4. The simulated profile was calculated for abrupt interfaces between the GaN and the AlN. The good agreement between the two profiles suggests that both interfaces of the GaN QW are abrupt.*

Strain distribution and Chemical composition

In Figure 4.7 (b), we observe that in the simulated profile the interplanar distance of the GaN QW is bigger than the experimental one. Translating the interplanar distances in terms of $\Delta c/c$, the strain in the simulated profile is 5.4% corresponding to a pure GaN QW which is completely strained by the AlN. If we use for the GaN the average experimental lattice parameter $\mathbf{c}_{GaN}^{exp}$ measured previously, this difference becomes equal to 5.1 %.

Several suggestions could explain this difference:

1. the chemical composition of the GaN QWs is not 100% in Ga,

2. the AlN has not its bulk lattice parameter,

3. the surfaces of the thin foil partially relax the GaN stress,

4. the GaN QWs are only partially strained by the AlN.

In order to examine the validity of the first suggestion, concerning the **chemical composition** of our layers, Energy Filetered TEM (EFTEM) experiments were realized [4]. In particular, a series of 10 filtered images was recorded near the Al K-edge (∼1560 eV) with a window width of 15 eV and steps of 15 eV. The drift between the recorded images was corrected with the use of cross correlation procedure. From this series, an Al elemental map, shown in Figure 4.8 (a), was extracted by subtracting the background and by integrating the signal over 45eV after the edge onset, that is to say by adding 3 images. Thickness effects were also corrected by dividing the Al map by the t/λ map. Figure 4.8 (b) illustrates a profile of several QWs extracted from the Al map (dotted area). It indicates that the aluminium signal falls to zero inside the GaN QWs, which excludes the presence of a ternary $Al_xGa_{1-x}N$ alloy. Therefore, we can state that there is neither GaN/AlN interdiffusion nor significant Ga incorporation during the growth of the AlN layers [12].

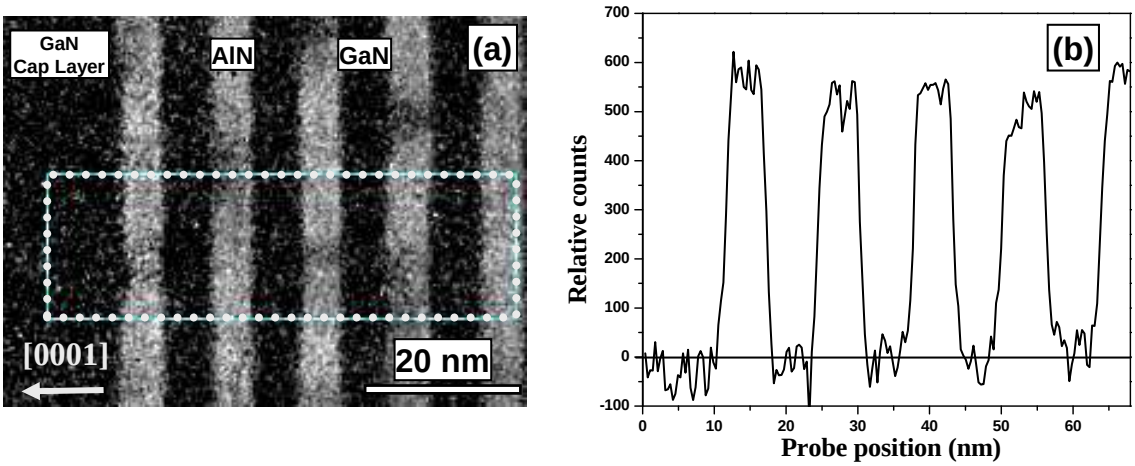

Figure 4.8 : *(a) Al elemental map. (b) Extracted profile of the outline area in (a). The Al signal drops almost to zero inside the GaN QWs.*

Previously, we have seen that X-ray experiments performed on the same sample, deduced that **both the AlN buffer layer and the AlN matrix in the superlattice were relaxed** and as a consequence have its bulk lattice parameters. Therefore, the second possibility is also excluded.

To investigate the validity of the third possibility concerning the thin foil relaxation effect [13], we have applied the geometric phase analysis on a HRTEM consisted of four

[4]For this sample (E201), the EFTEM experiments were realized by G. Radtke and P. Bayle-Guillemaud. At this time I was not yet trained in the EFTEM technique.

GaN QWs. Figure 4.9 shows the examined HRTEM image (Figure 4.9 (a)) together with the corresponding strain map and strain profile as calculated by GPA (Figures 4.9 (b) and (c) respectively) and the strain map and profile (Figures 4.9 (d) and (e) respectively) after correcting the distortions introduced by the CCD camera (see section 3.4). We remind that in GPA the strain is calculated with respect to a reference area in the HRTEM image. Thus, the strain map describes the variation of the crystal lattice across the image. In our case the strain was measured only along the growth direction and as reference lattice we have chosen the AlN matrix. A gaussian mask of size $\mathbf{g}/4\,\mathrm{nm}^{-1}$ was used in the analysis.

From the strain profile before corrections (Figure 4.9 (c)) we observe that the strain in the GaN QWs is not the same but it increases as we are moving along the growth direction from ∼4.2% (right part of the image) to ∼5.4% (left part of the image). In order to be sure that this evolution in strain is not resulting from the distortions introduced by the CCD camera, we have corrected the strain map by applying the procedure described in chapter 3.4. From the corrected strain profile (Figure 4.9 (e)) we notice that the evolution in strain is still present. In particular, the strain changes as we are moving along the [0001] direction from ∼4.2% to ∼5.1%.

If this evolution was due to the thin foil effect, we would expect that the strain becomes smaller as we are reaching thinner areas (from right to left in the image because TEM samples have generally a wedge shape near the edge of the hole). However, the experimental strain profile shows the opposite behavior. Therefore, we can not attribute this evolution in strain to the thin foil effect unless if we consider that for example the thinning of the TEM sample was made in an non uniform way. Such an hypothesis is however difficult to model/simulate. Moreover, a more precise way to correct the distortion introduced by the CCD camera would be necessary. Thus, for all our measurements we did not take into account the thin foil relaxation effect. In general, modifications of the relative displacement as a function of the distance in the examined HRTEM images, were in the same order as distortions introduced by the image formation system (see section 3.4. The example given at the end of this paragraph use the Ga-face SL examined here).

To examine now the strain state of the GaN QWs, the same strain analysis as previously was performed for the corresponding simulated HRTEM image (defocus=40 nm, thickness=7 nm). In GPA, we have used the same parameters as before (mask type= gaussian, mask size $=\mathbf{g}/4\,\mathrm{nm}^{-1}$). The results are shown in Figure 4.10. The simulated GaN QW was completely strained by the AlN. As expected, the calculated by the GPA strain (equation 3.71) is equal to $5.44 \pm 0.02\%$ for the GaN QW and zero for the AlN which is our reference lattice.

We remind here that the strain along the growth direction, for the case of one-

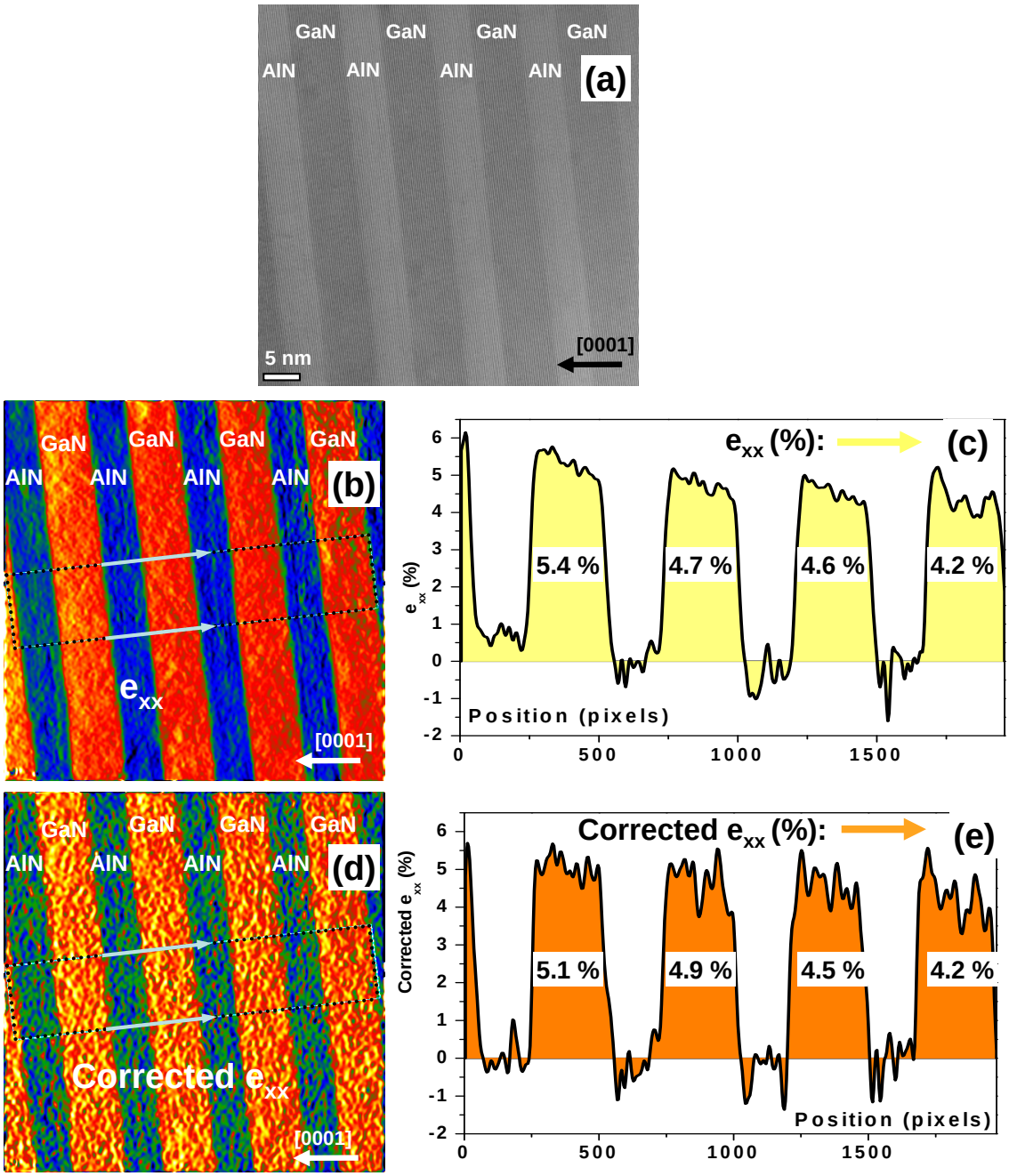

Figure 4.9 : *(a) HRTEM image of 4 GaN QWs. (b) Resulting from GPA strain map. (c) Strain profile corresponding to the outline area in (d). (d) Corrected from distortions introduced by the CCD strain map. (e) Strain profile corresponding to the outline area in (d). (Type of mask: Gaussian, Size:* $\mathbf{g}/4\,nm^{-1}$*). In the image, thinner areas are on the left.*

dimensional analysis (see 3.2.3) is given by the relationship:

$$e_{zz} = \frac{c_e - c_{ref}}{c_{ref}} \tag{4.1}$$

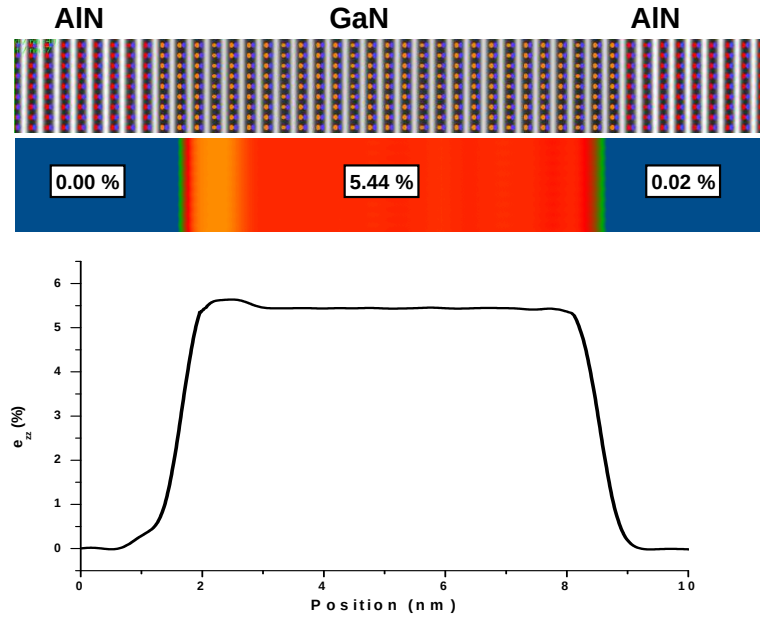

Figure 4.10 : *Strain analysis of a simulated HRTEM image corresponding to the experimental image of Figure 4.9 (a) (defocus=40 nm, thickness=7 nm).*

where c_e and c_{ref} are the lattice parameter of the epilayer and the selected reference area respectively.

The theory of elasticity, predicts for a GaN layer which is completely strain by an AlN matrix a lattice parameter $\mathbf{c}_{GaN}^{ela}$ equal to 0.5250 nm (equation B.8). Replacing this value in equation 4.1 (same as equation 3.71) we find a strain along the growth axis of 5.4%. If now we put as c_e the measured lattice parameter $\mathbf{c}_{GaN}^{exp}$ we have that $e_{zz} = 5.1\%$. As a result we can conclude that the GaN QWs along the growth directions are only **partially strained** by the relaxed AlN matrix.

Concerning now the **in-plane strain**, we know that for the case of GaN on AlN, the lattice mismatch f_0^a is equal to 2.47% (equation B.4). This mismatch can be separated in two parts: a residual strain (e_r) and a relaxed part (δ). Thus:

$$f_0 = e_r + \delta = 2.47\% \tag{4.2}$$

Based on the framework of linear elasticity (Appendix B), by replacing in equation 3.12 the c(x) with the average lattice parameter $\mathbf{c}_{GaN}^{exp}$ that we have previously measured, the strain e_r can be calculated as follows:

$$e_r = \frac{C_{33}}{2C_{13}} * \left(\frac{c_{GaN}^{exp}}{c_{GaN}^{bulk}} - 1 \right) \tag{4.3}$$

Equation 4.3 gave us a value of strain equal to:

$$e_r = 0.0197 = 1.97\%$$

which corresponds to the residual strain. The relaxed part δ, based on equation 4.2 is found equal to:

$$\delta = f_0 - e_r = 0.00503 = 0.5\%$$

With the values of e_r and δ known, the experimental lattice parameter a^{exp}_{GaN} of the GaN layers can be calculated from the relation:

$$a^{exp}_{GaN} = a^{bulk}_{GaN} - \epsilon_r * a^{bulk}_{AlN} = a^{bulk}_{AlN} + \delta * a^{bulk}_{AlN} = 0.3128 \text{ nm}$$

Since the biaxial strain is relaxed through the introduction of interfacial (misfit) dislocations, if we suppose that every n $\{0, 1, -1, 0\}$ planes of the substrate (AlN) we have *(n-1)* $\{0, 1, -1, 0\}$ planes in the epilayer (GaN) then n is equal to:

$$n = \frac{d^{epi}_{\{0,1,-1,0\}}}{d^{epi}_{\{0,1,-1,0\}} - d^{sub}_{\{0,1,-1,0\}}} = \frac{a^{exp}_{GaN}}{a^{exp}_{GaN} - a^{bulk}_{AlN}} \tag{4.4}$$

as $d^{epi}_{\{0,1,-1,0\}} = a^{exp}_{GaN}/2$ and $d^{sub}_{\{0,1,-1,0\}} = a^{bulk}_{AlN}/2$.

Equation 4.4 gives n=200 i.e we should find one misfit dislocation every 200 $\{0, 1, -1, 0\}$ planes. In the sample, the formation of threading dislocations of **a**+**c**-type (mixed) in the SL (see Figure 4.1) could be associated to the presence of interfacial (misfit) dislocations [14], however we have not observed these dislocations.

Therefore, we can conclude that **in average the GaN layers are only partially strained by the AlN**. With the electron microscopy technique we were able to measure the local lattice parameter and as a result the local strain of most of the QWs. However, from Figure 4.5 we can see that the distribution of the lattice parameter $\mathbf{c}_{GaN}$ is quite large. In particular, in the case of on-axis images the variation in the lattice parameter of the GaN can reach the order to 1.3%. A possible explanation could be that the relaxation in the superlattice is not homogeneous. However, we should not forget the important density of dislocations in the sample which, although hardly visible in our HRTEM images, are present. Their displacement field could slightly shift the local lattice parameters of GaN.

4.1.3 N-face polarity GaN/AlN superlattice

Growth conditions

The examined N-face[5] sample was similar to the Ga-face sample. It consists of a 25-period GaN/AlN (7nm / 5nm) QW superlattice grown by PAMBE. A NOVASIC-

[5] Sample number E274.

polished C-face 4H-SiC substrate was used and the substrate temperature was equal to $T_S = 730°C$. An AlN buffer layer was initially deposited before the growth of the SL. The thickness of the buffer layer was 100 nm. As for the Ga-face sample, the use of Ga as surfactant gave the best interface results. Again, the Ga shutter remained permanently opened during growth and no growth interruptions were performed at the interfaces. The high sticking coefficient of Al (compared to Ga), derives from the higher energy of Al-N bonds (compared to Ga-N bonds), and guarantees a preferential incorporation of Al under these growth conditions. Consequently, Ga atoms segregate at the growth front and act as a surfactant.

Sample polarity.

First, it was important to verify in a reliable way, that samples grown under these growth conditions exhibit a N-face polarity. It is generally known that polar substrates can be prepared with a defined polarity and thus can set the polarity of heteroepitaxially grown III-nitride layers accordingly. In particular, for the case of a 4H-(or 6H-) SiC substrate, it is known that when GaN is grown on a Si-face SiC it presents systematically Ga-face polarity, while the use of C-face SiC results in N-face material [15–18]. The polarity was firstly identified *in situ* by RHEED. Under nitrogen flux, a metal-face polarity sample shows a 2x2 reconstruction (Figure 4.11 (a)), whereas during the cooling-down process, structures with N-face polarity shows a distinct 3x3 reconstruction (Figure 4.11 (b)).

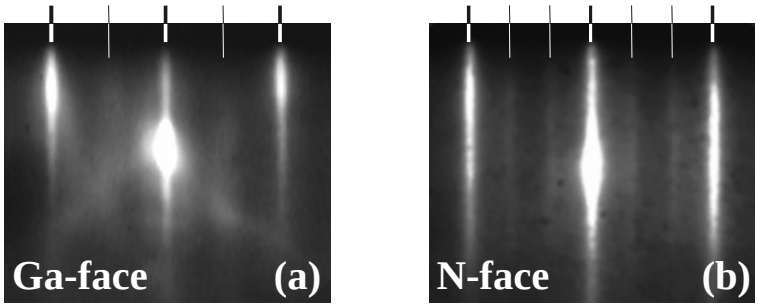

Figure 4.11 : *RHEED pattern in the* $< 11\bar{2}0 >$ *azimuth of (a) Ga-face and (b) N-face polarity GaN at low temperature.*

These observations are in agreement with the work of A. R. Smith *et al.* and Feenstra *et al.* [7,19,20]. Moreover, it has been verified that the choice of polarity was independent of the III/V ratio and of the nature of the buffer layer, either AlN or GaN. Furthermore, no change of polarity was observed during the growth of $Al_xGa_{1-x}N$ heterotructures and quantum-well or quantum-dot superlattices.

The polarity was also checked *ex situ* by convergent beam electron diffraction (CBED). In particular, the previous results obtained by RHEED, were verified for a sample[6] which

[6]Sample name S1321.

consisted of a 500 nm GaN layer grown by PAMBE on NOVASIC-polished C-face 4H-SiC substrate at substrate temperature of $T_S = 730°C$. In section 2.2.3 we have described how the CBED technique can determine the polarity of noncentrosymmetric crystals (case of wurtzite GaN) by comparing relative orientations of experimental CBED patterns with associated TEM images of the crystal. The CBED experiments were realized in the JEOL3010 LaB6 electron microscope and the necessary simulations were performed with the JEMS software [21]. In Figure 4.12 (a) a cross section [0,1,-1,0] TEM image of the examined GaN layer is shown. Figure 4.12 (b) presents two experimental CBED patterns taken inside the GaN layer together with the corresponding simulated ones. Comparing the orientation of each pattern with the corresponding simulated pattern we can assert that the GaN layer has the c-axis oriented downwards, indicated that the layer presents a N-polarity. The 180^o rotation introduced by the microscope was taken into account.

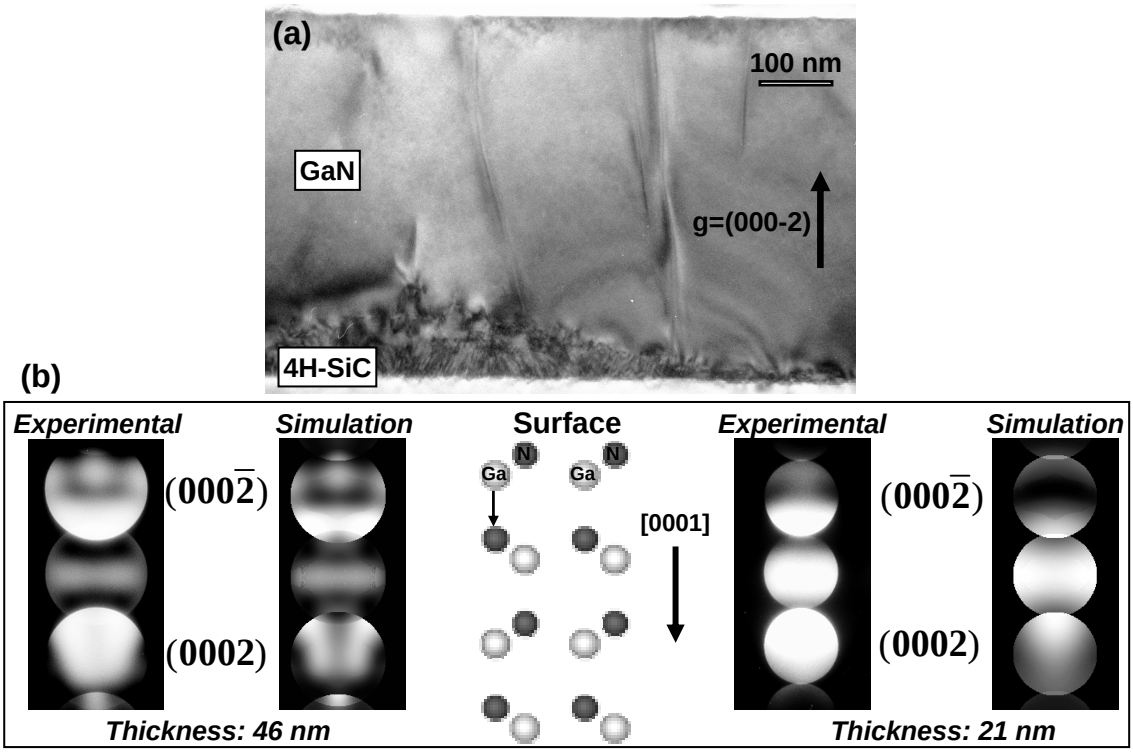

Figure 4.12 : *(a) Cross section [0,1,-1,0] TEM image of a GaN layer grown on C-face 4H-SiC substrate. (b) Experimental CBED patterns obtained inside the GaN layer with the corresponding simulated pattern for crystal thicknesses of 46 and 21 nm. The c-axis is oriented downwards leading to a N-polarity GaN layer. The asymmetry of the (0002) and (000-2) spots can be seen. The atomic structure of a N-polarity GaN crystal view along the [2,-1,-1,0] direction is also given. The* 180^o *rotation introduced by the microscope was taken into account.*

Sample structure and defects

The conventional CTEM image of Figure 4.13 illustrates an overall view of the N-face polarity GaN/AlN superlattice. The arrows indicate the presence of planar defects, which are originate at the SiC/AlN interface. We see that they are crossing the SL and terminate at the GaN top surface area.

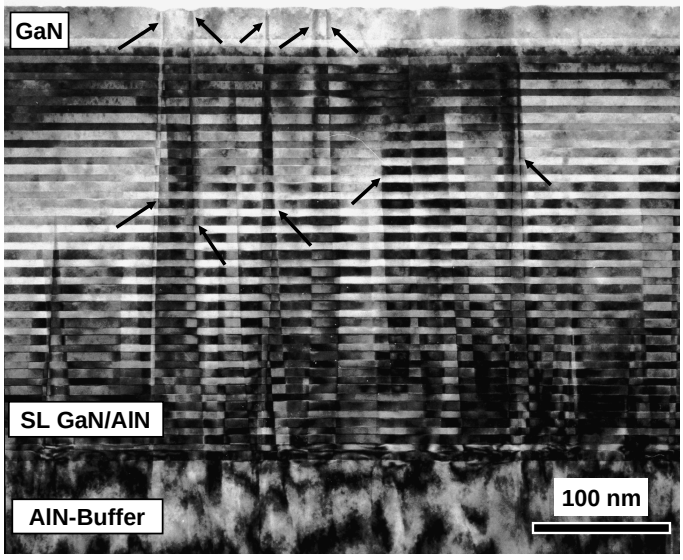

Figure 4.13 : *Two-beam image of the N-face GaN/AlN superlattice, viewed with the* $01\bar{1}0$ *reflections. The arrows indicate the presence of planar defects, which are crossing the SL.*

In order to identify the type and the structure of these planar defects, we have realized defocus series of HRTEM images. Figure 4.14 shows HRTEM images of the same area taken along the [2,-1,-1,0] zone axis, for two defocus values, which contains a narrow domain bounded by two planar defects. Specifically , in Figures 4.14 (a)-(b) the defocus was equal to $\sim 50nm$, while in (c)-(d) the defocus value was $\sim 75nm$. This defocus values were determined by calculating the map of through defocus-thickness simulated images of perfect GaN. The stacking sequences inside and outside of the domain, (the arrows indicate the domain limits) are marked on Figures 4.14 (b) and (d), which are the outline regions in (a) and (c) respectively. We notice that for a defocus value around 50 nm, the stacking sequence inside and on either side of the domain remains unchanged, whereas, when the defocus becomes equal to $\sim$ 75 nm, the sequence is reverse inside and outside of the domain. This behavior, is characteristic of the $\{01\bar{1}0\}$ inversion domain boundaries (IDB) [22].

Regarding the translation domain boundaries (TDB), two models of {1-210} prismatic TDBs have been observed experimentally in wurtzite GaN structure [23–25]. The Amelinckx model [26], which is characterized by 1/6<20-23> translation vector (Figure 4.15 (a)) and the Drum model [27] having a 1/2 <10-11> translation vector (Figure 4.15 (b)). Both of them have a 1/2 <0001> component. The Amelinckx model has

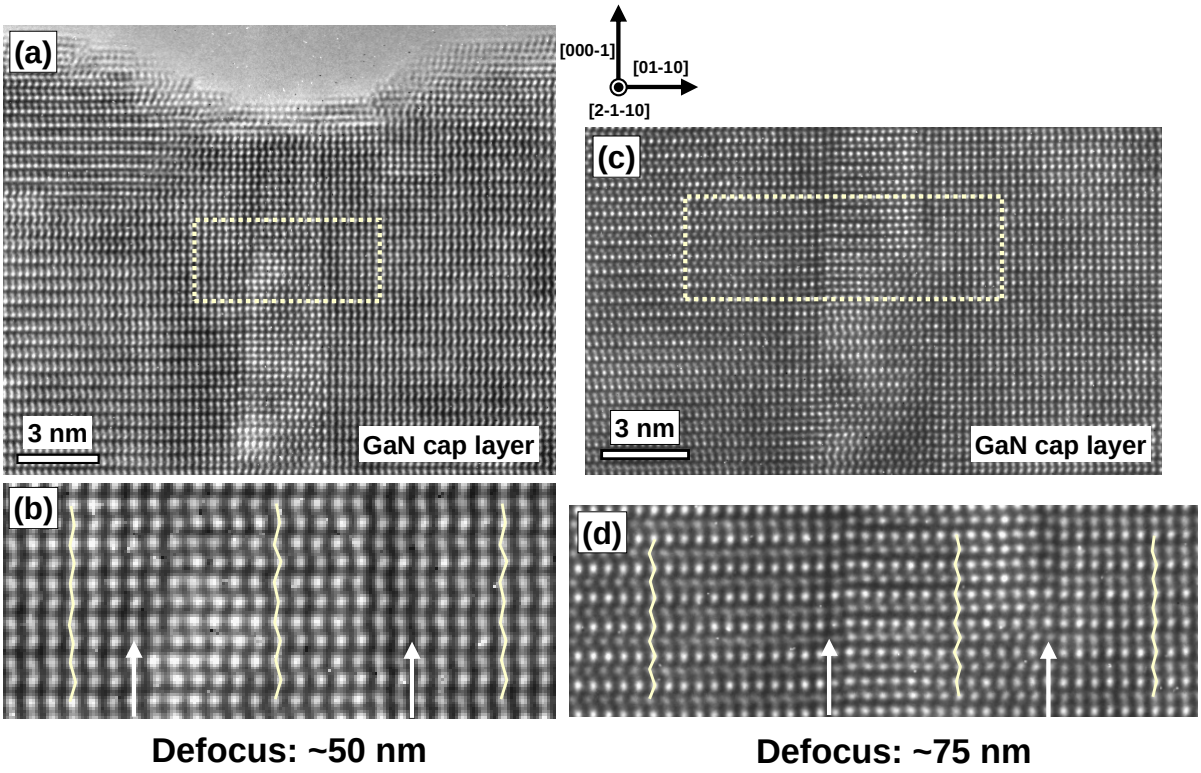

Figure 4.14 : *(a) HRTEM image depicting a narrow domain bounded by two planar defects. The defocus value was ∼50 nm, meaning that tunnels are projected onto white spots. (b) Outline area of (a). The stacking sequences outside and inside the domain are identical. (c) Same area as in (a) but for defocus value of 75 nm. Atomic columns are projected onto white spots. (d) Outline area of (b). The senses in the stacking sequences appear opposite inside and outside the domain. Arrows indicate the plane of the defects.*

a basal component equal to 1/3<10-10> while the basal component of the Drum model is equal to 1/2 <1010>, i.e. a 1/6<10-10> shift converts the Amelinckx model to the Drum model.

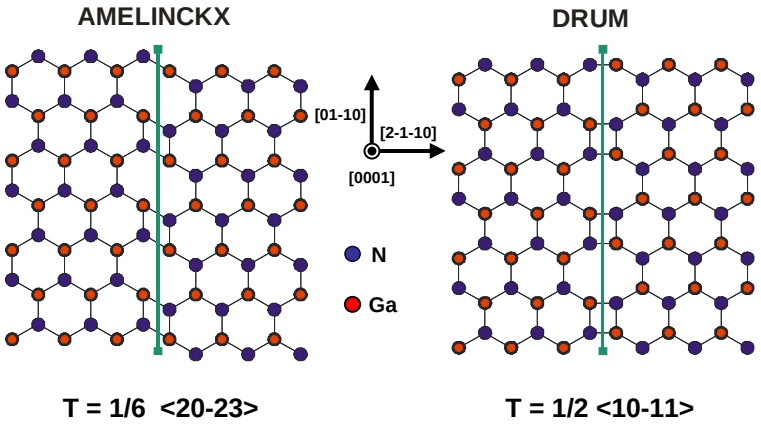

Figure 4.15 : *Schematic illustration of the two {1-210} prismatic TDBs observed in wurtzite GaN structures. (a) The Amelinckx model and (b) The Drum model.*

Image simulations of the TDBs along the <2-1-10> direction (TDBs inclined) have been carried out by P. Vermaut *et al.* [28]. It is clear that, due to the 1/2 <0001> component, the stacking sequence at any defocus values, before and after the projected defect area must be opposite [28]. It is obvious that this is not our case, since in our experimental images, independently of the defocus, the stacking sequence remains unchanged before and after the narrow domain which was bounded by the two planar defects (see Figures 4.14 (c)-(d)).

Table 4.1 summarize the previous observations and gives the relative displacements of the different types of planar defects.

	TDBs		IDBs	
Model	Amelinckx [26]	Drum [27]	IDB* [29–31]	Holt [32]
Relative displacement	1/2 **c**	1/2 **c**	1/8 **c**	-3/8 **c**
Stacking sequence before and after the narrow domain	opposite	opposite	same	same

Table 4.1 : *Relative displacements of the different type of planar defects. The stacking sequence before and after the narrow domain is independent of the defocus value.*

To be sure about the character of the observed planar defect (IDBs or TDBs) the GPA was applied on images where only the (0002) planes are visible. *Why these kinds of images?* We know, that both TDBs and IDBs have a translation along the [0001] axis. In the TDBs the translation is equal to 1/2<0001> (c/2). As a result, in a phase image which is produced by a HRTEM image where only the (0002) planes are visible, this translation can not be visualized. On the contrary, the translation of an IDB^* is equal to 1/8<0001> (or c/8) and in a Holt model is equal to -3c/8. Consequently, in a phase image, independently of the model of IDB, a translation of c/8 would be visible.

To obtain these off-axis images, I kept the viewing direction in the plane of the interfaces and tilt the sample ($\sim 19°$) away the [2,-1,-1,0] zone axis. The resulting viewing direction was close to the [5,-1,-4,0] secondary zone axis. In images taken under these conditions only the (0002) planes are visible (see section 3.5). Figure 4.16 (a) is one of them and illustrates exactly the same area with the images in Figure 4.14. The outline region of the image was extracted and treated with the GPA. The resulting geometric phase image is shown in Figure 4.16 (b). The projected phase profile is superimposed in the image. From the phase image (and the profile) we have measured a ΔP equal to ~ -1.5343. The relation between ΔP and the displacement field u is given by equation:

$$\Delta P = -2\pi \mathbf{g} u \tag{4.5}$$

In our case the phase image was procuded by selecting the 0002 reflection in the reciprocal lattice. If now in equation 4.5 we replace ΔP with the measured value and $\mathbf{g}_{0002} = 1/d_{0002} = 1/(\mathbf{c}/2) = 2/\mathbf{c}$, we find that the displacement is equal to:

$$u = 0.1221\mathbf{c} \simeq c/8$$

Therefore, we can be now **sure that the planar defects** in Figure 4.14 **are IDBs**.

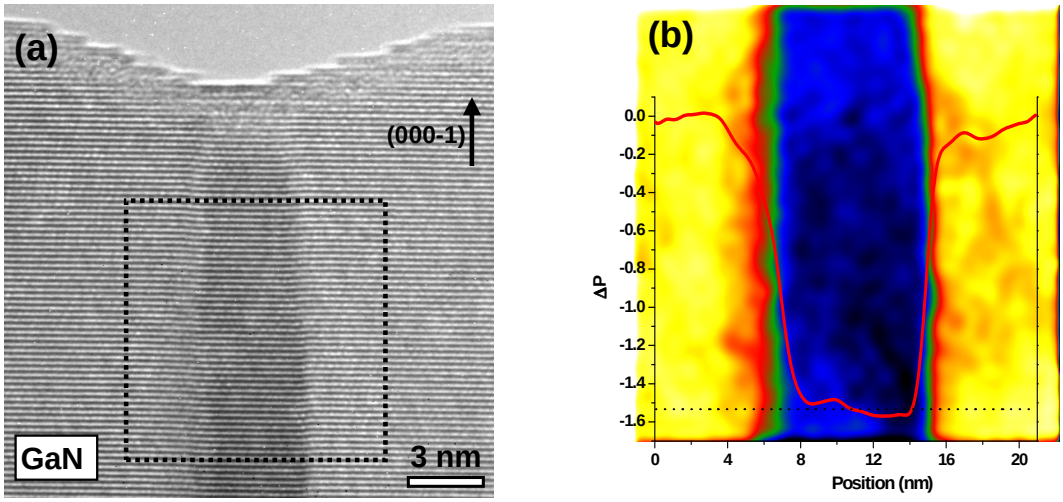

Figure 4.16 : *(a) HRTEM image viewed along the [5,-1,-4,0] zone axis of the same area as in Figure 4.14. Only the (0002) planes are visible. (b) Geometric phase image resulting from the outline area iin (a). The phase profile is superimposed on the image.*

In order now to find the exact structure of these IDBs we have firstly created supercells in the [2,-1,-1,0] projection, and used the JEMS software to construct series of simulated images of all the created IDB structural models. It exists two basic types of IDBs. In the so called IDB* type (Figure 4.17 (a)), apart from an inversion of the atomic species across the boundary, there is an additional translation of c/8 along the c axis. This type of domains are electrically inert and energetically favorable [23, 29–31, 33]. The other basic type of $\{01\bar{1}0\}$ IDBs is the so called Holt type [32] (Figure 4.17 (b)). Holt type IDBs contain Ga-Ga and N-N bonds, are electrically active and have a formation energy higher than the one of IDB* type [29].

For each IDB model, we can distinguish two types depending on whether the IDB plane cuts single bonds (type 1) or double bonds (type 2) [22] or equivalently whether the IDB plane cuts the bonds which are in the (2,-1,-1,0) plane perpendicular to the interface or the bonds which are out of the (2,-1,-1,0) plane. In 4.17 a schematic illustration along the [2,-1,-1,0] projection of the two models of IDBs of type 1 is given together with the corresponding simulated images for two values of defocus, 50 nm and 75 nm, and for

thickness equal to 1.9 nm. By examining the stacking sequencing in the simulated images we notice that for the Holt model of IDB the stacking sequences on either side of the IDB plane are identical when the defocus is 50 nm and opposite for 75 nm of defocus. This is in agreement with what we have observed previously in our experimental images (see Figures 4.14). Thus, based on this observation we can conclude that the $\{01\bar{1}0\}$ IDBs of our sample correspond to the Holt model.

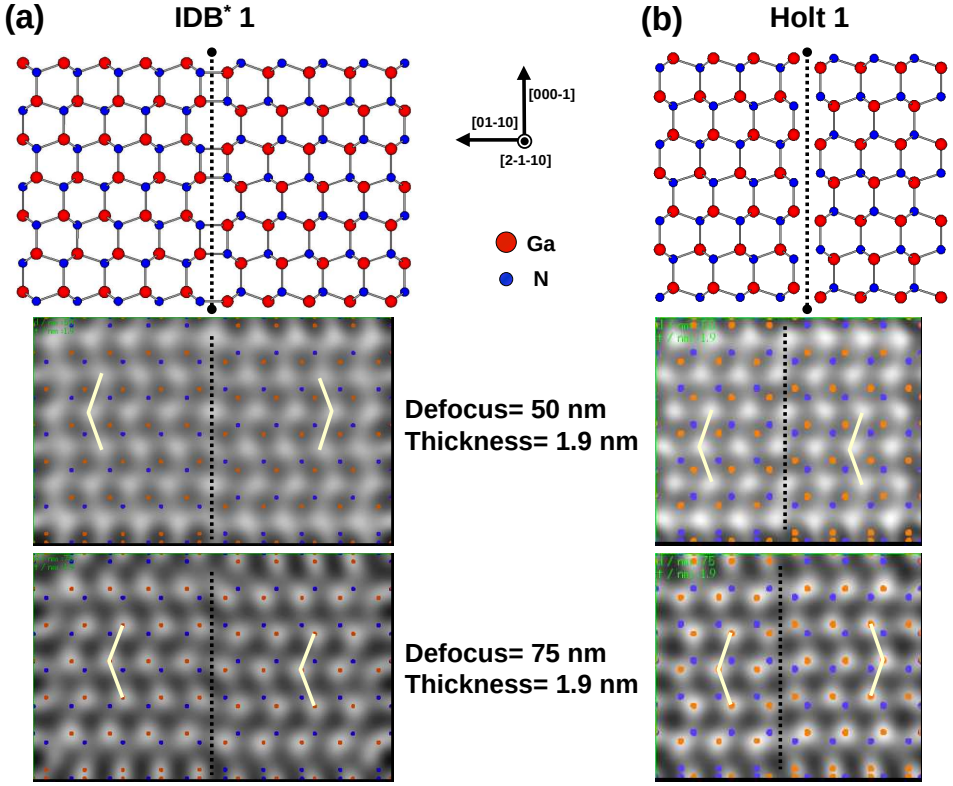

Figure 4.17 : *Schematic illustration and the corresponding simulated images for two defocus values of (a) a* $\{01\bar{1}0\}IDB^*$ *type planar defect and (b) a* $\{01\bar{1}0\}$ *Holt type IDB. The dotted lines indicate the IDB plane. Stacking sequences on either side of the boundary are also indicated. The atomic positions are superimposed on the simulated images.*

Further simulations were realized in order to distinguish which type of Holt IDB correspond to the boundaries shown in Figure 4.14. In particular, in Figure 4.18 (a) a bigger area of the HRTEM image in Figure 4.14 (b) is shown. For the particular imaging conditions (defocus=75 nm), atomic columns in the structure are projected onto white spots. In particular, Ga atoms (orange) are at the center of the white dots while N atoms (blue) are at the edge of the dots. The outline area of Figure 4.18 (a) with the corresponding simulated images is illustrated in Figure 4.18 (b). The position of the IDB planes is indicated by arrows. It can be seen, that the left IDB plane is put onto black tunnels while the right one is put onto white spots. This evidences that the type

of the IDBs is different. Taking into account the defocus value for which this image was taken together with image simulations of the different Holt type IDBs, we found that the left side IDB is a Holt of type 1 (Holt1) while the right side is a Holt 2. A schematic illustration along the [2,-1,-1,0] projection of these two types of Holt IDBs is shown in Figure 4.18 (b).

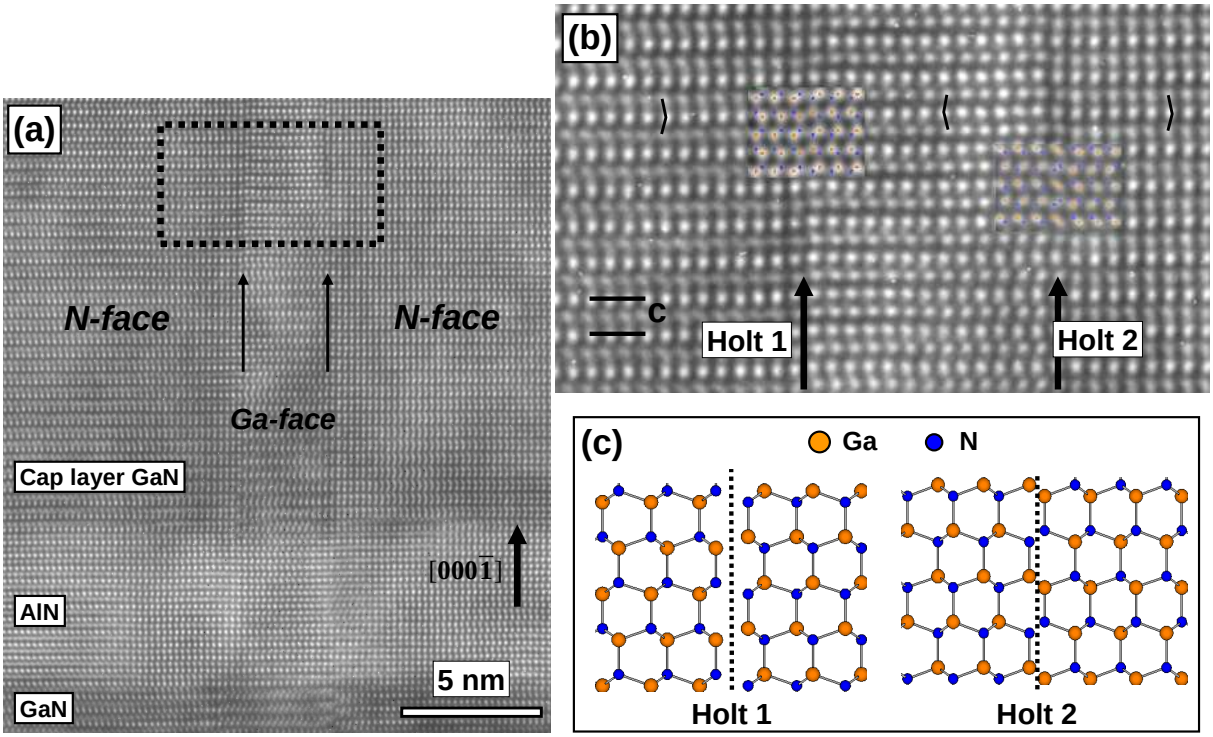

Figure 4.18 : *(a) HRTEM image viewed along the [2,-1,-1,0] zone axis (same as in Figure 4.14 (b)) of the top area of the N-face superlattice (thickness=1.9nm, defocus=75nm). Atomic columns are situated onto white spots. A narrow inversion domain bounded by two IDBs is shown. (b) The outlined region of (a) with the corresponding simulated images. The stacking sequences on either side of the IDBs are shown and appear to have opposite sense, indicating that both IDBs are Holt type. The one in the left side is a Holt 1 type, since the IDB plane is traced onto black tunnels while the one in the right side is of Holt 2 type. (c) Schematic illustrations of the two types of a Holt IDB.*

Quantitative analysis

We have started the quantitative analysis of N-face SL by measuring the lattice parameter **c** of the GaN layers from different interplanar distances profiles and geometrical phase images. We have used the same values for the parameters n_p and mask type and size as for the Ga-face ($n_p = 2$, mask type= gaussian and mask size= $\sim \mathbf{g}/6\,\mathrm{nm}^{-1}$). Again, prior to the analysis of the HRTEM images, the experimental imaging conditions were

first determined by calculating the map of through defocus-thickness simulated images of a completely strain GaN QW embedded in a AlN matrix. Only on-axis HRTEM images viewed along the [0,1,-1,0] direction, with defocus value close to the Scherzer were used to extract the desirable quantitative information. One of them is illustrated in Figure 4.19.

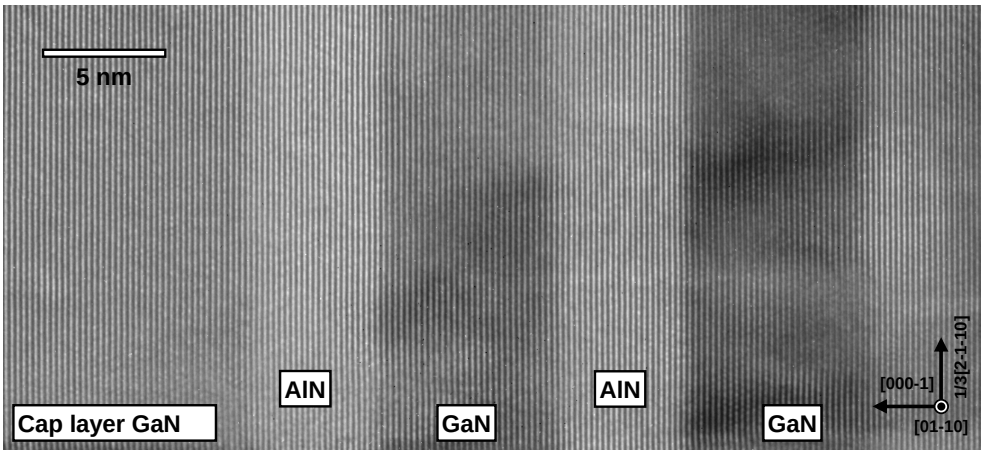

Figure 4.19 : *Cross-section HRTEM image viewed with the [0,1,-1,0] zone axis, depicting the last two GaN QWs of the N-face polarity superlattice.*

In particular, we have analyzed 12 different areas of 7 GaN QWs. No significant difference was measured concerning the lattice parameter $\mathbf{c/2}$ between the AlN buffer layer ($12.6359 \pm 0.003\ pixels$) and the AlN matrix in the SL ($12.6402 \pm 0.013\ pixels$). As a result, we have taken as $\mathbf{c/2_{AlN} = 12.6389 \pm 0.011\ pixels}$ (average of the previous two values). For the GaN QWs we measured $\mathbf{c/2_{GaN} = 13.332 \pm 0.086\ pixels}$. A frequency count of the measured values of $\mathbf{c/2}$ of the GaN QWs is shown in Figure 4.20. Applying the Spapiro-Wilk normality test [34], we found that our values of $\mathbf{c/2}$ (AlN and GaN) follow a normal distribution for a significance level of 95%.

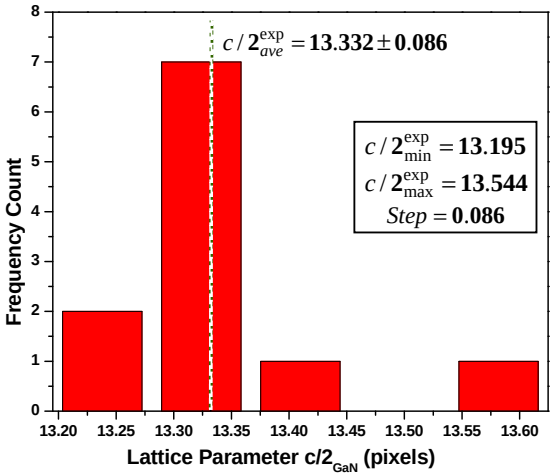

Figure 4.20 : *Frequency count of the lattice parameter $\mathbf{c/2}_{GaN}$ measured from on-axis HRTEM by a projection and the GPA.*

For these experimental **c/2** values, we measure a lattice mismatch $\Delta c/c = \frac{c_{GaN}-c_{AlN}}{c_{AlN}}$ of about **5.48%**. This value is bigger from what the theory of elasticity predicts for a the case of a completely strained GaN QW by a relaxed AlN matrix (**5.38%**). This result suggests that the GaN is completely strained by a AlN which is *not relaxed*. Having in mind that the thickness of the buffer layer is only 100 nm and that it was directly deposited on the SiC substrate, we can justify the fact that the AlN is not relaxed. This is in agreement with X-ray experiments realized on the same sample. In particular, from a map of the reciprocal space of the under study sample obtained on the (10.5) reflex, we have measured the lattice parameters **a** and **c** of the AlN buffer layer (Figure 4.21). We found that **a** is equal to 0.3092±0.0002 nm and **c** is 0.5001±0.0002 nm. Using the latest as reference (12.6389 pixels=0.5001 nm), we find a lattice parameter **c** of the GaN QWs equal to $\mathbf{c}_{\mathbf{GaN}}^{\mathbf{exp}} = \mathbf{0.5275 \pm 0.0034\ nm}$.

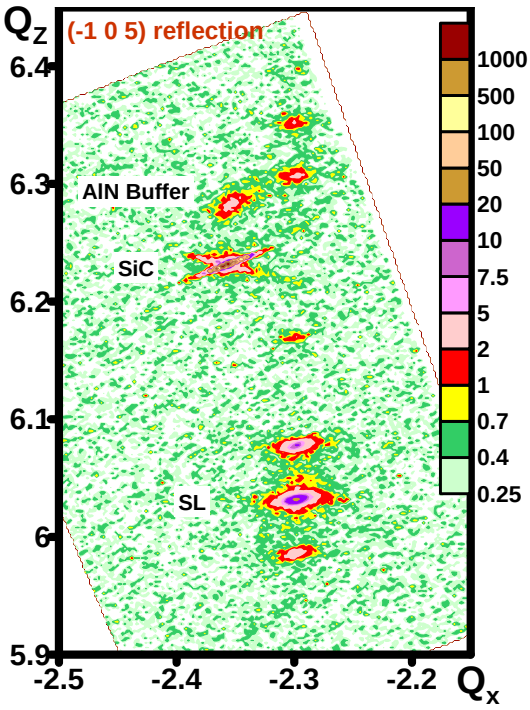

Figure 4.21 : *Reciprocal space map of the N-face sample.*

The **thickness** and the **interface width** of the examined GaN QWs were measured using the previous images. The modulus variation of the local reciprocal lattice vector $\mathbf{g}_{0002}$ of the HRTEM image of Figure 4.19 is given in Figure 4.22. We can see that along the QWs, the interfaces are not uniform but their width is varying between 2-3 ML. This is better seen in Figure 4.23 where extracted profiles are given. We notice that the ~ 0.5 nm difference between the two interfaces is due to roughness and not to interdiffusion. The roughness of the interfaces affect the thickness of the layers in the superlattice. In

particular, the thickness of the GaN and AlN QWs was found in average equal to:

$$\mathbf{t}_{GaN} = \mathbf{7.3 \pm 0.4\ nm}$$
$$\mathbf{t}_{AlN} = \mathbf{5.2 \pm 0.4\ nm}$$

which is a little bit higher than the nominal values of thickness, 7 and 5 nm respectively.

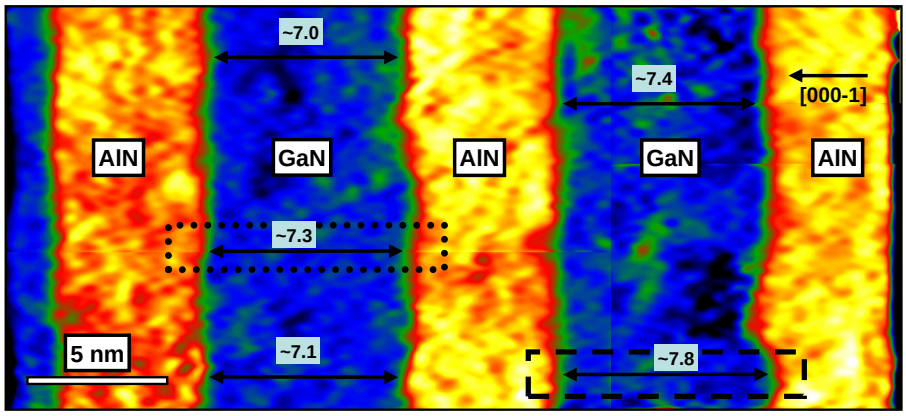

Figure 4.22 : *Resulting by the GPA image illustrating how the modulus of the reciprocal lattice vector* $\mathbf{g}_{0002}$ *is varying in the HRTEM image of Figure 4.19. It clearly demonstrates the interface roughness which results in a variation of the layer thickness.*

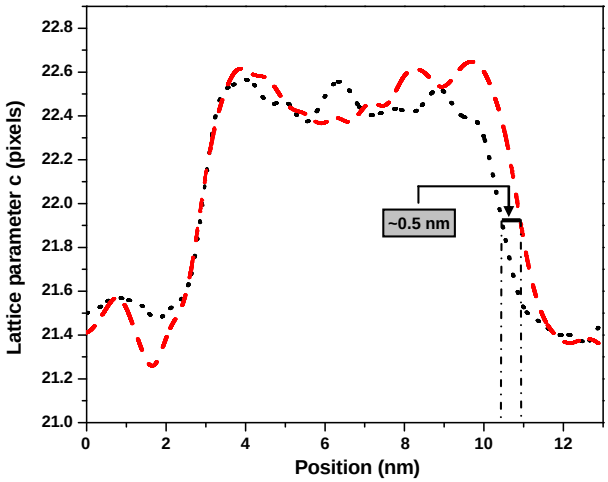

Figure 4.23 : *Profiles resulting from the outline dotted (dot black line) and the dashed (dash red line) regions in Figure 4.22. The interface roughness causes a difference of* $\sim$ *0.5 nm between the interfaces.*

4.1.4 Conclusions

In this section a comparison between a Ga-face GaN/AlN quantum well superlatttice and a N-face one has been presented. Experimental and simulated HRTEM images were quantitatively analyzed by both a projection method and the geometric phase analysis (GPA). The local lattice parameters, the thickness of the different layers and the strain state of the SLs were measured.

We found that the interfaces in the Ga-face SL are uniform along the different QWs and abrupt with a thickness that does not exceed 1 ML. On the contrary, interfaces in the N-face SL are rough and their width varies between 2-3 ML. Moreover, although nominally the period of the two SLs was equal, in the N-face sample, due to the interface roughness, the thickness of the different layers was found a little bit higher than the nominal values. $\{01\bar{1}0\}$ planar defects were only found in the N-face sample. They were identified to be inversion domain boundaries of Holt model. This model of IDBs is energetically unfavorable. In particular, both types (1 and 2) of the Holt model were identified in our images.

In the framework of the theory of elasticity, the lattice parameter **c** of a completely strained GaN QW inside a relaxed AlN matrix is equal to 0.525 nm. By combination of X-rays reciprocal maps and HRTEM image analysis, we measured the lattice parameters of the GaN QWs.

In the N-face SL the measured value for $\mathbf{c}_{GaN}$ was found equal to:

$$\mathbf{c}_{GaN}^{N-face} = \mathbf{0.5275} \pm 0.0034\,\mathrm{nm}$$

suggesting that the GaN QWs are almost *completely strained* on the AlN but *the AlN is itself strained by the SiC substrate i.e is not relaxed.*

In the Ga-face SL, we found that:

$$\mathbf{c}_{GaN}^{Ga-face} = \mathbf{0.5237} \pm 0.002\,nm$$

By eliminating the possibilities of: (i) an GaN/AlN interdiffusion (thanks to EFTEM experiments), (ii) a partially strained AlN matrix (thanks to X-rays measurements) and (iii) a relaxation due to the thin foil effect, we concluded that in the Ga-face SL the GaN QWs are only *partially strained*. Dislocations have to be introduced every 200 planes. Unfortunately we did not succeed to observe these interfacial dislocations.

4.2 Effect of AlN overgrowth on the structural quality of GaN QWs

4.2.1 Introduction

The use of nanostructures, quantum wells and quantum dots, in electronic and opto-electronic devices requires a good knowledge of their formation during the heteroepitaxial growth and also a precise control of their size and the quality of the interfaces.

The overgrowth process, which follows the deposition of the nanostructures, is known to have an important impact on their structural and optical properties. Although many studies have demonstrated the effect of the cap layer mostly on QD systems such as InAs/Ga(In)As [35–37] or Si/Ge [38–41], the influence of AlN overgrowth on the structural properties of GaN nanostructures was not addressed so far. Our work was hence the first report on the effects of the capping process on GaN heterostructures (QDs and QWs) [42].

In this section we investigate the evolution of GaN quantum wells during the AlN overgrowth process and analyze the change in their dimensions as a function of the amount of GaN nominally deposited and the capping temperature. Using TEM, Rutherford backscattering spectroscopy and RHEED measurements we demonstrate that the overgrowth process implies a thinning of the GaN QW. We prove that the diminution of the amount of GaN contained into the QWs affects only the top GaN/AlN interface. The phenomenon is attributed to a thermally activated exchange mechanism between Al from the capping layer and Ga atoms from nanostructures.

4.2.2 Experimental growth conditions

All samples used to study the effects of AlN overgrowth on the structural properties of GaN quantum wells were grown by PAMBE on AlN templates. The templates consisted of a 1 μm thick AlN layer, grown on c-sapphire by metal-organic chemical vapor deposition (MOCVD). To avoid any possible surface contamination, prior to GaN deposition, an AlN buffer layer was grown on the pseudo-substrates at a substrate temperature of 750°C. For all the samples presented in this study, the GaN QWs were grown at a fixed substrate temperature of 750°C, and the AlN capping layers were deposited in the range of substrate temperatures between 700°C and 750°C. The typical PAMBE growth temperature of GaN/AlN heterostructures is comprised between 720°C and 750°C. All samples presented metal-face polarity.

GaN was always grown under Ga-rich conditions, with a Ga-flux high enough to form a continuous Ga adlayer of about 2ML thick on the growing surface. Thereby, the GaN layers followed the two-dimensional (2D) Frank-Van der Merwe growth mode and plastic relaxation occurred with the formation of misfit dislocations [5, 14, 43]. The GaN QWs

were covered with an AlN layer grown under Al-rich conditions by switching from Ga to Al flux while the N flux remained constant. Under these conditions, the Ga excess forming the adlayer during the growth of the GaN well, segregates on the AlN surface and desorbs rapidly during the AlN growth. The thickness of the AlN layer varied between 50 to 100 nm.

One key point in the investigation of the capping effects is the precise calibration of the amount of GaN nominally deposited. Thus, in order to have good estimation of the amount of GaN contained into the QW before the capping process, an uncapped GaN QW was systematically deposited on the surface and served as a reference.

4.2.3 RBS Measurements

The amount of GaN deposited on AlN, was evaluated by Rutherford backscattering spectroscopy (RBS) using a 2MeV $^4He^+$ ion beam. The detection angle was 165° and the detector resolution was 16 keV. To avoid channelling effects, which could influence the thickness/size reduction measurements, the samples were tilted about 7° off the sample normal in two perpendicular directions. The absolute uncertainty in the thickness was estimated to be 1.2 Å. It is important to mention that the RBS technique does not measure directly the thickness of a GaN layer, but the amount of Ga which is contained in it. As a result, the thickness/size reduction measurements were realized by comparing the amount of Ga contained in the different GaN QWs which were capped by an AlN layer with the amount of Ga of the corresponding uncapped GaN QWs situated at the surface. To prevent an overestimation of the Ga in the well on the surface, it was necessary to anneal it under vacuum in order to desorb the Ga excess of 2 ML. In particular, we have considered that the Ga bilayer was totally desorbed when the 2D layer starts to roughen, just before the 2D/3D transition. Then, the temperature was abruptly decreased to preserve the morphology of the layer.

Figure 4.24 illustrates a measured (open circles) and a fitted (solid line) RBS spectrum of a GaN/AlN sample grown at 750°C. It consisted of two identical GaN QWs with nominal thickness equal to 20 Å, one capped inside the AlN matrix (QW_{capped}) and the other one was situated at the surface (QW_{surf}). We can see that the thickness of the uncapped GaN QW was found around 19.6 Å, a value which is very close to the nominal amount of GaN deposited before the capping (20 Å). On the contrary, the thickness of the capped GaN QW was measured equal to 16.7 Å, significantly thinner compared to the nominal thickness. This result, testifies that the AlN overgrowth results in a thinning of the underneath GaN QW.

The reduction of the GaN well thickness caused by the overgrowth process was further investigated as a function of the nominal QW thickness (noted as Θ) for a range between 4.5 to 60 Å. Each sample used for this study comprised two GaN QWs, one embedded into

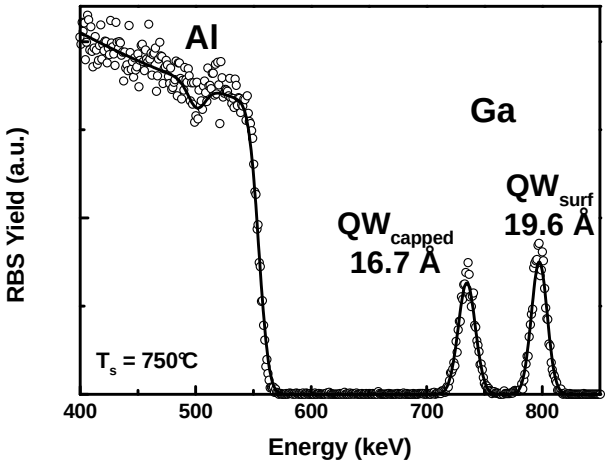

Figure 4.24 : *Measured (open circles) and fitted (solid line) RBS spectrum of a sample containing two identical GaN QWs with nominal thickness of 20 Å. The thickness of the QW on the surface and that which was capped into the AlN matrix was found equal to 19.6 and 16.7 Åsrespectively. The surface channels are marked by the corresponding elements.*

the AlN and one on the surface. The substrate temperature of all samples was equal to 750°C for both GaN and AlN. Specifically, by comparing the thickness of the capped wells with the ones on the surface measured by RBS, we could calculate the well thinning, which is plotted in Figure 4.25 as a function of Θ. We can observe a progressive enhancement of the thinning of the capped GaN well, followed by saturation for nominal thickness Θ bigger than 30 Å. This behavior suggests that the QW thickness has a significant effect on the reduction of the amount of GaN contained into the well during the capping process.

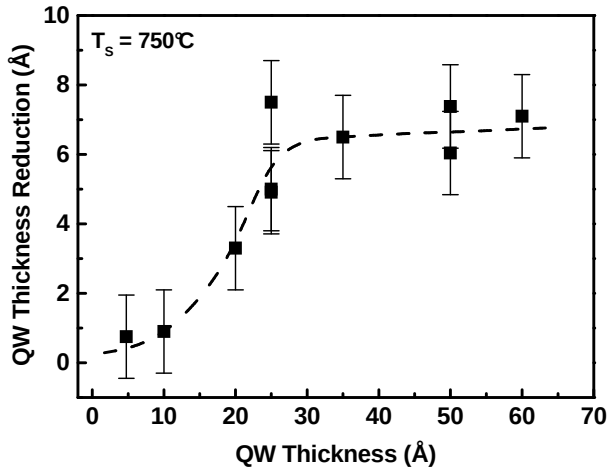

Figure 4.25 : *Variation of the thickness reduction of GaN QWs embedded into an AlN matrix as a function of the nominal QW thickness Θ.*

Next, the influence of the AlN overgrowth layer on the thickness of GaN QWs was studied as a function of the capping temperature. Figure 4.26 presents the variation of the well thinning as a function of the capping temperature. In particular, all GaN QWs used in this study were grown at 750°C and had a nominal thickness of 50 Å. The temperature of the AlN capping layer varied in the range from 700 to 750 °C. We can observe that the thickness reduction becomes more important when the capping temperature is increased.

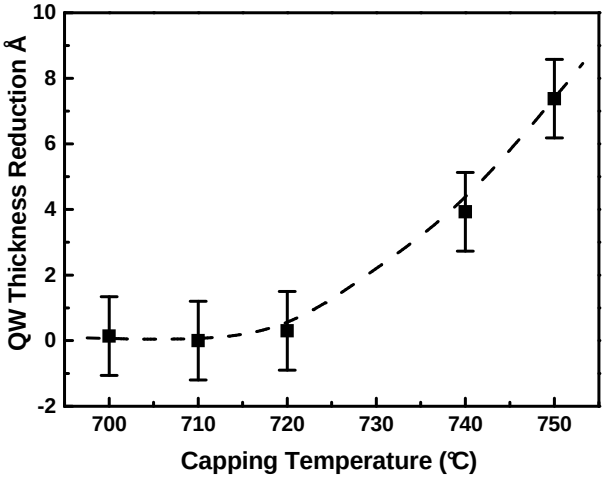

Figure 4.26 : *Variatioin of the thickness reduction of a nominally 50 ÅGaN QW embedded in AlN as a function of the capping temperature. The substrate temperature T_S was fixed at 750° C for the growth of the wells.*

4.2.4 TEM Measurements

Sample Structure

The RBS measurements reported in the previous section, demonstrate that the capping process significantly changes the GaN QW dimensions. The GaN QW thickness is reduced during the overgrowth process and in particular, this thickness reduction is more important when the nominal thickness Θ of the well increases (see Figure 4.25) and when the capping temperature is higher (see Figure 4.26). However, the RBS technique measures average values and cannot provide any pieces of local information about the structural properties of the GaN QWs and where this thickness reduction is occurred.

TEM techniques, like high-resolution TEM, are the most adapted to provide this kind of information. For this purpose, we have investigated a sample[7] which consisted of two identical GaN QWs and two series of quantum dots (QDs) grown at 750°C and embedded into an AlN grown at 750°C for the first QW and QDs (QW1 and QDs1) and 700°C for the second one (QW2 and QDs2). The nominal thickness of the two QWs was equal to 20 Å. Figure 4.27 is a two-beam image of the examined sample, depicting a general view of the sample structure. From the contrast of the image we can detect that although the second GaN QW (QW2) is quite uniform with a constant thickness, the first QW which is capped with an AlN layer grown at 750°C appears to be slightly thinner and less uniform. However, conventional TEM images are not the most adapted images to measure accurately the thickness of thin layers and/or to examine the quality of an interface. In our case, we have used HRTEM and EFTEM images to evaluate the exact thickness and characterize the interfaces of the QWs. The results are presented in the following

[7]Sample name S1608. It is important to note that 2 other samples (S1569 and S1393) with structures similar to that of S1608 were examined. Since the obtained results were in agreement with each other, we will only present the results coming from sample S1608.

paragraphs.

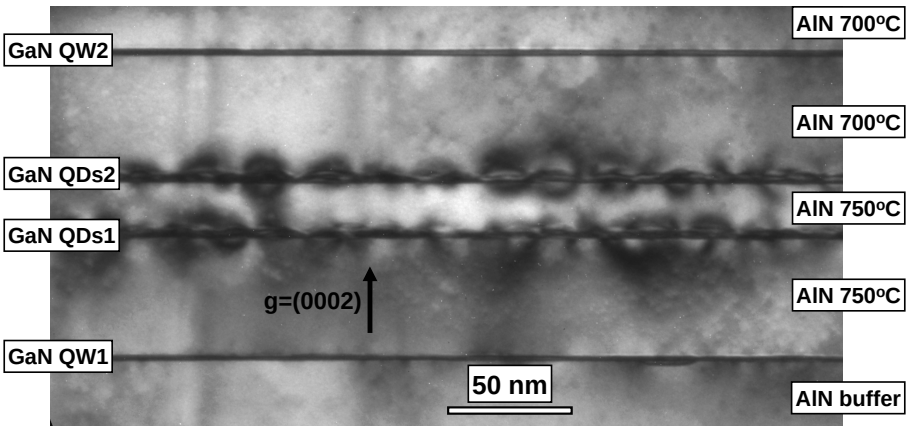

Figure 4.27 : *Conventional two-beam image (**g**=(0002)) illustrating the structure of the examined sample. QW1 which is embedded into an AlN grown at 750°C appears to be thinner and less uniform compared to QW2.*

Size and Interface quality

The exact size of the QWs and the quality of the interfaces were examined by analyzing quantitatively HRTEM images. Once more, both a projection method and the GPA were applied. In particular, for the first GaN QW (QW1) which was embedded into an AlN matrix grown at 750°C, 18 areas coming from 7 different images were analyzed. We found that in average the thickness of this QW was equal to:

$$\mathbf{t}_{QW1}^{ave} = \mathbf{14.9 \pm 1.5}\ \text{Å}$$

Thus, the thickness of the QW is reduced with respect to the nominal value (20 Å). Figure 4.28 (a) gives a frequency count of the measured thickness values for QW1. We can see that the thickness of the well varies significantly and does not follow a normal distribution around the average value.

On the contrary, for the second GaN QW (QW2) which was capped by an AlN grown at 700°C, the average value was measured equal to:

$$\mathbf{t}_{QW2}^{ave} = \mathbf{20.1 \pm 1.5}\ \text{Å}$$

which is in very good agreement with the nominal value of thickness (20 Å). The results were obtained from the analysis of 11 different areas coming from 7 HRTEM images. The histogram of these measurements is shown in Figure 4.28 (b). The thickness values follow a normal distribution based on the Spapiro-Wilk normality test [34] for a significance level of 95%.

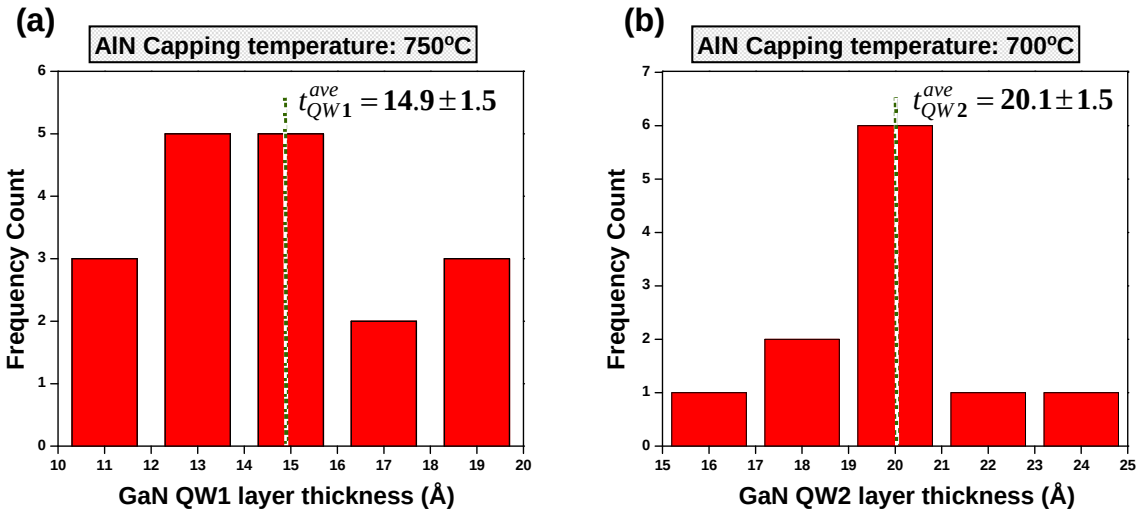

Figure 4.28 : *Frequency count of the thickness of: (a) the GaN QW1 which was capped with an AlN grown at 750° C and (b) the GaN QW2 which was embedded in an AlN matrix grown at 700° C. The average values of each QW are given.*

These results demonstrate that the structural properties of the GaN well, at low capping temperature, remain unchanged. They are in agreement with the measurements realized by RBS (Figure 4.26). Therefore, this is a confirmation that the reduction of the well thickness is ***thermally activated***.

The question that one may wonder is where this thickness thinning is taking place. In particular, if the reduction of the GaN QW occurs at the AlN buffer layer/GaN QW interface (noted as AlN/GaN interface) or on the contrary at the GaN QW/AlN capping layer interface (noted as GaN/AlN interface). HRTEM images gave the answer to this question. Figure 4.29 presents cross-section HRTEM images viewed along the [0,1,-1,0] zone axis of the two GaN QWs. The corresponding images of the variation of the modulus of the reciprocal lattice vector $\mathbf{g}_{0002}$ are also given. We can observe that concerning QW1 (Figure 4.29 (a)), the AlN/GaN interface appears relatively uniform with an interdiffusion in the order of one to two atomic layer. By contrast, the GaN/AlN interface appears more irregular and diffuse. For the QW2 (Figure 4.29 (b)), we see that the thickness of the well remains constant and equal to the nominal value, while the asymmetry of the two interfaces is still present but less intense compared to the case of QW1. Similar asymmetry in the GaN/AlN interface has been reported by I. Waki *et al.* [44] and by K.A. Mkhoyan *et al.* [45].

From these observations we can conclude that the thinning of the embedded QW is ***irregular and occurs at the top GaN/AlN interface during the AlN overgrowth***.

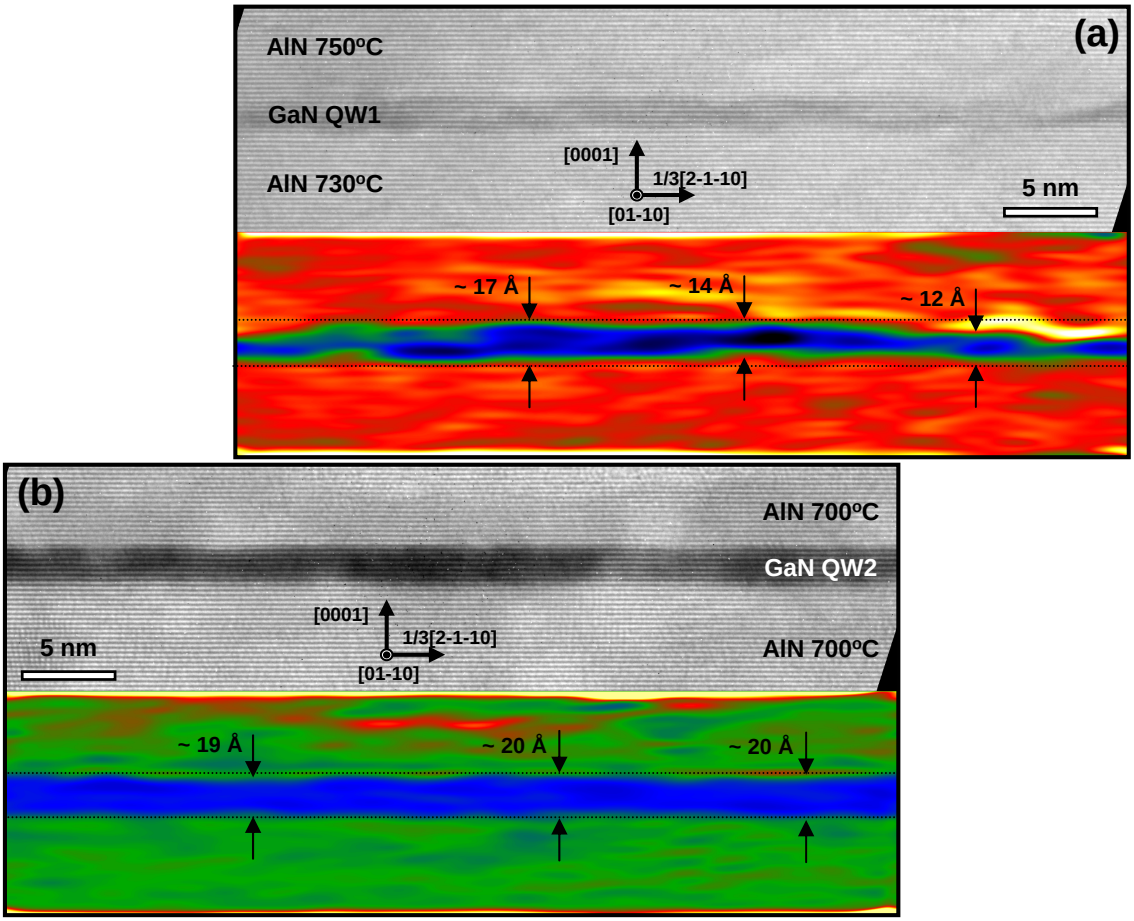

Figure 4.29 : *High resolution TEM images of embedded GaN quantum well inside an AlN matrix grown at (a) 750°C and (b) 700°C and their corresponding images of the variation of the modulus of the reciprocal vector* $\mathbf{g}_{0002}$*. The thickness of the well capped by an AlN at 750°C (QW1) varies from 10 Åto 17 Å. On the contrary, the thickness of the well capped at 700°C (QW2) remains constant and equal to the nominal value of 20 Å. The AlN/GaN interface appears relatively more regular and uniform than the GaN/AlN interface.*

The irregularity of the GaN QWs is also related to the presence of an important number of dislocations. In order to evaluate the number of dislocations which are present, weak beam images were realized. Figure 4.30 illustrates two weak beam images of the same area of the sample but acquired for different **g** vectors. By the combination of these two images, we can distinguish the three kinds of perfect dislocations contained in the wurtzite structure (see 2.2.2). In particular, in Figure 4.30 (a) only dislocations having a [0001] component in their Burgers vector are in contrast (**c**- and **a**+**c**-type). By contrast, in Figure 4.30 (b) only the **a**-type dislocations with Burgers vector **b**$= 1/3 < 11\bar{2}0$ and again the **a**+**c**-type are in contrast. We can detect, that not all the dislocations contained in the AlN template are continuing in the buffer layer. Furthermore, we see that some of

the **a**-type dislocations stop at the second series of QDs and does not continue in the AlN matrix grown at 700°C. The arrows in Figure 4.30 (b) indicate their position.

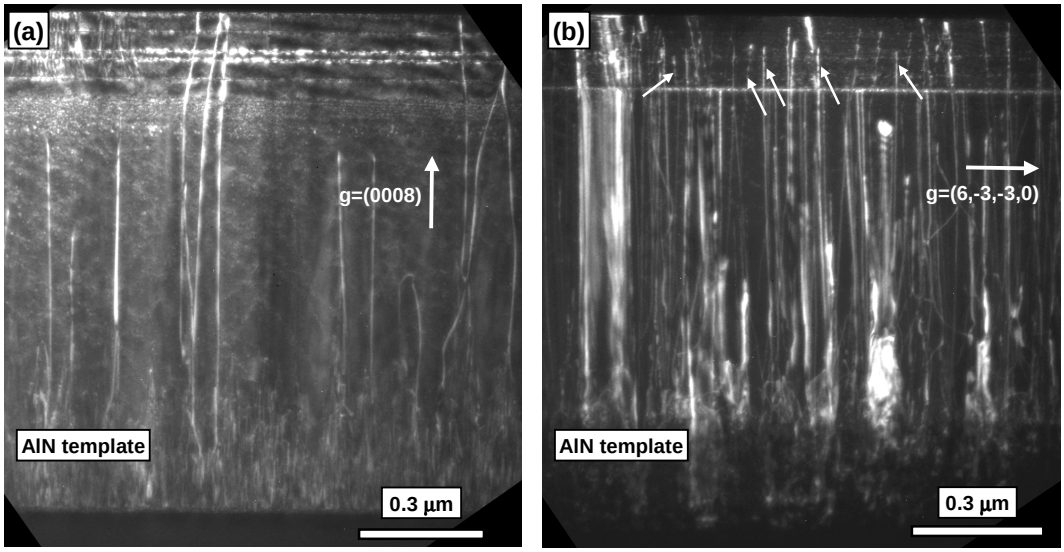

Figure 4.30 : *Weak beam images observed along the [0,1,-1,0] direction of the examined sample. (a) Conditions (g,4g) with* $\mathbf{g}$*=(0002). Only screw (***c***-type) and mixed (***a***+***c***-type) dislocations are in contrast. (b) Conditions (g,3g) with* $\mathbf{g}$*=(2,-1,-1,0). Only edge (***a***-type) and mixed dislocations are in contrast. The arrows indicate the position of some edge dislocations which doesn't continue to the AlN matrix which was grown at 700° C.*

The dislocation density at $0.6\mu m$ away the c-sapphire was measured equal to $\sim 3 \times 10^{10}$ dislocations/cm^2 with 85% of which having an edge character (**a**-type). At the AlN buffer layer, the dislocation density was found equal to 1.5×10^{10} dislocations/cm^2 and finally, at 70 nm from the surface was equal to 9×10^9 dislocations/cm^2.

4.2.5 Origin of thickness reduction

We have demonstrated previously that capping a GaN QW with an AlN layer grown at high temperature induces a reduction in the thickness of the GaN QW. This thickness reduction is thermally activated and take place at the upper GaN/AlN interface. From all these observations, we can conclude that the thinning of the overgrowth well results from a decomposition of the GaN. However, what is the origin of this decomposition? Different possibilities can be identified:

1. a GaN thermal decomposition,

2. a diffusion of the Al atoms from the cap layer into the GaN well,

3. an exchange mechanism between the Ga atoms from the nanostructure and the Al atoms from the cap layer.

Firstly, in order to verify the validity of the *first hypothesis*, the decomposition rate of a GaN layer grown at 750°C was studied. The GaN layer was grown on an AlN layer under Ga-rich conditions and was let evolving under vacuum. In order to avoid the re-arrangement of the GaN QW into quantum dots during the annealing under vacuum, the GaN layer was grown on a thin (∼20 nm) AlN layer deposited on a GaN template. Thus, the AlN was partially strained on the GaN substrate and the lattice mismatch between the AlN buffer and the GaN top layer was small enough to prevent a 2D/3D transition under vacuum, which is characteristic of the modified Stranski-Krastanov growth mode [46]. It has been found that the thermal decomposition of GaN occurs by the formation of $\{1\bar{1}03\}$ facets, characterized by a spotty RHEED pattern with additional lines as it can be seen in Figure 4.31 (a). When the GaN is totally decomposed, the RHEED pattern becomes streaky again, as corresponding to a two-dimensional AlN layer (Figure 4.31 (b)).

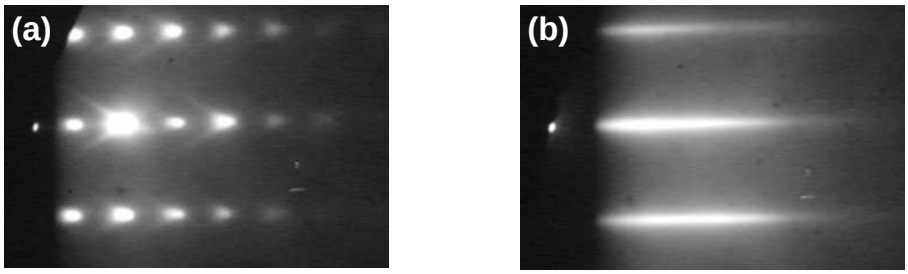

Figure 4.31 : *Reflection high-energy electron diffraction (RHEED) pattern of a GaN quantum well grown on AlN during (a) the thermal decomposition process at 750°C and (b) the surface of AlN after the total decomposition of the GaN QW.*

The decomposition time of GaN at 750°C as a function of the nominal amount of GaN deposited was measured using the variation of the RHEED specular intensity of the Bragg spot. The results are shown in Figure 4.32. We see that the decomposition time of GaN is proportional to the thickness of the layer. Therefore, from the linear fit (dashed line in Figure 4.32) we deduced a decomposition rate of 0.28 Å/min. Taking into account this rate, the well thinning observed previously (see Figure 4.25), and the characteristic time to switch from Ga to Al cell (typically 1 second), the hypothesis that the thickness difference observed between the uncapped and the capped QW is due to GaN thermal decomposition can be discarded. In addition, we have observed that the GaN decomposition is hindered by the deposition of < 1 ML of Al. This effect demonstrates that the Al adatoms stabilize the GaN surface by blocking the GaN decomposition sites, likely step edges.

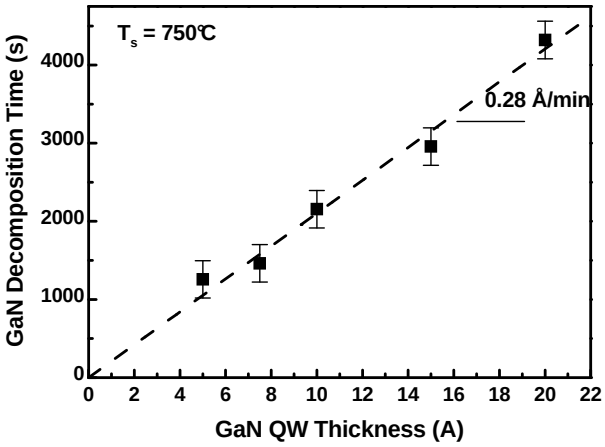

Figure 4.32 : *Variation of the GaN decomposition rate at 750°C as a function of the amount of GaN nominally deposited. From the linear fit (dashed line), we have estimated the decomposition rate to be around 0.28 Å/min.*

Regarding the *second hypothesis*, which considers that the thickness reduction of the capped QWs is due to a diffusion of the Al atoms of the cap layer into the nanostructure, we have examined the chemical composition of the GaN QWs by EFTEM experiments. Specifically, we have used the so-called "three-window" method to extract the desirable elemental maps. Figure 4.33 (a) illustrates a Ga elemental map of the GaN QW which was capped by an AlN grown at 750°C. The two pre-edge windows, used to extrapolate the background intensity, were centered at 1020 and 1080 eV. For the post-edge image of the Ga $L_{2,3}$-edge the window was centered at 1190 eV. The slit size was 10 eV. The cross correlation procedure was used to correct the drift between the recorded images. The thickness effects were also corrected by divided the Ga map by the t/λ map. We notice that the concentration in Ga is not homogenous along the GaN QW. A profile of the GaN QW extracted from the dotted area of the Ga map is shown in Figure 4.33 (b). It indicates that the gallium signal is only located inside the GaN QW. The asymmetry of the two interfaces can be also observed, with the GaN/AlN interface being less regular compared to the AlN/GaN one. The absence of any $Al_xGa_{1-x}N$ alloy in the GaN/AlN interface is in agreement with previous studies published on this subject [47].

This result indicates that the Ga excess formed on the surface of the GaN QW during the growth segregates on the surface of AlN and is evaporated due to the high temperature (750°C) during the overgrowth process.

For a further confirmation that AlN/GaN interdiffusion is not involved in the capping process, we have covered with Al three identical GaN QWs with nominal thickness of 50 Å and let them evolve for different times before capping them with AlN at 750°C. It is important to note that the Al flux was high enough to guarantee that the GaN surface was rapidly covered by several Al ML. Figure 4.34 presents the measured and fitted (solid line) RBS spectrum of the structure described before. The three GaN quantum wells

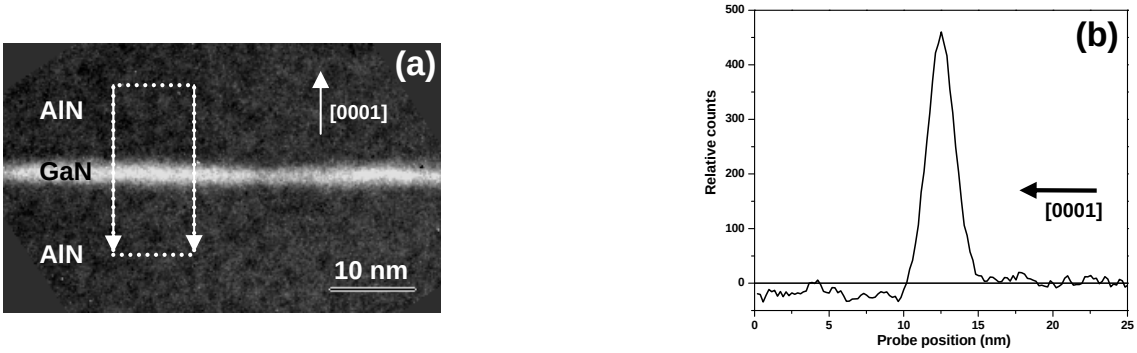

Figure 4.33 : *(a) Ga elemental map of the GaN QW embedded inside an AlN matrix grown at 750° C. (b) Extracted profile of the outline area in (a). The Ga signal drops to zero inside the AlN matrix.*

QW1, QW2 and QW3 were covered with Al for 1, 10 and 30 minutes respectively. If the QW thinning were due to a Al diffusion mechanism, we would expect that the QW thickness should depend on the Al cover time. However, from Figure 4.34 we can see that all the three GaN QWs embedded in AlN at 750°C present the same thickness. This result implies that the thinning of the GaN QWs does not result from the diffusion of Al atoms from the overgrowth layer into the GaN well. This conclusion is further supported by the relatively abrupt and flat AlN/GaN interface observed both in HRTEM (Figure 4.29) and EFTEM images (Figure 4.33).

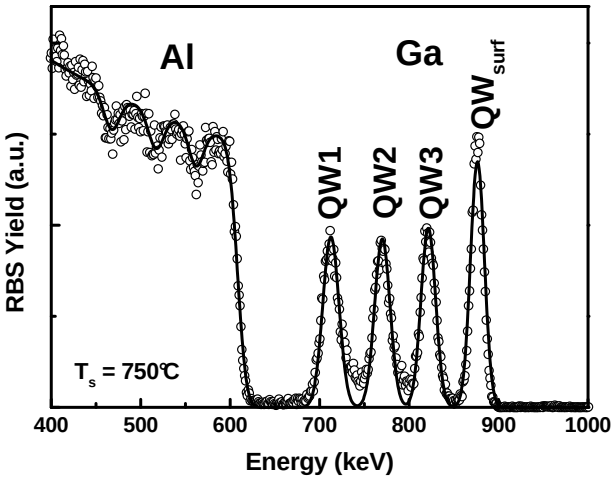

Figure 4.34 : *Measured and calculated (solid line) RBS spectrum of a sample containing three identical GaN QWs, nominally 50 Å thick, covered by an Al flux before capping. The Al flux was high enough to completely cover the GaN surface. QW1, QW2 and QW3 are respectively covered during 1, 10 and 30 minutes.*

All the experiments described above are consistent with the hypothesis of an exchange mechanism which takes place between the Al atoms from the cap layer and the Ga atoms from the GaN well. This process is thermally activated and it is favored by the high binding energy of AlN compared to GaN.

4.2.6 Conclusions

We have investigated in this part of the chapter the effect of AlN overgrowth on the structural properties of GaN quantum wells grown on AlN by PAMBE. We have seen that the growth of an AlN cap layer on a GaN QW at high temperature (750°C) leads to a remarkable change in the dimension of the nanostructures. In particular, the GaN QW thickness decreases during the AlN overgrowth. This result was obtained both from RBS and TEM measurements.

The possibility that the thickness thinning is due to a GaN thermal decomposition or to a diffusion of the Al atoms from the cap layer into the GaN well was excluded. As a result, we have assigned this thickness reduction to an exchange mechanism between the Al atoms from the cap layer and the Ga atoms from the nanostructure.

Thanks to TEM measurements, we have demonstrated that the Ga decomposition, resulting from the Al/Ga exchange mechanism, is irregular and affects the top GaN/AlN interface. No AlN/GaN intermixing has been observed. Finally, we have shown that the thinning of GaN QW is thermally activated.

Bibliography

[1] E. Monroy, E. Sarigiannidou, F. Fossard, N. Gogneau, E. Bellet-Amalric, J.-L. Rouviere, S. Monnoye, H. Mank, and B. Daudin. *Appl. Phys. Lett.*, 84(18):3684, 2004.

[2] F. Bernardini, V. Fiorentini, and D. Vanderbilt. *Phys. Rev. B*, 56(16):10024, 1997.

[3] E.S. Hellman. *MRS Internet J. Nitride Semicond. Res.*, 3:11, 1998.

[4] O. Ambacher, J. Smart, J. R. Shealy, N. G. Weimann, K.Chu, M. Murphy, R. Dimitrov, L. Wittmer, M. Stutzmann, W. Rieger, and J. Hilsenbeck. *J. Appl. Phys.*, 85:3222, 1999.

[5] C. Adelmann, J. Brault, G. Mula, B. Daudin, L. Lymperakis, and J. Neugebauer. *Phys. Rev. B*, 67:165419, 2003.

[6] J. Neugebauer, T. K. Zywietz, M. Scheffler, J. E. Northrup, H. Chen, and R. M. Feenstra. *Phys. Rev. Lett.*, 90:056101, 2003.

[7] A. R. Smith, R. M. Feenstra, D. W. Greve, J.Neugebauer, and J. E. Northrup. *Phys. Rev. Lett.*, 79:3934, 1997.

[8] B. Heying, R. Averbeck, L. F. Chen, E. Haus, H. Riechert, and J. S. Speck. *J. Appl. Phys.*, 88:1855, 2000.

[9] E. Iliopoulos and T.D. Moustakas. *Appl. Phys. Lett.*, 81:295, 2002.

[10] E. Monroy, B. Daudin, E. Bellet-Amalric, N. Gogneau, D. Jalabert, F. Enjalbert, J. Brault, J. Barjon, and Le Si Dang. *J. Appl. Phys.*, 93:1550, 2003.

[11] C. Stampfl and C. G. Van der Walle. *Phys. Rev. B*, 259:5521, 1999.

[12] E. Sarigiannidou, E. Monroy, P. Bayle-Guillemaud, N. Gogneau, B. Daudin, and J. L. Rouvière. *Superlattices Superlattices and Microsctructures to appear.*

[13] M.M.J. Treacy, J.M. Gibson, and A. Howie. *Phil. Mag. A*, 51:389, 1985.

[14] A. Bourret, C. Adelmann, B. Daudin, J.L. Rouviere, G. Feuillet, and G. Mula. *Phys. Rev. B*, 63:245307, 2001.

[15] T. Sasaki and T. Matsuoka. *J. Appl. Phys.*, 64:4531, 1988.

[16] J. Lu, L. Haworth, D. I. Westwood, and J. E. Macdonald. *Appl. Phys. Lett.*, 78:1080, 2001.

[17] Q. Guo and A. Yoshida. *Jpn. J. Appl. Phys.*, 33:2453, 1994.

[18] X. Xue, Q.K. Xue, S. Kuwano, K. Nakayama, and T. Sakurai. *Jpn. J. Appl. Phys.*, 40:4388, 2001.

[19] A. R. Smith, R. M. Feenstra, D. W. Greve, M.-S. Shin, M. Skowronski, J.Neugebauer, and J. E. Northrup. *Appl. Phys. Lett.*, 72:2114, 1998.

[20] R. M. Feenstra, J. E. Northrup, and J. Neugebauer. *MRS Internet J. Nitride Semicond. Res.*, 7:3, 2002.

[21] P. Stadelmann. *EMS Java version.* http://cimewww.epfl.ch/people/stadelmann/jemsWebSite/jems.html.

[22] V. Potin, G. Nouet, and P. Ruterana. *Philos. Mag. A*, 79:2899, 1999.

[23] Ph. Komninou, Th. Kehagias, J. Kioseoglou, E. Sarigiannidou, Th. Karakostas, G. Nouet, P. Ruterana, K. Amimer, S. Mikroulis, and A. Georgakilas. *Mat. Res. Soc. Symp. Proc.*, 639:G3.47.1, 2001.

[24] S. Kret, P. Ruterana, and G. Nouet. *J. Phys.: Condens. Matter*, 12:10249, 2000.

[25] G.P. Dimitrakopulos, Th. Kehagias, Ph. Komninou, G. Nouet, and Th. Karakostas. *J. Phys.: Condens. Matter*, 14:12709, 2002.

[26] H. Blank, P. Delavignette, R. Gevers, and S. Amelinckx. *Phys. Stat. Solidi*, 7:747, 1964.

[27] C.M. Drum. *Phil Mag. A*, 11:313, 1965.

[28] P. Vermaut, P Ruterana, G Nouet, and H. Morkoç. *Phil. Mag. A*, 875:239, 1997.

[29] J.E. Northrup, J. Neugebauer, and L.T. Romano. *Phys. Rev. Lett.*, 77:103, 1996.

[30] J.L. Rouviere, M. Arlery, R. Niebuhr, K.H. Bachem, and O. Briot. *Mater. Sci. Eng., B*, 43:161, 1997.

[31] D. Cherns, W.T. Young, M. Saunders, J.W. Steeds, F.A. Ponce, and S. Nakamura. *Philos. Mag. A*, 77:273, 1998.

[32] D.B. Holt. *J. Phys. Chem. Solids*, 30:1297, 1969.

[33] V. Potin, G. Nouet, and P. Ruterana. *Appl. Phys. Lett.*, 74:947, 1999.

[34] S.S. Shapiro and M.B. Wilk. *Biometrika*, 52(3-4):591, 1965.

[35] J. M. Garcia, G. Medeiros-Ribeiro, K. Schmidt, T. Ngo, J.L. Feng, A. Lorke, J. Kotthaus, and P. M. Petroff. *Appl. Phys. Lett.*, 71:2014, 1997.

[36] P. B. Joyce, T. J. Krzyzewski, G. R. Bell, and T. S. Jones. *Appl. Phys. Lett.*, 79:3615, 2001.

[37] F. Ferdos, S. Wang, Y. Wei, M. Sadeghi, Q. Zhao, and A. Larsson. *J. Crystal Growth*, 251:145, 2003.

[38] A. Hesse, J. Stangl, V. Holy, T. Roch, G. Bauer, O. G. Schmidt, U. Denker, and B. Struth. *Phys. Rev. B*, 66:085321, 2002.

[39] P. Sutter and M. G. Lagally. *Phys. Rev. Lett.*, 81:3471, 1998.

[40] Z. Zhong, J. Stangl, F. Schaffler, and G. Bauer. *Appl. Phys. Lett.*, 83:3695, 2003.

[41] A. Rastelli, E. Muller, and H. von Kanel. *Appl. Phys. Lett.*, 80:1438, 2002.

[42] N. Gogneau, D. Jalabert, E. Monroy, E. Sarigiannidou, J.L. Rouviere adn T. Shibata, M. Tanaka, J.M. Gerard, and B. Daudin. *J. Appl. Phys.*, 96:1104, 2004.

[43] G. Mula, C. Adelmann, S. Moehl, J. Oullier, and B. Daudin. *Phys. Rev. B*, 64:195406, 2001.

[44] I. Waki, C. Kumtornkittikul, K. Sato, Y. Shimogaki, and Y. Nakano. *Phys. Stat. Sol. (b)*, 234:961, 2002.

[45] K. A. Mkhoyan, J. Silcox, H. Wu, W. J. Schaff, and L. F. Eastman. *Appl. Phys. Lett.*, 83:2668, 2003.

[46] N. Gogneau, D. Jalabert, E. Monroy, T. Shibata, M. Tanaka, and B. Daudin. *J. Appl. Phys.*, 94:2254, 2003.

[47] C. Adelmann, E. Sarigiannidou, D. Jalabert, Y. Hori, J.-L. Rouvière, B. Daudin, S. Fanget, C. Bru-Chevallier, T. Shibata, and M. Tanaka. *Appl. Phys. Lett.*, 82:4154, 2003.

Chapter 5

GaN/AlN Quantum Dot Structures

GaN quantum dots can emit light with a photon energy well below the GaN band gap due to the quantum-confined Stark effect, which makes them interesting for visible light emission [1, 2]. In order to obtain specific optical properties of GaN quantum dots, one has to control their sizes and their density. This chapter contains the analysis realized on GaN/AlN quantum dot structures. In the first part of the chapter, a quantitative strain analysis of a GaN/AlN QD superlattice is presented. Using the GPA, we will put in evidence a modulation in the lattice parameters of the AlN matrix. This result will be further supported by theoretical calculations and X-ray diffraction experiments. In the second part we will describe the effects of the capping process on the structural properties of GaN QDs grown on AlN. We will demonstrate that the AlN overgrowth lead to an isotropic reduction of the island size.

5.1 Quantitative strain analysis in GaN/AlN quantum dots superlattice

5.1.1 Introduction

Nitride quantum dots grown in the wurtzite phase have gained special attention due to their potential applications in optoelectronic devices in the visible to ultraviolet energy range [3]. In wurtzite materials, the piezoelectric and spontaneous polarization induces a significant blue-shift of the luminescence lines of GaN/AlN QD heterostructures. Therefore, the knowledge of the strain distribution in QDs is essential to understand the luminescence and to tune the emission wavelength to the desired application.

For application purposes, it is necessary to bury the GaN QDs in an AlN matrix and

to stack them in different layers, i.e. to form a superlattice of dots. When doing so, a strong vertical QD correlation develops. Only few experimental or theoretical works have studied the local strain in a GaN/AlN QD system. They successively address the absence of intermixing between GaN and AlN, the epitaxial relation between the dot and the matrix and the strain in the buried dot and in the surrounding matrix [4–6].

In this section we investigate the strain distribution in a superlattice of GaN QDs embedded in an AlN matrix using HRTEM. A modulation in the lattice parameters of the AlN is identified and attributed to a difference in the strain state of the AlN spacer later.

The obtained results are compared with theoretical calculations and x-ray diffraction measurements.

5.1.2 Experimental details

The wurtzite QD GaN/AlN superlattice (SL) sample studied in this section[1], was grown by plasma-assisted molecular beam epitaxy (PAMBE). The substrate consisted of a bulk 6H-SiC. Prior to it a (0001) oriented AlN buffer layer of $0.5\mu m$ thickness was deposited. The substrate temperature was fixed to 730°C. The SL comprised 80 GaN QDs layers embedded in an AlN matrix, with nominal thickness of 1.5 nm and 10 nm for GaN and AlN respectively. The growth of GaN was made under N-rich conditions. Under these conditions, the deposition of the about 6 GaN monolayers (ML) (1 ML$\simeq$ 0.25 nm) leads first to the growth of a 2 ML wetting layer (WL) pseudomorphically strained to the AlN. The elastic relaxation of the mismatch-induced strain leads after to the spontaneous formation of QDs (Stranski-Krastanov growth mode) [7]. A steady state of the QD growth is reached after the deposition of 2–3 bilayers [8]. Finally, an uncapped QD layer was grown additionally on the top of the structure.

To measure and map the strain fields in the HRTEM images the GPA was used [9] (chapter 3.2). The theoretical strain field calculations were carried out using a combination of the Fourier transform and the Green's function technique [5]. The x-ray diffraction measurements were realized in the grazing incidence geometry combined with the tunability of the beam energy for anomalous scattering at the beamline ID1 of the European Synchrotron Radiation Facility [10].

[1]Sample name S1051.

5.1.3 Morphology of quantum dots

The cross-sectional HRTEM image of Figure 5.1 illustrates a general view of five GaN QDs layers embedded inside the AlN matrix. The image was taken along the [2,-1,-1,0] zone axis. We can see that the dots are vertically aligned and well separated from each other. The wetting layer aside the QDs is also visible.

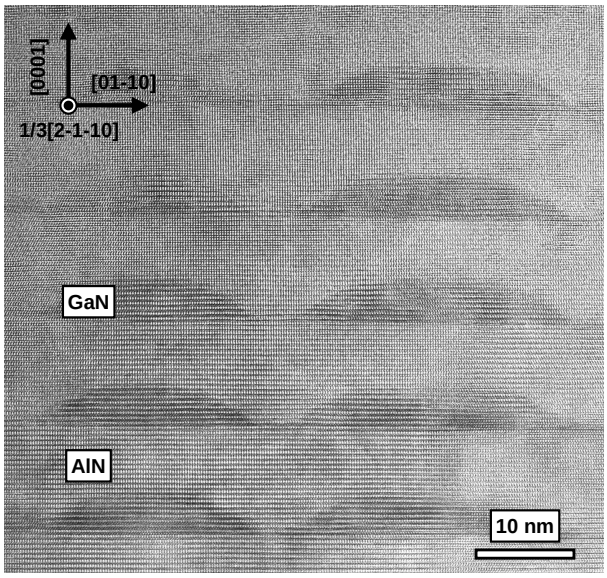

Figure 5.1 : *High resolution TEM image, taken along the [2,-1,-1,0] direction, of five GaN QDs layers of the superlattice. The vertical alignment of the QDs is visible.*

GaN QDs embedded inside an AlN matrix and synthesized by the Stranski-Krastnov growth mode present a truncated pyramidal shape with $\{1\bar{1}03\}$ facets and an hexagonal base with a typical diameter of a few tens of nm and a typical height to base ratio of 0.2 [11]. The dots are standing on a thin 2D wetting layer. Figure 5.2 (a) illustrates a schematic 3D view of one such dot. The geometry of the dot, when viewed along the z axis, is given in Figure 5.2 (b). Note that when HRTEM images are acquired with the [2,-1,-1,0] zone axis, the base diameter of the dots is equal to $D_b' = R_b\sqrt{3} = D_b\sqrt{3}/2$, where R_b is the length of one edge of the hexagonal base.

By analyzing HRTEM images taken along the [2,-1,-1,0] or the [5,-1,-4,0] direction (see section 3.5) in combination with AFM measurements, the dots are found to present the classic truncated pyramidal shape with walls inclined by about 30° from the surface plane, corresponding to the usual $\{1\bar{1}03\}$ facets (Figure 5.3 (a)). The average **height** (h) and **base diameter** (D_b) was found in average equal to **4 nm** and **30 nm** respectively. A schematic view of the examined QD structure in the x-z plane is shown in Figure 5.3 (b). The QD density was measured with AFM from the uncapped QD layer. It was found equal to about $\mathbf{5.5x10^{10}cm^{-2}}$ (Figure 5.4).

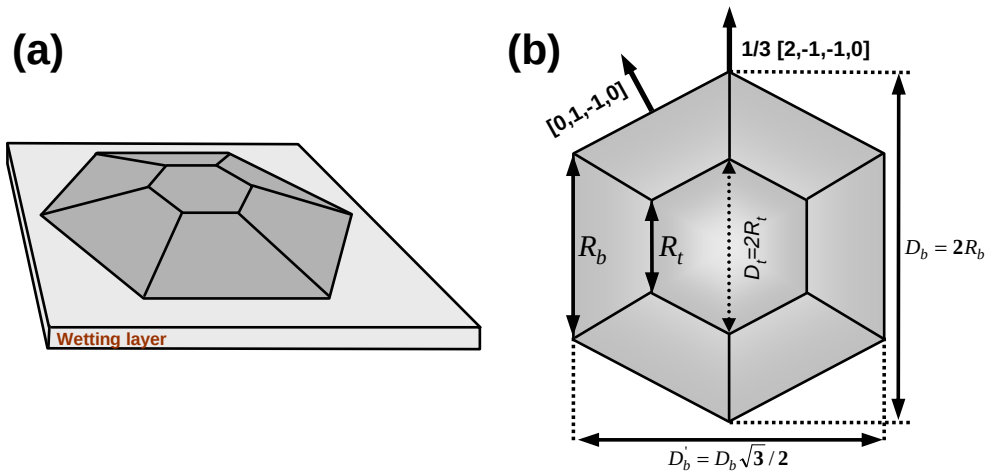

Figure 5.2 : *Schematic illustration of the shape of GaN/AlN QDs grown with the Stranski-Krastanov mode. (a) 3D view of a single QD standing on a 2D wetting layer. (b) View along the z-axis. D_b and D_t are the diameters of the pyramid base and top respectively. $D_b^{'}$ is the diameter of the dot when is viewed along the [2,-1,-1,0] direction.*

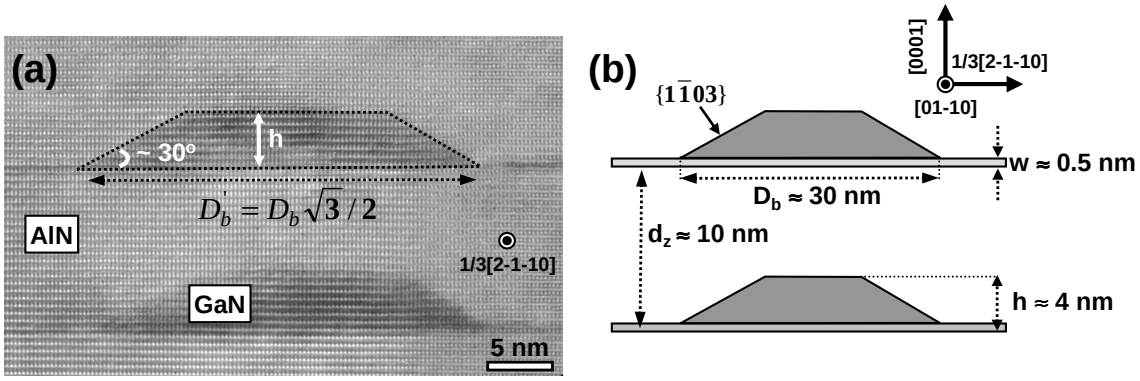

Figure 5.3 : *(a) HRTEM image viewed along the [2,-1,-1,0] zone axis of two QDs layers of the sample structure. The shape of the dot has been outlined. (b) Schematic view of the examined QD structure viewed in the* x-z *plane.*

The thickness of the wetting layer (WL) was measured by applying the projection method on off-axis HRTEM images like the one shown in Figure 5.5 (a). However, due to the very small size of the WL, the direct analysis of the resulting interplanar distances profiles is difficult. For this reason, off-axis image simulations were realized (direction [5,-1,-4,0]) in order to have detailed information. A thin GaN layer located between two AlN layers was simulated. The thickness and the chemical composition of the GaN layer were varied in order to come to an interplanar distance profile which fits with the experimental one.

First of all it was necessary to determine the imaging conditions of the experimental images. For the case of Figure 5.5 (a), we found that the defocus was equal to 40±10 nm

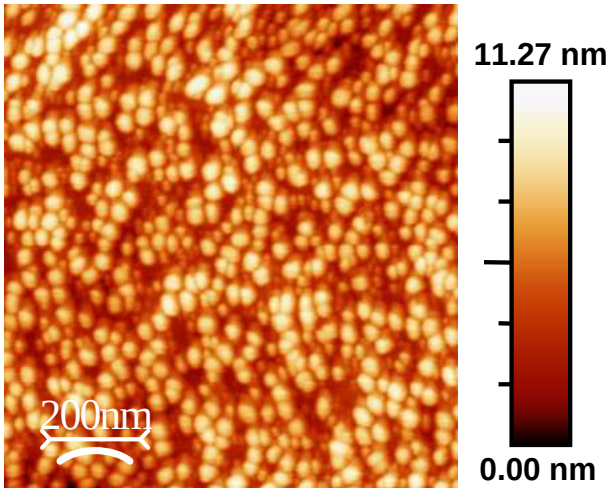

Figure 5.4 : *Atomic force microscopy image of the uncapped QDs at the surface of the QD superlattice sample.*

and the thickness was 5±1.5 nm. The defocus value was calculated from the diffraction pattern of an amorphous zone which was present on the photographic film. The thickness was estimated by "trial and error comparison" between the experimental image and simulations from a thickness/defocus contrast map of a GaN QW embedded in an AlN matrix. For the image shown in Figure 5.5 (b) (outline area of the HRTEM image in Figure 5.5 (a)) the best fit was obtained for a defocus of 40 nm and a sample thickness of 4.9 nm. The corresponding HRTEM simulated image is given as an inset. At the bottom of Figure 5.5 (b) we give the corresponding simulated image in which the atomic structure has been superimposed. In particular, the simulated WL is a pure GaN with thickness equal to two monolayers and completely strained by the AlN matrix. The interfaces are abrupt.

The experimental interplanar distance profile together with the corresponding simulated one are shown in Figure 5.6. The good agreement between the two curves suggests that the GaN WL is completely strained by the AlN matrix and has a thickness of 2 ± 0.5 ML. Moreover we can see that when following the growth direction, the extremum maxima M is first met and not the characteristic minima m. Based on this observation and according to the rule that we have establish in chapter 3 section 3.3, we can verify that the examined superlattice has a Ga-(or Al-) face polarity.

5.1.4 Lattice parameter measurement

With HRTEM images we can have access to information concerning the strain state (see chapter 3). To do so, we have mostly analyzed off-axis HRTEM images like the one in Figure 5.7 (a), in which only the (0002) planes are visible. The corresponding diffraction pattern is superimposed to the image.

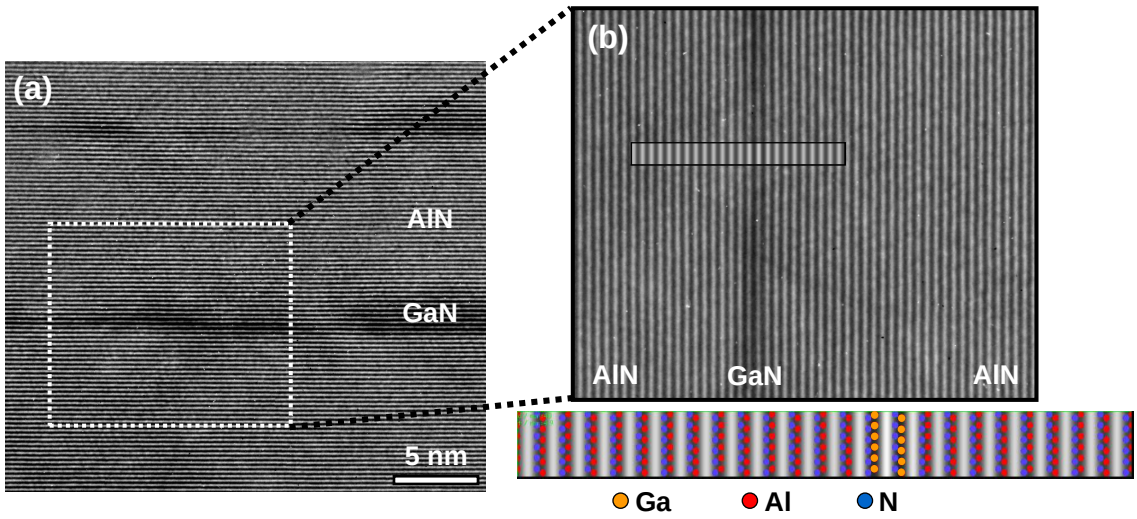

Figure 5.5 : *(a) Off-axis HRTEM image in which the thin wetting layer is clearly visible. (b) Outline area of (a) in which the corresponding simulated image is superimposed. The simulated structure (bottom of figure) consisted of a 2 ML pure GaN layer, completely strain by the AlN and with abrupt interfaces. Thickness= 4.9 nm and Defocus= 40 nm.*

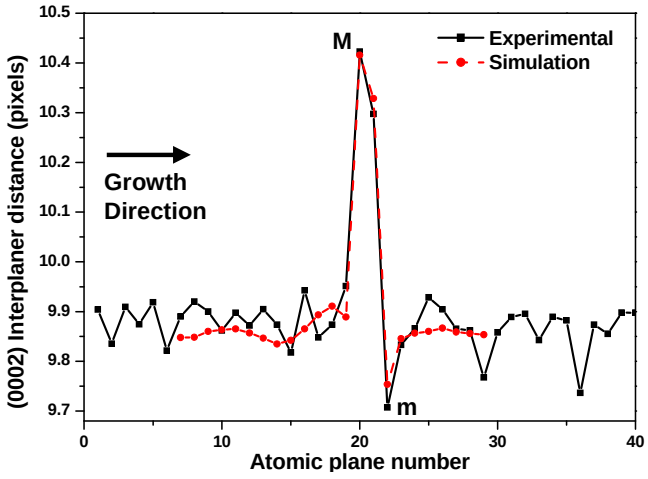

Figure 5.6 : *Experimental and simulated interplanar distances profiles resulting from the analysis of the images shown in Figure 5.5 (b). The good agreement between the graphs suggest that the thickness of the WL is equal to* 2 ± 0.5 *ML.*

The projection method was first applied in order to measure the lattice parameter **c** of the AlN and GaN layers. In total 7 experimental images were analyzed. We observed that the lattice parameter **c** of the AlN was not the same in areas where the AlN was situated between vertically stacked GaN QDs and in areas where the AlN was located between consecutive wetting layers. This is clearly shown in Figure 5.7 (b), where two typical interplanar distances profiles extracted from the outline areas of Figure 5.7 (a) are given. The graph of full squares corresponds to region 1 (through the QD) and the open triangles graph results from region 2 (through the wetting layer). The average values of the interplanar distance along the *c*-axis in the AlN matrix are indicated as dotted lines.

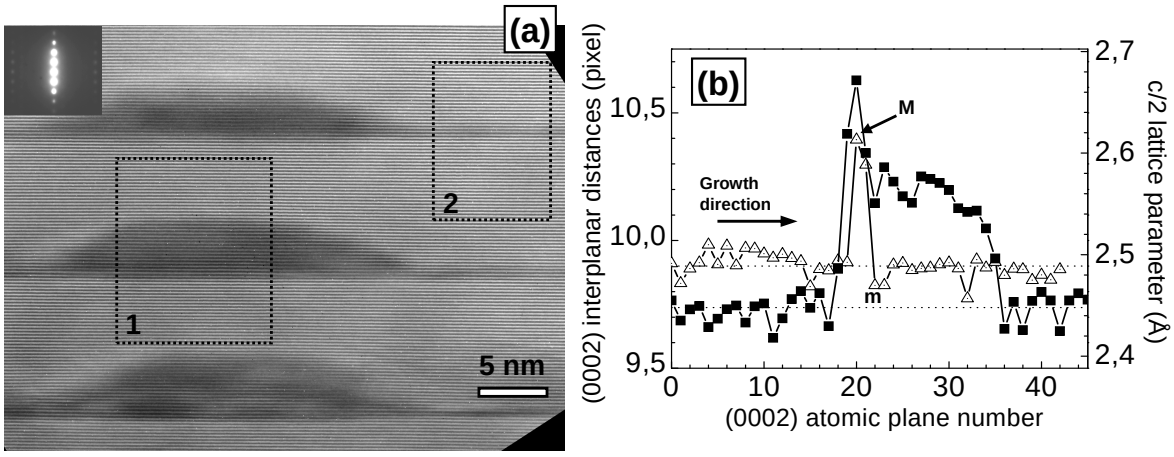

Figure 5.7 : *(a) Off-axis HRTEM image of three vertically aligned GaN QDs. Only the (0002) planes are visible. The diffraction pattern corresponding to the particular* $[5, \overline{1}, \overline{4}, 0]$ *zone axis is superimposed. (b) Interplanar distances profiles in pixel units and in Å measured through the regions 1 (full squares) and 2 (open triangles) defined in picture (a) (The solid line is only a guide for the eye). The horizontal dotted lines represent the average values in the AlN matrix.*

From the asymmetry of the profile of the wetting layer (open triangles), we could once more verify that the superlattice presents Ga-(or Al-) face polarity (see chapter 3.3).

The average values for the AlN, as calculated by the projection method are:

$\mathbf{c/2}_{AlN}$(WL)=**10.035** pixels, *AlN located between two consecutive wetting layers*

$\mathbf{c/2}_{AlN}$(QD)=**9.907** pixels, *AlN located between two vertically stacked QDs*

We see that there is a difference between those two values, which is equal to $\mathbf{1.3 \pm 0.5}\%$. Analyzing the same images with the GPA gave the same result.

Two hypothesis could explain this difference in the AlN lattice parameters:

- Ga atoms could have diffused in the AlN matrix.
- The strain is not the same for the AlN located between wetting layers and for the AlN situated between vertically stacked dots.

These two possibilities are discussed in the following paragraphs.

5.1.5 Chemical composition-EFTEM measurements

If Ga was present in AlN, it would be present where the lattice parameter **c** is larger, that is to say essentially in the AlN region situated between consecutive WLs. In

particular, to produce the measured 1.3% difference in the lattice parameter, about 30% of Ga should be present in the AlN.

In order to determine the eventual presence of Ga in the AlN regions, energy-filtered TEM experiments (EFTEM) were realized.

In Figure 5.8 an Al elemental map of a series of GaN QDs that was obtained by the "three-window" technique, is shown. Specifically, Figures 5.8 (a) and (b) correspond to the first (centered at 1490 eV) and the second (centered at 1547 eV) pre-edge images respectively, used to extrapolate the background intensity. The post-edge image of the Al K-edge is shown in Figure 5.8 (c). The window was centered at 1568 eV (the Al K-edge is at 1560 eV). The slit size was taken equal to 15 eV and the exposure time was 20 sec for each image. After correcting the drift between the recorded images with a correlation procedure and the thickness effects, we obtained the Al elemental map illustrated in Figure 5.8 (d). From the extracted profile (Figure 5.8 (e)), coming from the outline area in the Al map, we notice that the composition in Al does not drop to zero in the GaN dots. However, we should not forget that the QDs are 3D objects and, because of their pyramidal shape for the case of GaN QDs, the observed Al signal might be due to the AlN which surrounds the QD, especially in the QD facets areas. Therefore, we can not interpret this Al signal as an interdiffusion between the GaN QD and the AlN matrix on the top of it.

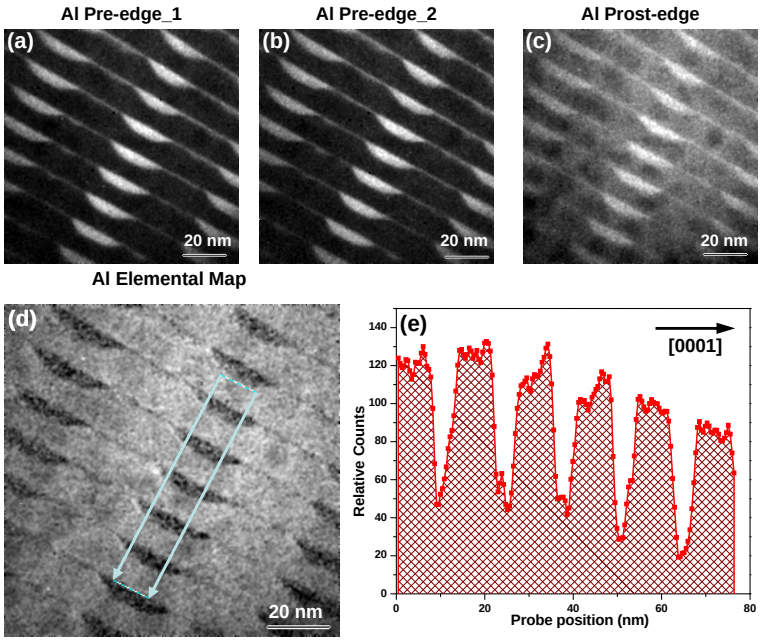

Figure 5.8 : *(a) First Al pre-edge centered at 1490 eV. (b) Second Al pre-edge centered at 1547 eV. (c) Post-edge image of the Al K-edge. The window was centered at 1568 eV. (d) Al elemental map. (e) Extracted profile of the outline area in (d). The Al signal observed in the GaN QD areas is due to the AlN around the facets of the dots.*

In the same area a Ga elemental map was also acquired. The obtained images are shown in Figure 5.9. The two pre-edge images, given in Figure 5.9 (a) and (b), were centered at 1075 eV and 1100 eV respectively. For the post-edge image of the Ga $L_{2,3}$-edge (Figure 5.9 (c)), the window was centered at 1175 eV. As previously for the Al images, the slit size was 15 eV and the exposure time 20 sec. The obtained Ga elemental map is shown in Figure 5.9 (d). A profile of the GaN QDs, extracted from the outline area of the Ga map, is given in Figure 5.9 (e). Within the noise error bar the gallium signal drops to zero inside the AlN matrix located between the vertically aligned dots.

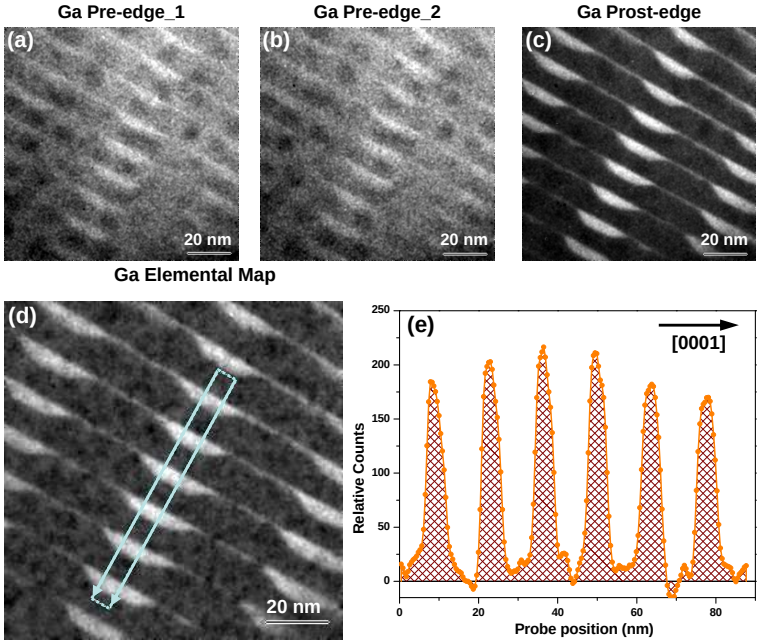

Figure 5.9 : *(a) First Ga pre-edge centered at 1075 eV. (b) Second Ga pre-edge centered at 1100 eV. (c) Post-edge image of the Ga $L_{2,3}$-edge. The window was centered at 1175 eV. (d) Ga elemental map. (e) Extracted profile of the outline area in (d). The Ga signal drops to zero inside the AlN matrix.*

In order to investigate in more detail, how the transition between the GaN QDs and the AlN matrix is taking place, we have acquired an Ga elemental map using a higher magnification and keeping the same conditions (energies, slit size and exposure time) as previously. The obtained map is shown in Figure 5.10 (a). From the extracted profiles we can see that the Ga signal becomes almost zero inside the AlN matrix. Moreover, we see that the interfaces are abrupt, with a width in the order of 1 nm, thus we can exclude the presence of a ternary $Al_xGa_{1-x}N$ alloy in the interfaces. As a result, we will neglect all Al-Ga exchanges at the interfaces and consider that the different regions in the superlattice are either made of GaN or of AlN.

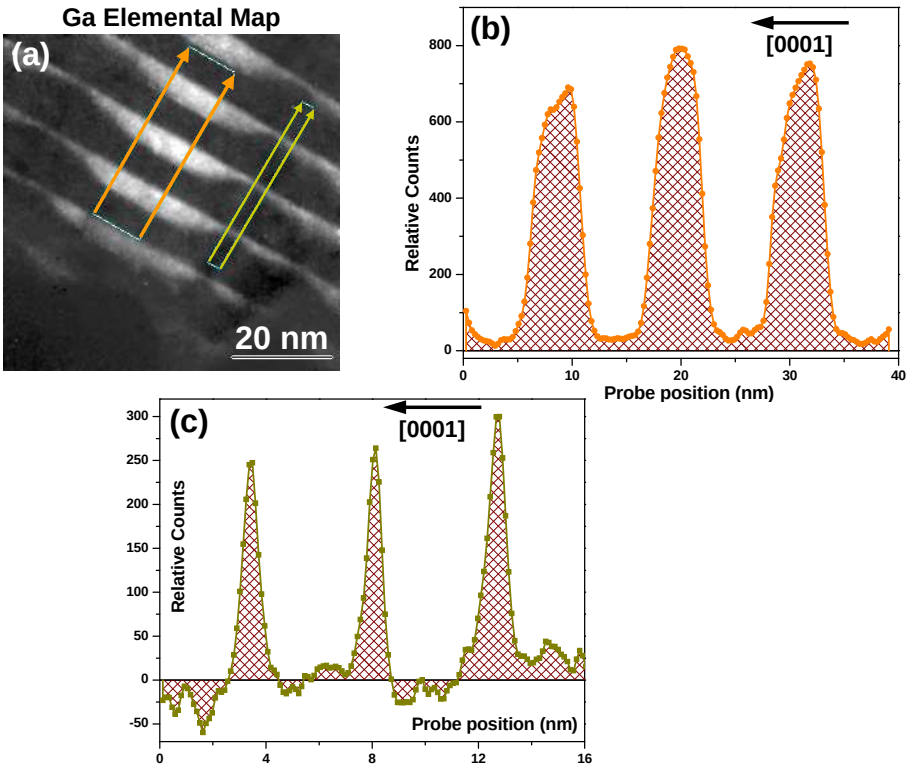

Figure 5.10 : *(a) Ga elemental map. (b) Extracted profile from the GaN QDs area. (c) Extracted profiles from the GaN WLs area. The Ga signals drops abruptly to zero inside the AlN matrix.*

To conclude, the hypothesis that the difference in the lattice parameter of the AlN matrix is due to Ga interdiffusion in the AlN either on the top of the QDs or above the WL, can be excluded.

5.1.6 Strain distribution in the superlattice

Strain maps were also obtained with the GPA. The experimental data where compared to theoretical strain calculations that combine Fourier transform and the Green's function technique. The reader can find details on the theoretical background of these calculations in the paper of A.D. Andreev and E.P. O'Reilly [5]. Additionally, the strain distribution in the examined SL was also investigated using anomalous grazing incidence x-ray diffraction experiments [10].

Strain definitions.

Before presenting the experimental and theoretical results, we find important to recall the different definitions of strain used by the various methods. GPA measures strain with respect to a reference area in the HRTEM image. As we have mentioned in section 3.2.1,

in the original paper of the GPA [9], bi-dimensional strain fields are analyzed. In this work, for simplicity and because in most cases we have measured the strain field only in one direction we have introduced one-dimensional strain field equations (details were given in section 3.2.3).

Therefore, the strain measured with GPA, is given by the equation (see also equation 3.71 in section 3.2.3) [12]:

$$e_{zz}^{GPA}(\mathbf{r}) = \frac{c(\mathbf{r}) - c^{ref}}{c^{ref}} = \frac{g^{ref} - g(\mathbf{r})}{g(\mathbf{r})} \tag{5.1}$$

This strain will be named as ***"GPA strain"*** or ***"relative deformation"***.

In the case of a *one material* system, the GPA strain $e_{zz}^{GPA}(\mathbf{r})$ gives the *real Lagrangian strain*, if the reference region is taken in the undeformed bulk crystal. When *two materials*, A and B, with two different bulk lattice parameters, respectively c_{bulk}^{A} and c_{bulk}^{B}, are present, it is generally adopted to measure strain with respect to the bulk lattice parameter of each material. A new strain $e_{zz}^{mat}(\mathbf{r})$ is then defined:

$$e_{zz}^{mat}(\mathbf{r}) = \frac{c(\mathbf{r}) - c_{bulk}^{A}}{c_{bulk}^{A}} \cdot compo(\mathbf{r}) + \frac{c(\mathbf{r}) - c_{bulk}^{B}}{c_{bulk}^{B}} \cdot (1 - compo(\mathbf{r})) \tag{5.2}$$

where $compo(\mathbf{r})$ defines the amount of material A at position $(\mathbf{r})$. In the previous section we have seen that we can neglect all Al-Ga exchanges at the interfaces and consider that the different regions in the superlattice are either made of GaN or of AlN. Therefore, $compo(\mathbf{r})$ is equal to 1 in material A and to zero in material B.

$e_{zz}^{mat}(\mathbf{r})$ will be named *"material related strain"* or shortly ***"material strain"***.

The GPA strain and the material strain are related to each other:

in material A, $$\left(e_{zz}^{mat}(\mathbf{r}) + 1\right) * c_{bulk}^{A} = \left(e_{zz}^{GPA}(\mathbf{r}) + 1\right) * c^{ref} \tag{5.3}$$

in material B, $$\left(e_{zz}^{mat}(\mathbf{r}) + 1\right) * c_{bulk}^{B} = \left(e_{zz}^{GPA}(\mathbf{r}) + 1\right) * c^{ref} \tag{5.4}$$

The GPA strain will depend on the chosen reference region, that is to say will depend on the value of c^{ref}.

In the following, material A will be AlN, material B will be GaN and the reference region will be chosen in an AlN region where c^{ref} is supposed to be close to the c_{bulk}^{AlN}.

In these conditions, the ratio c_{bulk}^{AlN}/c^{ref} can be written $e_0^{AlN}+1$, with e_0^{AlN} close to zero. Introducing $(e_0^{AlN}+1)$ into equation 5.3 we get in material A:

$$\left(e_{zz}^{mat}(\mathbf{r})+1\right) * \left(e_0^{AlN}+1\right) = e_{zz}^{GPA}+1 \simeq e_0^{AlN}+e_{zz}^{mat}+1 \tag{5.5}$$

$$\text{or} \quad e_{zz}^{GPA} \simeq e_0^{AlN}+e_{zz}^{mat} \tag{5.6}$$

A similar approximation can be obtained for GaN using equation 5.4:

$$e_{zz}^{GPA} \simeq e_0^{GaN}+e_{zz}^{mat} \tag{5.7}$$

where $e_0^{GaN}=\frac{c_{bulk}^{GaN}}{c^{ref}}$.

Both definitions of strain are interesting. The GPA strain is what we measure experimentally. The material strain permits to evaluate which material is more stressed, i.e. which material differs more from its bulk value.

e_{zz} strain component.

Figure 5.11 presents the analysis of the e_{zz} strain component for the case of two vertically aligned GaN QDs of the superlattice. An off-axis HRTEM image of these dots and their wetting layer ([5,-1,-4,0] direction), is shown in Figure 5.11 (a), where only the (0002) planes are visible. The GPA strain (or relative deformation) map of the high-resolution image is shown in Figure 5.11 (b). It was calculated by placing a Gaussian mask of size approximately $\mathbf{g}/5$ around the $\mathbf{g}$=0002 reflection. As reference area we have chosen the AlN matrix situated between the two successive wetting layers (WLs).

Table 5.1 summarizes the average values of strain for the 4 regions we are going to discuss.

It is clear that on average the e_{zz}^{GPA} value is almost zero for the reference area (noted AlN (WLs) in Table 5.1), and it becomes negative and equal to $-1.9 \pm 0.4\%$ for the AlN located between the GaN QDs (noted AlN (QDs)). This result is identical to that seen in section 5.1.4, where a variation of the AlN crystal lattice has been reported. For the GaN we find that the relative deformation inside the QDs is equal on average to $2.7 \pm 0.4\%$ and in the WL is $5.1 \pm 0.4\%$ (outline areas in Figure 5.11(b)).

The experimental results were compared to theoretical calculations[2]. In the calculations, a bulk infinite periodic superlattice of GaN QDs embedded in an AlN matrix was modelled. The size and shape of the QDs and the barrier thickness were the same as the experimental values defined by HRTEM and AFM measurements (section 5.1.3).

[2]All theoretical calculations presented in this section were performed by Dr. A.D. Andreev from the University of Surrey.

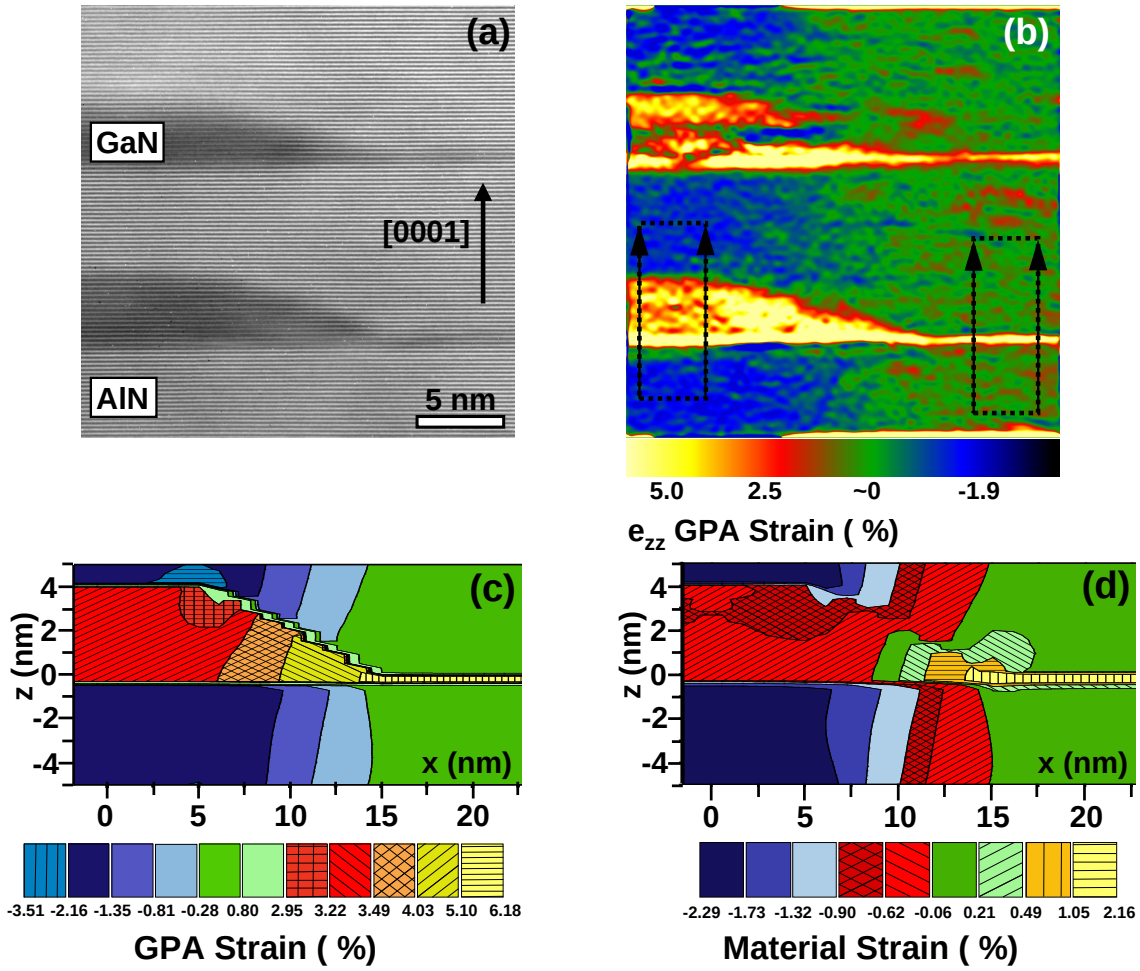

Figure 5.11 : *(a) Off-axis HRTEM image of two vertically aligned GaN QDs embedded inside an AlN matrix. (b) Corresponding to (a) experimental e_{zz} GPA strain map taken with the 0002 reflection. (c) Calculated 2D GPA strain map. (d) Calculated 2D map of the material strain in the GaN/AlN QDs superlattice. A difference in the order of about 2% is observed between the AlN matrix situated between the two WLs (reference area) and the AlN located between the QDs.*

The elastic constant values for AlN and GaN were taken from a theoretical study by Wright [13], which are the values that we have adopted in this thesis. Different in-plane distances between QDs were simulated. These distances were varied between 5 nm to 20 nm. In the case of the QDs shown in Figure 5.11, the in-plane distance is equal to 20 nm and all calculations presented below use this value.

For every strain component, two set of calculations were realized. One in order to calculate the material strain using equation 5.2 (third column of Table 5.1, Figure 5.11 (d)) and a second one to calculate the relative deformation using equation 5.1 (second column of Table 5.1, Figure 5.11 (c)). In the latest type of calculations, similarly to the experimental measurements, as c^{ref} we have taken the lattice parameter of the AlN

	GPA Strain		Material Strain
	Experimental eq. 5.1 (±0.4%) $c^{ref} = c_{WL}^{AlN}$	Calculated eq. 5.1 (%) $c^{ref} = c_{WL}^{AlN}$	Calculated (%) eq. 5.2
AlN (WLs)	≈ 0	0	0.14
AlN (QDs)	-1.9	-1.92	-1.78
GaN (WLs)	5.1	5.54	1.55
GaN (QDs)	2.7	3.31	-0.60

Table 5.1 : *Experimental and theoretically calculated values for the e_{zz} strain component.*

matrix situated between consecutive WLs (c_{WL}^{AlN}). The value of c_{WL}^{AlN} was calculated from the value of the material strain since:

$$e_{zz}^{AlN(WLs)}(\mathbf{r}) = \frac{\mathbf{c}(\mathbf{r}) - \mathbf{c}_{bulk}^{AlN}}{\mathbf{c}_{bulk}^{AlN}} \Rightarrow \mathbf{c}(\mathbf{r}) = e_{zz}^{AlN}(\mathbf{r}) \cdot \mathbf{c}_{bulk}^{AlN} + \mathbf{c}_{bulk}^{AlN} \equiv \mathbf{c}^{\mathbf{ref}}(\mathbf{r}) \tag{5.8}$$

The second set of calculations were realized in order to be able to directly compare the obtained results with the ones from the GPA analysis.

We can observe the relatively good agreement between experimental and calculated values as far as it concerns the GPA strain. This is better shown in Figure 5.12 where experimental and calculated GPA strain profiles are given. In particular, the experimental profiles are resulting from the outlined areas in Figure 5.11 (b). The calculated profiles were taken: (a) along a line through the pyramid center – x= y= 0 – for the QDs and (b) though the wetting layer between pyramids – y= 0, x= $d_x/2$ – with d_x being the in-plane distance between QDs. The relatively good agreement can be seen. In the experimental profile of the QD area, we observed a peak of height similar to the one in WL profile. This certainly results from the fact that the thickness of the GaN QD is smaller that the TEM sample thickness. Therefore, in the profile we see a superposition of the QD and the bare wetting layer. Generally, in the GaN areas the agreement is less good due to the fact that the GaN QDs are cut.

Finally, concerning the strain along the growth direction (material strain analysis shown in Figure 5.11 (d)) the theoretical calculations revealed that the AlN between consecutive WLs is slightly strained to about 0.14%. Additionally, we observe that *although the GaN QDs are relatively relaxed, the AlN matrix located between consecutive QDs is almost completely strained by them.* Therefore, we can conclude that it is this local strain which causes the vertical alignment of the QDs inside the superlattice structure.

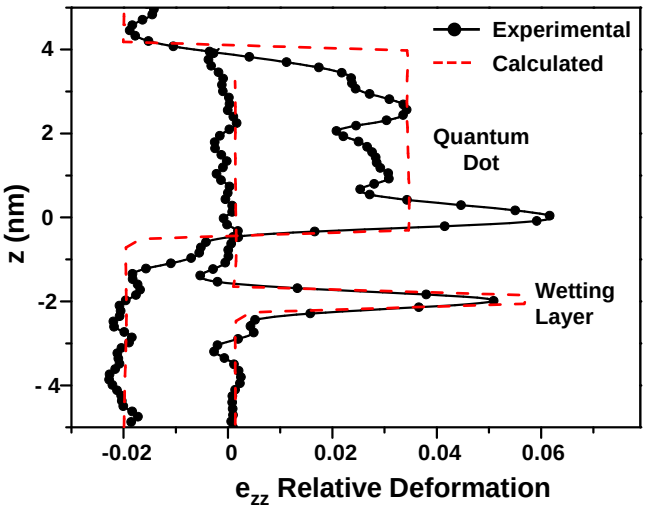

Figure 5.12 : *1D relative deformation profiles. The experimental profiles resulting from the outline areas in Figure 5.11 (b). The calculated are coming from lines through the pyramid center and through the wetting layer between the pyramids.*

e_{xx} strain component.

The e_{xx} strain was analyzed in a similar way. For this purpose, HRTEM images along the [2,-1,-1,0] direction were realized. A high-resolution image of two GaN QDs viewed along the [2,-1,-1,0] direction and the corresponding relative deformation map are shown in Figures 5.13 (a) and (b) respectively. The latest is calculated by the GPA by placing a gaussian mask of size $\sim \mathbf{g}/9$ around the $\{01\bar{1}0\}$ reflection. The reference area was chosen between the wetting layers.

We observe that the GPA strain remains unchanged and equal in average to $0.9 \pm 0.6\%$ inside the QDs and the AlN spacer between them, whereas it becomes approximately equal to zero for the AlN situated between the WLs. We notice that the accuracy in measuring the e_{xx} strain component is now $\pm 0.6\%$, while for the e_{zz} strain tensor was equal to $\pm 0.4\%$. The reasons are *firstly* that when analyzing HRTEM images taken along the [2,-1,-1,0] direction, the largest mask that we can apply around the $\{01\bar{1}0\}$ reflection that does not include the origin or the $\{01\bar{1} \pm 1\}$ reflections is equal to $\sim \mathbf{g}/7$. In chapter 3 section 3.2.4 we have reported that the smallest the mask we place around a reflection $\mathbf{g}$ the largest becomes the region R over which the GPA averages the information. In our case, to measure the e_{xx} strain component we have used a mask of size $\sim \mathbf{g}/9$ which means that in the direct space larger areas were analyzed in order to provide us the desirable strain information. *Secondly*, we have seen in chapter 3.5 that an on-axis HRTEM image with dots is more noisy than an off-axis image. For these reasons the error in measuring the e_{xx} strain component is higher compared to the one resulting from the measurements of the e_{zz} component where only off-axis HRTEM images were analyzed.

Additionally, in the experimental GPA strain map (Figure 5.13 (b)) we observe that the thin WL cannot be detected. This is because it is almost completely strained by

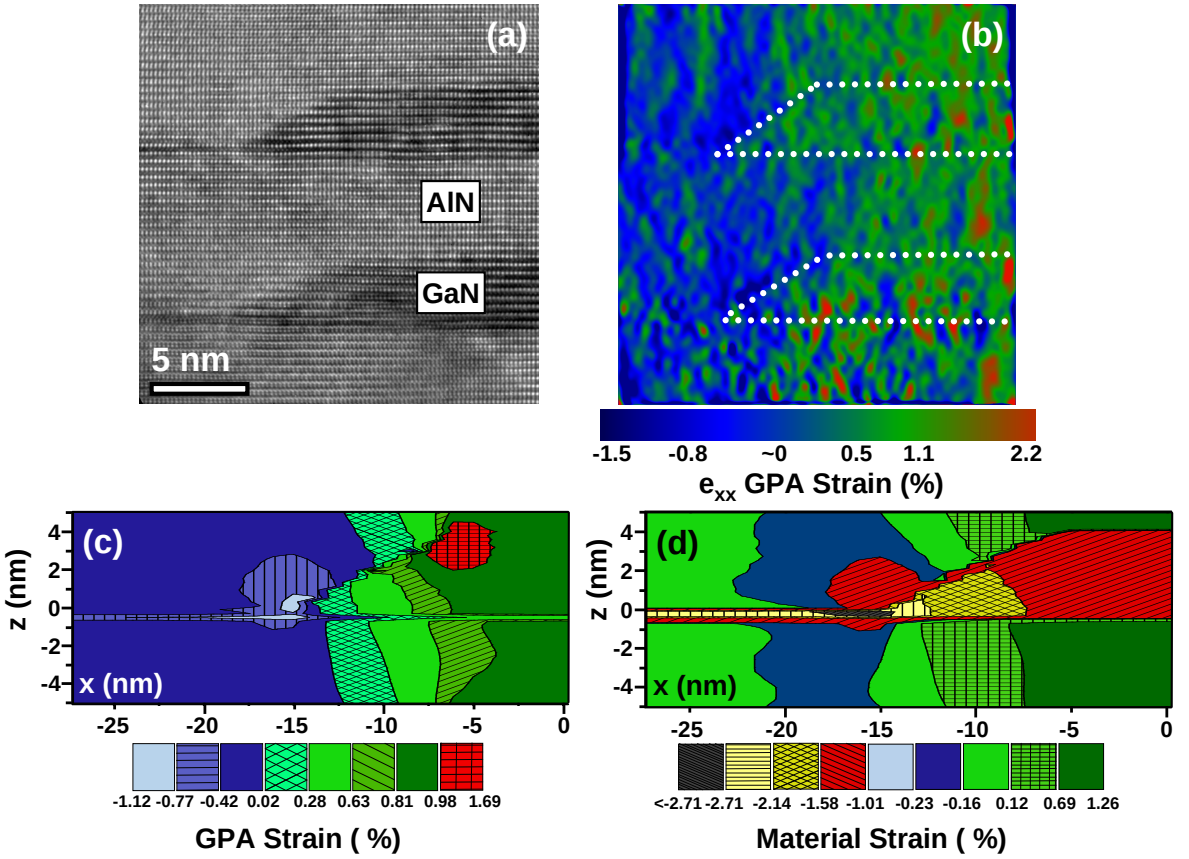

Figure 5.13 : *(a) High-resolution image of two GaN QDs of the superlattice taken along the [2,-1,-1,0] direction. (b) Corresponding GPA strain map calculated by the GPA using the* $\{01\bar{1}0\}$ *reflection. (c) Calculated 2D map of the GPA strain for the examined GaN/AlN QDs superlattice. (d) Calculated 2D material strain map.*

the AlN matrix and adapts its lattice parameter to that of the AlN substrate. However, elastic relaxation indicates that the WL is slightly relaxed. This small relaxation could not be measured.

The previous GPA experimental results are in good agreement with the calculated ones as it concerns the relative deformation (Figure 5.13 (c)). For the theoretical calculations the same superlattice as in the analysis of the e_{zz} strain component was used.

All results are summarized in Table 5.2.

Finally, from the material strain analysis ((Figure 5.13 (d)), we can detect the modulation of the in-plane strain in the AlN matrix. In particular, *while the AlN spacer located between two wetting layers is almost relaxed, the AlN matrix situated between two vertically aligned QDs is strained to about 0.87 %. For the GaN QDs a compressive strain of about 1.39 % is calculated.*

	Relative Deformation		Material Strain
	Experimental eq. 5.1 (±0.6%) $a^{ref} = a_{WL}^{AlN}$	Calculated eq. 5.1 (%) $a^{ref} = a_{WL}^{AlN}$	Calculated (%) eq. 5.2
AlN (WLs)	≈ 0	0	-0.13
AlN (QDs)	0.9	1.00	0.87
GaN (WLs)	≈ 0	-0.03	-2.57
GaN (QDs)	0.9	1.18	-1.39

Table 5.2 : *Experimental and theoretically calculated values for the e_{xx} strain component.*

Anomalous grazing incidence x-ray diffraction experiments.

The strain distribution in the previous sample was also investigated by x-ray diffraction in the grazing incidence geometry [10]. Due to the small amount of material in the SL, x-ray investigations were possible only by the use of a highly brilliant x-ray beam delivered by the third generation synchrotron facilities. For this reason the experiments described below were realized in the European Synchrotron Radiation Facility (ESRF) in Grenoble and more specifically in the ID1 beamline[3]. A detailed description of the geometry used in the experiments can be found in Reference [14].

For the experiments, the beam energy was tuned to the Ga-K edge ($E_{Ga} = 10.367$ keV). In order to measure accurately the Ga K-edge, a fluorescence spectra in the classical large angle geometry was first measured with the sample (Figure 5.14 (a), solid line). We see that the experimental Ga K-edge was found at the expected energy within an absolute accuracy of less than 1 eV. A series of diffraction curves in the grazing incidence geometry was then measured at the in-plane $(22\bar{4}0)$ reflection for the two energies marked by a vertical line on the Figure 5.14 (a): the reference curve (open circles) was measured 67 eV below the Ga K-edge ($E_{Ref} = 10.3$ keV) and the second one, the anomalous curve, (open squares) directly at E_{Ga} (Figures 5.14 (b) and (c)). To improve the statistics and to avoid the contribution of the periodicity of the superlattice (for incidence angle α_i bigger than the critical angle α_c), the α_f spectra were integrated along the linear detector between α_c and $2.4 \times \alpha_c$. The relaxed $q_{22\bar{4}0}$ values for GaN and AlN are indicated on the graph as q_{GaN} and q_{AlN}, respectively.

The *first series* presented on Figure 5.14 (b) was obtained for an angle of incidence $\alpha_i = 0.07°$, much smaller than α_c (measured at about 0.22° for E_{Ref} and E_{Ga}). For this incidence angle, the penetration depth was about 100 Å for both energies. Both reference and anomalous measurements present an intense diffraction peak, denoted A,

[3]The anomalous grazing incidence x-ray diffraction experiments were realized by Dr. Virginie Chamard now at LTPCM/Saint Martin d'Hères/Grenoble.

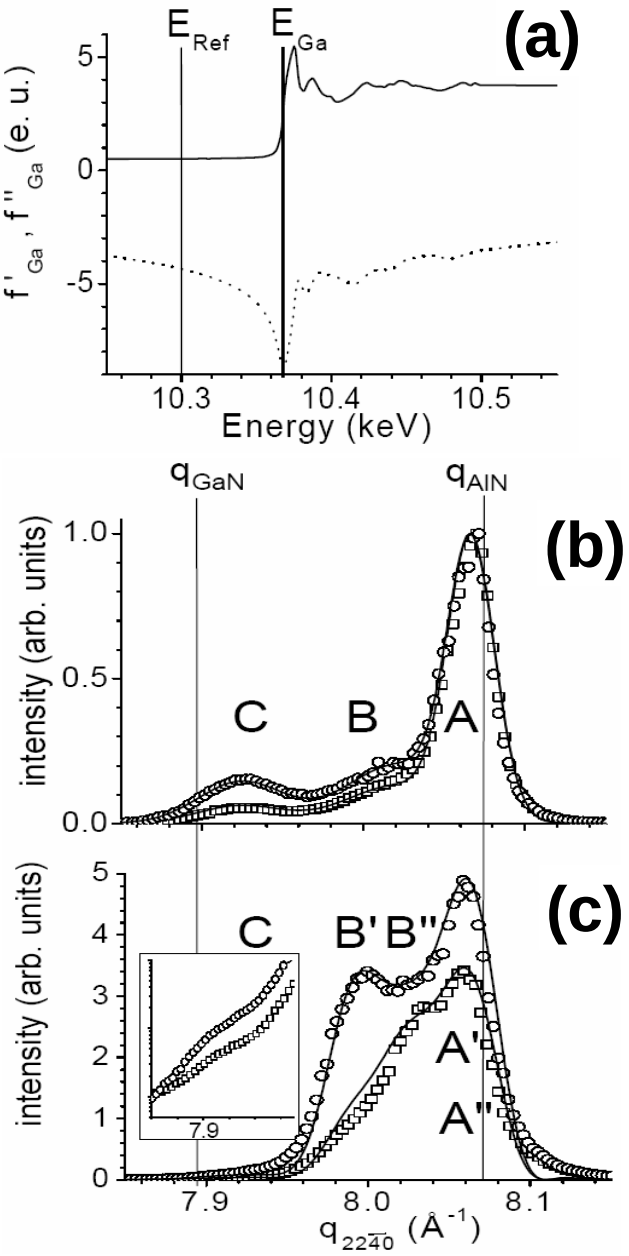

Figure 5.14 : *(a) Anomalous corrections f' (dotted line) and f'' (solid line) for Ga in the vicinity of the K-absorption edge. f'' was measured by fluorescence and f' was deduced by the Kramers-Kronig algorithm. The two vertical lines indicate the reference energy (E_{ref} = 10.3 keV) and the Ga K-edge (E_{Ga} = 10.367 keV). Grazing incidence anomalous x-ray diffraction measurements at the in-plane $(22\bar{4}0)$ reflection along the $q_{<22\bar{4}0>}$ radial direction. The measurements at E_{ref} are given by open circles while the squares represent the measurements at E_{Ga} for (b) $\alpha_i = 0.07°$ and (c) $\alpha_i = 0.25°$. The solid lines in (b) and (c) are the results of the best fits using the same model as described in the text. The inset in (c) is a lin-log plot of the region C.*

located around q_{AlN}. On the low $q_{22\bar{4}0}$ range but for $q_{22\bar{4}0} > q_{\mathrm{GaN}}$, a weak double peak intensity was observed on the reference curve (denoted B and C). On the anomalous measurement, this part was strongly reduced, indicating the presence of Ga. The *second series* presented on Figure 5.14 (c) was measured for $\alpha_i = 0.25°$. For such a large incident angle, a large number of bilayers was probed as the penetration depth was increased to about 0.5–1 μm. However, in the $\alpha_i > \alpha_c$ region, the penetration depth depends strongly on the energy. Therefore the exact number of probed bilayers was difficult to evaluate. The intense peak located near q_{AlN} remained on the reference curve together with another

strong peak located at 8 $Å^{-1}$. A weak shoulder was also visible around 7.92 $Å^{-1}$. In the anomalous measurement, a strong modification of the intensity distribution was observed with an important decrease of about all intensity components except in the $q_{22\bar{4}0} \approx 8.03$ $Å^{-1}$ region.

A schematic view of the *structural models* used to fit the anomalous grazing incidence diffraction measurements and consequently to measure the strain in the different areas of the SL are shown in Figure 5.15. Figure 5.15(a) and (b) give the models used for the measurements realized respectively for $\alpha_i < \alpha_c$ and $\alpha_i > \alpha_c$. The main assumption of these models was the absence of interdiffusion, which is true based on the EFTEM experiments described in section 5.1.5. The reader can be addressed to reference [10] for more details of the used models. Here we will report the obtained results, in order to compare them with our HRTEM strain analysis and the theoretical calculations.

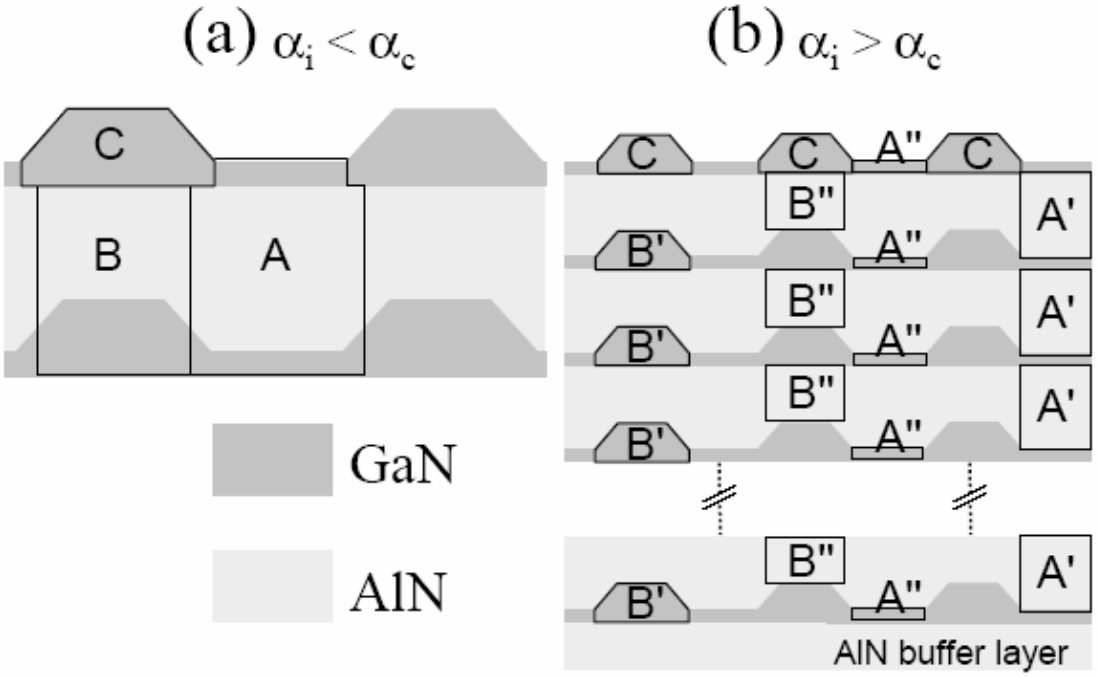

Figure 5.15 : *Schematic views of the structural models used to fit the anomalous grazing incidence diffraction measurements at (a) $\alpha_i < \alpha_c$ (Figure 5.14 (b)) and at (b) $\alpha_i > \alpha_c$ (Figure 5.14 (c)). The zones labelled on the draws indicate the iso-strain regions, which are in: (a) between two wetting layers (A), in the last embedded dot layer and the corresponding above AlN matrix (B) and in the free standing QDs (C); (b) in the AlN between two wetting layer ($A^{'}$), in the wetting layers ($A^{''}$), in the embedded GaN dots ($B^{'}$), in the corresponding above AlN matrix ($B^{''}$) and in the free standing QDs (C). The same definition also refers to the peaks of Figures 5.14 (b) and (x).*

For the **free-standing QDs** ($\alpha_i < \alpha_c$), a slight compressive strain of about 1.85% is obtained instead of 2.4% which is the lattice mismatch between the bulk GaN and AlN in-plane lattice parameters. This result is slightly different from previous observations, where fully relaxed QDs are reported on the basis of RHEED measurements performed *in situ* during growth [15]. However, this difference is easily understood if we consider the strong surface sensitivity of RHEED (about 10 Å), which probes the very last layers of the deposited material. On the contrary, the diffraction measurements concern the average strain *in* the entire dot and *after* growth.

Using the GPA we have also investigated the strain of the free-standing GaN QDs. The obtained results for the e_{xx} strain component are given in Figure 5.16. In the GPA we have used the same parameters as previously. The examined HRTEM image and the corresponding GPA strain map are shown in Figures 5.16 (a) and (b) respectively. From the profile resulting from the outline area of Figure 5.16 (b) we can clearly see an evolution of the GPA strain as we are approaching the surface of the sample. This suggests that the free-standing GaN QDs relax.

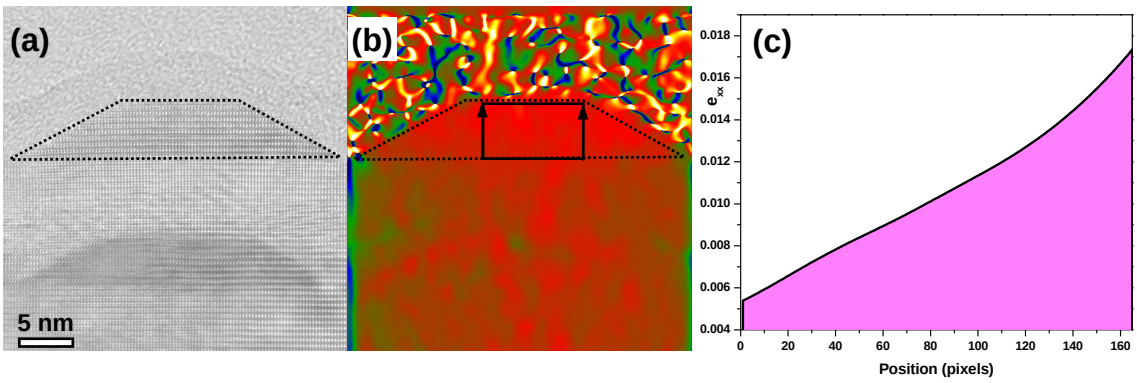

Figure 5.16 : *(a) HRTEM viewed along the [2,-1,-1,0] direction image of two GaN QDs. One free-standing and one capped by the AlN matrix. (b) Corresponding to (a) relative deformation map obtained by the GPA. (c) Profile resulting from the outline area in (b). As we are reaching the surface, an evolution in the relative deformation is clearly identified.*

In the rotation map, obtained also by the GPA, (Figure 5.17 (a)) we notice that at the edges of the free-standing GaN QD, the [0,1,-1,0] planes are bent by $\sim 2.3°$ due to the relaxation of the free-standing GaN QDs. This is also seen in the moire image given in Figure 5.17 (b).

The anomalous grazing incidence x-ray diffraction measurements realized for $\alpha_i > \alpha_c$ also depict the modulation of the in-plane strain in the AlN matrix, in agreement with the HRTEM measurements and the theoretical calculations presented previously. It was measured that although the AlN between two WLs is almost fully relaxed, the AlN matrix

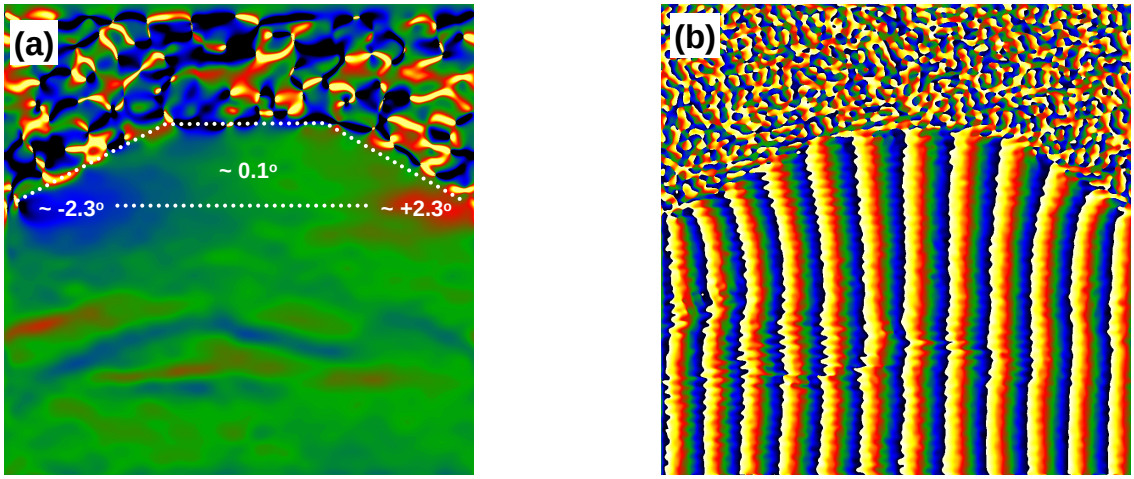

Figure 5.17 : *(a) Rotation map obtained by the GPA, of the image shown in Figure 5.16 (a). (b) Corresponding moire image. The bending of the [0,1,-1,0] planes, resulting from the relaxation of the free-standing GaN QD, is clearly visible.*

between two vertically stacked GaN QDs is strained to about 0.55%. In the theoretical calculations this strain (material strain) was calculated equal to 0.87%. This local strain results from the stressor action of the QDs on the surrounding matrix and leads to the QD vertical alignment [16, 17].

Table 5.3 summarize the obtained from the x-ray diffraction measurements results and the material strain values obtained from theoretical calculations.

e_{xx} Material Strain (%)		
	Experimental (x-rays)	Calculated
AlN (WLs)	≈0	-0.13
AlN (QDs)	0.55	0.87
GaN (QDs)	≈-1	-1.39
GaN (free-standing QDs)	-1.85	-

Table 5.3 : *Experimental from anomalous grazing incidence x-ray diffraction measurements and theoretically calculated values for the e_{xx} strain component.*

Thin Foil effect.

The good agreement between the experimental HRTEM measurements and the theoretical calculations, allowed us to suppose that the thin foil relaxation effect was not important.

Additionally, no significant modifications in the GPA strain were observed as a function of distance in different examined images. For instance, for the HRTEM image of

Figure 5.11 (a), we have applied the GPA using the same conditions as previously (gaussian mask of size $\mathbf{g}/5$) but by choosing as reference area the AlN situated below the first from the bottom WL. Afterwards. we have examined how the e_{zz} component is varying as a function of the distance in the image. The obtained results are shown in Figure 5.18.

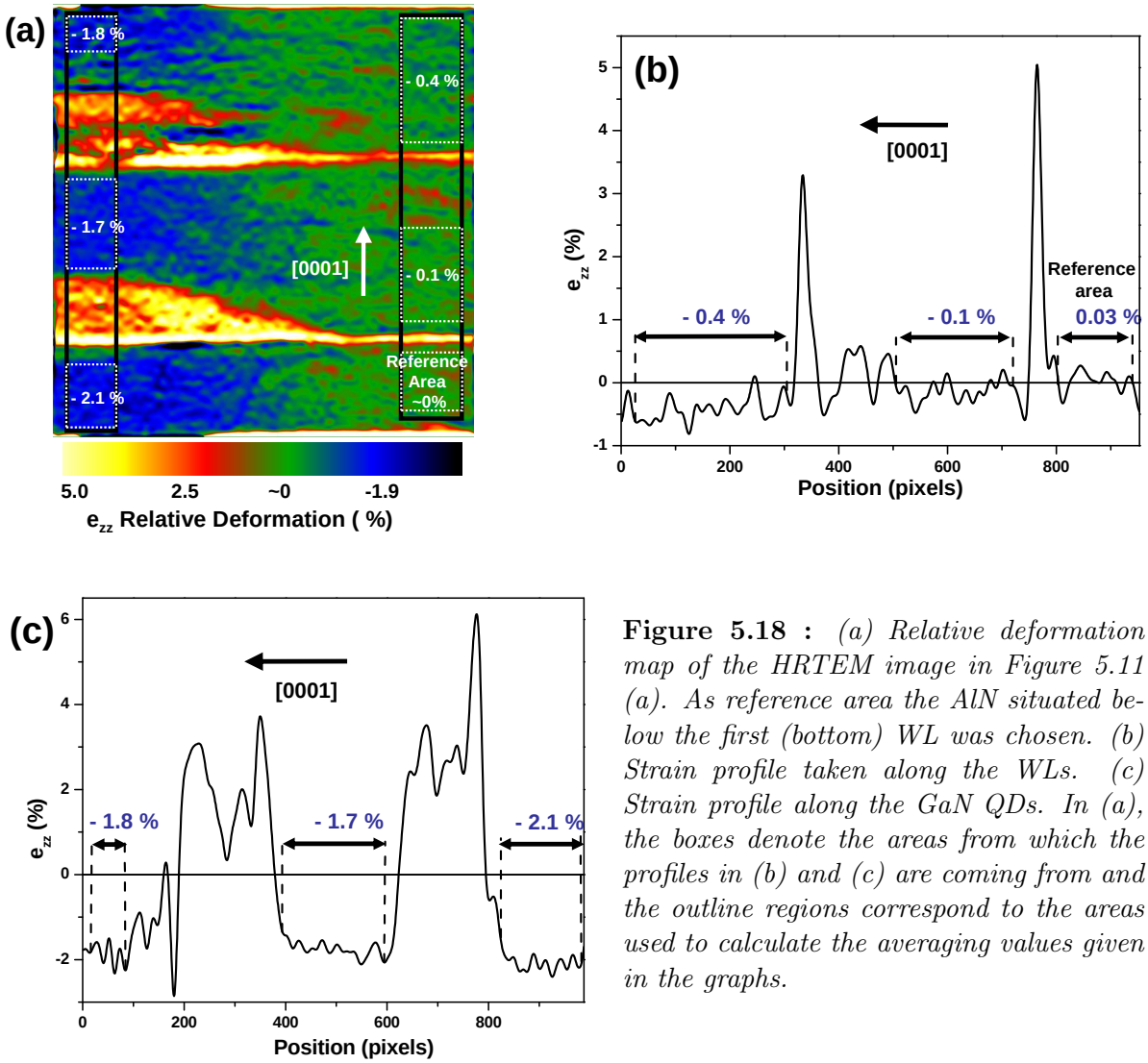

Figure 5.18 : *(a) Relative deformation map of the HRTEM image in Figure 5.11 (a). As reference area the AlN situated below the first (bottom) WL was chosen. (b) Strain profile taken along the WLs. (c) Strain profile along the GaN QDs. In (a), the boxes denote the areas from which the profiles in (b) and (c) are coming from and the outline regions correspond to the areas used to calculate the averaging values given in the graphs.*

From a profile taken along the WLs (see Figure 5.18 (b)) we notice that following the growth direction [0001], the e_{zz} strain component is equal to zero in the reference area and becomes smaller and equal to about -0.4 % at the top of the second WL. Concerning the WLs, we observe that the strain of the top (second) WL becomes 1.5 times smaller than the strain of the bottom (first) WL. However, we have not to forget that the thickness of the WL is only 2ML. From this profile (Figure 5.18 (b)), we could say that as we are moving closer to the surface and as a result to thinner areas, the strain is getting smaller

or in other words the structure is more relaxed.

However, from the profile taken along the GaN QDs (see Figure 5.18 (c)), we do not obtain the same result. In particular, the strain of the AlN matrix situated below the first (bottom) QD is equal to -2.1 % and just on the top of the same QD it becomes higher and equal to -1.7 %. Unfortunately, due to the not so good quality of the image of the second (top) GaN QD, we couldn't compare the values in the dots.

Finally, we can not be sure that the observed variations in the GPA strain are due to the thin foil relaxation effect or due to the distortions introduced by the image formation system of our microscope (section 3.4). Thus, surface relaxation is present but certainly plays a second role.

5.1.7 Conclusions

In this section we investigated the strain distribution in the different parts of a GaN/AlN QD superlattice using HRTEM measurements in combination with theoretical calculations and x-ray diffraction in the grazing incidence geometry.

From HRTEM together with AFM measurements we found that the average height and base diameter of the dots were about 4 and 30 nm respectively. Their shape was a truncated pyramid with $\{1\bar{1}03\}$ facets and they were sitting on a wetting layer of about 2ML thickness. The GaN QDs were vertically aligned.

The most important aspect of our study concerns the difference in the lattice parameter **c** of the AlN matrix, depending on whether it is situated between the vertically aligned QDs or consecutive WLs. We have proven by realizing EFTEM experiments that the observed modulation can not be attributed to an interdiffusion between the GaN QDs and the surrounding AlN matrix. As a result, it is due to a difference in the strain state of the AlN spacer layer. In particular, we found that **although the AlN spacer situated between two consecutive wetting layers is almost fully relaxed, the AlN located between the GaN QDs is strained.** This local strain is generated by the dots on the surrounding AlN matrix and causes the vertical alignment of the dots inside the superlattice.

In addition it is observed that the embedded QDs are compressively strained while the uncapped ones are almost completely relaxed.

Finally, we need to mention that in our HRTEM measurements, we considered the thin foil relaxation effect as negligible based on the good agreement between experimental and calculated values in which a bulk QDs superlattice was used. Finite element simulations

could give a direct a definite answer as it concerns the influence of this effect. However, III-nitride based materials and their ternary and quaternary alloys are not a "model" system. In particular, nitride-based devices involve quite complex heterostructures constituted for example of SLs of quantum wells and/or quantum dots with an important number of repetitions. Additionally, we have not to forget the significant number of defects included in nitrides (density of dislocations actually at $10^7 - 10^{10}/cm^2$).

5.2 AlN overgrowth and structural quality of GaN quantum dots

5.2.1 Introduction

We have seen in section 4.2.2 that the AlN overgrowth of GaN QWs introduce an important modification in the thickness and uniformity of the wells. However, what could be the effect of this overgrowth process on GaN QDs, which present a 3-D structure?

From the literature we know that capping InAs QDs with a GaAs matrix results in a variation of the size, shape and composition of the islands [18–23], which depends on the growth conditions of the overlayer [24, 25]. These changes are attributed to a material redistribution occurring during the capping process [20, 25, 26]. Nevertheless, when InAs QDs are capped with $Ga_{0.8}In_{0.2}As$ or AlAs, tend to preserve their initial shape and to limit or suppress the In segregation and the In-Ga intermixing [23, 27–29].

For the Si/Ge system, the characteristics of embedded Ge dots inside the Si matrix are affected by the overgrowth process, resulting in the transformation of Ge pyramidal islands into flat truncated pyramids with a wide base. This evolution of the dots shape is attributed to a segregation of Ge atoms from the dot top to the base [30–33], which can be prevented by reducing the capping temperature [34, 35].

In this section, we discuss the influence of the overgrowth process on the structural properties of GaN QDs embedded inside an AlN matrix. We demonstrate that capping implies an isotropic reduction of the island size, in contrast with the InAs/GaAs or Si/Ge systems.

5.2.2 Experimental growth conditions

To investigate the AlN overgrowth process on GaN QDs, the same growth conditions as for the QWs samples were applied (see section 4.2.2). In particular all samples were grown by PAMBE on AlN templates. The substrate temperature was fixed at 750°C, and the AlN capping layers were deposited in the range of temperatures between 700°C and 750°C. The growth of GaN was always effectuated under Ga-rich conditions and all samples presented metal-face polarity.

The GaN QDs were synthesized using the modified Stranski-Krastanov growth mode. They are hexagonal truncated pyramids with $\{1\bar{1}03\}$ facets, inclined by $\sim 30^o$ with respect to the basal plane and they are connected to the underlying AlN layer by a continuous 2D GaN wetting layer [36].

5.2.3 RBS measurements

Figure 5.19 illustrates the measured and calculated (solid line) RBS spectrum of two identical GaN QD layers, the first one is embedded inside an AlN matrix grown at 750°C, while the second one is situated at the surface and was used as a reference. The nominal thickness of the QDs was equal to about 18 Å. We can observe that, similar to the GaN/AlN QW system, the embedded GaN QD layer is thinner that the one on the surface. In particular, the QD layer at the surface has a thickness of approximately 17.9 Å, which is very close to the nominal value, while the embedded QDs present a thickness of about 15.6 Å. This result demonstrates that the AlN overgrowth also affects the GaN QDs.

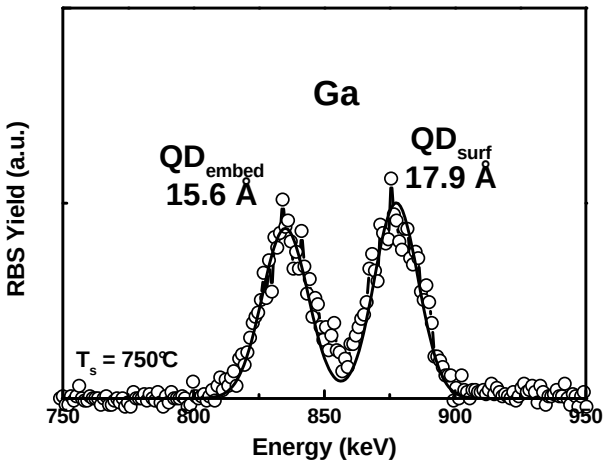

Figure 5.19 : *Measured and calculated (solid line) RBS spectrum of a sample containing two identical GaN QD layer, about 18 Ånominally thick, one embedded in AlN and the other one on the surface. The substrate temperature was fixed at 750° C for the growth of both samples. The surface channels are marked by the corresponding elements.*

5.2.4 Origin of thickness reduction

We performed TEM experiments in order to verify the thickness reduction revealed by the RBS measurements (Figure 5.19) and to identify the origin of this effect.

In the HRTEM image of Figure 5.20 two GaN QDs are illustrated, one uncapped and one embedded in a AlN matrix. By outlining the shape of the dots we can clearly see that the size of the embedded one is reduced compared to the free-standing QD.

From the analysis of the GaN/AlN QW systems (section 4.2.2), we have demonstrated that the thinning of the GaN nanostructures occurs at the top GaN/AlN interface. In order to understand the effect of the AlN cap layer on the GaN QDs, it is important to know how the AlN covers the islands. Does AlN envelops the GaN QD layer (dots and wetting layer) from the first steps of the growth or does AlN grows laterally between the dots in order to smooth the surface, and afterwards vertically?

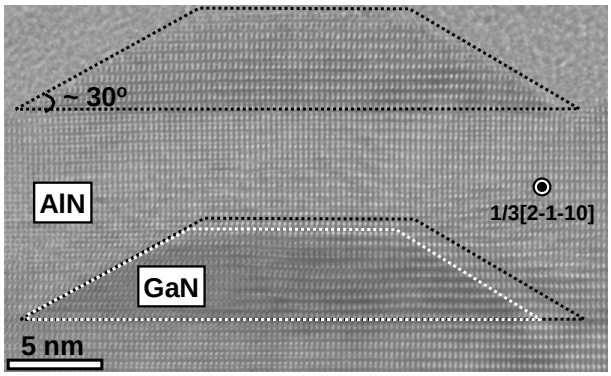

Figure 5.20 : *HRTEM image taken along the [2,-1,-1,0] zone axis of two GaN QDs: one uncapped above an embedded one.*

To answer this question, we have performed TEM experiments in a sample[4] consisting of a superlattice of GaN QDs , grown at 730°C inside an AlN matrix. In this sample the thickness of the AlN layer was either equal to 10 or 20 nm (spacer 1) or equal to 1 or 2 nm (spacer 2).

Figure 5.21 is a cross-section HRTEM image, taken along the [0,1,-1,0] zone axis, in which spacer 1 is 10 nm and spacer 2 is 2 nm. We can observe that QDs which are embedded inside spacer 1, present a smooth top surface. On the contrary, for QDs embedded in spacer 2, the roughness induced by the underlying GaN QD layer is reproduced at the AlN surface. Based on these observations, we could conclude that *the AlN cap layer wets and covers totally the GaN QDs from the first stage of the overgrowth.* This results is in contrast with the InP/GaInP [37] or InAs/GaAs [21] systems, where the capping process occurs first by lateral growth followed by vertical growth.

Another question that we wanted to clarify using HRTEM experiments, was whether the GaN decomposition affects the wetting layer. For this purpose, we have analyzed the same sample used for the investigation of the structural properties of GaN QWs.s We remind that the sample apart from the QWs also contained two series of QDs embedded into AlN grown at 750°C for the first (QDs1) and at 700°C for the second one (QDs2).

In the HRTEM image of Figure 5.22, the two nominally 1.5 nm thick GaN QDs layers embedded into an AlN matrix grown under different temperatures are illustrated. The corresponding to the outline area interplanar distances profile is superimposed to the image. From measurements realized by the projection method, we observed that the thickness of the wetting layer of the dots which are capped with an AlN grown at 750°C, can be locally to about 0.25 nm, compared to the 0.5 nm measured for the GaN QDs capped at 700°C. From the literature we know that the thickness of the wetting layer for GaN QDs capped at 730°C [38] or for uncapped [36] ones is equal to about 0.5 nm. This result demonstrates that the AlN overgrowth process affects the wetting layer.

[4]Sample name S676.

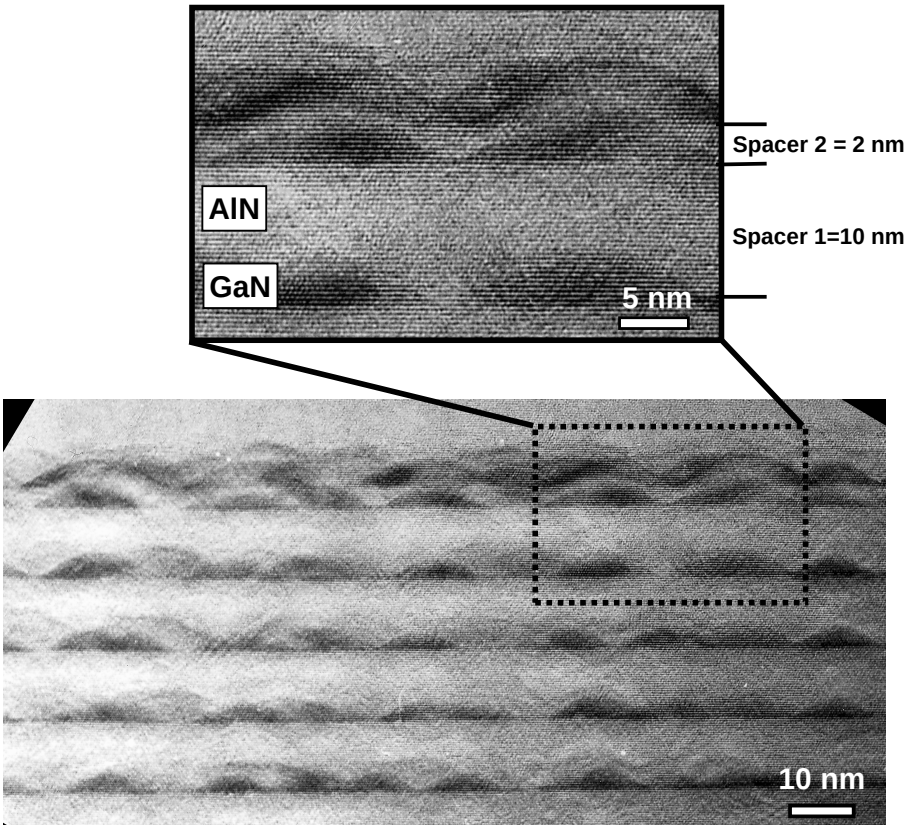

Figure 5.21 : *HRTEM image, viewed along the [0,1,-1,0] directions, of a GaN/AlN QDs superlattice grown at 730° C. If the AlN spacer is thick enough, a smooth AlN top surface is observed. By contrast, if the spacer is very thin (∼20 Å), the roughness induced by the GaN QD layer is reproduced at the AlN top surface.*

In order to investigate where the thickness/size reduction of the GaN QDs, (see Figures 5.19 and 5.20), is taking place, the reduced TEM sample thickness constituted an obstacle. In particular, in the areas where the HRTEM images were acquired the sample thickness was in the order of 10 nm and, because of its wedge-shaped it was getting smaller as we approached the sample surface. As a result, in our HRTEM images we can not be certain that the average intensity contrast that we see in the images is coming from the whole dots or only a part of the hexagonal pyramid. Especially in the latest case we can not be sure how and where exactly this cut took place. This effect is visualized in the HRTEM image of Figure 5.23, where the dimensions of the two neighborhood GaN QDs are different and moreover we can distinguish between them the presence of a third one.

To overcome this problem, Atomic Force Microscopy (AFM) experiments were performed. In particular, with purpose to investigate where the thickness/size reduction of the GaN QDs occurs, we have studied how the (0001), the $(1\bar{1}03)$ and the total free surface

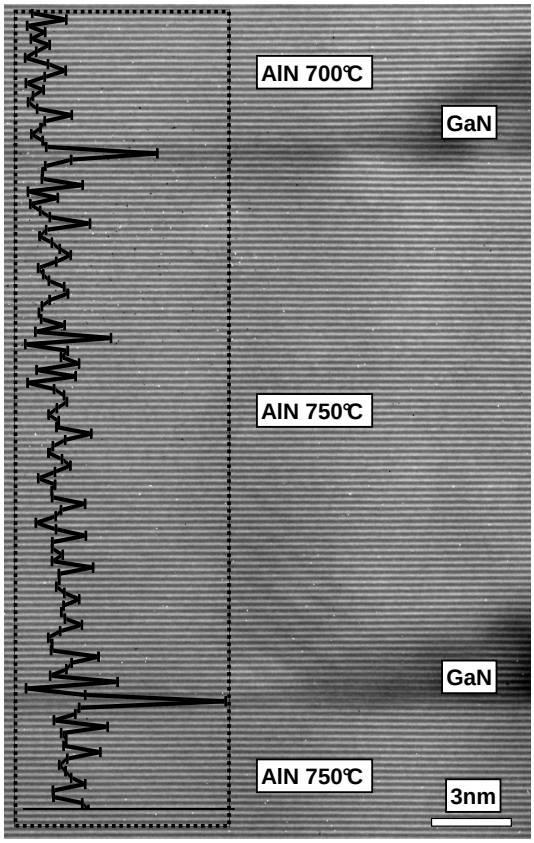

Figure 5.22 : *Off axis HRTEM image of the wetting layers of two GaN QDs capped into an AlN matrix at 700° C (top one) and 750° C (bottom one). The corresponding to the outline area (0002) interplanar distances profile is superimposed to the image. The thickness of the wetting layer of the bottom QD (AlN grown at 750° C) was reduced to about 2.5 Å.*

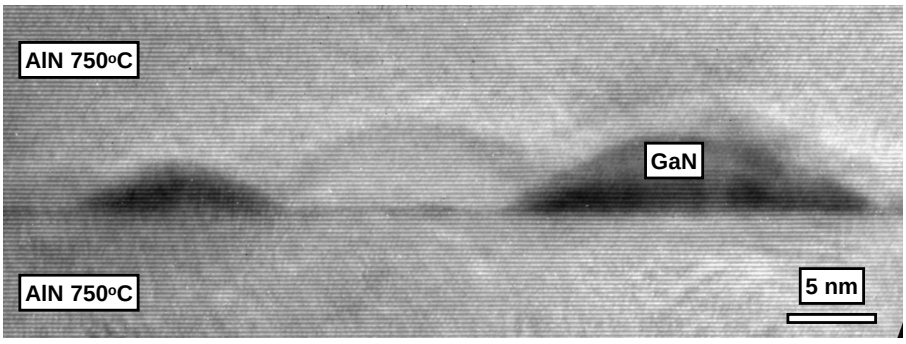

Figure 5.23 : *HRTEM image, viewed along the [0,1,-1,0] zone axis, of GaN QDs embedded inside an AlN matrix grown at 750° C. Due to the very thin TEM sample the exact size of the dots is difficult to be calculated.*

of GaN varies as a function of the amount of GaN nominally deposited. The surfaces were calculated from AFM data obtained by the analysis of the GaN QD layer situated at the surface [36]. The results are shown in Figure 5.24. The total surface of GaN consisted of both the $\{0001\}$ surface and of the $\{1\bar{1}03\}$ surface remains approximately constant. In particular, the $\{0001\}$ surface corresponds to the top of the GaN QDs and the wetting layer orientation, while the $\{1\bar{1}03\}$ surface corresponds to the facets of the dots.

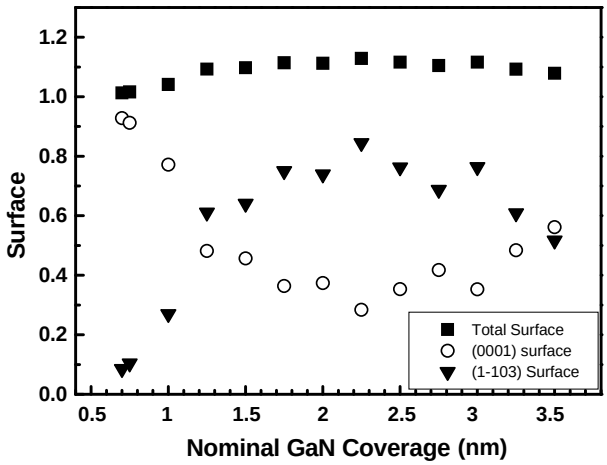

Figure 5.24 : *Variation of the total surface of the GaN QDs layer and the (0001) and the (1$\bar{1}$03) surfaces, corresponding respectively to the island top plus wetting layer and to the facets, as a function of the amount of GaN nominally deposited. Surfaces have been calculated from AFM data [36].*

We notice that for low coverage ($\Theta <$ 1.3 nm) the (0001) surface is dominant, whereas for GaN coverage larger than 1.3 nm it is the (1$\bar{1}$03) surface which becomes dominant. However, for GaN coverage up to 2 nm, the thinning of the GaN QD layer remains unchanged whatever is the dominant surface. This is shown in Figure 5.25. This result indicates that the overgrowth process influences not only the wetting layer but also the dots and that the two surfaces have an equal thickness reduction. It means that the GaN island decomposition certainly occur isotropically, contrary to the InAs/GaAs system where the capping process induces an anisotropic modification of the island shape [21].

5.2.5 Effect of relaxation

Figure 5.25 obtained by RBS, displays the variation of the thinning of a capped GaN QD layer as a function of the nominal amount of GaN deposited before stopping the growth under vacuum. This diagram is quite different compared to the results obtained for the QW system (see figure 4.25). In particular, we observe that the thinning of the GaN QD layer remains approximately constant for GaN coverage up to 20 Å, and it increases unambiguously for larger coverage.

Based on this result, one may wonder why the reduction thickness of the GaN nanostructure increases for a GaN coverage higher than 20 Å. To understand this feature, we must recall that in the specific case of GaN QDs grown on AlN at 750°C with the modified Stranski-Krastanov growth mode, the relaxation state of the GaN QD layer depends on the GaN coverage. In fact, for $\theta \leq$20 Å, elastically relaxed GaN QDs are connected to the buffer layer by a continuous 2D wetting layer perfectly matched to AlN and about 5 Å thick. However, for coverage higher than 20 Å, the islands are formed on a partially relaxed 2D GaN layer, thicker than 5 Å and with the presence of misfit dislocations [36]. As a result, by comparing this information with the data plotted in Figures 5.25, 5.22,

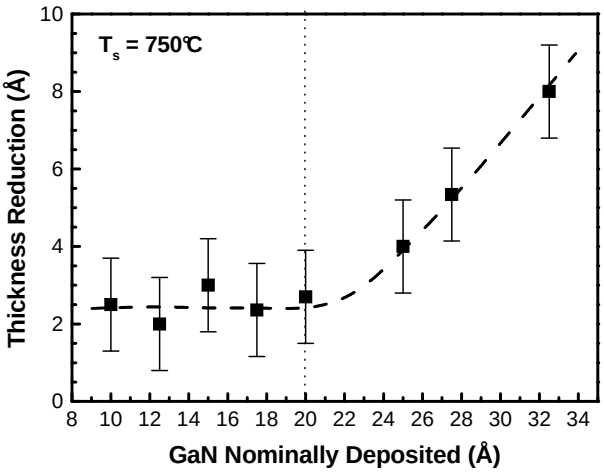

Figure 5.25 : *Variation of the thickness reduction of GaN QD layer grown and embedded in AlN at 750°C as a function of the amount of GaN nominally deposited.*

and 5.24, we can conclude that there is a strong correlation between the thinning of the GaN nanostructure and its relaxation state. Hence, for $\theta \leq$20 Å, the Al/Ga exchange is homogeneous for both the wetting layer and the islands. By contrast, for $\theta \succeq$20 Å, the increase of the QD layer thinning should result from an enhancement of the Al/Ga exchange in the partially relaxed 2D GaN layer due to the presence of misfit dislocations. However, it is important to note that so far, by Fourier filtering HRTEM images of the investigated sample, taken along the [2,-1,-1,0] zone axis, the presence of misfit dislocations could not be confirmed.

5.2.6 Conclusion

We have studied in this section, the influence of the AlN overgrowth process on the structural properties of GaN quantum dots grown on AlN. We have demonstrated that the capping process lead to an isotropic reduction of the island size. This thickness/size reduction, as for the case of QW structures, was attributed to an exchange mechanism between the Al atoms of the cap layer and the Ga atoms from the nanostructure. This exchange depends on the relaxation state of the GaN layer as explained previously.

Bibliography

[1] F. Widmann, J. Simon, B. Daudin, G. Feuillet, J. L. Rouvière, N. T. Pelekanos, and G. Fishman. *Phys. Rev. B*, 58(24):R15989, 1998.

[2] B. Damilano, N. Grandjean, F. Semond, J. Massies, and M. Leroux. *Appl. Phys. Lett.*, 75(7):962, 1999.

[3] S. Nakamura, S. Pearton, and G. Fosol. *The blue laser diode : The complete story.* Springer - Verlag, Berlin, 2000.

[4] M. Arlery, J. L. Rouviere, F. Widmann, B. Daudin, G. Feuillet, and H. Mariette. *Appl. Phys. Lett.*, 74(22):3287, 1999.

[5] A.D. Andreev and E.P. O'Reilly. *Phys. Rev. B*, 62(23):15851, 2000.

[6] J. Gleize, J. Frandon, F. Damangeot, M.A. Renucci, C. Adelmann, D. Daudin, G. Feuillet, B. Damilano, N. Grandjean, and J. Massies. *Appl. Phys. Lett.*, 77:2174, 2000.

[7] B. Daudin, F. Widmann, G. Feuillet, Y. Samson, M. Arlery, and J. L. Rouvière. *Phys. Rev. B*, 56:R7069, 1997.

[8] J. L. Rouviere, J. Simon, N. Pelekanos, B. Daudin, and G. Feuillet. *Appl. Phys. Lett.*, 75:3562, 1999.

[9] M.J. Hÿtch, E. Snoeck, and R. Kilaas. *Ultramicroscopy*, 74:131, 1998.

[10] V. Chamard, T. Schülli, M. Sztucki, T. H. Metzger, E. Sarigiannidou, J. L. Rouvière, M. Tolan, C. Adelmann, and B. Daudin. *Phys. Rev. B*, 69:125327, 2004.

[11] F. Widmann, B. Daudin, G. Feuillet, Y. Samson, J. L. Rouviere, and N. Pelekanos. *J. Appl. Phys.*, 83:7618, 1998.

[12] J.L. Rouviere and E. Sarigiannidou. *Ultramicroscopy to appear.*

[13] A.F. Wright. *J. Appl. Phys.*, 82(6):2833, 1997.

[14] I. Kegel, T. H. Metzger, J. Peisl, J. Stangl, G. Bauer, and D. Smilgies. *Phys. Rev. B*, 60:2516, 1999.

[15] C. Adelmann. *Growth and Strain Relaxation Mechanisms of Group III Nitride Heterostructures.* PhD thesis, Université Joseph Fourier, Grenoble 1.

[16] Q. Xie, A. Madhukar P. Chen, , and N.P. Kobayashi. *Phys. Rev. Lett.*, 75:2542, 1995.

[17] F. Liu, S.E. Davenport, H.M. Evans, and M.G. Lagally. *Phys. Rev. Lett.*, 82:2528, 1999.

[18] X. W. Lin, Z. Liliental-Weber, J. Washburn, E. R. Weber, A. Sasaki, A. Wakahara, and Y. Nabetani. *J. Vac. Sci. Technol. B*, 12:2562, 1994.

[19] J. M. Gerard, J. Y. Marzin, G. Zimmermann, A. Ponchet, O. Cabrol, D. Barrier, B. Jusserand, and B. Sermage. *Solid-State Electronics*, 40:807, 1996.

[20] J. M. Garcia, G. Medeiros-Ribeiro, K. Schmidt, T. Ngo, J.L. Feng, A. Lorke, J. Kotthaus, and P. M. Petroff. *Appl. Phys. Lett.*, 71:2014, 1997.

[21] P. B. Joyce, T. J. Krzyzewski, G. R. Bell, and T. S. Jones. *Appl. Phys. Lett.*, 79:3615, 2001.

[22] H. Heidemeyer, S. Kiravittaya, C. Muller, N. Y. Jin-Phillipp, and O. G. Schmidt. *Appl. Phys. Lett.*, 80:1544, 2002.

[23] F. Ferdos, S. Wang, Y. Wei, M. Sadeghi, Q. Zhao, and A. Larsson. *J. Crystal Growth*, 251:145, 2003.

[24] G. D. Lian, J. Yuan, L. M. Brown, G. H. Kim, and A. Ritchie. *Appl. Phys. Lett.*, 73:49, 1998.

[25] F. Y. Chang, C. C. Wu, and H. H. Lin. *Appl. Phys. Lett.*, 82:4477, 2003.

[26] Q. Xie, P. Chen, and A. Madhukar. *Appl. Phys. Lett.*, 65:2051, 1994.

[27] H. Y. Liu, X. D. Wang, J. Wu, B. Xu, Y. Q. Wei, W. H. Jiang, D. Ding, X. L. Ye, F. Lin, J. F. Zhang, J. B. Liang, and Z. G. Wang. *J. Appl. Phys.*, 88:3392, 2000.

[28] M. Arzberger, U. Kasberger, G. Bohm, and G. Abstreiter. *Appl. Phys. Lett.*, 75:3968, 1999.

[29] R. Songmuang, S. Kiravittaya, and O. G. Schmidt. *J. Crystal Growth*, 249:416, 2003.

[30] A. Hesse, J. Stangl, V. Holy, T. Roch, G. Bauer, O. G. Schmidt, U. Denker, and B. Struth. *Phys. Rev. B*, 66:085321, 2002.

[31] Z. Zhong, J. Stangl, F. Schaffler, and G. Bauer. *Appl. Phys. Lett.*, 83:3695, 2003.

[32] P. Sutter, E. Mateeva, and G. Lagally. *J. Vac. Sci. Technol. B*, 16:1560, 1998.

[33] O. G. Schmidt, U. Denker, K. Ebert, O. Kienzle, and F. Ernst. *Appl. Phys. Lett.*, 77:2509, 2000.

[34] A. Rastelli, E. Muller, and H. von Kanel. *Appl. Phys. Lett.*, 80:1438, 2002.

[35] P. Sutter and M. G. Lagally. *Phys. Rev. Lett.*, 81:3471, 1998.

[36] N. Gogneau, D. Jalabert, E. Monroy, T. Shibata, M. Tanaka, and B. Daudin. *J. Appl. Phys.*, 94:2254, 2003.

[37] M. K.-J. Johansson, U. Hakanson, M. Holm, J. Persson, T. Sass, J. Johansson, C. Pryor, L. Montelius, W. Seifert, L. Samuenson, and M.-E. Piston. *Phys. Rev. B*, 68:125303, 2003.

[38] C. Adelmann, N. Gogneau, E. Sarigiannidou, J. L. Rouviere, , and B. Daudin. *Appl. Phys. Lett.*, 81:3064, 2002.

Chapter 6

Mg Doping of GaN layers

In this chapter, we investigate the effects of Mg doping on the structural and optical properties of GaN with nominal N-face polarity. TEM experiments will demonstrate the polytype conversion of a GaN layer from wurtzite (2H-) to zinc-blende (3C-) structure for Mg concentrations as low as $[Mg_{SIMS}] = 3 \times 10^{18}\, atoms/cm^3$. *The alignment of the cubic phase with the [111] axis perpendicular to the substrate will be also revealed [1, 2]. The way the optical characteristics of GaN:Mg layers are influenced by the presence of the cubic polytype will be also discussed [1].*

6.1 Introduction

The achievement of p-type wurtzite GaN by Mg-doping in metalorganic chemical vapor deposition (MOCVD) was a critical step that propelled the development of GaN optoelectronics [3]. Nowadays magnesium is the most widely used acceptor in III-nitride technology, despite its high thermal activation energy of ∼200 meV. Plasma-assisted molecular-beam epitaxy (PAMBE) presents some advantages for the synthesis of p-type doped GaN, derived from the lower temperature growth when compared with metalorganic vapor phase epitaxy (MOVPE). Therefore, the formation of compensating Mg complexes is reduced [4] and sharper doping profiles are possible [5]. However, the high vapor pressure of Mg at standard GaN growth temperatures by PAMBE results in a low Mg incorporation efficiency [5–7], and segregating Mg can modify the growth kinetics of GaN.

6.2 Experimental conditions

The samples used in this study consisted of 0.6 to 1.7 μm of Mg-doped GaN with nominal *N-face polarity*. They were grown by PAMBE on either C-face 4H-SiC [8] or

on c-plane sapphire [9]. The substrate temperature was equal to 680-700°C. The results presented in this study are **independent of the substrate**. All investigated samples showed n-type conductivity. The incorporation of Mg has been quantified by secondary ion mass spectroscopy (SIMS), using a Cs+ primary ion beam with an incident angle of 50° and an impact energy of 2 keV. Photoluminescence (PL) was measured by exciting with the 334 nm line of an Ar+ laser, with an excitation power of 1 mW.

We remind that, in the case of GaN growth by PAMBE, optimum Ga-face GaN is achieved with 2 monolayers (ML) of Ga excess (Ga bilayer) adsorbed at the growing surface [10, 11]. In the case of N-face GaN, the stabilization of the second Ga monolayer is not possible, and optimum growth is performed with only 1 ML of Ga excess [8]. Small Mg doses (∼0.2 ML) are known to behave as a surfactant on Ga-face GaN which smoothes the rough N-rich-grown surface [12]. Larger Mg doses (∼1 ML) lead to a transition from Ga-face to N-face material [13].

6.3 Optical properties

The obtained optical characteristics of GaN:Mg layers, analyzed by photoluminescence (PL), are summarized in Figure 6.1. We clearly see that for the case of heavily Mg-doped GaN layers with N-face polarity ($[Mg]_{SIMS} > 2 \times 10^{18} cm^{-3}$) a broad blue band appears around 2.8-2.9 eV, similar to the blue band in heavily Mg-doped Ga-polarity GaN layers grown by MOVPE ($[Mg]_{SIMS} \geq 1 \times 10^{19} cm^{-3}$) [14, 15]. We need to mention that this blue band has not be observed in any of our Mg-doped Ga-polarity GaN samples ($[Mg]_{SIMS} \leq 4 \times 10^{19} cm^{-3}$) in agreement with the data reported in the work of Leroux *et. al* for MBE-grown samples [14].

We know from the literature that high Mg doping results in the formation of structural defects. Specifically, for samples grown with MOVPE, the introduction of Mg with concentrations higher than $2 \times 10^{19} cm^{-3}$ results in the formation of pyramidal inversion domains and the observed blue PL band is related to them [16, 17]. These pyramidal inversion domains were observed in both Ga- and N- polarity samples. Their orientation depends on the polarity of the material and their tip always points toward the $[000\bar{1}]$ direction [18].

In GaN samples grown by MBE using a Si-polar 6H-SiC as substrate, Ramachandran *et al.* found that Mg exposures of 1.2 ± 0.4 ML or more lead to an inversion of the sample polarity from Ga-face to N-face through a basal inversion domain boundary [13]. However, the opposite inversion, from N-face to Ga-face, couldn't be achieved. The same inversion of the polarity (from Ga-face to N-face) has also reported by Romano *et al.* again in MBE grown GaN samples using this time an undoped GaN film grown by MOCVD on c-plane sapphire as substrate and for sufficiently high Mg concentrations (about $8 \times 10^{19} cm^{-3}$) [19].

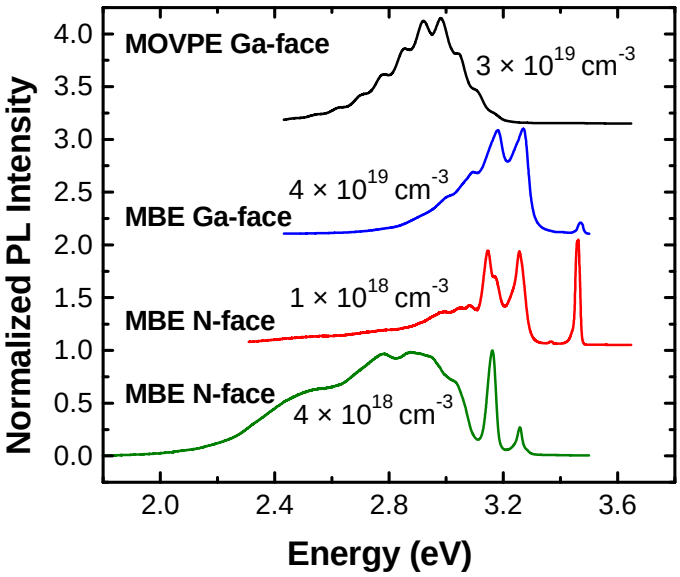

Figure 6.1 : *Typical low temperature (10 K) photoluminescence spectra of Mg-doped GaN samples with either Ga polarity or N polarity and grown either by PAMBE or MOVPE. The atomic Mg concentration measured by SIMS is indicated in the figure.*

At the interface between the undoped and the Mg doped GaN film, an inversion domain boundary with facets along the $\{h, h, -2h, l\}$ and $\{0001\}$ planes was observed.

In MOCVD grown GaN samples and for Mg concentrations higher than $10^{20} cm^{-3}$ inversion domains and a reduction in the hole concentration was observed [20]. The blue PL band has also been observed in MOCVD GaN samples for Mg concentrations higher than $\approx 2.4 \times 10^{19} cm^{-3}$. The blue luminescence was attributed to Mg-nitrogen vacancy (V_N) complexes [21, 22].

In Mg-doped GaN crystals grown with the high nitrogen pressure solution (HNPS) method [23] two different type of defects were observed depending on the polarity of the samples [24, 25]. In particular, tetrahedral defects with a triangular or rectangular shape were found in samples presented Ga-polarity, while planar defects consisted of inversion domain pairs were detected in samples with N-polarity.

As a result, it is obvious that Mg doping influence the microstructure of GaN films independent of the grown mode and the substrate. TEM experiments were realized in order to investigate the structural quality of our samples and to detect the presence of the previously mentioned defects which could justify the observed blue band in our PL spectra. The results are discussed in the next section.

6.4 TEM measurements

In order to determine the origin of the different photoluminescence features, two samples were examined with TEM. The first one[1] consisted of 540 nm Mg-doped GaN layer

[1]Sample name E391.

grown by PAMBE on a C-face 4H-SiC substrate. The Mg concentration, measured by SIMS, was equal to $2.9 \times 10^{18} cm^{-3}$. Since, as we have mentioned above the results were independent of the substrate, the second sample[2] was grown on *c*-plane sapphire. The thickness of the GaN:Mg layer was nominally equal to 1.7 μm and the concentration in Mg was equal to $1 \times 10^{17} cm^{-3}$. Both samples presented nominally N-face polarity.

Before presenting the TEM results it is important to mention that the **Mg concentrations were uniform along the GaN layers**. This can be seen in the SIMS depth profiles displayed in Figure 6.2, of two Mg-doped GaN samples grown under the same conditions, one showing Ga-face polarity, and the other one N-face polarity. What is also visible is that the Mg incorporation rate in Ga-face polarity GaN significantly higher than in N-face polarity layers, as already reported by Ptak *et al.* [7] and in agreement with theoretical predictions by Bungaro *et al.* [26].

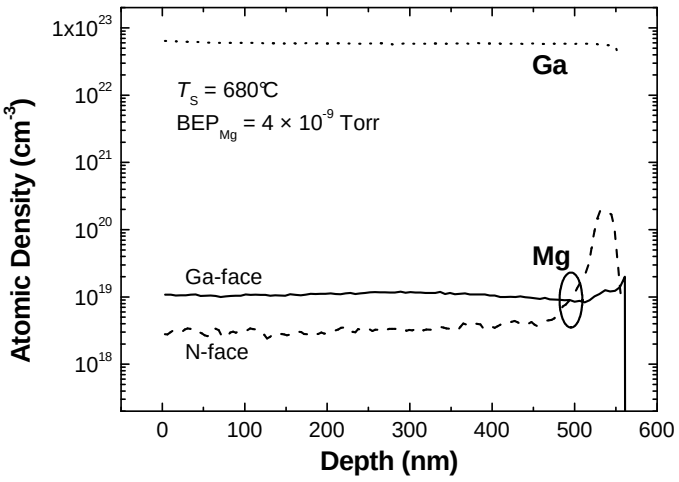

Figure 6.2 : *SIMS depth profiles of the Mg concentration in two Mg-doped GaN with nominal Ga-polarity and N-polarity grown under the same conditions.*

6.4.1 Heavily Mg-doped GaN samples

To our surprise, in the heavily Mg-doped GaN sample we did not detect any inversion domains in the sample structure but we revealed a **cubic ordering** of the GaN lattice with the [111]-axis perpendicular to the substrate. In the conventional two-beam TEM image of Figure 6.3, it is clearly shown that the cubic polytype (3C-GaN) is the dominant polytype although some regions of wurtzite GaN (2H-GaN) are also present in the sample. In the cubic materieal, the presence of stacking faults aligned with the {111} planes is also visible. The total density of stacking faults at ∼280 nm away the substrate was measured equal to around $7 \times 10^9\ cm^{-2}$.

[2]Sample name 140799.

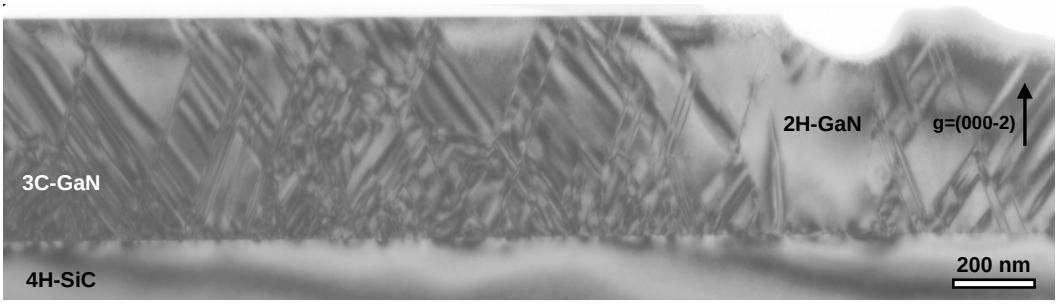

Figure 6.3 : *Two-beam TEM image of the heavily Mg-doped GaN sample. The cubic ordering is the dominant polytype in the sample. Stacking faults aligned with the* {111} *planes are also visible.*

From HRTEM images like the one shown in Figure 6.4 which is taken along the [011] direction, we can see that a thin intermediate region of 2H-GaN exists between the substrate and the 3C-GaN. This region was observed all along the 4H-SiC/GaN interface and its width varied from 3-8 monolayers. From the corresponding diffraction pattern, which is given as an inset in Figure 6.4, we see that the growth axis of the cubic GaN:Mg layer is the [111]. The observed stacking faults are aligned with the {111} planes.

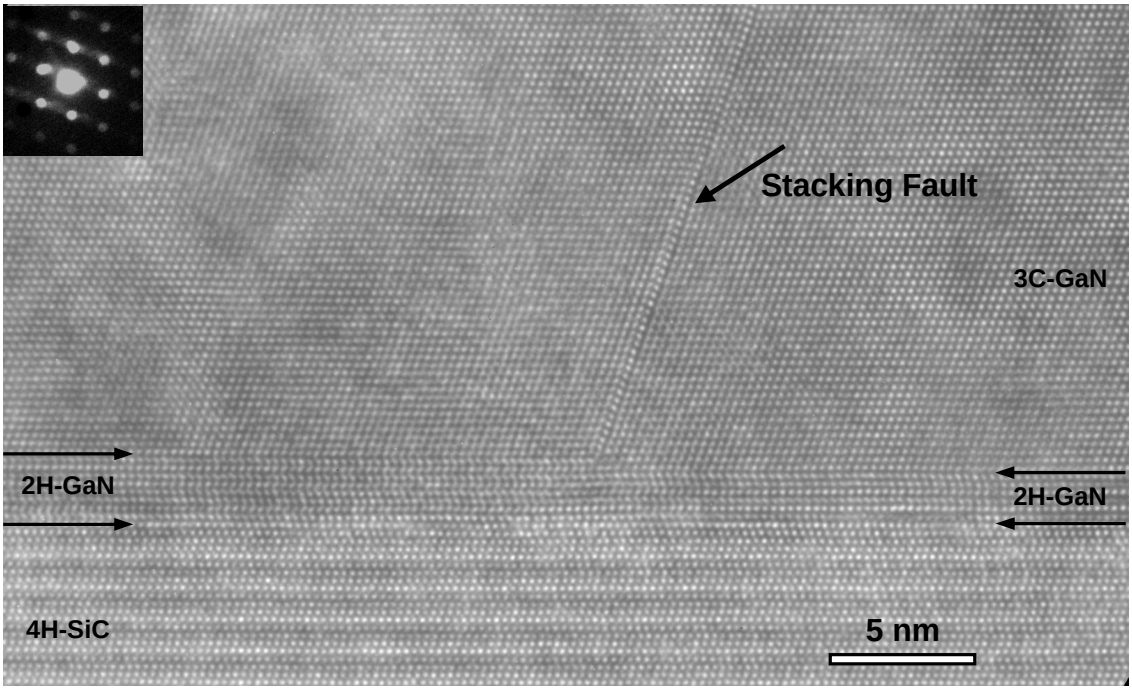

Figure 6.4 : *HRTEM image viewed along the [011] direction of the Mg-doped GaN sample with concentration in Mg equal to* $2.9 \times 10^{18} cm^{-3}$*. The transition from wurtzite to cubic phase occurs 6-8 ML away from the substrate surface. The corresponding diffraction pattern, displayed as an inset reveals the cubic ordering with the [111] axis perpendicular to the substrate.*

In order to examine the strain state of the 3C-GaN:Mg layer, we have measured the lattice parameter α from a series of HRTEM images with the GPA. In particular, we applied a gaussian mask of size $\sim \mathbf{g}/9$ around the {111} and the {200} reflections. The procedure was repeated in 6 HRTEM images, obtaining the average values:

- $\alpha_{\{111\}} = 0.451 \pm 0.004\ nm$
- $\alpha_{\{200\}} = 0.450 \pm 0.004\ nm$

The obtained values are in good agreement with the values reported in the literature for the lattice constant of cubic 3C-GaN [27, 28]. Therefore, we can conclude that the 3C-GaN:Mg layer is almost relaxed. This is in good agreement with high-resolution X-ray diffraction (HRXRD) measurements performed in the heavily Mg-doped GaN samples [1].

In this point we need to mention that a typical $2\Theta/\Omega$ HRXRD scan for a Ψ angle of 0.42^o could not detect if the structure of a heavily Mg-doped GaN layer is hexagonal or cubic. This is because in such a spectra, in addition to reflections from the hexagonal silicon carbide substrate, we found contributions which could originate either from the hexagonal or from the cubic phase (Figure 6.5 (a)). Once the TEM measurements revealed the cubic phase in a heavily doped sample, HRXRD measurements were again performed but this time for an angle Ψ equal to 55.19^o. This time, as shown in Figure 6.5 (b), only the reflections from the cubic phase, namely the (002)-peak and higher orders, contribute to the signal. The HRXRD experiments confirmed the alignment of the cubic phase with the [111]-axis perpendicular to the substrate, as the (002) cubic reflection was located very close to its theoretical value and its Φ-scan presented the six-fold symmetry characteristic of the [111] rotation axis. The diffractograms given in Figure 6.5 were measured from a sample with concentration in Mg equal to $3.8 \times 10^{18} cm^{-3}$, in which we found no indication of the presence of hexagonal GaN phase.

The previous TEM and HRXRD results demonstrate that Mg behaves as a surfactant on N-face GaN, favoring the growth of the cubic polytype. However, there are no theoretical predictions of a polytype inversion in presence of Mg. *Ab initio* calculations reported by Bungaro *et al.* [26] describe a clearly different behavior of adsorbed Mg atoms on the Ga-face and N-face of GaN. In particular, at the Ga-polar surface, the most stable configuration is incorporation of Mg on the Ga-substitutional site, and the Mg excess arranges on Ga sites on the surface [26]. However, the energetic equilibrium on the N-polar surface is different and makes the incorporation of Mg unfavorable. A schematic top view of the two last atomic layers of the N-polar surface can be seen in Figure 6.6 (a). As T_3 and H_3 we denote the sites above a subsurface atom and the hollow site, respectively. Under *moderate* Ga-rich or N-rich conditions, Mg prefers remaining on the surface. The most stable

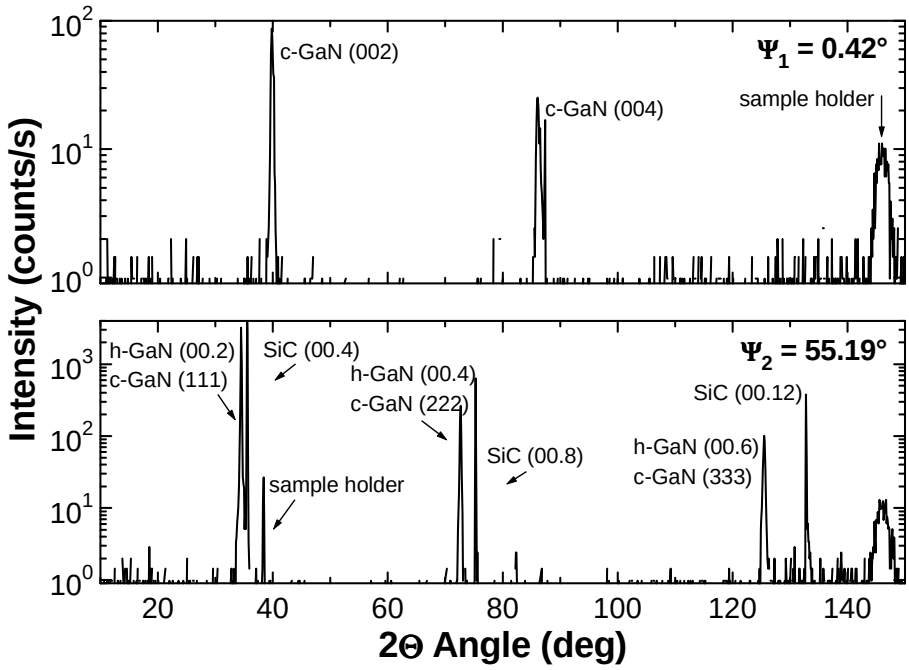

Figure 6.5 : *HRXRD measurements of a heavily Mg-doped GaN layer* $[Mg_{SIMS}] = 3.8 \times 10^{18} cm^{-3}$ *grown on 4H-SiC.* $2\Theta/\Omega$*-scans with* Ψ*-angles of (a)* 0.42^o *and (b)* 55.19^o.

surface configuration is a complex consisting of Ga and Mg on the H_3 site [26]. Under *highly* Ga-rich conditions, Mg tends to remain in the Ga excess layer, finding a minimum energy in the T_3 or H_3 site. Interstitial Mg atoms on H_3 might reduce the energy for nitrogen incorporation above H_3 [N_{3C} site in Figure 6.6 (b)], inducing the formation of a cubic bond, rotated 60° with respect to the hexagonal bond [N_{2H} site in Figure 6.6 (b)]. To confirm this point further theoretical analysis is necessary.

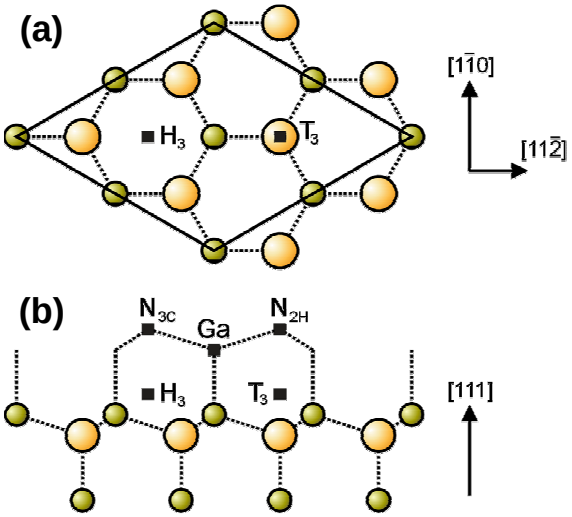

Figure 6.6 : *(a) Top view of the (111) surface. (b) Cross-section of the top atomic layers. In a* T_3 *site an atom sits above a subsurface atom, whereas an atom in the* H_3 *site sits on the hollow site. The solid-line rhomboid indicates the 2x2 cell.*

Magnesium is not the only dopant that favors the 3C-polytype of the GaN lattice. It has been reported that beryllium (Be) induce inversion domains and cubic inclusions in Ga-face wurtzite GaN [29]. Additionally, the deposition of 1 ML of manganese (Mn) also favors the growth of cubic GaN on Ga-face wurtzite GaN [30]. Indeed, both Be and Mn have a tendency to incorporate on interstitial sites in Ga-face GaN [31, 32], the same tendency that Mg on N-face GaN as reported in this section.

6.4.2 Slightly Mg-doped GaN sample

In the second N-face Mg-doped GaN sample, with a concentration of Mg was equal to $1 \times 10^{17} cm^{-3}$, as expected neither phase transition or inversion domain boundaries were observed. The GaN:Mg layer presented wurtzite structure with a total density of dislocations at $\sim 1\mu m$ away the substrate of $9.68 \times 10^{10}\ cm^{-2}$. In particular, from the weak beam images illustrated in Figure 6.7, we measured the density of each of the three types of perfect dislocations which are present in a wurtzite lattice (see also section 2.2.2). Table 6.1 summarize the results concerning the density of the three types of dislocations as measured in the slightly Mg-doped GaN sample at $\sim 1\mu m$ away the substrate.

Dislocation character	**Screw** [0001]	**Edge** $1/3 < 2, -1, -1, 0 >$	**Mixed** $1/3 < 2, -1, -1, 3 >$
Density ($\times 10^{10}\ cm^{-2}$)	1.48	7.39	0.78
Proportion (%)	15.3	76.6	8.1

Table 6.1 : *Dislocation Density and relative proportion of the three types of dislocations present at the slightly Mg-doped GaN sample. The density was measured at* $\sim 1\mu m$ *away the substrate*

6.4.3 Interpretation of the PL spectra

Once the TEM experiments revealed the presence of the cubic phase in highly Mg-doped GaN samples, the complete interpretation of the corresponding PL spectra, shown in Figure 6.1, was possible. This is because the optical characteristics of GaN:Mg layers are very sensitive to the presence of the cubic polytype since the latter has a smaller bandgap than the wurtzite material. In the case of PAMBE-grown **Ga-face GaN**, PL spectra are dominated by a phonon-replicated donor-acceptor pair at ∼3.27 eV, related to the Mg shallow acceptor level (Figure 6.1 blue line). For the nominal **N-face polarity** samples and for **low Mg doping**, the main PL emission also corresponds to the donor-acceptor pair related to the Mg shallow acceptor level. They are also accompanied by a

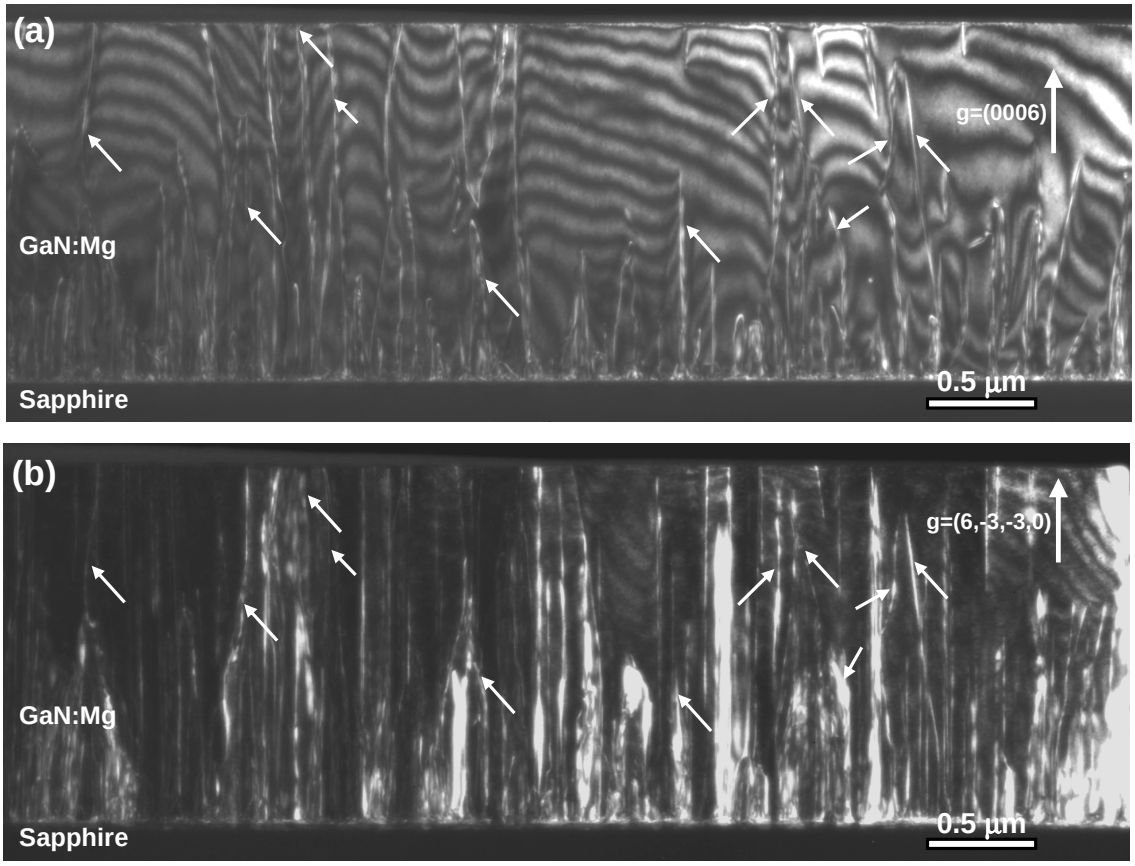

Figure 6.7 : *Weak beam images viewed along the [0,1,-1,0] direction of the examined slightly Mg-doped GaN sample. (a) Conditions (g,3g) with* $\mathbf{g}$*=(0002). Only screw and mixed dislocations are in contrast. (b) Conditions (g,3g) with* $\mathbf{g}$*=(2,-1,-1,0). Only edge and mixed dislocations are in contrast. The arrows indicate the position of the mixed dislocations which are in contrast in both images.*

narrow excitonic emission at 3.452 for samples grown on SiC or at 3.472 eV in samples grown on sapphire. This difference is due to the respective tensile or compressive strain in the epilayers. For the spectra shown in Figure 6.1 as red line the GaN:Mg layer was grown on a sapphire substrate. Finally, for nominal **N-face polarity** samples and for **high Mg doping**, the PL spectra present also a line around 3.25 eV, but this emission displays the behavior of the excitonic luminescence from cubic GaN. A cubic-related donor-acceptor transition at 3.16 eV is also observed, together with a broad blue band around 2.8 eV, previously reported in heavily Mg-doped 3C-GaN(001) [33].

6.5 Conclusions

In this section we have demonstrated that Mg doping favors the polytype conversion from N-face wurtzite (2H-) GaN to zinc-blende (3C-) structure during growth by plasma-assisted molecular-beam epitaxy. The cubic polytype becomes dominant for Mg concentrations higher than $[Mg_{SIMS}] = 3 \times 10^{18} cm^{-3}$. For lower concentrations the GaN:Mg layers presents the wurtzite structure with a dislocation density in the order of $\sim 9.7 \times 10^{10}\ cm^{-2}$. HRTEM experiments revealed an alignment of the cubic phase with the [111]-axis perpendicular to the substrate. This was also confirmed by HRXRD measurements. The optical characteristics of GaN:Mg layers are very sensitive to the presence of the cubic polytype. For low Mg doping, photoluminescence is dominated by a phonon-replicated donor-acceptor pair at ∼3.25 eV, related to Mg shallow acceptor level, accompanied by a narrow excitonic emission. For high Mg doping, the PL spectra are also dominated by a line around 3.25 eV, but this emission displays the behavior of excitonic luminescence from cubic GaN. A cubic-related donor-acceptor transition at ∼3.16 eV is also observed, together with a broad blue band around 2.9 eV, previously reported in heavily Mg-doped 3C-GaN(001).

Bibliography

[1] E. Monroy, M. Hermann, E. Sarigiannidou, T. Andreev, P. Holliger, S. Monnoye, H. Mank, B. Daudin, and M. Eickhoff. *J. Appl. Phys.*, 96:3709, 2004.

[2] E. Sarigiannidou, E. Monroy, M. Hermann, T. Andreev, P. Holliger, S. Monnoye, H. Mank, B. Daudin, and M. Eickhoff. *Phys. Stat. Sol. (c) to appear.*

[3] H. Amano, M. Kito, K. Hiramatsu, and I. Akasaki. *Jpn. J. Appl. Phys.*, 28:2112, 1989.

[4] H. Alves, F. Leiter, D. Pfisterer, D. M. Hofmann, B. K. Meyer, S. Einfeld, H. Heinke, and D. Hommel. *Phys. Stat. Sol. (c)*, 6:1770, 2003.

[5] E. Haus, I. P. Smorchkova, B. Heying, P. Fini, C. Poblenz, T. Mates, U. K. Mishra, and J. S. Speck. *J. Cryst. Growth*, 24:55, 2002.

[6] S. Guha, N. A. Bojarczuk, and F. Cardone. *Appl. Phys. Lett.*, 71:1685, 1997.

[7] A. J. Ptak, T. H. Myers, L. T. Romano, C. G. Van de Walle, and J. E. Northrup. *Appl. Phys. Lett.*, 78:285, 2001.

[8] E. Monroy, E. Sarigiannidou, F. Fossard, N. Gogneau, E. Bellet-Amalric, J.-L. Rouviere, S. Monnoye, H. Mank, and B. Daudin. *Appl. Phys. Lett.*, 84(18):3684, 2004.

[9] M. Stutzmann, O. Ambacher, M. Eickhoff, U. Karrer, A. Lima Pimenta, R. Neuberger, J. Schalwig, R. Dimitrov, P.J. Schuck, and R.D. Grober. *Phys. Stat. Sol. (b)*, 228:505, 2001.

[10] B. Heying, I. Smorchkova, C. Poblenz, C. Elsass, P. Fini, S. Den Baars, U. Mishra, and J. S. Speck. *Appl. Phys. Lett.*, 77:2885, 2000.

[11] C. Adelmann, J. Brault, G. Mula, B. Daudin, L. Lymperakis, and J. Neugebauer. *Phys. Rev. B*, 67:165419, 2003.

[12] V. Ramachandran, R. Feenstra, J. E. Northrup, and D. W. Greve. *Nitride J. Semicond. Res.*, 5S1:W3.65, 2000.

[13] V. Ramachandran, R. Feenstra, W. L. Sarney, L. Salamanca-Riba, J. E. Northrup, L. T. Romano, and D. W. Greve. *Appl. Phys. Lett.*, 75:808, 1999.

[14] M. Leroux, N. Grandjean, B. Beaumont, G. Nataf, F. Semond, J. Massies, and P. Gibart. *J. Appl. Phys.*, 86:3721, 1999.

[15] B. Z. Qu, Q. S. Zhu, X. H. Sun, S. K. Wan, Z. G. Wang, H. Nagai, Y. Kawaguchi, K. Hiramatsu, and N. Sawaki. *J. Vac. Sci. Technol. A*, 21:838, 2003.

[16] P. Vennéguès, M. Benaissa, S. Dalmasso, M. Leroux, E. Feltin, P. De Mierry, B. Beaumont, B. Damilano, N. Grandjean, and P. Gibart. *Materials Science and Engineering B*, 93:224, 2002.

[17] M. Leroux, P. Vennéguès, S. Dalmasso, M. Benaissa, E. Feltin, P. De Mierry, B. Beaumont, B. Damilano, N. Grandjean, and P. Gibart. *Phys. Stat. Sol (a)*, 192(2):394, 2002.

[18] P. Vennéguès, M. Benaissa, B. Beaumont, E. Feltin, P. De Mierry, S. Dalmasso, M. Leroux, and P. Gibart. *Appl. Phys. Lett.*, 77(6):880, 2000.

[19] L.T. Romano, J.E. Northrup, A.J. Ptak, and T.H. Myers. *Appl. Phys. Lett.*, 77(16):2479, 2000.

[20] L.T. Romano, M. Kneissl, J.E. Northrup, C.G. Van de Walle, and D.W. Treat. *Appl. Phys. Lett.*, 79(17):2734, 2001.

[21] U. Kaufmann, M. Kunzer, M. Maier, H. Obloh, A. Ramakrishnan, B. Santic, and P. Schlotter. *Appl. Phys. Lett.*, 72(11):1326, 1998.

[22] U. Kaufmann, M. Kunzer, H. Obloh, M. Maier, Ch. Manz, A. Ramakrishnan, and B. Santic. *Phys. Rev. B.*, 59(8):5561, 1999.

[23] I. Grzegory, J. Jun, M. Bockowski, St. Krukowski, M. Wroblewski, B. Lucznik, and S. Porowski. *J. Phys. Chem. Solids*, 56:639, 1995.

[24] Z. Liliental-Weber, M. Benamara, J. Washburn, I. Grzegory, and S. Porowski. *Phys. Rev. Lett.*, 83(12):2370, 1999.

[25] Z. Liliental-Weber, M. Benamara, W. Swider, J. Washburn, I. Grzegory, S. Porowski, R.D. Dupuis, and C.J. Eiting. *Physica B*, 273-274:124, 1999.

[26] C. Bungaro, K. Rapcewicz, and J. Bernholc. *Phys. Rev. B*, 59:9771, 1999.

[27] H. Morkoç, S. Strite, G.B. Gao, M.E. Lin, B. Sverdlov, and M.Burns. *J. Appl. Phys.*, 76:1363, 1994.

[28] J. Wu, H. Yaguchi, B. P. Zhang, Y. Segawa, K. Onabe, and Y. Shiraki. *Phys. Stat. Sol. (a)*, 180:403, 2000.

[29] A. J. Ptak, L. Wanf, N. C. Giles, T. H. Myers, L. T. Romano, C. Tian, R. A. Hockett, S. Mitha, and P. Van Lierde. *Appl. Phys. Lett.*, 79:4524, 2001.

[30] Y. Cui, V. K. Lazarov, M. M. Goetz, H. Liu, D. P. Robertson, M. Gajdardziska-Josifovska, and L. Li. *Appl. Phys. Lett.*, 82:4666, 2003.

[31] C. G. Van de Walle and J. Neugebauer. *J. Appl. Phys.*, 95:3851, 2004.

[32] G. Thaler, R. Frazier, B. Gila, J. Stapleton, M. Davidson, C. R. Abernathy, S. P. Pearton, and C. Segre. *Appl. Phys. Lett.*, 84:1314, 2004.

[33] D. J. As, T. Simonsmeier, B. Schöttker, T. Frey, D. Schikora, W. Kriegseis, W. Burkhardt, and B. K. Meyer. *Appl. Phys. Lett.*, 73:1835, 1998.

General Conclusions

The aim of this work was the investigation and characterization of GaN/AlN quantum wells and quantum dots heterostructures using TEM techniques. Such heterostructures constitute the active part of various III-nitride based electronic and optoelectronic devices. A thorough structural characterization of heterostructures is necessary for the comprehension and optimization of their growth process, which directly results in the achievement of efficient and reproducible devices.

All the samples studied in this thesis were elaborated by Plasma Assisted Molecular Beam Epitaxy in the laboratory "Nanophysique et Semiconducteurs" (NPSC) of CEA-Grenoble. The very close and fruitful collaboration with the elaborators gave me the opportunity to interact with a number of scientists coming from different fields and having the same goal: improve our knowledge on GaN heterostructures. My thesis work has contributed in the structural characterization of the nitride samples using different TEM techniques.

The basic TEM technique that I have learned and used to characterize quantitatively the different nitride nanostructures was the high-resolution electron microscopy (HRTEM). However, in order to achieve a complete and precise structural characterization of the samples, additional TEM techniques was used. Therefore, to have a general view of the structural quality and to analyze and identify the type of defects (i.e. dislocations, planar defect etc.) which are present at a sample, I have realized conventional TEM (CTEM) experiments in both two-beam and weak-beam conditions. To determine the polarity of the nitride layers, I have applied the Convergent Beam Electron Diffraction (CBED) technique. Finally, to extract information about the chemical composition of the heterostructures I have performed Energy Filtered TEM (EFTEM) measurements.

In particular, concerning the HRTEM images, I have examined in details under which conditions and with which methods I could extract the desirable quantitative information in the most precise way. My effort in realizing this has been exposed in chapter 3.

Two different methods were applied in order to analyze quantitatively the HRTEM images: a projection method (chapter 3.1) and the geometrical phase analysis (GPA) (chap-

ter 3.2). I have invested time to understand, define and optimize the different parameters that influence the precision of either method, in order to obtain the most accurate results. Special attention has been given in the GPA, which is a novel method for analyzing quantitatively HRTEM images. We have tried to approach this method in a more theoretical way by discussing in details its mathematical basis, with purpose to understand why it is so efficient although simple (chapter 3.2.2). We can conclude that both methods are very well adapted in measuring quickly and accurately the local lattice parameters. However, the projection method is more appropriate for the analysis of interfacial profiles (e.g. chapters 4.1.2, 5.1.4, 5.2.4), whereas, GPA has the advantage of being able to measure and map directly displacements and strain fields (e.g. chapters 4.1.2, 4.1.3, 5.1.6).

We hope that the use of the geometrical phase analysis, which is a novel method for measuring and mapping displacement and strain fields from HRTEM images, and especially our theoretical approach, which aimed at understanding this method, will be of interest to other users of this method.

In this thesis, HRTEM images using off-axis conditions were also acquired, in order to increase the contrast and to improve the signal-to-noise ratio (chapter 3.5). In particular, to be able to simulate easily the under investigation structures, secondary zone axis were usually selected. In off-axis images only the (0002) are visible as continuous straight lines. The superiority of the off-axis images was verified in several parts of this thesis. For example, we have seen in chapter 4.1.2 that the precision in calculating the local lattice parameters of an QW heterostructure becomes higher when off-axis HRTEM are used. Another example is given chapter 5.1.6, where we have demonstrated that the use of off-axis images results in increasing the accuracy of our strain measurements.

At the beginning of the second year of my thesis (January 2003), the JEOL4000EX microscope, that I have been served to acquire my HRTEM images, was equipped with an $Ultrascan^{TM}1000$ charge-coupled device (CCD) camera of size (2048 x 2048) pixels. All HRTEM images presented in this manuscript were acquired using the CCD camera. The CCD camera was of a major benefit, because its use has greatly facilitated my research work since, it was possible to realize "on line" a preliminary analysis of the acquired images using the GPA routines in the Digital micrograph software. However, we have seen in chapter 3.4 that the CCD camera introduces distortions in HRTEM images. Once identified, we have proposed in the same chapter a way to correct them. In general, when measuring the displacement or strain with the GPA we have always pay attention that the examined area is situated at the center of the HRTEM image where the distortions related to the image formation system (CCD camera and projection system of the microscope) are less important.

The results concerning the characterization of GaN heterostructures are presented in chapters 4, 5 and 6. It is important to note that the results exposed in each of these chapters concern a selection of the samples analyzed in this thesis. However, the reader can be refer to appendix E where, a list of all examined samples together with the interest of each one of them are given.

The issue of chapter 4 is the structural characterization of GaN/AlN quantum well structures. Two basic themes have been treated.

The first one is the comparison between a Ga-face and a N-face GaN/AlN superlattice (SL). The higher structural quality of the Ga-face SL has been proven. In particular, we found that although the interfaces in the N-face SL are rough with a thickness which varies between 2-3 ML, the interfaces in the Ga-face SL are uniform and abrupt and their thickness does not exceed 1 ML. $\{01\bar{1}0\}$ planar defects were only present in the N-face sample. From the analysis of experimental and simulated HRTEM images, we identified these defects as inversion domain boundaries of the energetically unfavorable Holt model. It is worth noting that both types (1 and 2) of the Holt model were identified in our images. Concerning the strain state of the GaN QWs we deduced that, in the N-face SL they are almost completely strained on the AlN, which is itself strained by the SiC substrate. For the Ga-face sample, by eliminating the possibilities of an GaN/AlN interdiffusion, a partially strained AlN matrix and a relaxation due to the thin foil effect, we concluded that the GaN QWs are only partially strained.

The second one deals with the effects of AlN overgrowth on the structural quality of GaN QWs. Both Rutherford backscattering spectroscopy (RBS) and TEM measurements revealed that the growth of an AlN cap layer on a GaN QW at high temperature (750°C) leads to reduction of the GaN QW thickness. By excluding the possibilities that the thickness thinning is due to a GaN thermal decomposition or to a diffusion of the Al atoms from the cap layer into the GaN well, we have attribute this phenomenon to a thermally activated exchange mechanism between the Al atoms from the cap layer and the Ga atoms from the nanostructure. The TEM measurements have also demonstrate that the Al/Ga exchange mechanism produces an irregular top GaN/AlN interface. Finally, no AlN/GaN intermixing has been observed.

In chapter 5 we have presented the analysis realized on quantum dot structures. In the first part of the chapter we have investigated the strain distribution in a superlattice of GaN QDs embedded in an AlN matrix using HRTEM measurements in combination with theoretical calculations and X-ray diffraction experiments in the grazing incidence geometry. The GaN QDs were synthesized by the Stranski-Krastanov growth mode and

presented a truncated pyramidal shape with $\{1\bar{1}03\}$ facets and an hexagonal base with a height to base ration of 0.14. Using the GPA, we have clearly identified a modulation in the lattice parameter **c** of the AlN matrix depending on whether it is situated between the vertically aligned QDs or consecutive WLs. We have proven that the observed modulation can not be attributed to an interdiffusion between the GaN QDs and the surrounding AlN matrix (EFTEM experiments). Therefore, it is due to a difference in the strain state of the AlN spacer layer. Specifically, in terms of the e_{zz} strain component, we showed that although the AlN located between the GaN QDs is strained, the AlN situated between consecutive WLs is almost fully relaxed. Thus, we have concluded that, it is this local strain generated by the dots on the surrounding matrix which causes the vertical alignment of the dots inside the superlattice. In addition, we have observed that the embedded QDs are compressively strained, in contrast with the uncapped ones which are almost completely relaxed. All these results were in good agreement especially in the AlN areas with: (a) theoretical strain calculations that combine Fourier transform and the Green's function technique and (ii) anomalous grazing incidence x-ray diffraction experiments in which the beam energy was tuned to the Ga-K edge. Concerning the GaN QD areas, TEM results are not very accurate because the dots are cut. Thus, precise information about the strain state of the dots has been provided by x-ray diffraction measurements and theoretical calculations. In the HRTEM images the thin foil relaxation effect was not taken into account based on the good agreement between experimental and calculated values in which a bulk QDs superlattice was used.

In the second part of chapter 5 we have investigated the influence of the capping process on the structural properties of GaN QDs grown on AlN. We have demonstrated with HRTEM and RBS experiments that the capping process lead to an isotropic reduction of the island size. This thickness/size reduction, as for the case of QW structures, was attributed to an exchange mechanism between the Al atoms of the cap layer and the Ga atoms from the nanostructure. Finally, we have proven that this exchange depends on the relaxation state of the GaN layer.

In the last chapter of this thesis (chapter 6), we have investigated the effects of Mg doping on the structural and optical properties of GaN with nominal N-face polarity. We have demonstrated with TEM experiments that Mg doping favors the polytype conversion from wurtzite (2H-) to zinc-blende (3C-) structure. In particular, for Mg concentrations higher than $[Mg_{SIMS}] = 3 \times 10^{18} cm^{-3}$ the cubic polytype becomes dominant while, for lower concentrations the GaN:Mg layers presents the wurtzite structure. We have proven that the alignment of the cubic phase is realized with the [111] axis perpendicular to the substrate. Finally, the optical characteristics of GaN:Mg layers have been analyzed by photoluminescence and has been seen that thye are importantly influenced by the pres-

ence of the cubic polytype. For low Mg doping, photoluminescence is dominated by a phonon-replicated donor-acceptor pair at ∼3.25 eV, related to Mg shallow acceptor level, accompanied by a narrow excitonic emission. For high Mg doping, the PL spectra are also dominated by a line around 3.25 eV, but this emission displays the behavior of excitonic luminescence from cubic GaN. A cubic-related donor-acceptor transition at ∼3.16 eV is also observed, together with a broad blue band around 2.9 eV.

Having recalled the principal results of the different chapters, we want to stress on the results we considered the most important. The contribution of other experimental techniques like X-ray Diffraction (XRD)(e.g. chapters 4.1 and 5.1.6), Rutherford backscattering spectroscopy (RBS)(chapters 4.2 and 5.2), Atomic Force Microscopy (chapter 5.2) and photoluminescence (chapter 6.3) together with theoretical calculations (chapter 5.1.6) was necessary for one hand to obtain complementary information about the quality of the examined nitride structures and for the other hand to overcome problems when reaching the limits of TEM techniques (e.g. limitations due to the reduced TEM sample thickness).

We would like to emphasize the combination of TEM with X-ray techniques. In particular, the association of TEM with X-ray Diffraction (XRD) reciprocal space mapping allow us to have the certitude that our reference area in GPA correspond indeed to an area where the crystal has its bulk lattice parameters (chapter 4.1).

Additionally, in chapter 5.1 we have demonstrated that by combining TEM (high-resolution and energy filtered) with X-ray diffraction measurements in the grazing incidence geometry, a complete and accurate information about the strain distribution in complex system like a quantum dot superlattice can be achieved. However, it is important to mention that for such a system due to the small amount of material (nominal thickness of GaN QDs ∼ 1.5 nm), X-ray investigations are possible only by the use of a highly brilliant x-ray beam delivered by the third generation synchrotron facilities. The two methods are complementary since in x-ray diffraction measurements an input structural model (necessary to determine the form factor) is required for the data analysis and TEM can give information about the parameters involved in this model (absence of interdiffusion, morphology of the dots, vertical alignment of the dots etc.). On the other hand, TEM measurements concerning the strain of GaN QDs are not so accurate since, due to the reduced TEM sample thickness the GaN QDs are cut (GaN QD hexagonal base (∼ 30 nm) > TEM sample thickness (∼5-20 nm)). In this case, x-ray diffraction can bring complementary results to TEM since it offers the possibility to extract accurate information concerning the strain distribution of the GaN QDs.

An originality of this thesis is the use of off-axis HRTEM images to provide infor-

mation about the local lattice parameters of a nitride nanostructure (quantum wells and quantum dots) and consequently about local strain.

In our effort to combine TEM with X-ray techniques we have also performed X-ray absorption spectroscopy experiments on GaN QDs superlattices at the Ga K-edge. These experiments have not been described in the main parts of the thesis but are shown in Appendix F. These preliminary results are very encouraging.

This thesis has given more insights in the structural characterization of GaN/AlN heterostructures but more experimental studies will be still necessary to understand completely the GaN/AlN system. X-ray absorption spectroscopy are part of these future new experimental studies. As far as TEM is concerned, more insights will be certainly gained with Cs-corrected microscopes, holography and 3D-tomography.

APPENDICES

Appendix A

Crystallographic relationships for the hexagonal lattice

In the hexagonal crystal structure, the Miller-Bravais system of indexing directions is not easy to visualize. In the Miller-Bravais notation the hexagonal system is described by four axes, three of which are coplanar. The three coplanar axes, named $\overrightarrow{a}_1$, $\overrightarrow{a}_2$ and $\overrightarrow{a}_3$, lie in the basal plane of the lattice and they are 120^o apart. The fourth axis, $\overrightarrow{c}$, is normal to this plane. This is shown in Figure A.1 where a schematic illustration of the wurtzite structure viewed along the [0001] direction and the associated diffraction pattern are illustrated. One of the easier ways to find the four-dimensional components of a vector from any three-dimensional representation is to consider its projection on to the crystallographic axes $\overrightarrow{a}_1$, $\overrightarrow{a}_2$, $\overrightarrow{a}_3$ and $\overrightarrow{c}$, which have the directions $[2\bar{1}\bar{1}0]$, $[\bar{1}2\bar{1}0]$, $[\bar{1}\bar{1}20]$ and [0001] respectively.

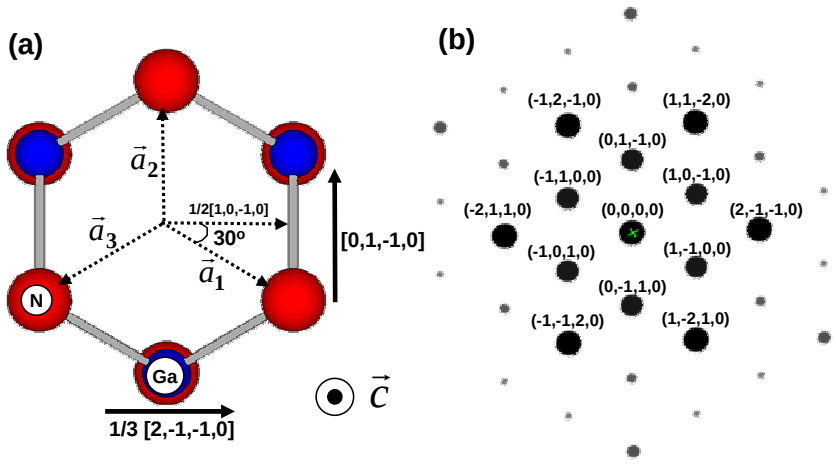

Figure A.1 : *(a) Projection of the wurtzite structure along the [0001] direction. (b) Corresponding diffraction pattern.*

In the hexagonal system system there is not simple relationship between the plane (hkil) and the direction [hkil]. The condition that a direction [uvtw] lies in or is parallel to a plane (hkil) is in four-dimensional notation the zero scalar product relationship:

$$uh + vk + ti + wl = 0 \tag{A.1}$$

The normal to the plane with indices (hkil) is the cartesian 4-vector [h,k,i,l/λ], where λ is equal to :

$$\lambda = (2/3)^{1/2}(c/a) \tag{A.2}$$

and a, c are the lattice constants of the examined material.

The relationships between four and three indices notations are:

- for directions (direct space coordinates):

$$[hkil] \rightarrow 1/3[(h-i),(k-i),l] \tag{A.3}$$

$$[stu] \rightarrow [(2s-t),(-s+2t),(-s-t),3u] \tag{A.4}$$

- for planes (reciprocal space coordinates):

$$(hkil) \rightarrow (h,k,l) \tag{A.5}$$

$$(stu) \rightarrow (s,t,(-s-t),u) \tag{A.6}$$

The angle between two directions symbolized by $[h_1k_1i_1l_1]$ and $[h_2k_2i_2l_2]$ is given by the following relationship:

$$\cos\alpha = \frac{h_1h_2 + k_1k_2 + i_1i_2 + \lambda^2 l_1l_2}{\sqrt{h_1^2 + k_1^2 + i_1^2 + \lambda^2 l_1^2}\,\sqrt{h_2^2 + k_2^2 + i_2^2 + \lambda^2 l_2^2}} \tag{A.7}$$

where λ is given by equation A.2.

Finally, the relationship that gives the angle between the direction $[h_1k_1i_1l_1]$ and the plane $(h_2k_2i_2l_2)$ is:

$$\sin\alpha' = \frac{h_1h_2 + k_1k_2 + i_1i_2 + l_1l_2}{\sqrt{h_1^2 + k_1^2 + i_1^2 + \lambda^2 l_1^2}\,\sqrt{h_2^2 + k_2^2 + i_2^2 + l_2^2/\lambda^2}} \tag{A.8}$$

Appendix B

Linear Elasticity

B.1 Elastic constants definition

In the framework of linear elasticity, according to the Hooke's law, the stress σ_{ij} of a material is directly proportional to the strain ϵ_{ij}.

$$\sigma_{ij} = \sum_{kl} C_{ijkl} \cdot \epsilon_{kl}, \tag{B.1}$$

where C_{ijkl} is the tensor of the elastic module.

In order to simplify notations pairs of indices $\{xx, yy, zz, yz, zx, xy\}$ are replaced by indices $\{1, 2, 3, 4, 5, 6\}$. This is possible because both stress σ_{ij} and strain ϵ_{ij} are required to be symmetric tensors. So strain and stress matrices become column vectors:

$$\epsilon_{ij} \rightarrow \epsilon = \begin{cases} \epsilon_1 = \epsilon_{11} \\ \epsilon_2 = \epsilon_{22} \\ \epsilon_3 = \epsilon_{33} \\ \epsilon_4 = 2\epsilon_{23} = 2\epsilon_{32} \\ \epsilon_5 = 2\epsilon_{13} = 2\epsilon_{31} \\ \epsilon_6 = 2\epsilon_{12} = 2\epsilon_{21} \end{cases} \qquad \sigma_{il} \rightarrow \sigma = \begin{cases} \sigma_1 = \sigma_{11} \\ \sigma_2 = \sigma_{22} \\ \sigma_3 = \sigma_{33} \\ \sigma_4 = \sigma_{23} = \sigma_{32} \\ \sigma_5 = \sigma_{13} = \sigma_{31} \\ \sigma_6 = \sigma_{12} = \sigma_{21} \end{cases} \tag{B.2}$$

And, the elastic module C_{ijkl} can be represented by a matrix (second-rank tensor). For

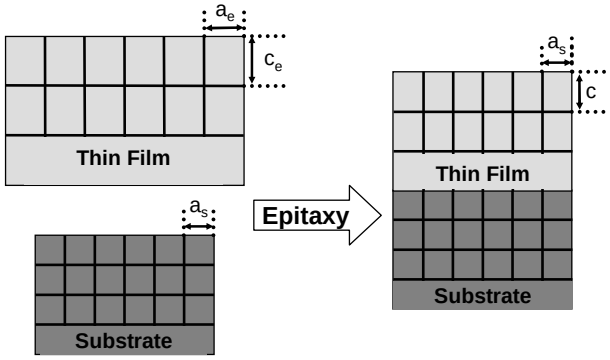

Figure B.1 : *Elastic deformation of a thin film deposited on a substrate due to biaxial strain. The epilayer adapts its lattice parameters to these of the substrate.*

the case of an hexagonal crystal this matrix takes the following form:

$$C = \begin{pmatrix} C_{11} & C_{12} & C_{13} & 0 & 0 & 0 \\ C_{12} & C_{11} & C_{13} & 0 & 0 & 0 \\ C_{13} & C_{13} & C_{33} & 0 & 0 & 0 \\ 0 & 0 & 0 & C_{44} & 0 & 0 \\ 0 & 0 & 0 & 0 & C_{44} & 0 \\ 0 & 0 & 0 & 0 & 0 & C_{66} \end{pmatrix}. \tag{B.3}$$

It contains six elastic modules, five of which are independent and $C_{66} = (C_{11} - C_{12})/2$. Table 1.3 in Chapter 1 summarize the values of the elastic coefficients of wurtzite III nitrides.

B.2 Coherent deposition of a film on a substrate

When a thin film is coherently deposited on a substrate with a misfit f_0, it is strained in order to adapt its lattice parameter to that of the substrate (see Figure B.1). The in-plane lattice misfit, f_0, between the film and the substrate is defined by the equation:

$$f_0 = \frac{a_e - a_s}{a_s} \tag{B.4}$$

Using the equation B.3, we can calculate the deformation of the film due to biaxial strain. For the hexagonal crystals and when the growth is carried out on a (0001) plane, the strain components ϵ_1 and ϵ_2 are equal to the lattice misfit f_0:

$$\epsilon_1 = \epsilon_2 = f_0 \tag{B.5}$$

Since along the growth axis the surface is free of stress, $\sigma_3 = 0$, considering in-plane isotropy the Hooke's law can be written as:

$$\begin{pmatrix} \sigma_1 \\ \sigma_1 \\ 0 \end{pmatrix} = \begin{pmatrix} C_{11} & C_{12} & C_{13} \\ C_{12} & C_{11} & C_{13} \\ C_{13} & C_{13} & C_{33} \end{pmatrix} \begin{pmatrix} \epsilon_1 \\ \epsilon_1 \\ \epsilon_3 \end{pmatrix} \tag{B.6}$$

As a consequence, the biaxial strain induces a strain ϵ_3 perpendicular to the surface and of opposite sign along the [0001] axis, which is equal to:

$$\epsilon_3 = -2\frac{C_{13}}{C_{33}}\epsilon_1 \tag{B.7}$$

Equation B.7 can be written in terms of lattice parameter c as following :

$$c = c_e + 2\,\frac{C_{13}}{C_{33}}\frac{c_e}{a_s}(a_e - a_s) \tag{B.8}$$

Finally, from equations B.6, B.5 and B.7 we obtain:

$$\sigma_1 = (C_{11} + C_{12} - 2\frac{C_{13}^2}{C_{33}})(\frac{a_e - a_s}{a_s}) \tag{B.9}$$

Appendix C

Basic Parameters of GaN and AlN

C.1 Gallium Nitride (GaN)

Crystal structure	Wurtzite	Zinc Blende
Group of Symmetry	$P6_3mc$ - C_{6V}^4	$F\bar{4}3m$ - T_d^2
Density (g/cm^3)	6.15 [1]	6.15 [1]
Dielectric constant		
Static	8.9-9.5 [1]	9.7 [1]
High frequency	5.35 [2]	5.3 [2]
Electron affinity (eV)	4.1 [3] ; 3.4 [4]	4.1 [3] ; 3.4 [4]
Lattice constants (nm)	**a**= 0.3189 [5] **c**= 0.5185 [5]	**a**=0.452 [6]
Optical phonon energy (meV)	91.8 [1]	91.9 [1]
BAND STRUCTURE		
Energy gap (eV) (Gamma Valley)	3.39 [5]	3.2 [7]
Temperature dependence of the energy gap $0 < T < 600$	$3.57 - 7.4 \times 10^{-4}$ $\times T^2/(T + 600)$	$3.37 - 7.4 \times 10^{-4}$ $\times T^2/(T + 600)$
Conduction Band		
Effective electron mass (in units of m_0)	0.22 [8]	0.15 [9]
Effective conduction band density of states (cm^{-3})	2.6×10^{18}	1.4×10^{18}
Valence Band		
Energy of spin-orbital splitting E_{SO} (eV)	0.011-0.018 [8]	0.017 [8]
Energy of crystal-field splitting E_{cr} (eV)	0.011-0.022 [8]	
Effective hole mass (in units of m_0) heavy	1.0 [8]	1.3 [9]
Effective valence band density of states (cm^{-3})	2.5×10^{19} [8]	4.1×10^{19} [8]

ELECTRICAL PROPERTIES		
Breakdown field (Vcm^{-1})	5×10^6 [1]	5×10^6
Mobility ($cm^2V^{-1}s^{-1}$)		
Electrons	1000 [10]	$\leq$ 1000 [11]
Holes	$\leq$ 200 [12]	$\leq$ 350 [13]
Diffusion coefficient (cm^2s^{-1})		
Electrons	25	25
Holes	5	9
Electron saturation velocity (10^7cms^{-1})	2 [14](exp) 2-2.5 [15] (calc)	2.0 [15]
Peak velocity (10^7cms^{-1})	2 [14](exp) 2.5-3 [15](calc)	2.5 [15]
Peak velocity field (kV/cm)	150-180 [15]	100-150 [15]
OPTICAL PROPERTIES		[9]
Infrared refractive index	2.3 [1]	2.3 [1]
Refractive index spectra	[16], [17]	[18]
Reflectance spectra	[19], [20], [21]	
Absorption spectra	[20], [16], [18]	
Photoluminescence spectra	[21], [22]	[23], [24]
THERMAL PROPERTIES		
Debye temperature (K)	820 [25]	820 [25]
Thermal conductivity ($Wcm^{-1}C^{-1}$)	$>$ 1.95 [26], [27], [28]	$>$ 1.95 [26], [27], [28]
Thermal diffusivity (cm^2s^{-1})	0.65	0.65
Thermal expansion, linear (C^{-1})	$\alpha_a = 5.59 \times 10^{-6}$ [1] $\alpha_c = 3.17 \times 10^{-6}$ [1]	
MECHANICAL PROPERTIES See Table 1.3		
PIEZOELECTRIC CONSTANTS (Cm^{-2}) [29], [30], [31], [8]		
e_{15}	-0.30	
e_{31}	(-0.3)-(-0.55)	
e_{33}	0.6-1.12 1.27	
e_{14}		0.4 [32]

Table C.1 : *Basic properties of GaN*

C.2 Aluminium Nitride (AlN)

Crystal structure	Wurtzite
Group of Symmetry	$P6_3mc$ - C_{6V}^4
Density (g/cm^3)	3.257 [33]
Dielectric constant	
Static	8.5 [1]
High frequency	4.68-4.84 [34],4.77 [1]
Electron affinity (eV)	0.6 [35] ; 1.9 [36]
Lattice constants (nm)	**a**= 0.3112 [37], **c**= 0.4982 [37]
Optical phonon energy (meV)	113 [1]
BAND STRUCTURE	
Energy gap (eV)	6.23 [8]
Temperature dependence of the energy gap [38]	$6.32 - 1.799 \times 10^{-3} \times T^2/(T + 1462)$
Conduction Band	
Effective electron mass (in units of m_0)	0.3 [8]
Effective conduction band density of states (cm^{-3})	4.1×10^{18}
Valence Band	
Effective hole mass (in units of m_0): Heavy	
for k_z direction m_{hz}	3.53 [39]
for k_x direction m_{hx}	10.42 [39]
Effective valence band density of states (cm^{-3})	4.8×10^{20}
ELECTRICAL PROPERTIES	
Breakdown field (Vcm^{-1})	$(1.2 \div 1.8) \times 10^6$
Mobility ($cm^2V^{-1}s^{-1}$)	
Electrons	135 [40]
Holes	14 [12]
Diffusion coefficient (cm^2s^{-1})	
Electrons	3.3
Holes	0.3
Electron saturation velocity (10^7cms^{-1})	1.4 [40]
Peak velocity (10^7cms^{-1})	1.7 [40]
Peak velocity field (kV/cm)	450 [40]
OPTICAL PROPERTIES	
Infrared refractive index	2.14 [1]
Refractive index spectra	[18], [41], [42], [43]
Reflectance spectra	[44], [45]
Absorption spectra	[46], [42], [47]
Photoluminescence spectra	[48], [49]

THERMAL PROPERTIES	
Debye temperature (K)	820 [50]
Thermal conductivity ($Wcm^{-1}C^{-1}$)	2.85 [51]
Thermal diffusivity (cm^2s^{-1})	1.47
Thermal expansion, linear (C^{-1})	$\alpha_a = 4.2 \times 10^{-6}$ [1] $\alpha_c = 5.3 \times 10^{-6}$ [1]
Specific heat at 300K ($Jg^{-1}C^{-1}$)	0.73 [52]
At $300K < T < 1800K$ [52]	$1.097 + 7.99 \times 10^{-5} \times T - 0.358 \times 10^5 \times T^{-2}$
At $1800K < T < 2700K$ [52]	$0.892 + 0.188 \times 10^{-3} \times T$
MECHANICAL PROPERTIES	
See Table 1.3	
PIEZOELECTRIC CONSTANTS (Cm^{-2})	[29], [31], [53]
e_{15}	(-0.4)-(-0.48)
e_{31}	(-0.58)-(-0.89)
e_{33}	0.74-1.55

Table C.2 : *Basic properties of AlN*

Bibliography

[1] H. Harima. *J. Phys.: Cond. Matt.*, 14:967, 2002.

[2] V. Bougrov, M. E. Levinshtein, S.L. Rumyantsev, and A.Zubrilov. *Properties of Advanced Semiconductor Material GaN, AlN, InN, BN, SiC, SiGe.* John Wiley and Sons, Inc., New York, 2001.

[3] J.L. Pankove and H. Schade. *Appl. Phys. Lett.*, 25:53, 1974.

[4] R.Y. Korotkov, J.M. Gregie, and B.W. Wessels. *Appl. Phys. Lett.*, 80:1731, 2002.

[5] H.P. Maruska and J.J. Tietjen. *Appl. Phys. Lett.*, 15:327, 1969.

[6] H. Morkoç, S. Strite, G.B. Gao, M.E. Lin, B. Sverdlov, and M.Burns. *J. Appl. Phys.*, 76:1363, 1994.

[7] T. Lei, T. D. Moustakas, R. J. Graham, Y. He, and S. J. Berkowitz. *J. Appl. Phys.*, 71:4933, 1992.

[8] I. Vurgaftman, J.R. Meyer, and L.R. Ram-Mohan. *J. Appl. Phys.*, 89:5815, 2001.

[9] M. Fanciulli, T. Lei, and T.D. Moustakas. *Phys. Rev. B*, 48:15144, 1993.

[10] S. Nakamura, T. Mukai, and M. Senoh. *J. Appl. Phys.*, 71:5543, 1992.

[11] J.G. Kim, A.C. Frenkel, H. Liu, and R.M. Park. *Appl. Phys. Lett.*, 65:91, 1994.

[12] D.K. Gaskill, L.B. Rowland, and K. Doverspike. *Properties of Group III Nitrides.* EMIS datareviews series No.11, 1995.

[13] D.J. As, D. Schikora, A. Greiner, M. Lubbers, J. Mimkes, and K. Lischka. *Phys. Rev. B*, 54:11118, 1996.

[14] M. Wraback, H. Shen, J.C. Carrano, T. Li, J.C. Campbell, M.J. Schurman, and I.T. Ferguson. *Appl. Phys. Lett.*, 76:1155, 2000.

[15] J. Kolnik, I.H. Oguzman, K.F. Brennan, R. Wang, P.P. Ruden, and Y. Wang. *J. Appl. Phys.*, 78:1033, 1995.

[16] J.F. Muth, J.D. Brown, M.A.L. Johnson, Z. Yu, R.M. Kolbas, J.W. Cook Jr., and J.F. Schetzina. *MRS Internet J. Nitride Semicond. Res.*, 4S1:G5.2, 1999.

[17] G. Yu, G. Wang, H. Ishikawa, M. Umeno, T. Soga, T. Egawa, J. Watanabe, and T. Jimbo. *Appl. Phys. Lett.*, 70(24):3209, 1997.

[18] R. Goldhan and S. Shokhovets. *III Nitride Semiconductors optical properties II.* Taylor and Francis, 2002.

[19] S. Bloom, G. Harbeke, E. Meier, and I.B. Ortenburger. *Phys. Stat. Solidi*, 66:161, 1974.

[20] R. Dingle, K.L. Shaklee, R.F. Leheny, and R.B. Zetterst. *Appl. Phys. Lett.*, 19(1):5, 1971.

[21] R. Stepniewski, A. Wysmolek, K.P. Korona, and J.M. Branowski. *III Nitride Semiconductors optical properties I.* Taylor and Francis, 2002.

[22] H.X. Jiang, J.Y. Lin, and W.W. Chow. *III Nitride Semiconductors optical properties I.* Taylor and Francis, 2002.

[23] J. Holst, L. Eckey, A. Hoffmann, I. Broser, B. Schottker, D.J. As, D. Schikora, and K. Lischka. *Appl. Phys. Lett.*, 72:1439, 1998.

[24] J. Wu, H. Yaguchi, and K. Onade. *III Nitride Semiconductors optical properties II.* Taylor and Francis, 2002.

[25] J.C. Nipko, C.K. Loong, C.M. Balkas, and R.F. Davis. *Appl. Phys. Lett.*, 73:34, 1998.

[26] D.I. Florescu, V.M. Asnin, F.H. Pollak, R.J. Molnar, and C.E.C. Wood. *J. Appl. Phys.*, 88:3295, 2000.

[27] E. K. Sichel and J.I. Pankove. *J. Phys. Xhem. Solids*, 38:330, 1977.

[28] J. Zou, D. Kotchetkov, A.A. Balandin, D.I. Florescu, and F.H. Pollak. *J. Appl. Phys.*, 92:2534, 2002.

[29] F. Bernardini and V. Fiorentini. *Appl. Phys. Lett.*, 80:4145, 2002.

[30] A.D. Bykhovski, B.L. Gelmont, and M.S. Shur. *J. Appl. Phys.*, 81:6332, 1997.

[31] I.L. Guy, S.Muensit, and E.M. Goldys. *Appl. Phys. Lett.*, 75:4133, 1999.

[32] M.S. Shur, B. Gelmont, and A. Khan. *J. Electronic Materials*, 25:777, 1996.

[33] G.A. Slack and T.F. McNelly. *J. Crystal Growth*, 34:263, 1976.

[34] S.Strite and H. Morkoç. *J. Vac. Sci. Technol. B*, 10(4):1237, 1992.

[35] V.M. Vermudez, T.M. Jung, K. Doverspike, and A.E. Wickenden. *J. Appl. Phys.*, 79:110, 1996.

[36] C.I. Wu and A.Kahn. *Appl. Phys. Lett.*, 74:546, 1999.

[37] W.M. Yim, E.J. Stofko, P.J. Zanzucchi, J.I. Pankove, M. Ettenberg, and S.L. Gilbert. *J. Appl. Phys.*, 44:292, 1973.

[38] Z. P. Guan, A. L. Cai, H. Porter, J. Cabalu, J. Chen, S. Huang, and R. E. Giedd. *J. Vac. Sci. Technol. A*, 19:280, 2001.

[39] M. Suzuki and T. Uenoyama. *J. Appl. Phys.*, 80:6868, 1996.

[40] S.K. O'Leary, B.E. Fouytz, M.S. Shur, U.V. Bhaphar, and L. Eastman. *Sol. St. Comm.*, 105:621, 1998.

[41] X. Xu, H. Liu, C. Shi, Y. Zhao, S. Fung, and C.D. Beling. *J. Appl. Phys.*, 90:6130, 2001.

[42] H. Demiryont, L.R. Thompson, and G.J. Collins. *Appl. Optics*, 25:1311, 1986.

[43] S.A. Geidur and A.D. Yaskov. *Opt. Spectrosc.*, 48:618, 1980.

[44] I. Akasaki and M. Hashimoto. *Sol. State Commun.*, 5:851, 1967.

[45] O. Quo, M. Nishio, H. Ogawa, and A. Yoshida. *Phys. Rev B*, 64:113105/1, 2001.

[46] C.R. Aita, C.J.G. Kubiak, and F.Y.H. Smith. *J. Appl. Phys.*, 66:4360, 1989.

[47] P.B. Perry and R.F. Rutz. *Appl. Phys. Lett.*, 33:319, 1978.

[48] Y.C. Lan, X.L. Chen, Y.G. Gao, Y.P. Xu, L.D. Xun, T. Xu, and J.K. Liang. *J. Cryst. Growth*, 207:247, 1999.

[49] J. Sun, J. Wu, H. Ling, W. Shi, Z. Ying, and F. Li. *Phys. Lett. A*, 280:381, 2001.

[50] J.C. Nipko and C.K. Loong. *Phys. Rev B*, 57:10550, 1998.

[51] G.A. Slack, R.A. Tanzilli, R.O Pohl, and J.W. Vandersande. *J. Phys. Chem. Solids*, 48:641, 1987.

[52] V.I. Koshchenko, Y.K. Grinberg, and A.F. Demidenko. *Inorg. Mater.*, 20:1550, 1985.

[53] D. Liufu and K.C. Kao. *J. Vac. Sci. Technol. A*, 16:2360, 1998.

Appendix D

Local lattices and Distances in the Direct and Reciprocal spaces

D.1 Local Lattices

Consider a local two-dimensional lattice appearing over a region R of the real space. This lattice is defined by two vectors $\mathbf{a_1}(R)$ and $\mathbf{a_2}(R)$ whose coordinates in an orthogonal basis B are respectively a_{x1}, a_{y1} and a_{x2}, a_{y2}. The corresponding reciprocal local lattice vectors $\mathbf{g_1}(R)$ and $\mathbf{g_1}(R)$ are defined by the usual relations :

$$\mathbf{a_1}(R)\cdot\mathbf{g_1}(R)=1\ ,\quad \mathbf{a_1}(R)\cdot\mathbf{g_2}(R)=0\ ,\quad \mathbf{a_2}(R)\cdot\mathbf{g_1}(R)=0\ ,\quad \mathbf{a_2}(R)\cdot\mathbf{g_1}(R)=1 \tag{D.1}$$

Introducing the identity matrix $\mathbf{I}$, the transpose $\mathbf{G^T}$ of a matrix $\mathbf{G}$ and the lattice matrices $\mathbf{A}(R)$ and $\mathbf{G}(R)$ defined by :

$$\mathbf{A}(R)=\begin{pmatrix} a_{x1}(R) & a_{x2}(R)\\ a_{y1}(R) & a_{y2}(R)\end{pmatrix}\ \mathbf{G}(R)=\begin{pmatrix} g_{x1}(R) & g_{x2}(R)\\ g_{y1}(R) & g_{y2}(R)\end{pmatrix}\ \mathbf{G^T}(R)=\begin{pmatrix} g_{x1}(R) & g_{y1}(R)\\ g_{x2}(R) & g_{y2}(R)\end{pmatrix} \tag{D.2}$$

the relations D.1 can be expressed in a matrix form by :

$$\mathbf{A}(R)\cdot\mathbf{G^T}(R)=\mathbf{I}\ \ or\ \mathbf{A}(R)=(\mathbf{G^T}(R))^{-1}\ \ or\ \mathbf{G^T}(R)=\mathbf{A^{-1}}(R) \tag{D.3}$$

The coordinates of vector $\mathbf{a_1}(R)$ are noted $(a_{x1}(R), a_{y1}(R))$ instead of $(a_{1x}(R), a_{1y}(R))$ in order that the first and second indexes of matrix coefficients refer respectively to the rows and columns of the matrix.

D.2 Distances in the Direct and Reciprocal spaces

In the presentation of the GPA method (Section3.2 of chapter 3), a number of conventions were used for the direct and reciprocal spaces. In particular $\mathbf{r}$ refer to two-dimensional vectors of the direct space, which is the image space. For HRTEM images, the natural and physical unit of $\mathbf{r}$ is the nanometer (nm). In digital form, this vector $\mathbf{r}$ is represented by a vector $\mathbf{r_p}$ evaluated in pixels. The relationship between $\mathbf{r}$ and $\mathbf{r_p}$ is:

$$\mathbf{r} = \text{scale}.\mathbf{r_p} \tag{D.4}$$

where scale is the length of a pixel in nm.

$\mathbf{g}$ designs a reciprocal lattice vector, whose physical unit is the inverse of a nanometer (nm^{-1}). In the numerical Fourier Transform, this vector is evaluated in pixels by the vector $\mathbf{g_p}$. The relation between $\mathbf{g}$ and $\mathbf{g_p}$ is given by:

$$g_x = \frac{g_{xp}}{N_x * \text{scale}} \qquad g_y = \frac{g_{yp}}{N_y * \text{scale}} \tag{D.5}$$

where N_x and N_y are the pixel size of the image and g_x,g_y and g_{xp},g_{yp} are the coordinates of the vectors $\mathbf{g}$ and $\mathbf{g_p}$ in the natural orthogonal basis B=(O,x,y) of the digitized image. Precisely, O is the pixel point having coordinates (0,0), and x and y are respectively parallel to the rows and columns of the images. For simplicity, in section3.2, it was assumed that scale=1 (or $\mathbf{r}$=$\mathbf{r_p}$).

Appendix E

List of examined samples

Name	**Substrate**	**Buffer layer**	**Sample**	**Interest**
S1018	6H-SiC (0001)	1μm AlN	(45 nm $Al_{0.25}Ga_{0.75}N$ /1 nm GaN (QDs) /15 nm $Al_{0.25}Ga_{0.75}N$ /1nm GaN (QDs) /45nm $Al_{0.25}Ga_{0.75}N$) $\times$4 / 120 nm AlN	Structures for a UV laser. Non-Correlated GaN QDs.
S1019	6H-SiC (0001)	1μm AlN	(40 nm $Al_{0.25}Ga_{0.75}N$ /1 nm GaN (QDs) /8 nm $Al_{0.25}Ga_{0.75}N$ /1 nm GaN (QDs) /40 nm $Al_{0.25}Ga_{0.75}N$) $\times$9 / 100 nm AlN	Structures for a UV laser. Correlated GaN QDs.
S1029	4H-SiC (0001) Vicinal 8^o	10 nm AlN	1μm GaN	Growth of GaN on a vicinal surface.
S1030	4H-SiC (0001) Vicinal 8^o	No	1μm AlN	Growth of AlN on a vicinal surface [1].
S1031	4H-SiC (0001) Vicinal 7.7^o	410 nm AlN	(1.25 nm GaN QDs / 16 nm AlN)$\times$7 / 1.25 nm GaN	Linear alignment of GaN QDs on AlN grown on vicinal SiC substrate [2, 3].
S1050	GaN MOCVD on sapphire	35 nm GaN	350 nm InN	Study of the InN/GaN interface [4].
S1051	6H-SiC (0001)	0.5μm AlN	(1.5 nm GaN QDs / 10 nm AlN) $\times$80	Strain distribution in the QD superlattice [5, 6].
S1058	1.5μm AlN (MOCVD) on Sapphire	0.5μm AlN	(0.75 nm GaN QDs / 25 nm AlN) $\times$3	GaN islanding by spontaneous rearrangement of a strained 2D layer on (0001) AlN [7, 8].
S1060	1.5μm AlN (MOCVD) on Sapphire	0.5μm AlN	0.25 nm GaN/ 40 nm AlN / 0.5 nm GaN/ 40 nm AlN/ (0.3 nm GaN QW/ 6 nm AlN/ 0.75 nm GaN QDs/ 40 nm AlN) $\times$3 / (0.2 nm GaN QW/ 4 nm AlN) $\times$3 / (0.4 nm GaN QW/ 8 nm AlN) $\times$3 / 0.12 nm GaN QW/ 6 nm AlN/ 0.25 nm GaN QW/ 6 nm AlN/ 0.4 nm GaN QW/ 60 nm AlN	Structural quality of QWs and QDs.
S1066	1.5μm AlN (MOCVD) on Sapphire	No	0.2μm $Al_{0.3}Ga_{0.7}N$ / 2.5 nm GaN QW/ 12 nm $Al_{0.3}Ga_{0.7}N$ / 1.5 nm GaN QW/ 12 nm $Al_{0.3}Ga_{0.7}N$ / 0.5 nm GaN QW / 40 nm $Al_{0.3}Ga_{0.7}N$	Structural quality of GaN QWs grown by Atomic Layer Epitaxy.

Name	Substrate	Buffer layer	Sample	Interest
S1303	$1\mu m$ AlN (MOCVD) on Sapphire	100 nm AlN	(1.5 nm GaN QDs / 10 nm AlN) $\times 50$	Morphology and Structural quality of the GaN QDs.
S1321	C-face 4H-SiC	No	500 nm GaN	Polarity of the sample [9, 10].
S1393	$1\mu m$ AlN (MOCVD) on Sapphire	70 nm AlN	2.5 nm GaN QDs / 50 nm AlN	Presence of misfit dislocations and structural quality of the GaN QDs.
S1569	$1\mu m$ AlN (MOCVD) on Sapphire	20 nm AlN	1.5 nm Gan QW/ 40 nm AlN ($T_S = 750^o$)/ 1.5 nm GaN QW/ 20 nm AlN ($T_S = 700^o$)/ 1.5 nm GaN QDs/ 50 nm AlN ($T_S = 700^o$)/ 3 nm GaN QW/ 20 nm AlN ($T_S = 700^o$)/ 3 nm GaN QDs/ 40 nm AlN ($T_S = 700^o$)	Influence of AlN overgrowth on the structural properties of GaN QWs and QDs [11].
S1599	$1\mu m$ AlN (MOCVD) on Sapphire	No	1 nm GaN QD / 12 nm AlN / (1 nm GaN:Eu (1.7%) QDs/ 12 nm AlN) $\times 10$ / 10 nm GaN	Structural analysis and chemical composition of GaN QDs doped with Eu.
S1608	$1\mu m$ AlN (MOCVD) on Sapphire	50 nm AlN	20 nm GaN QW/ 50 nm AlN ($T_S = 750^o$)/ 1.5 nm GaN QDs/ 20 nm AlN ($T_S = 750^o$)/ 1.5 nm GaN QDs/ 50 nm AlN ($T_S = 700^o$)/20 nm GaN QW/ 50 nm AlN ($T_S = 700^o$)	Influence of AlN overgrowth on the structural properties of GaN QWs and QDs [11].
S1725	C-face 6H-SiC	90 nm AlN	(1.125 nm GaN QDs/ 15 nm AlN) $\times 4$/ 25 nm AlN/ (1.125 nm GaN QDs/ 6 nm AlN) $\times 4$/ 50 nm AlN	Morphology and Structural quality of N-face polarity GaN QDs [12].
S1832	(11-20) SiC	40 nm AlN	(0.4 nm GaN QDs / 6 nm AlN) $\times 5$/ 6 nm AlN/ 0.4 nm GaN QDs	Morphology and Structural quality of GaN QDs grown along the [1,1,-2,0] direction.
E201	$1\mu m$ AlN (MOCVD) on Sapphire	200 nm AlN	(7 nm GaN QW / 5 nm AlN)$\times 25$ / 35 nm GaN	Structural quality of the Ga-face GaN QW superlattice [13, 14].
E274	C-face 4H-SiC	100 nm AlN	(7 nm GaN QW / 5 nm AlN)$\times 25$ / 20 nm GaN	Structural quality of the N-face GaN QW superlattice [14].
E289	Sapphire	$1\mu m$ AlN	$1.2\mu m$ GaN	Dislocation density.

Name	**Substrate**	**Buffer layer**	**Sample**	**Interest**
E391	C-face 4H-SiC	No	540 nm GaN:Mg $[Mg_{SIMS}] = 2.9 \times 10^{18} cm^{-3}$	Structural quality of heavily Mg doped GaN layer [15, 16].
140799	c-plane Sapphire	No	1.7 μm GaN:Mg $[Mg_{SIMS}] = 1 \times 10^{17} cm^{-3}$	Structural quality of slightly Mg-doped GaN layer [15, 16].
N231	$2\mu m$ GaN (MOCVD) on Sapphire	10 nm GaN	90 nm $In_{0.069}Al_{0.261}GaN$ / (3 nm GaN / 7.5 nm $In_{0.069}Al_{0.261}GaN$ QW)×10	Structural quality and chemical composition of the $In_{0.069}Al_{0.261}GaN$ QWs.
No10	$1\mu m$ AlN (MOCVD) on Sapphire	100 nm AlN	0.7 nm GaN QW / 50 nm AlN	Structural quality of the GaN QW.
No40	$1\mu m$ AlN (MOCVD) on Sapphire	100 nm AlN	2.6 nm GaN QW /50 nm AlN	Structural quality of the GaN QW [17].
S1638	6H-SiC	10 nm AlN	(1.5 nm GaN / 7 nm AlN QDs)×200	ESRF XLD measurements.
E242	6H-SiC	10 nm AlN	(1.5 nm GaN / 7 nm AlN QDs)×75 Non correlated QDs	ESRF XLD measurements.
S1626	6H-SiC	10 nm AlN	(1.5 nm GaN / 7 nm AlN QDs)×50	ESRF XLD measurements.
S1635	6H-SiC	10 nm AlN	(1.5 nm GaN / 7 nm AlN QDs)×10	ESRF XLD measurements.
S1580	6H-SiC	10 nm AlN	(1.5 nm GaN / 7 nm AlN QDs)×3	ESRF XLD measurements.

Table E.1 : *Samples analyzed during this thesis.*

Bibliography

[1] J. Brault, E. Bellet-Amalric, S. Tanaka, F. Enjalbert, D. Le Si Dang, E. Sarigiannidou, J.-L. Rouviere, G. Feuillet, and B. Daudin. *Phys. Stat. Sol. (b)*, 240:314, 2003.

[2] J. Brault, S. Tanaka, E. Sarigiannidou, J.-L. Rouviere, B. Daudin, G. Feuillet, and H. Nakagawa. *J. Appl. Physics*, 93:3108, 2003.

[3] J. Brault, S. Tanaka, E. Sarigiannidou, H. Nakagawa, J.-L. Rouviere, G. Feuillet, and B. Daudin. *Phys. Stat. Sol. (b)*, 234(3):939, 2002.

[4] E. Bellet-Amalric, C. Adelmann, E. Sarigiannidou, J. L. Rouviere, G. Feuillet, E. Monroy, and B. Daudin. *J. Appl. Phys.*, 95:1127, 2004.

[5] V. Chamard, T. Schülli, M. Sztucki, T. H. Metzger, E. Sarigiannidou, J. L. Rouvière, M. Tolan, C. Adelmann, and B. Daudin. *Phys. Rev. B*, 69:125327, 2004.

[6] E. Sarigiannidou, A.D. Andreev, B. Daudin, and J. L. Rouviere. *Phys. Rev. Lett. to be submitted.*

[7] C. Adelmann, N. Gogneau, E. Sarigiannidou, J. L. Rouviere, , and B. Daudin. *Appl. Phys. Lett.*, 81:3064, 2002.

[8] C. Adelmann, B. Daudin, E. Monroy, E. Sarigiannidou, J. L. Rouviere, Y. Hori, J. Brault, N. Gogneau, S. Fanget, and C. Bru-Chevallier. *Phys. Stat. Sol. (b)*, 234:931, 2002.

[9] E. Monroy, E. Sarigiannidou, F. Fossard, N. Gogneau, E. Bellet-Amalric, J.-L. Rouviere, S. Monnoye, H. Mank, and B. Daudin. *Appl. Phys. Lett.*, 84(18):3684, 2004.

[10] E. Monroy, E. Sarigiannidou, F. Fossard, F. Enjalbert, N. Gogneau, E. Bellet-Amalric, J. Brault, J.-L. Rouviere, Le Si Dang, S. Monnoye, H. Mank, and B. Daudin. *Mat. Sci. Forum*, 457-460:1573, 2004.

[11] N. Gogneau, D. Jalabert, E. Monroy, E. Sarigiannidou, J.L. Rouviere adn T. Shibata, M. Tanaka, J.M. Gerard, and B. Daudin. *J. Appl. Phys.*, 96:1104, 2004.

[12] N. Gogneau, E. Sarigiannidou, E. Monroy, S. Monnoye, H. Mank, and B. Daudin. *Appl. Phys. Lett.*, 85:1421, 2004.

[13] E Sarigiannidou, J L Rouvière, G Radtke, P Bayle-Guillemaud, E Monroy, and B Daudin. *Inst. Phys. Conf. Ser. to appear.*

[14] E. Sarigiannidou, E. Monroy, P. Bayle-Guillemaud, N. Gogneau, B. Daudin, and J. L. Rouvière. *Superlattices Superlattices and Microsctructures to appear.*

[15] E. Monroy, M. Hermann, E. Sarigiannidou, T. Andreev, P. Holliger, S. Monnoye, H. Mank, B. Daudin, and M. Eickhoff. *J. Appl. Phys.*, 96:3709, 2004.

[16] E. Sarigiannidou, E. Monroy, M. Hermann, T. Andreev, P. Holliger, S. Monnoye, H. Mank, B. Daudin, and M. Eickhoff. *Phys. Stat. Sol. (c) to appear.*

[17] C. Adelmann, E. Sarigiannidou, D. Jalabert, Y. Hori, J.-L. Rouvière, B. Daudin, S. Fanget, C. Bru-Chevallier, T. Shibata, and M. Tanaka. *Appl. Phys. Lett.*, 82:4154, 2003.

Appendix F

X-ray absorption spectroscopy experiments

The X-ray absorption spectroscopy (XAS) is an extremely sensitive element selective technique and is commonly used to study local electronic and structural properties of systems with or without a long-range order [1]. X-ray absorption spectra recorded at an absorption edge of a given atom are a fingerprint of its electronic empty density of states. Since the density of states is linked to the structure, tiny structural changes should be reflected in x-ray absorption spectra. Moreover, polarization dependent XAS is a very efficient tool to study anisotropy of the density of states in ordered systems [2] *e.g.,* crystals, multilayers *etc.* In order to probe the strain of GaN quantum dots superlattices we used x-ray linear dichroism (XLD) spectroscopy that measures a difference in X-ray absorption cross-sections recorded with two orthogonally linearly polarized X-rays. To extract information about the strain state of the GaN QDs, the obtained XLD spectra were compared with the spectra recorded on a thick bulk like GaN epilayer.

We have performed XLD measurements at the Ga K-edge with the linear polarization vector either parallel or perpendicular to the c-axis of the superlattice. The X-ray linear dichroism measurements have been performed at the ID 12 beamline at the ESRF (Grenoble, France) in March 2004 [3]. The XLD spectra from QDs SLs were compared with the spectra recorded on a thick bulk like GaN epilayer (Figure F.1). Finally, the experimental results were compared with the x-ray linear dichroism spectra calculated with FDMNES code [4].

The question that we wanted to address is to know if there are any variations of the average strain of wurtzite GaN quantum dots SL embedded in an AlN matrix as a function of the number of repetitions. All investigated samples were grown by plasma-assisted molecular beam epitaxy on 6H-SiC substrate. An AlN buffer layer of 10 nm thickness was initially deposited before the growth of the SL. The nominal thickness of

the GaN QDs and the AlN matrix was 1.5 nm and 7 nm respectively. The number of repetitions was varied from 200 down to 3.

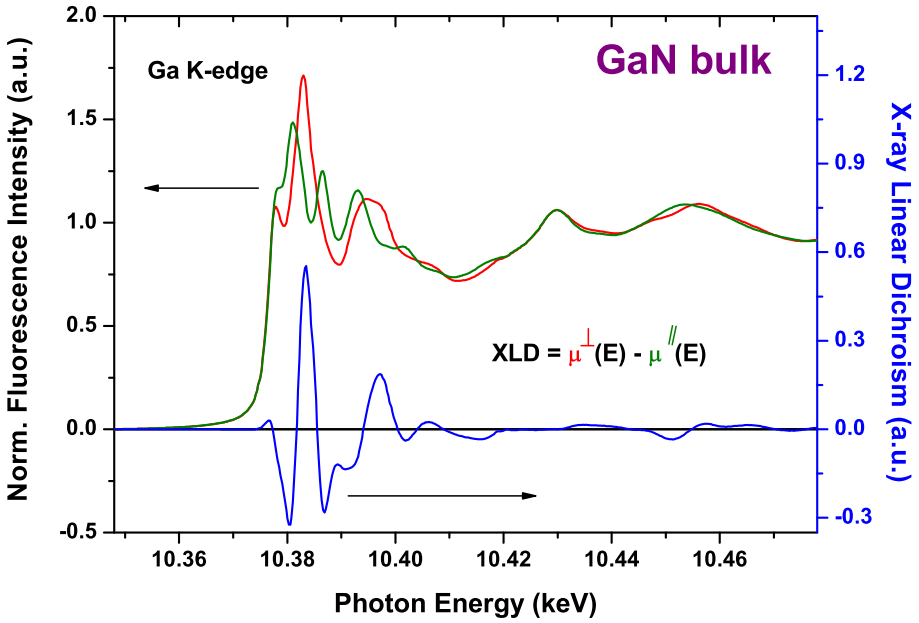

Figure F.1 : *Normalized fluorescence intensity measured at the Ga K-edge in GaN epilayer for two orthogonal linear polarization direction perpendicular to the sample surface (along the* ***c****-axis)[red line] and parallel to the sample surface (in the* ***a,b****-plane) [green line]. The difference is the so-called x-ray linear dichroism (right scale)[blue line]. The measurements have been performed at a grazing incidence of 10º. The absorption spectra have been corrected for self-absorption effects.*

Figure F.2 shows a magnified area of the x-ray linear dichroism spectra recorded at the Ga K-edge in GaN bulk epilayer (cyan line) and in several GaN QDs SLs with different number of repetitions. At a first sight, all the XLD spectra have nearly an identical spectral shape, which confirms that they possess the same local wurtzite symmetry as the bulk GaN. However, we can observe that: (i) the amplitude of the XLD signal increases for the peaks A' to D' when the number of QDs repetitions decreases from 200 down to 3 and is always stronger than the XLD signal of the GaN bulk, (ii) the XLD signal of the peak A" increases towards the bulk XLD signal when the number of repetitions decreases (iii) the XLD of the GaN bulk (cyan line) is shifted to lower energies (more pronounced at peak D' and higher energies).

From a preliminary analysis of the experimental results and simulations realized with the FDMNES code we can conclude several interesting points:

- the average strain state of the GaN QDs is always different compared to bulk GaN even for the highest number of repetitions

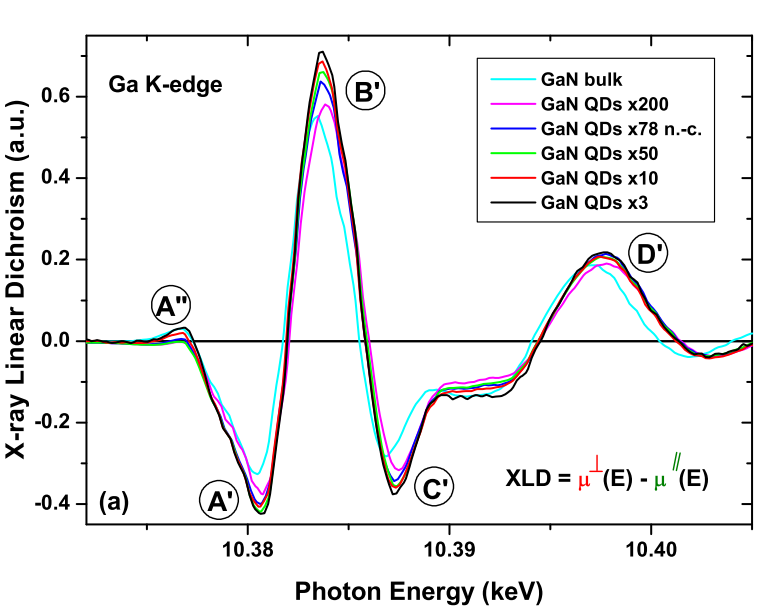

Figure F.2 : *X-ray linear dichroism measured at the Ga K-edge in GaN epilayer and in GaN quantum dots superlattcies embedded in AlN matrix with different number of repetitions. The measurements have been performed at a grazing incidence of 10°.*

- the dependance with the repetition number indicates that the GaN QDs located near the interface with the AlN buffer layer (first 1-3 QDs layers) are more strained compared to GaN QDs located away from the interface.

Further analysis are under way in order to extract quantitative information regarding the values of the strain distribution in the GaN QDs superlattices.

Bibliography

[1] J. Stöhr. *NEXAFS Spectroscopy*. Springer-Ferlag, Berlin, 1996.

[2] C. Brouder. *J. Phys.: Condens. Matter*, 2:701, 1990.

[3] A. Rogalev, J. Goulon, C. Goulon-Ginet, and C. Malgrange. *Magnetism and Synchrotron Radiation*, volume 565, Lecture Notes in Physics. E. Beaurepaire and F. Scheurer and G. Krill and J.P. Kappler (Eds.), Springer, 2001.

[4] Y. Joli. *Phys. Rev. B*, 63:125120, 2001.

Appendix G

Acronym

AFM: Atomic Force Microscopy

BF: Bright Field

CBED: Convergent Beam Electron Diffraction

CTEM: Conventional Transmission Electron Microscopy

DF: Dark Field

ECR: Electron Cyclotron Resonance

EELS: Electron Energy-Loss Spectrometry

EFTEM: Energy Filtered Transmission Electron Microscopy

EM: Electron Microscopy

ESI: Electron Spectroscopic Imaging

ESRF: European Synchrotron Radiation Facility

GPA: Geometric Phase Analysis

GIF: Gatan Image Filter

HPS: High-Pressure Synthesis

HRTEM: High Resolution Transmission Electron Microscopy

HRXRD: High-Resolution X-Ray Diffraction

HVPE: Hydride Vapor Phase Epitaxy

IDB: Inversion Domain Boundary

LDs: Laser Diodes

LEDs: Light-EmittingDiodes

MBE: Molecular Beam Epitaxy

ML: MonoLayer

MOCVD: Metal-Organic Chemical Vapor Deposition

MOVPE: Metal-Organic Vapor Phase Epitaxy

PAMBE: Plasma-Assisted Molecular-Beam Epitaxy

PL: PhotoLuminescence

QD: Quantum Dot

QW: Quantum Well

RBS: Rutherford Backscattering Spectroscopy

RF: Radio Frequency

RHEED: Reflection High-Energy Electron Diffraction

PLD: Pulsed Laser Deposition

SAD: Selected-Area Diffraction

SIMS: Secondary Ion Mass Spectroscopy

SL: SuperLattice

TDB: Translation Domain Boundary

TEM: Transmission Electron Microscopy

WB: Weak Beam

WL: Wetting Layer

XAS: X-ray Absorption Spectroscopy

XLD: X-ray Linear Dichroism

XRD: X-Ray Diffraction

XTEM: Cross section Transmission Electron Microscopy